Plasmonic interactions of gold nanoparticles with photoluminescent materials

A PhD thesis

by:

Carolyn Elliott

Supervisor:

Prof Louise Bradley

School of Physics

Trinity College Dublin

May 2024

ii

Abstract

The variable plasmonic resonances of metal nanoparticles have many applications across a wide range of fields, including the modification of the emission of photoluminescent materials. The plasmonic interactions of gold nanoparticles with two types of photoluminescent nanoparticles are explored. Plasmonic gold nanoparticles are synthesised: nanorods, bipyramids, and nanostars. The concentration of the reagents used in their syntheses are varied to produce nanoparticles with both sharp and broad plasmon resonances across the visible and near infrared spectrum, from 600 nm to above 1100 nm. The particles are also simulated, to observe the electric field enhancements of each particle type. A full investigation into the effect of varying the concentration of the reducing agent, l-ascorbic acid, in the synthesis of bipyramids is carried out. A nonlinear dependence is found, with a sharp increase at lower l-ascorbic acid concentrations and a plateau at higher concentrations, likely due to the change in ratio between l-ascorbic acid and $HAuCl_4$. Bipyramids with plasmon resonance wavelengths longer than 1000 nm are synthesised without the use of a regrowth step[1,2] or reducing seed concentration[3], but by only varying AA concentration, which has not been previously achieved in the literature.

Using the high electric field enhancements and small mode volume of the gold bipyramids, plasmon-induced two-photon polymerisation is shown. Polymerisation is demonstrated at powers far below the threshold typically required, as the bipyramids enhance the electric field of incoming laser light. A linear relationship between polymerised area (visible from SEM) and applied laser power is discovered, further corroborating this enhancement as the polymerised area depends on the electric field strength.

This enhanced polymerisation allows for spatial confinement of quantum dots. When quantum dots are added to the monomer, they remain wherever the solution is polymerised, and all other quantum dots are removed. They are trapped at the location of highest field enhancement, by design, and thus also interact with the plasmonic bipyramid. This provides a novel fabrication method for bipyramid-quantum dot pairs, with quantum dots preferentially confined at one tip of a bipyramid. The localisation of the quantum dots in this high field enhancement area results in emission rate enhancement and even strong coupling between the quantum dots and bipyramids, shown by Rabi splitting in the bipyramid scattering spectra.

Upconverting nanoparticles of various sizes, dopants, and emission wavelengths are synthesised. The dopants, Yb^{3+}, Er^{3+} and Tm^{3+}, give emission wavelengths from 450-800 nm and the sizes obtained by varying synthesis reaction volume and the speed of injecting the nucleation solution

were between ≈ 5-40 nm. Layer-by-layer deposition of these particles is carried out, resulting in samples with even and consistent upconversion emission. These are topped with polyelectrolyte spacer layers followed by nanostars, nanorods and bipyramids, resulting in enhancement by nanorods and bipyramids, with bipyramid enhancement of up to 7.5x, the first time such enhancement has been demonstrated.
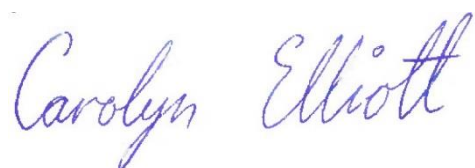
In order to create samples with higher plasmonic nanoparticle concentrations, spin-coating is employed. Multiresonant gold nanostars, coated with silica shells as spacers, are spin-coated atop upconverting nanoparticle layers. Samples with high nanostar concentration demonstrate enhancement, with nanostar clusters showing enhancement of up to 9.7x. This high enhancement value likely occurs due to plasmonic hotspots between the nanostars, and could have applications in the enhancement of upconverting nanoparticle emission for use in solar cell efficiency improvement[4,5].

Declaration

I declare that this thesis has not been submitted as an exercise for a degree at this or any other university and it is entirely my own work. Any assistance or collaboration is recognised in the acknowledgements and throughout the thesis where applicable.

I agree to deposit this thesis in the University's open access institutional repository or allow the Library to do so on my behalf, subject to Irish Copyright Legislation and Trinity College Library conditions of use and acknowledgement.

I consent to the examiner retaining a copy of the thesis beyond the examining period, should they so wish (EU GDPR May 2018).

Carolyn Elliott

Acknowledgements

Firstly, I would like to acknowledge and thank my supervisor Prof. Louise Bradley, for giving me the opportunity to do my PhD in her group, and for all her guidance, help, and support on my PhD journey.

I would like to acknowledge all the current and past Bradley group members: Dr. Calin Hrelescu, Dr. Xia Zhang, Dr. Jorge Garcia, Dr. Oisín McCormack, Dr. Hodjat Hajian, Dr. Sony Udayan, Dr. Yongliang Zhang, Dr. Stephen Cunningham, Dr. Julia Lawless, Dr. Fionnuala McGrath, Jing Qian, Sara Pelivani, Oleksandra Ivakhno-Tsehelnyk, Kseniia Mamaeva, and Jack Dobie. Thank you all for the conversation and tea over the years! A special thanks to Calin for teaching me how to synthesise gold nanoparticles, Julia for sharing her knowledge and experience in BP synthesis variation, Stephen for his help with Lumerical simulations, Fionnuala for teaching me how to use the FLIM, and Kseniia for her collaboration and assistance with the two-photon polymerisation project.

I would also like to thank Dr. Finn Purcell-Milton for his invaluable knowledge in high-temperature nanoparticle synthesis, and all his help in designing and carrying out the UCNP syntheses for this work.

I would like to thank my parents, Kevin and Tina, and my siblings, Kate and Ryan, and our family's lovely cat, Cassie, for always supporting me and being there for me. I would like to thank all my friends for listening to me talk about nanoparticles for the last five years and always being there for a chat or a cuppa, especially Dovy, Gaurav, Jack, Ross, Dáire, Julia, Stephen, Fionnuala, Kseniia, Prajwal, Brian, Jorge, Anais, Devika, Romina, Oisín, Killian, Annie, Simon, Dearbhla, Sean, Conor, Bláthnaid, all my friends from school and circus, and everyone who joined me on the Thursday trips to the Ginger Man.

Last but not least, I would like to thank my wonderful partner, Hannah O'Brennan. Thank you for always being there for me these last 8.5 years, and for making me a million cups of tea while I was writing my thesis. I couldn't have done this without all your love and support.

List of Publications and Conference Contributions

1. **<u>Carolyn Elliott</u>** (2018) "Plasmon Enhanced Upconversion for Biological Applications." Biophotonics and Imaging Graduate Summer School, 28th Aug – 1st Sep 2018, Ballyvaughan, Ireland. (Poster)

2. **<u>Carolyn Elliott</u>**, Julia Lawless, Calin Hrelescu, A. Louise Bradley (2019) "Multi-resonant plasmonic nanoparticles for enhanced light-matter interactions." IEEE Pride in Photonics Workshop, Conference on Lasers and Electro-Optics (CLEO), May 2019, San Jose, USA. (Oral Presentation)

3. Julia Lawless, Calin Hrelescu, **<u>Carolyn Elliott</u>**, Lisanne Peters, Niall McEvoy, & A. Louise Bradley (2020) "Influence of gold nano-bipyramid dimensions on strong coupling with excitons of monolayer MoS2." ACS Applied Materials & Interfaces, 12(41), 46406-46415.

4. Julia Lawless, Calin Hrelescu, **<u>Carolyn Elliott</u>**, Lisanne Peters, Niall McEvoy, & A. Louise Bradley "Rabi Splitting between Plasmons of Gold Nano-bipyramids and Excitons of Monolayer MoS2 revealed by Single-particle Dark Field Spectroscopy." Microscopy Society of Ireland Symposium 2020, 8th - 10th January 2020, Dublin, Ireland. (Oral Presentation)

5. Julia Lawless, Calin Hrelescu, **<u>Carolyn Elliott</u>**, Lisanne Peters, Niall McEvoy, & A. Louise Bradley "Rabi Splitting of Gold Nano-bipyramids coupled to Monolayer MoS2." Physics of Light-Matter Coupling in Nanostructures (PLMCN) 2020, 27th - 30th October 2020, Clermont-Ferrand, France (Virtual conference). (Poster)

6. Julia Lawless, Calin Hrelescu, **<u>Carolyn Elliott</u>**, Lisanne Peters, Niall McEvoy, & A. Louise Bradley "Influence of nanoparticle dimensions on Rabi splitting strength." Conference on Lasers and Electro-Optics (CLEO) 2021, 9th - 14th May 2021, San Jose, USA. (Poster)

7. Julia Lawless, Calin Hrelescu, **<u>Carolyn Elliott</u>**, Lisanne Peters, Niall McEvoy, & A. Louise Bradley "Rabi Splitting of Gold Nano-bipyramids coupled to Monolayer MoS2." European Materials Research Society (EMRS) 2021, 31st May - 4th June 2021, France (Virtual conference). (Oral Presentation)

8. **<u>Carolyn Elliott</u>**, Calin Hrelescu, Finn Purcell-Milton, Yurii K. Gun'ko, A. Louise Bradley (2021) "Plasmon Modulation of Upconversion" Photonics Ireland 2021, 14th - 16th June 2021, Dublin (Virtual conference). (Poster)

9. Julia Lawless, Calin Hrelescu, **<u>Carolyn Elliott</u>**, Lisanne Peters, Niall McEvoy, & A. Louise Bradley "Use of Gold Nano-Bipyramids with monolayer MoS2 for the Manipulation of Rabi Splitting Strength." Photonics Ireland 2021, 14th - 16th June 2021, Dublin (Virtual conference). (Oral Presentation)

10. Julia Lawless, Calin Hrelescu, **<u>Carolyn Elliott</u>**, Lisanne Peters, Niall McEvoy, & A. Louise Bradley "Rabi Splitting using Gold Nano-Bipyramids and Monolayer MoS2." Conference on Lasers and Electro-Optics (CLEO) Europe 2021, 21st - 25th June 2021, Germany (Virtual conference). (Oral Presentation)

11. Julia Lawless, Calin Hrelescu, **<u>Carolyn Elliott</u>**, Lisanne Peters, Niall McEvoy, & A. Louise Bradley "Influence of Nanoparticle Dimensions on Rabi Splitting Strength." Applied Photonics Physics School 2021, 5th - 10th September 2021, Bad Honnef, Germany. (Poster)

12. Julia Lawless, Calin Hrelescu, **<u>Carolyn Elliott</u>**, Lisanne Peters, Niall McEvoy, & A. Louise Bradley "The Effect of Nano-Bipyramid Size on Rabi Splitting Strength when Coupled to MoS2." European Congress and Exhibition on Advanced Materials and Processes (EUROMAT) 2021, 13th - 17th September 2021, Austria (Virtual conference). (Oral Presentation)

13. Julia Lawless, Calin Hrelescu, **<u>Carolyn Elliott</u>**, Lisanne Peters, Niall McEvoy, & A. Louise Bradley "Size Dependence of Rabi Splitting Using Gold Nano-Bipyramids on Monolayer MoS2." Smart NanoMaterials: Advances, Innovation, and Applications (SNAIA) 2021, 7th - 10th December 2021, Paris, France (Hybrid conference). (Oral Presentation)

14. **<u>Carolyn Elliott</u>**, Kseniia Mamaeva, Teodora Faraone, Julia Lawless, Colm Delaney, A. Louise Bradley (2023) "Plasmonically induced trapping of photoemitters" Photonics Ireland, Limerick, Ireland. (Poster)

15. Kseniia Mamaeva, **<u>Carolyn Elliott</u>**, Teodora Faraone, Colm Delaney, A. Louise Bradley (2024) "Two-photon-polymerization as a method to place a single quantum dot near a single Au bipyramid to achieve room temperature strong coupling" Nanophotonics X, SPIE Photonics Europe 2024, Strasbourg, France. (In preparation)

Contents

x

List of Figures

xvi

xviii

1 Introduction

For centuries, humans have studied and interacted with light. In order to observe the night sky and magnify microscopic objects, the telescope and compound microscope were invented at the end of the 16th and start of the 17th centuries, attributed to Hans and Zacharias Janssen and Hans Lipperhey, respectively[6,7]. While these inventions and previous inventions such as spectacles allowed for the manipulation of light, the physics governing its behaviour was still not well understood, only considering light as rays.

The discovery of Snell's law improved the understanding of refraction of light through materials of different refractive indices[8]. This corresponded with one theory of light emerging at the time, that of light as a wave. This theory was championed by Christiaan Huygens, who developed a complete theory of light including laws for refraction and reflection. This was opposed by the theory of light as a set of moving particles, advocated for by Isaac Newton[9]. In 1802, Thomas Young demonstrated experimentally the wavelike properties of light using a double slit experiment[10]. The description of light as specifically an electromagnetic wave was put forward by James Clerk Maxwell, when he developed a theory for electromagnetic radiation that showed magnetic and electric fields propagated through space at the speed of light, thus supposing that they were indeed light[11]. In 1888, Heinrich Hertz demonstrated the existence of transverse electromagnetic waves propagating through space, proving Maxwell's theory[12]. This electromagnetic description of light paved the way for the field of photonics. In 1911, Albert Einstein published his findings on the photoelectric effect, finding that light was made up of photons of discrete energies[13], leading to the more complete understanding of light as both a wave and a particle, and winning him the Nobel Prize in 1922. This theory allows for the comprehension of light absorption and emission by photoluminescent materials, as individual photons are absorbed and emitted, promoting and de-exciting electrons to and from energy levels within molecules or nanomaterials.

In 1959, Richard Feynman gave his well-known lecture titled "There's Plenty of Room at the Bottom", discussing the possibilities that miniaturising materials to the nanoscale could offer[14]. This was the dawn of the era of nanomaterials and nanoscience, and what followed was a rapid increase in advancement of the science in this area. Nanomaterials or nanoparticles generally have a size from 1-100 nm for one or more dimensions, and represent a type of material with properties very different from a single molecule, or from the macroscopic properties of the bulk material[15].

In recent years, a great many techniques have been developed for the fabrication of nanomaterials, which can be grouped mainly into "top-down" and "bottom-up" techniques. Top-down techniques commence with a larger amount of the bulk material and remove material to obtain nanoscale structures. Such methods include photolithography and focused ion beam lithography, which can create detailed nanoparticle arrays, and mechanical exfoliation to obtain 2D materials from bulk materials such as graphene and MoS_2[16,17]. Bottom-up techniques begin with only a few atoms or molecules of a given material, which build upon each other to form a larger nanoscale material[18]. Bottom-up techniques include chemical vapour deposition, nanoparticle synthesis, and sputtering. While both types of technique have advantages and disadvantages, the sharp features obtained using bottom-up chemical synthesis, as well as its comparative ease and lower cost, make it ideal for use in creating the nanoparticles used in this work.

The study of light at the nanoscale is called nanophotonics. Metal nanoparticles are of particular interest in nanophotonics due to their localised surface plasmon resonance (LSPR), an oscillation of the conduction electrons confined to the surface of the nanoparticle when hit by an incident electromagnetic wave. This occurs for metal nanoparticles close to the size of the wavelength of light, and their shape and size modify the wavelength of their resonance. At resonance, plasmonic nanoparticles can be used to modify the emission of other emitters in their vicinity. Evidence of plasmonic nanoparticles can be seen as far back as the 4th century in the Lycurgus cup, a Roman artefact which demonstrates different colours in reflection and transmission[19]. Since then, the understanding of plasmonic nanoparticles has improved, with Faraday predicting the dependence of gold nanoparticle colour due to LSPR peak wavelength on particle size in 1857, and Turkevich demonstrating this experimentally in 1954[20,21]. In more recent years, they have been further explored and used for many applications, including emission enhancement[22] and plasmonic confinement and trapping[23].

Another more recent result of the theory of light as a wave and photons is a full understanding of photopolymerisation. Photoactivators typically absorb single photons of blue light to enter an excited state, which then creates a free radical which commences a polymerisation chain reaction. This can also occur with the absorption of two red/near-infrared photons, known as two-photon polymerisation. Photopolymerisation has been used in dentistry[24] and to confine emitters[25] such as quantum dots, which themselves have many applications such as for light harvesting in solar cells[26], and as single photon emitters.

Lanthanides (Ln), or rare earth metals, first isolated in the 1700s in Ytterby, Sweden, possess unique luminescent properties due to their 4f orbitals that have made them useful across a variety of fields. In the 1960s, rare earth metals began to be used in cathode ray tube televisions

2

as bright, coloured emitters (the first being a Eu-doped phosphor)[27,28]. The transitions between f orbitals are formally Laporte forbidden, and thus the lifetimes of lanthanide emissions are very long. This has allowed them to be an ideal addition to the gain medium and light emitting components of lasers[29], as the necessary population inversion is easier in materials with long emission lifetimes[30]. Nd:YAG lasers are very commonly used today, but Er, Yb, Tm, and Ho can also be used in lasers[31]. Lanthanides also have sharp emission bands, with emission wavelengths across the visible and IR regions[32].

Ln^{3+}-doped phosphors can undergo upconversion, wherein two photons are sequentially absorbed by a molecule or nanoparticle, and a single photon of higher energy is emitted. This is facilitated by the use of one Ln^{3+} ion as an activator which absorbs the photon and transmits it to a second Ln^{3+}, the sensitiser, which then absorbs a second photon, and emits[33]. The emission in this case can be strengthened by choosing a non-centrosymmetric host lattice, which alters the energy levels of the system and results in the "forbidden" transitions becoming more allowed. $NaYF_4$, $NaEuF_4$, or $NaGdF_4$ are preferred lattices which have been extensively used[34,35]. Upconverting materials have seen recent interest in the form of nanoparticles, which can be used for applications where the size is limited. Upconverting nanoparticles have a wide variety of uses, such as in the enhancement of solar cell efficiency by absorbing light with lower energy than the bandgap and emitting light which can be absorbed by the solar cell[4,36–38], and in biological applications such as diagnostics and therapeutics (light emitted being used to photoactivate drug molecules)[39,40]. However, their efficiency remains low due to quenching effects from their small size, and methods to overcome this low efficiency are currently being extensively researched[41–44].

1.1 Thesis aims

The overall aim of this thesis is to investigate the interactions of plasmonic nanoparticles with nanoemitters, with the goal of enhancing their emission. To do this, several objectives were identified. The first objective was to synthesise various types of plasmonic gold nanoparticles, and to tune their plasmon resonance peak positions over a large wavelength range (from 665 nm to 980 nm), so that they can interact with both types of nanoemitters (upconverting nanoparticles and quantum dots). The second was to utilise these plasmonic nanoparticles to trap quantum dots using plasmon-enhanced two-photon polymerisation, requiring the demonstration of plasmon-induced subthreshold two-photon polymerisation around the plasmonic nanoparticles, and the co-location of quantum dots with the plasmonic nanoparticles. The third objective was to synthesise upconverting nanoparticles, and deposit them alongside plasmonic nanoparticles in order to demonstrate plasmonic enhancement of upconversion.

1.2   Thesis overview

In this thesis, **Chapter 2** provides the theory and background underpinning the work. The theory of plasmons, specifically localised surface plasmons and their resonances and effects in metal nanoparticles, is introduced. Weak and strong coupling regimes between emitters and plasmonic nanostructures are compared, and the theory and simulation of the Purcell factor are discussed. The mechanism of two-photon absorption, photopolymerisation, and their combination (two-photon polymerisation) are described. Upconversion luminescence is discussed, along with the physics of upconverting nanoparticles, the reasons for their low efficiency, and potential methods for enhancing their emission.

Chapter 3 describes the methods used for synthesising nanoparticles, preparing samples, and characterising them. The synthesis methods for lanthanide doped $NaYF_4$ upconverting nanoparticles, gold nanorods, gold bipyramids, and gold nanostars are provided. The method for coating these nanoparticles with silica shells is also described, as well as two methods for depositing nanoparticles onto substrates: layer-by-layer deposition and spin coating. Various characterisation methods are outlined, namely darkfield and brightfield microscopy, optical extinction and emission spectroscopies, scanning and transmission electron microscopies, and fluorescence lifetime imaging microscopy. The calculations and methods utilised for FDTD simulations (using commercial Lumerical software) are included. Finally, the chemicals and techniques used to create samples using two-photon lithography are detailed.

Chapter 4 covers the variation in the synthesis of the plasmonic gold particles, and the resulting plasmon resonances. It discusses the desired plasmon resonance wavelengths for use in Chapters 5 and 6. The influence of seed type and crystallinity on final nanoparticle shape is noted. The variation of final nanoparticle plasmon peak wavelengths upon adjusting reagent concentrations is explored, especially in the case of l-ascorbic acid concentration. Simulated and synthesised bipyramids of different aspect ratios are analysed and the relationship between aspect ratio and longitudinal plasmon resonance wavelength described. Final nanoparticle spectra and shapes are varied via changing seed concentration. The coating of nanostars with varying thicknesses of silica shells is also demonstrated.

Chapter 5 concerns the plasmon enhancement of two-photon polymerisation in order to trap quantum dots and plasmonically modify their emission. The background and evidence in the literature for a similar system is laid out. The size tuning of the relevant plasmonic particles, gold bipyramids, as well as the spin coating of these particles onto substrates, is described. Evidence of two-photon polymerisation (below the typical threshold laser energy required) in the vicinity of the plasmonic bipyramids is provided. The dependence of the volume of polymer visible around

the bipyramids on the applied femtosecond laser power is shown. The addition of quantum dots to the polymerised areas, *via* their inclusion in the precursor monomer solution, is described, as is fluorescence and lifetime data demonstrating their co-location with the bipyramids. Strong coupling of the quantum dots and bipyramids is shown.

Chapter 6 discusses the plasmon enhancement of upconversion. The synthesis of upconverting nanoparticles is described, including the varying of their sizes and the dopants contained within them. The layer-by-layer deposition of upconverting nanoparticles and plasmonic nanoparticles is described. Gold nanostars, nanorods, and bipyramids are deposited, with highly concentrated nanorods and bipyramids giving enhancement. Higher concentrations of nanostars on spin-coated samples are shown. Evidence of higher upconversion enhancement by nanostar clusters than by any less concentrated nanostar layers is provided.

Chapter 7 includes a conclusion based on the results put forth in the thesis, and a description of potential future work on the topics presented in the thesis.

2 Theory and Background

2.1 Plasmonic gold nanoparticles

When conduction band electrons rapidly oscillate in a conducting material (such as a metal) in response to an external electric field, a quantum of this oscillation is called a plasmon. Plasmons which are confined to the surface of a metal (i.e. its interface with a dielectric medium) are known as surface plasmons (SPs), and they can interact very strongly with passing photons[45]. In planar metallic structures, these SPs can propagate, however when the size of a structure is smaller than the wavelength of light, the SP is confined to the nanostructure's surface, resulting in a localised surface plasmon (LSP), as shown in Figure 2.1.
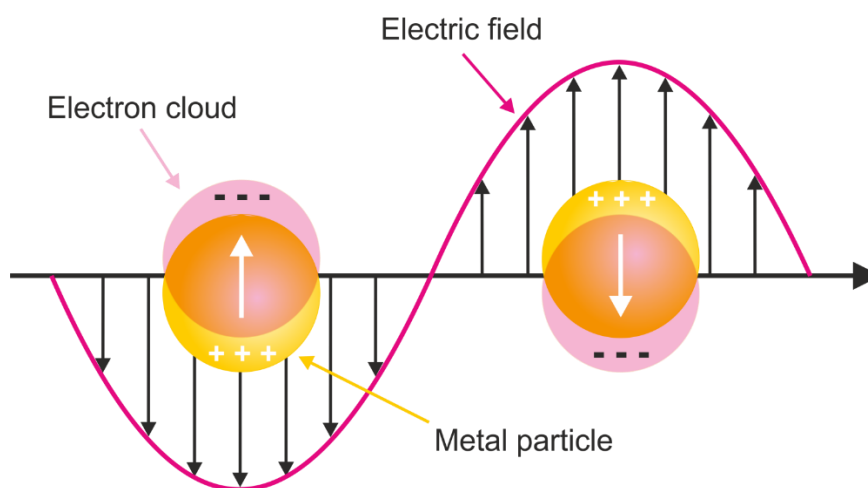
Figure 2.1: Schematic representation of a localised surface plasmon in a spherical metal nanoparticle.

In bulk metals, the plasmon wavelength is controlled only by the materials (metal and dielectric) being used, but in smaller plasmonic structures the resonant frequency of the surface plasmons is also controlled by both the size and shape. Plasmonic structures can couple with light at their different resonant frequencies, known as a localised surface plasmon resonance (LSPR). These resonances include the dipole mode, quadrupole mode, octupole mode, and higher order modes. For structures much smaller than the wavelength of light, the dipole mode resonance is dominant[46]. Nanoparticles are particularly useful as plasmonic structures as, due to their small size, they can be incorporated in various applications where a planar structure might not be appropriate, such as in-vivo (for imaging etc). Nanoparticles also provide an opportunity for very high field enhancement and have a very small mode volume, strongly confining the electromagnetic field.

In order to describe the conditions for resonance in a nanoparticle, we consider a spherical metallic nanoparticle, with diameter less than the wavelength of light, surrounded by an isotropic dielectric material, in a uniform static electric field with amplitude E_0. For this quasi-static approximation, the size of the particle, d, must be much less than the wavelength of light; $d \ll \lambda$. The polarisability of a nanoparticle, α_P, is the ratio of the dipole moment, μ, induced by an applied electromagnetic field, and the amplitude of the electric displacement field, D. This is shown in Equation (1):

$$\alpha_P = \frac{\mu}{D} = \frac{\mu}{\varepsilon_0 \varepsilon_d E_0} \qquad (1)$$

with ε_0 and ε_d being the permittivity of free space and of the dielectric material, respectively. For such a nanoparticle with radius R, the polarisability of the nanoparticle is:

$$\alpha_P = 4\pi R^3 \frac{\varepsilon(\omega) - \varepsilon_d}{\varepsilon(\omega) + 2\varepsilon_d} \qquad (2)$$

where $\varepsilon(\omega)$ is the wavelength-dependent permittivity of the metal. The polarisability of the nanoparticle is greatly enhanced when the denominator of the fraction in Equation (2) above, $\varepsilon(\omega) + 2\varepsilon_d$, is minimised, i.e., when $\varepsilon(\omega) = -2\varepsilon_d$ (or, to be exact, when $Re[\varepsilon(\omega)] = -2\varepsilon_d$). This is when the system is at resonance. Given this resonance condition (the Fröhlich condition), metals such as Au and Ag are optimal for plasmon resonances in the visible region, as they have negative values for the real part of their permittivity in this region of the spectrum[47]. However, due to the rapid tarnishing of silver nanoparticles in ambient conditions[48], this work will only be concerned with Au nanoparticles. It can also be shown that when ε_d increases, for example when changing the medium from air to water or to silica, the resonance will red-shift[49], as has been seen in Sections 4.5.2 and 4.7, respectively.

However, this quasi-static model does not take into account the impact that the size of nanoparticles has on the energy of the resonance, and is only applicable for particles less than ≈ 100 nm[49]. Mie theory, first developed by Gustav Mie in his 1908 paper, "Beiträge zur Optik trüber Medien, speziell kolloidaler Metallösungen"[50], can be used to describe the interaction of light with larger particles, of a size closer to the wavelength of light. Mie theory predicts a redshift of the spectral position of the dipole resonance as the size of a particle increases. This can be understood by considering that the surface charges on opposite sides of the particle are now further apart from each other. Thus, the charges interact less, and the restoring force for the oscillation of the charges decreases[49,51]. This lowers the resonance frequency, resulting in the redshift of the resonance.

While Mie theory only describes the interaction of light with spheres, particles of other shapes demonstrate similar resonances and size dependences. Simulations based on Mie theory have

8

been used to show the redshift of gold nanorod resonances with an increase in aspect ratio[52]. Mie theory has been used in this work to calibrate simulations, by first modelling spheres and comparing simulated results to the analytical solutions to ensure accuracy, and subsequently expanding the simulations to more complex geometries. The variation of plasmon resonance of several nanoparticle shapes can be seen in Chapter 4.

The scattering and absorption of nanoparticles are strongest at their resonant frequency. The extinction cross section of a nanoparticle (σ_{ext}) can be expressed as the sum of the absorption and scattering cross sections (σ_{abs} and σ_{scatt}):

$$\sigma_{ext} = \sigma_{abs} + \sigma_{scatt} \qquad (3)$$

The extinction cross section of a nanoparticle is very large, up to 10x larger than the geometric cross section of the particle[53,54]. The size of the extinction cross section represents the strength of the particle's interaction with incident light. Simulating σ_{ext} for different particle shapes and sizes can allow their plasmon resonances to be tuned, and the results applied to tuning their shapes and sizes synthetically. Synthetic tuning of the nanoparticles is carried out by varying the concentrations of various reagents such as HCl, AgNO3, HAuCl4 (gold precursor) and l-ascorbic acid, as well as the seed concentration. This tuning, as well as a discussion of the growth mechanism of bipyramids, can be seen in Chapter 3, Sections 3.2, 3.3, and 3.4.

If excited resonantly, as discussed above, the surface plasmon resonance of a nanoparticle can enhance the absorption and scattering of incoming light. Various nanoparticle shapes exist which can couple with more than one frequency, for example nanoparticles with an elongated axis in one direction might plasmonically couple with two different frequencies, one along the longer axis (longitudinal mode) and one along the shorter axes (transverse mode). The lower frequency coupling with the longer axis of the nanoparticle can again be understood as occurring due to the increased distance between surface charges on opposite sides of the particle along this axis. Some examples of these elongated particles are gold bipyramids (see Figure 2.2(a) and (b)) and nanorods (NRs). Gold bipyramids (BPs) have very sharp tips, which can lead to larger field enhancements than are seen with NRs, as field enhancements are proportional to the curvature of a surface[55,56] due to the higher concentration of conduction electrons on a very curved surface.
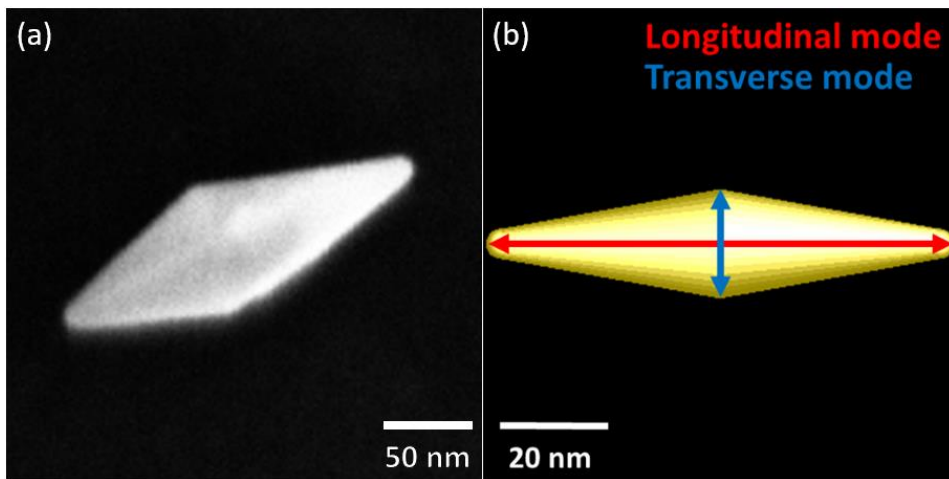
Figure 2.2: (a) SEM image of a gold BP, (b) schematic of a BP showing the directions of the transverse and longitudinal plasmon modes.

Gold nanostars (NSs) are nanoparticles with multiple sharp tips. The tips, the core, and a core-tip hybridisation of the NSs can give rise to multiple different SPRs. The sharpness of the tips can also cause significant enhancement of the electric field (see Figure 2.3(a)). These advantageous properties mean that NSs have been used to enhance many optical phenomena, including Raman scattering and fluorescence[57]. Their multiple resonances and tunability mean that they can be used to enhance light across the optical spectrum and could potentially be used to enhance multiple wavelengths simultaneously.
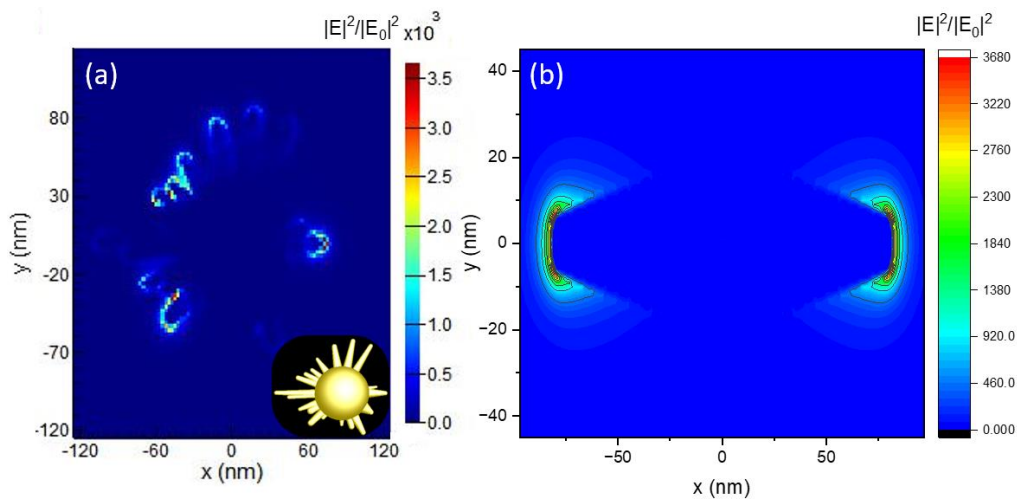
Figure 2.3: (a) Electric field intensity enhancement map at 803 nm, showing the excitation of plasmon modes and strong field enhancement at the tips of a simulated NS with multiple pointed tips. Schematic of the NS, inset. (b) Electric field intensity map at 780 nm for a BP, showing strong field enhancement at the tips.

2.2 Weak vs strong coupling

In materials such as semiconductors and insulators, when a photon is absorbed by the material, it promotes an electron (e⁻) from the valence band to the conduction band, leaving behind a positively charged "hole" in the material (h⁺). This e⁻-h⁺ pair forms a quasiparticle known as an exciton, first described in 1931 by Frenkel[58]. The electron and hole orbit each other in a bulk material, at a distance known as their "Bohr radius", but when the size of the material is smaller than this radius, such as in the case of a quantum dot, the exciton energy is greatly increased[59]. The exciton energy changes with the degree of quantum confinement, and is thus dependent on the size of the quantum dot[60,61]. When the electron and hole recombine, a photon is emitted.

When such an emitter is placed in the vicinity of a plasmonic structure with a plasmon resonance at a similar energy to the exciton energy, the two can couple together. There are two coupling regimes: weak coupling and strong coupling, characterised by an increase in coupling strength, g, from $g < 1$ to $g \geq 1$.

In the case of weak coupling, the photoluminescence of an emitter can change; its intensity can be enhanced or quenched and its radiative and nonradiative decay rates can be altered. The Purcell effect describes the enhancement or quenching of the emission of a system, via changing the spontaneous emission rate of the atoms/molecules involved. It was first described by Purcell in 1995 for an emitter in a microcavity[62]. The Purcell factor, F_P, is defined as

$$F_P = \frac{\gamma_c}{\gamma_0}$$

where γ_c is the spontaneous emission rate in a cavity and γ_0 is the spontaneous emission rate in free space. The Purcell factor is proportional to g^2 [59].

In this weakly coupled system, the excitation rate and emission rate are both affected by coupling to the plasmonic structure. The field enhancement of the plasmonic structure enhances the excitation rate of the emitter, and the presence of the plasmonic structure also modifies the emission rate. The wavefunctions of the emitter and the plasmonic structure are not affected by weak coupling. A discussion of the simulation of the Purcell factor can be seen in Section 2.2.1.

In the case of strong coupling, the wavefunctions of the emitter and plasmonic structure are mixed together, forming two distinct new energy levels. The photon and exciton combine to form a hybrid light-matter quasiparticle called a polariton. Strong coupling occurs when the energy transferred between the plasmonic structure and the exciton is larger than the energy dissipated by each[63]. This phenomenon is called Rabi splitting, and can be seen in a splitting of peaks in the emission spectra of the system, as well as in the scattering and absorption spectra[64]. The

difference in scattering spectra for weakly and strongly coupled system can be seen in Figure 2.4 below.

Weak Coupling

(a)

Purcell Effect

Scattering

Energy

Strong Coupling

(b)

Rabi Splitting

Scattering

Energy
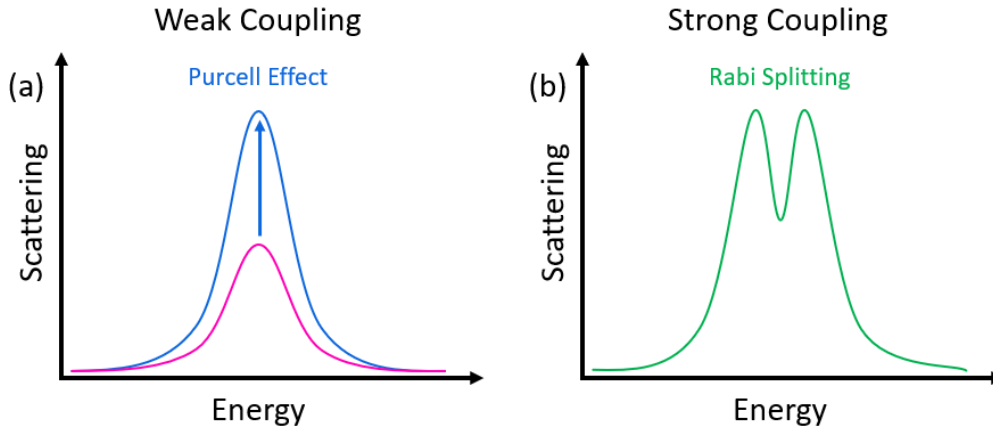
Figure 2.4: Schematic illustrations of (a) scattering enhancement via the Purcell effect (weak coupling) and (b) Rabi splitting in a scattering spectrum (strong coupling).

2.2.1 Simulating Purcell factor

In order to simulate the Purcell factor for an emitter near a plasmonic structure using FDTD simulations (see Section 3.12), there are certain values which cannot be calculated directly. The Purcell effect can be expressed as:

$$\frac{\gamma_{em}}{\gamma_{em}^0} = \frac{\gamma_{exc}}{\gamma_{exc}^0} * \frac{QE}{QE^0} \tag{4}$$

or   Fluorescence enhancement = excitation rate enhancement of fluorophore

after optical excitement * quantum efficiency enhancement.

where the 0 superscript indicates a measurement in free space, γ_{em} is the fluorescence emission rate, γ_{exc} is the excitation rate, and QE is the quantum efficiency of the fluorescence process, with $QE^0 = 1$.

Plasmonic nanoparticles can enhance the emission of fluorophores in two ways, as described in Section 2.2: excitation enhancement and emission enhancement (enhancing the quantum efficiency of the fluorescence emission rate). These are simulated separately. Excitation enhancement can be expressed as follows:

$$\frac{\gamma_{exc}}{\gamma_{exc}^0} = \frac{|E|^2}{|E^0|^2}, \tag{5}$$

where $|E|$ is the modulus of the electric field. A TFSF (total-field scattered-field) light source is used to excite the plasmonic particle, and a frequency monitor used to measure the field enhancement ($|E^0|^2 \equiv 1$).

12

Fluorescence enhancement involves using a dipole source to represent the fluorophore. It is placed at the position with maximum field enhancement. The quantum efficiency of fluorescence emission is expressed as:

$$QE = \frac{\gamma_{rad}}{\gamma_{rad} + \gamma_{loss} + \gamma_{nonrad}} \qquad (6)$$

Where γ_{rad} is the decay rate of excited states which give photons that leave the system by radiation and γ_{loss} is the decay rate of excited states which give photons that are lost/absorbed in the system. γ_{nonrad} is the nonradiative decay rate. As this is not an electromagnetic decay, it can't be modelled by FDTD, and is taken to be 0. For a radiative dipole transition:

$$\frac{\gamma}{\gamma^0} = \frac{P}{P^0} \qquad (7)$$

Where γ is the decay rate and P is the radiated power. Thus, the quantum efficiency can be expressed as:

$$QE = \frac{P_{rad}}{P_{rad} + P_{loss}} \qquad (8)$$

P_{loss} cannot be measured directly in the system. $P_{rad} + P_{loss}$ is the total electromagnetic decay rate, represented by total power injected by the dipole source, and P_{rad} is the power detected by a power transmission box around the plasmonic particle. These powers can be used to calculate the enhancement of the quantum efficiency (QE), taking $QE^0 = 1$. Thus, the overall fluorescence enhancement can be calculated from the excitation enhancement at the excitation wavelength, multiplied by the quantum efficiency enhancement at the emission wavelength (from Equations (5) and (8)):

$$\frac{\gamma_{em}}{\gamma_{em}^0} = \frac{|E|^2}{|E^0|^2} * \frac{P_{rad}}{P_{rad} + P_{loss}} \qquad (9)$$

2.3 Two-photon polymerisation

Two-photon absorption is a nonlinear optical process wherein two photons are simultaneously absorbed by an atom or molecule. The process was first conceived of by Maria Göppert-Mayer in her 1931 dissertation, "Über Elementarakte mit zwei Quantensprüngen"[65], however it was not experimentally shown until 1961, when Kaiser and Garrett demonstrated the generation of blue light (λ = 425 nm) *via* two-photon excitation of a CaF_2:Eu^{2+} crystal with red light (λ = 694.3 nm) from a maser[66]. Two-photon absorption is a third-order ($\chi^{(3)}$) nonlinear optical process[67], and can

occur in both centrosymmetric and non-centrosymmetric materials, unlike second-order nonlinear processes which can only occur in non-centrosymmetric materials[68].
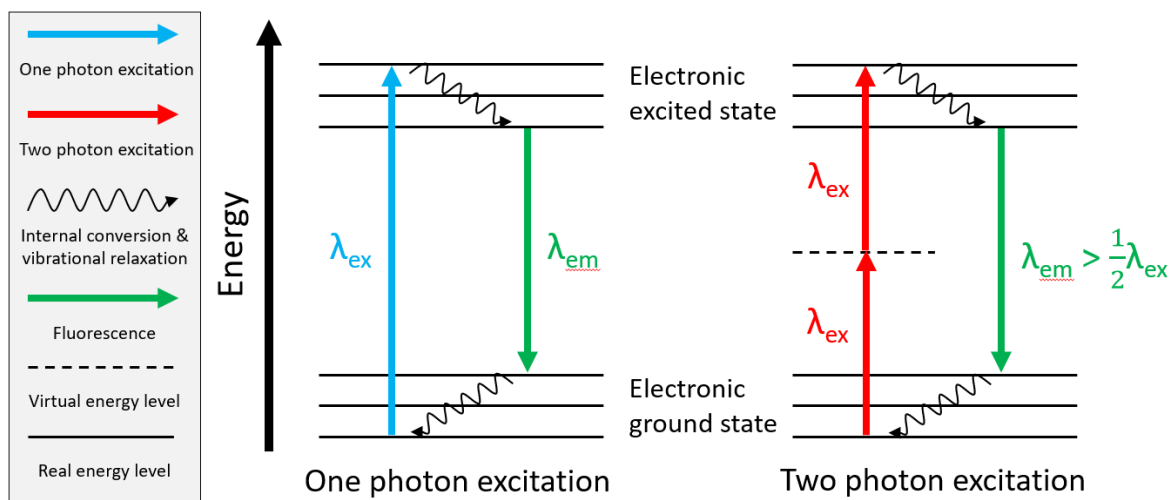
Figure 2.5: Jablonski diagram of one- and two-photon excitation followed by fluorescence.

Figure 2.5 is a Jablonski diagram showing the energy levels of an atom/molecule and the excitation of an electron to a higher energy state via one- and two-photon excitation. This is followed by non-radiative relaxation of the electron to a lower vibrational level in the electronic excited state, then emission of a photon as the electron returns to the electronic ground state (fluorescence). For the one photon process, the intensity of the emission (I_{em}) is proportional to the intensity of the excitation (I_{ex}), $I_{em} \propto I_{ex}$. As the process is a nonlinear two photon process, the intensity of the emission is proportional to the square of the intensity of the excitation, $I_{em} \propto I_{ex}^2$ [69].
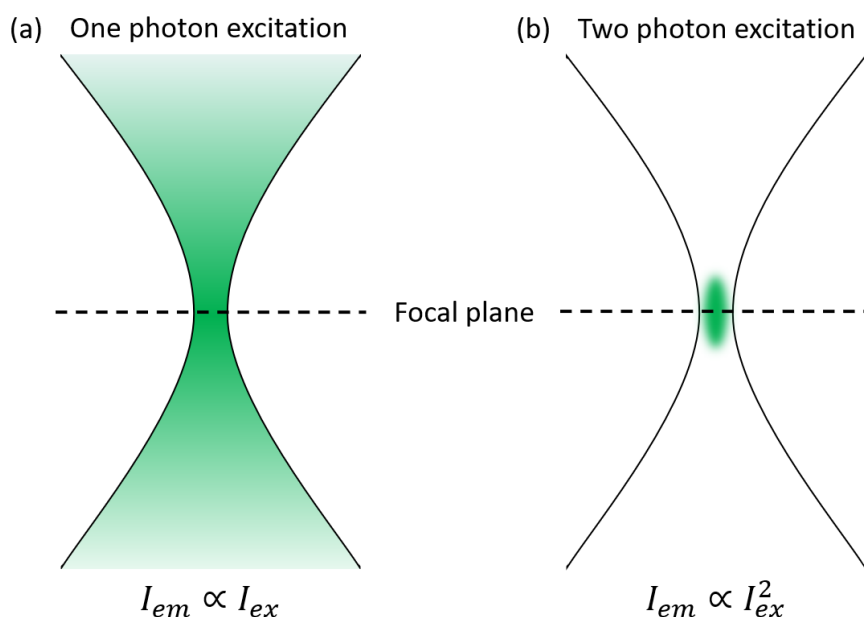
Figure 2.6: Schematic of fluorescence intensity from excitation via a focused laser beam. (a) Fluorescence from one photon excitation, spread over the entire illuminated area. (b) Emission from two photon excitation, only seen at the focal point.

Figure 2.6 shows the fluorescence intensity obtained from a focused laser beam (a double cone, represented here in 2 dimensions), in the case of one- and two-photon excitation. For emission from one-photon excitation, fluorescence occurs over the entire illuminated area (Figure 2.6(a)). For emission from two-photon excitation, fluorescence only occurs at the focal spot (Figure 2.6(b)), as the fluorescence depends nonlinearly on the illumination intensity[70]. The intensity of one-photon fluorescence is Gaussian in shape, whereas the intensity of two-photon fluorescence is Gaussian-squared in shape. Also, the threshold intensity required for two-photon excitation fluorescence is higher than for the one-photon case, thus fluorescence will only occur in a region of very high excitation intensity (i.e., the focal volume).
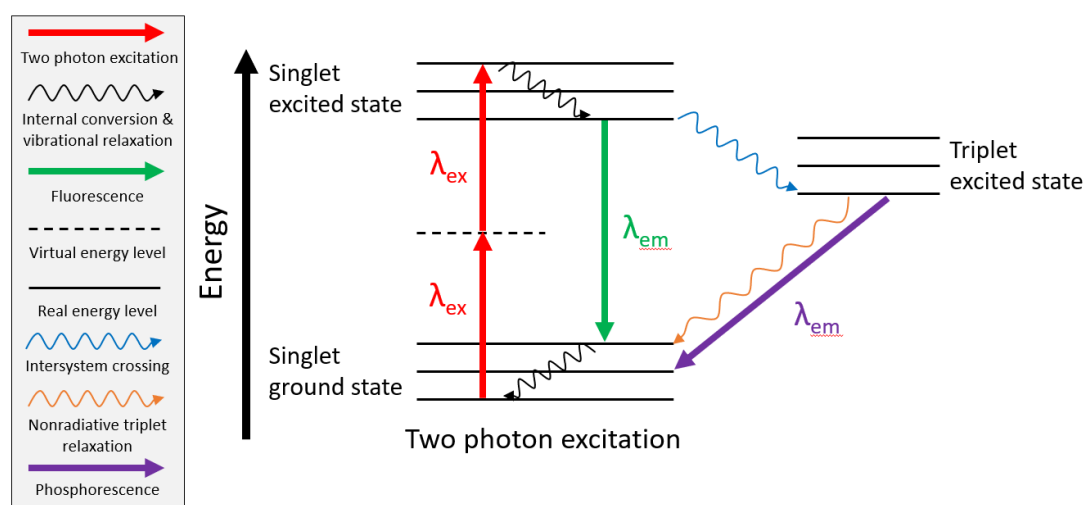
Figure 2.7: Jablonski diagram of two-photon excitation followed by intersystem crossing to a triplet state.

In some cases, a molecule will undergo intersystem crossing to a triplet excited state (a state with unpaired electrons). The Jablonski diagram of this process is seen in Figure 2.7. Such molecules can then undergo a reaction called α-cleavage, wherein the α-carbon bond in the molecule in either excited state (singlet or triplet state) dissociates, leaving two molecular fragments, each having one of the electrons in the bond[71]. This occurs more rapidly from the triplet state than the singlet state[72]. These resulting molecular fragments, each with one unpaired electron, are free radicals. Materials which can carry out this process can initiate and propagate further reactions, and are called photoinitiators (in this case, Type I)[71,73].

When a photoinitiator is combined with a monomer, the radicals initiate a polymerisation chain reaction[74]. First, the photoinitiator (I) splits into two radicals ($R^\bullet$), as described above.

$$I \rightarrow 2R^\bullet$$
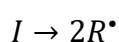
Secondly, the radicals react with the monomer (M), forming a polymer radical, which then continues to propagate a chain reaction, resulting in the growth of long polymer chain radicals ($P_n^{\bullet}$).

$$R^{\bullet} + M \rightarrow P_1^{\bullet}$$

$$\vdots$$

$$P_n^{\bullet} + M \rightarrow P_{n+1}^{\bullet}$$
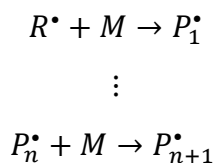
Finally, two polymer radicals react together and form covalent bonds, or one transfers a hydrogen atom to the other, resulting in either one or two stable polymer chains, terminating the chain reaction.

$$P_n^{\bullet} + P_q^{\bullet} \rightarrow P_{n+q} \;\; \text{or} \;\; P_n + P_q$$
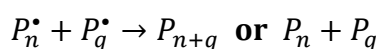
This process, when initiated by two photon absorption, is two-photon polymerisation. Two-photon polymerisation is frequently used in 3D microfabrication (two-photon lithography). A liquid consisting of monomer and photoinitiator is dropped onto a substrate, and a femtosecond infrared laser is used to write the desired 3D shape. As shown in Figure 2.6, the volume in which the laser provides sufficient intensity to cause two-photon absorption is very small, due to the high threshold intensity required and the dependence on the square of the incoming light intensity. Because of this, two-photon lithography can achieve much smaller features than traditional one-photon lithography, allowing for sub-diffraction limited feature sizes[75,76]. The unpolymerised monomer solution is then washed away, leaving solid 3D polymer structures with very fine features.

As the two-photon polymerisation process requires very high powers, it can potentially be instigated at lower powers by plasmonic nanoparticles which increase the light intensity in their vicinity, as discussed in Section 2.1. This can be used to trap quantum emitters close to these plasmonic nanoparticles[25], which is discussed further in Chapter 5.

2.4   Upconverting nanoparticles

Upconversion is a non-linear optical process wherein two or more photons of low energy incident light are sequentially absorbed by a sensitiser ion, their energy transferred to an activator ion, and a photon of higher energy light emitted by this activator ion[33]. As the process involves photons being absorbed into real energy levels within the ion, it can be up to 11x more efficient than other non-linear processes such as second harmonic generation[77]. This process can convert infrared light into higher energy IR, visible, or UV light, making it of particular interest for biological

applications due to the possibility of using excitation light within the biological transparency window (750-1000 nm)[78].

The main types of upconversion processes are: excited state absorption (ESA), energy transfer upconversion (ETU), and cooperative sensitisation upconversion (CSU)[36]. While Er^{3+} ions have the required energy level configuration for ESA, the higher efficiency of Yb^{3+}-Er^{3+} ETU means it is much more likely[36]. The mechanisms of ESA, ETU, and CSU are shown in Figure 2.8 below.
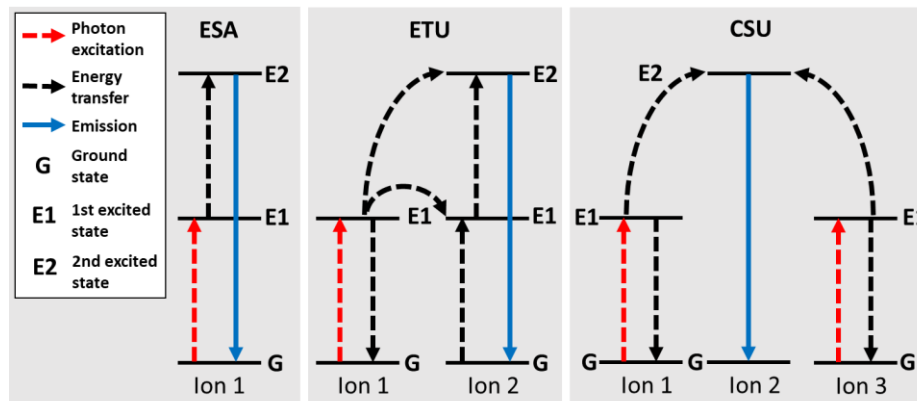
Figure 2.8: Energy level diagrams for different types of upconversion processes, namely excited state absorption, energy transfer upconversion, and cooperative sensitisation upconversion[36].

Excited state absorption (ESA) is a straightforward UC process involving only one ion, where a photon with energy matching a particular excited state is absorbed, bringing the ion to that excited state (E1). Another photon is absorbed with energy matching the next excited state (E2). The total energy is then released as an emitted photon while the ion decays to the ground state. Energy transfer upconversion (ETU) requires a second ion as activator and the first ion as sensitiser. The sensitiser ion absorbs the energy of a photon, becoming excited to state E1. This energy is transferred to a nearby activator ion, which is excited to its first excited state E1 while the sensitiser ion returns to the ground state. The process then happens a second time, with the activator ion subsequently being excited from state E1 to E2. An upconverted photon is then emitted by the activator ion from E2[79].

Cooperative sensitisation upconversion (CSU) involves three ions. Ions 1 and 3 are sensitisers and ion 2 is the activator. Ions 2 and 3 absorb one photon each, bringing them to their excited states E1. They then simultaneously transfer the energy to the activator ion, exciting it to a higher excited state, E2.

ETU does not require the excitation photon energy to be resonant with multiple transitions between energy levels (unlike ESA). It is the most efficient type of upconversion and is the type used in the upconversion systems of this project. For a two-photon system, at low powers, upconversion intensity is proportional to the incident power squared ($I \propto P^2$), and generally for

an n-photon process, $I \propto P^n$[80]. The power dependence of upconversion emission is discussed in Section 6.4.

Commonly, upconverting materials comprise trivalent lanthanide ions (Ln^{3+}) embedded in a host matrix. The upconversion emissions from these ions result from intra-4f transitions of electrons, which are parity forbidden in centrosymmetric environments (Laporte's Rule: transitions between electronic orbitals must result in a change in parity from symmetric to asymmetric or vice versa[81]). However, these transitions can become weakly allowed by placing the Ln^{3+} ions in an asymmetric crystal environment, which gives rise to mixing of electronic states, resulting in slight overlap with states of a different parity. Thus, in order to obtain the strongest emission, it is necessary to use host materials with asymmetric hexagonal crystal structures rather than the centrosymmetric cubic phase of the same material[33,82].

The host matrix should also be a material with low phonon energy such as a fluoride, to minimise nonradiative decay pathways which could reduce the lifetime of the excited state and hence reduce the overall upconversion efficiency[33,45]. Oxide materials, while similar in structure to some fluoride materials, should not be used, as they have higher phonon energy and will ultimately result in higher amounts of quenching[83,84]. Consequently, hexagonal-phase rare-earth fluoride crystals, such as $NaYF_4$, are commonly used materials for upconversion, and thus $NaYF_4$ is the host material being used in this project. The dopants used are Yb^{3+} (sensitiser) and either Er^{3+} or Tm^{3+}. Their energy level diagrams are shown in Figure 2.9.
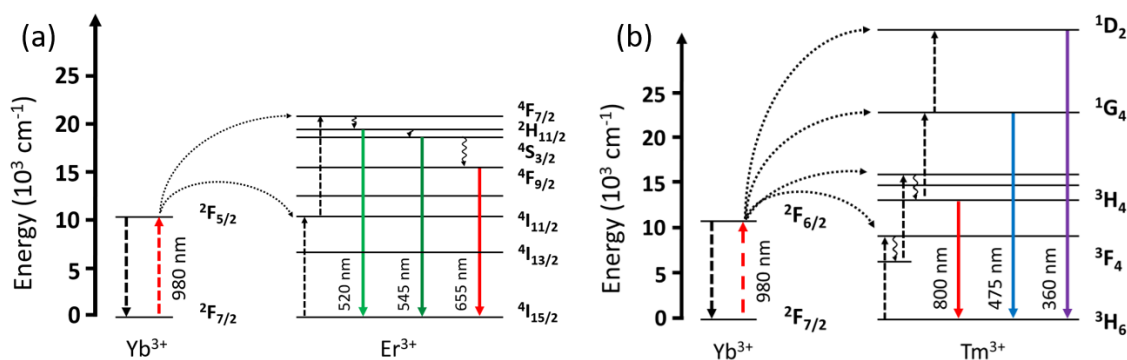
Figure 2.9: Energy level diagrams of Yb^{3+}+ Er^{3+} and Yb^{3+}+ Tm^{3+} upconversion systems showing a two-photon process for Er^{3+} emission and a three-photon process for Tm^{3+} emission[33,85,86].

Upconversion can occur both in bulk materials and in nanoparticles. Upconverting nanoparticles (UCNPs) are of particular interest to the scientific community. While they are typically synthesised in organic solvents, they can be made water dispersible using ligand exchange or shells, making them more biocompatible[87,88]. Their anti-Stokes emission makes them useful in the realm of bio-imaging, diagnostics, and therapeutics, as they absorb light within the near infrared biological transparency window (800-1000 nm, resulting in increased penetration depth) and emit higher

energy light, which can then be used for imaging or photoactivation of drug molecules[39,40]. The NIR excitation wavelength also minimises background autofluorescence[33,89], a significant issue in bio-imaging which occurs when irradiating with higher energy light, as well as and reducing photodamage to biological samples by requiring lower excitation powers due to the transparency.

They can also be used in photovoltaics, where they can absorb light with less energy than the bandgap of the photovoltaic material (which cannot be absorbed by the solar cell) and upconvert it into higher energy light which can be absorbed[4,36–38]. This improves the efficiency of the cell. Upconversion emission is also highly photostable[89,90], with long lifetimes (on the order of $\approx$ 100 μs[91]), and gives continuous emission over time with no bleaching[92] which is desirable for most applications. Their small size also means that they can be incorporated easily into biological materials or solar cells.

2.4.1 Concentration quenching

A significant obstacle to high upconversion efficiencies is concentration quenching[77]. In order for any upconversion to occur, there need to be sensitiser and activator ions present. Decreasing the distance between these ions can enhance the efficiency of the energy transfer from sensitiser to activator[82], however past a certain concentration the decreased inter-dopant distances can give rise to both non-radiative cross relaxation and energy migration to surface sites (leading to surface quenching). The high surface-to-volume ratio in nanoparticles makes this surface quenching much more likely than in bulk materials[93]. These effects result in a considerably lower quantum yield of UC luminescence for small unmodified particles (<0.1%)[35], which is much lower than other emitters which use single photon fluorescence. Solvents can also interact with the surfaces of the UCNPs, particularly water, which strongly quenches upconversion luminescence[94]. This low efficiency increases the excitation powers needed in order to produce upconversion luminescence. However, UCNPs remain popular despite their low efficiency, as they are small and can be easily processed in solution. Hence a solution to overcome the low efficiency is needed in order to be able to take full advantage of these particles for biological imaging and solar cell applications.

Some current counteraction methods for concentration/surface quenching include homogeneous doping[43] (to prevent localised concentration quenching), and coating the UCNPs with a passive or active shell[44]. Passive shell coating involves coating the particle with an inert (undoped $NaYF_4$ host lattice) or amorphous (another material such as silica) shell, to prevent energy from migrating to the particle surface, reduce surface quenching effects and prevent solvent quenching. Active shell coating instead requires the shell to be a partially doped host lattice. The shell contains sensitiser

ions, which can absorb light and transfer the energy to core emitters. The shell protects the core emitters from surface quenching.

The most frequently used wavelength for exciting UCNPs is 980 nm. However, water strongly absorbs at this wavelength which can instigate heating, and is not ideal for any biological applications which require penetration deep into tissues[95]. One method of preventing this is dye sensitisation. This involves the use of a dye molecule, which has a large σ_{abs} and thus can effectively absorb light at a wavelength closer to 800 nm and transfer energy nonradiatively to sensitiser ions, which begin the upconversion process. This has been done using several IR dyes, such as IR-806 and IR-808[41,42]. This means that lower incident light power is required, and the wavelength no longer overlaps so strongly with the water absorption peak. Additionally, any process which can enhance UCNP absorption or efficiency can reduce water heating via simply reducing the input power needed for the UC process.

The objective in this work is to investigate plasmon enhancement of upconversion. This has been carried out previously[77,96–98], however enhancement with nanostars has not been shown[99,100]. The multiple tips of NSs give them the potential to enhance several wavelengths of light at once, which could be used to enhance both absorption and emission of UCNPs. The sharp tips of both NSs BPs could also potentially offer an avenue to enhancement of upconversion, due to their strong field enhancements at the tips.

2.5   Conclusion

In this chapter, the theory and background underpinning the work in this thesis is described. The theory of plasmon resonances as they appear in metal nanoparticles has been laid out, as well as their coupling to emitters. This is the background for Chapter 4, concerning plasmonic nanoparticles, as well as Chapters 5 and 6, which utilise these nanoparticles for enhancement and trapping of emitters. The mechanism of two-photon polymerisation has been explained, as a background to the results in Chapter 5 on the plasmonic enhancement of this process and its use to trap quantum dots. Additionally, the process of upconversion in upconverting nanoparticles has been discussed, as well as the reasons for their low efficiency. This motivates Chapter 6, where the synthesis of upconverting nanoparticles and their enhancement by plasmonic nanoparticles is covered.

3 Methods

All chemicals used were obtained from Merck/Sigma Aldrich.

3.1 UCNP synthesis

Lanthanide-doped $NaYF_4$ UCNPs were synthesised using a modified protocol based on those of Wang *et al.* and Wisser *et al.*[101,102]. First, 0.2 M aqueous solutions of Lanthanide acetate salts ($LnCH_3COOH$) were mixed in the appropriate ratios to achieve UCNPs of different sizes and emission wavelengths. The ratios used were 80% Y, 18% Yb, 2% Er for the Er-doped UCNPs, and 79.5% Y, 20% Yb, 0.5% Tm for the Tm-doped UCNPs.

These were added to a flask along with 35 mL octadecene (ODE) and 15 mL oleic acid (OA). The mixture was heated to 150°C in order to form lanthanide-oleate complexes (precursor for the UCNPs). A mixture of solutions of NH_4F (0.4 M, 16.5 mL) and NaOH (1 M, 5 mL) in methanol was then made up and injected into the cooled solution to nucleate the growth of the UCNPs. The temperature was raised to 50°C and left there for 40 mins to grow the nuclei. The solution was heated to 100°C to boil off the methanol and kept at 100°C under vacuum for 25 mins.

The solution was then heated to 315°C under argon for 1hr to facilitate further growth of the particles. For size variation, a fraction of the Y was replaced with Gd, the ratios of ODE and OA were varied, and the time at 315°C was varied. It should also be noted that injection speed has a significant impact on the size of the particles, with a slower injection speed resulting in much smaller UCNPs.

The UCNPs were then washed three times using ethanol. The particles were precipitated from the solution using ethanol, centrifuged, and then redispersed in a small amount of cyclohexane or toluene. This was repeated 3 times and the particles redispersed in cyclohexane or toluene. Figure 3.1 shows TEM (transmission electron microscopy) images of a batch of the synthesised UCNPs.
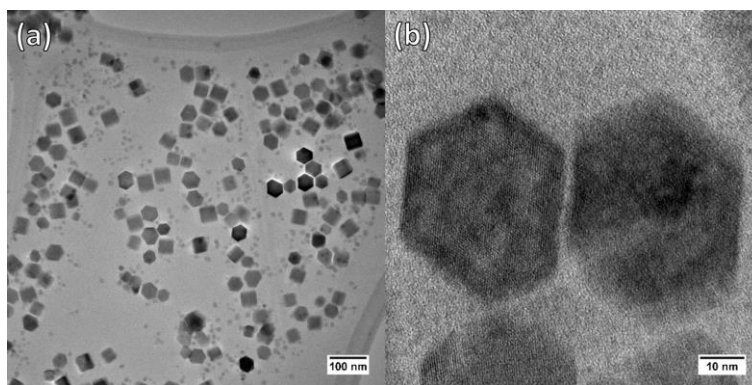
Figure 3.1: (a) TEM image of UCNPs. (b) TEM image of UCNPs at higher magnification.

3.1.1 Ligand exchange

As the UCNPs were capped with oleate ligands, and synthesised and dispersed in non-polar solvents, they were not soluble in water. In order to render them suitable for use in aqueous solutions for applications such as layer-by-layer deposition or silica shelling, ligand exchanges were performed.

For the first ligand exchange (to facilitate silica shelling), an oleate-citrate ligand exchange was carried out[103]. 5 mL of trisodium citrate in water (0.2 M, adjusted to pH 4 using HCl) was mixed with oleate-capped UCNPs (dispersed in 5 mL of hexane). This was mixed for 3 hours, the aqueous phase removed, and the citrate-UCNPs precipitated using acetone. The particles were centrifuged, the supernatant removed, and the particles redispersed in 5 mL trisodium citrate buffer solution (pH 7) in order to further remove remaining oleic acid. This mixture was mixed for 2 hours and the citrate capped UCNPs were precipitated with acetone. They were washed with acetone and water and centrifuged three times and redispersed in $\approx$ 2 mL Millipore water.

For smaller UCNPs, a larger volume of solvents were required to disperse the particles fully, and to precipitate them later. 1 mL of UCNPs in toluene was added to 19 mL hexane (across two vials). 15 mL citrate buffer solution (aqueous, 0.2 mM) was added to each vial and left to mix for 48 hours. Acetone was added to bring the total solution volume up to 600 mL. The particles were centrifuged, redispersed in 5 mL citrate buffer solution (0.2 mM), and left to mix for 2 hours. They were washed with acetone and water and centrifuged three times and redispersed in $\approx$ 3 mL Millipore water.

For the second ligand exchange (used to prepare for layer-by-layer deposition), poly(acrylic acid) (PAA) was used to replace the initial oleate ligands[104]. 2 mL PAA in ethanol (MW 1800g/mol, 1 wt%) was mixed with 1 mL UCNPs in chloroform (1 wt%) and stirred overnight (at sufficient speed to make a vortex in the liquids) to facilitate the ligand exchange at the interface between the

solvents. Centrifugation was carried out for 30 minutes at 14000 rpm. The particles were washed with ethanol 3 times, centrifuged, and finally redispersed in Millipore water.

3.2 Nanorod synthesis

$HAuCl_4$ and CTAB solutions were made ahead of time and diluted/used as necessary, whereas $NaBH_4$ decomposes rapidly in water to form hydrogen gas[105], ascorbic acid can oxidise at room temperature if reaction vessels are not perfectly devoid of metals[106], and $AgNO_3$ decomposes when exposed to light[107]. Thus, these latter solutions were made on the day of the synthesis, and not in advance.

Monocrystalline gold seeds ("Type I seeds") (following the methods from Nikoobakht *et al.*[108], also Liu *et al.*[56]) were synthesised as follows: 0.25 mL $HAuCl_4$ (10 mM) was added to 10 mL cetyltrimethyl-ammonium bromide (CTAB)(0.1 M) at 30 °C. 0.6 mL fresh $NaBH_4$ (10 mM) was added to the solution while stirring. This was then stirred for 5 min to ensure the remaining $NaBH_4$ was fully decomposed and that the reaction was finished. The seeds were kept at room temperature.

After the seeds were grown, the synthesis was carried out similarly to that of the BPs (Section 3.3), in order to obtain short ($\lambda_{SPR} \leq 850$ nm) NRs. 0.5 mL $HAuCl_4$ (10 mM) and 0.1 mL $AgNO_3$ (10 mM) were added to a vial along with 10 mL CTAB (0.1 M). This was then acidified with 0.2 mL HCl (1.0 M). This step was added by Liu *et al.*[56] in order to prevent growth of the NRs into a dumbbell shape (causing plasmon resonance blue-shift[109,110]) after synthesis. 80 μL of l-ascorbic acid (0.1 M) was then added to reduce the gold ions, followed by 24 μL of the type I seeds. A smaller volume of the type I seeds is used than the type II seeds for the BPs, because type II seeds are larger and therefore the number of individual seeds to nucleate nanoparticle growth is lower[56]. The vial was then placed into a water bath at 30 °C, for 2 hours until the reduction of the gold ions and growth of the NRs were completed. These NRs were short, with aspect ratios (defined as length of NR along its longest axis divided by its width) ≤ 4.7. These short NRs can be seen in the scanning electron microscope (SEM) image in Figure 3.2(a).

The volume of $AgNO_3$ added was varied in order to vary the SPR wavelength of the NRs. The silver concentration affects the length of the NRs[108].

In order to grow longer NRs (to obtain wavelengths closer to the 980 nm excitation wavelength of the UCNPs, as described in Chapter 6), a binary surfactant mixture of benzyldimethylhexadecyl-ammoniumchloride (BDAC) and CTAB was used. A solution (**A**) was made of a 2.7 molar ratio of BDAC/CTAB in water (5 mL 0.15 M BDAC + 0.100 g CTAB). A ratio of 2.7 favours less NS growth than other ratios[108]. The BDAC/CTAB were dissolved by sonication. 200 μL $AgNO_3$ (4.0 mM) was added, followed by 5.0 mL $HAuCl_4$ (1.0 mM). 12 μL of seeds were added to initiate the NR growth.

A growth solution (**B**) was then made, with the same BDAC/CTAB ratio. 5.0 mL of the BDAC/CTAB mixture was added to 200 μL AgNO$_3$ (4.0 mM). 5 mL HAuCl$_4$ (0.5 mM) was then added, followed by 36 μL ascorbic acid (77.8 mM). 1.0 mL of this solution (B) was added to solution A every 20 minutes. With each addition of 1.0 mL of solution B, the plasmon resonance wavelength could be expected to redshift. Additions continued until the necessary plasmon wavelength was reached. NRs with larger aspect ratios (defined as the length of a particle along its long axis divided by its length along the short axis) synthesised using this method are shown in Figure 3.2(b).
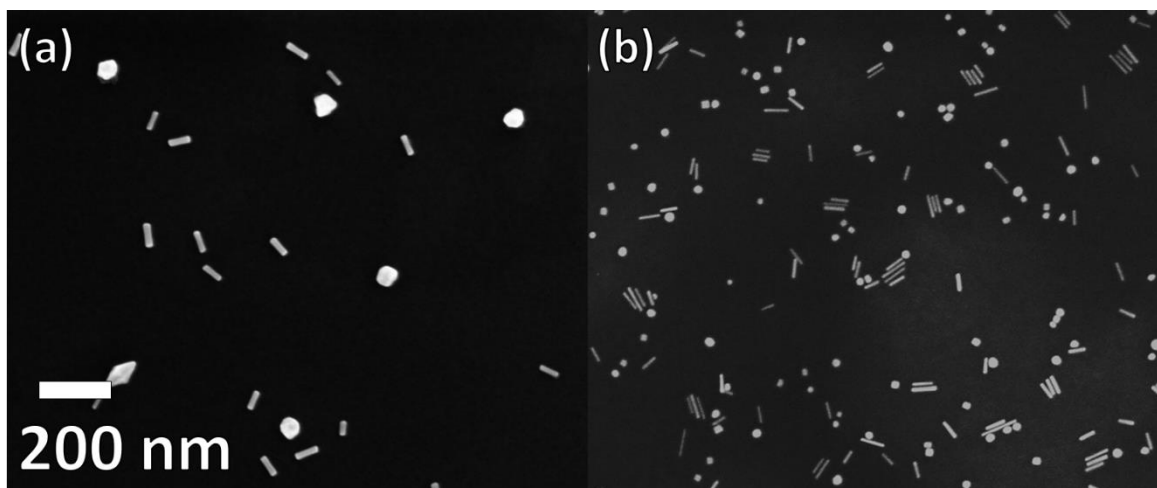
Figure 3.2: SEM images of (a) NRs synthesised using the original synthesis method and (b) NRs synthesised using the multistep method with growth solution. Scale is the same for both images.

3.3   Bipyramid synthesis

Penta-twinned gold nano BPs were grown using the silver-assisted growth method developed by Liu and Guyot-Sionnest[56], based on work by Jana *et al.*[111]. All solutions are aqueous unless otherwise stated. First, penta-twinned gold seeds ("Type II seeds") were synthesised. 250 μL sodium citrate (10 mM) and 125 μL HAuCl$_4$ (10 mM) were added to a vial, with 9.63 mL water added (resulting in final concentrations of 0.5 and 0.25 mM, respectively). To this solution 0.15 mL of fresh NaBH$_4$ solution (10 mM) was added at room temperature and the solution thoroughly inverted to ensure complete mixing. This was then aged at room temperature for 2 hours, before use in the synthesis, and discarded after 1 week.

Subsequently, 0.5 mL HAuCl$_4$ (10 mM) and 0.1 mL freshly prepared AgNO$_3$ (10 mM) were added to a 10 mL solution of cetyltrimethylammonium bromide ("CTAB", 0.1 M). To this, 0.2 mL HCl (1.0 M) was added in order to acidify the solution. 80 μL freshly prepared l-ascorbic acid (0.1 M) was added, reducing the gold ions from Au(III) to Au(I). 80 μL of the gold seed solution was added as the last step, for the reduced gold to grow upon. The reaction was performed in a water bath at

30-31 °C and was completed within 2 hours. The nanoparticles were then washed twice by centrifugation and redispersed in approx. 300 μL of Millipore water.
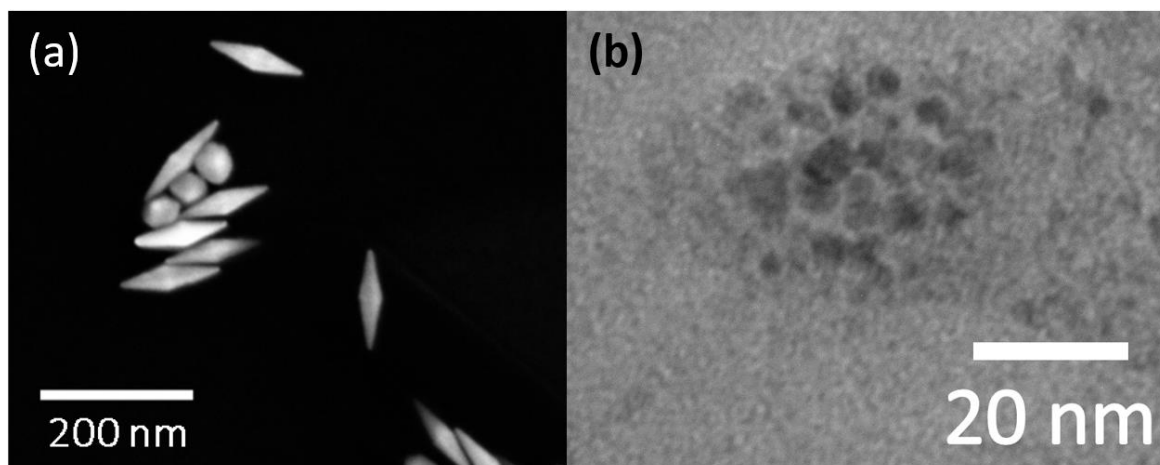
Figure 3.3: (a) SEM image of gold BPs, (b) TEM image of penta-twinned gold seeds (Type II).

Figure 3.3 shows electron microscope images of BPs and their seeds. BPs always sit on a substrate on one facet, with one end at the substrate and another end pointing slightly upwards[112].

The concentrations of the reagents in this synthesis was varied in order to obtain BPs with a range of lengths and aspect ratios, further to that previously reported by our group[17]. The concentrations of $AgNO_3$ and l-ascorbic acid could be varied in order to change the aspect ratio ($\frac{length}{width}$) of the particles. The seed and $HAuCl_4$ concentrations could be varied to alter the size of the BPs, as fewer seeds or a higher gold concentration will result in larger particles.

3.3.1 Bipyramid growth mechanism

The penta-twinned crystal structure of the Type II seeds remains in the final nanoparticles, resulting in penta-twinned gold BPs[56] which are very monodisperse, resulting in very sharp longitudinal plasmon resonances. Liu and Guyot-Sionnest demonstrated that the unique growth mechanism using $AgNO_3$ was the reason for this seed structure persistence. The addition of $AgNO_3$ slows the overall growth, allowing the gold atoms to deposit in the most energetically favourable location, introducing no new defects.

The presence of CTAB in solution results in a more rapid growth along the twinning axis of the seeds ([110] direction) than perpendicular to it, as the CTAB preferentially binds to the side {100} faces[113]. This should result in 1D nanoparticles with flat {100} faces (NRs), however the sides of the BPs are stepped (11n) facets, which are very energetically unfavourable and do not typically form in gold nanoparticle syntheses. The presence of $AgNO_3$ provides the opportunity for these (11n) facets to form.

Monolayers of silver can deposit on gold via underpotential deposition, where a metal can adsorb from a solution at less negative potentials than are required for it to deposit on itself[114]. Silver can only be deposited on gold in bulk in basic conditions, but underpotential deposition allows a monolayer to be deposited as long as the bulk work function of the adsorbing metal is lower than that of the adsorbate[115]. This is the case for silver and gold, and so some silver is deposited on the nanoparticles during the growth.

The (11n) facets have a very open structure, which allows the adsorbed silver atoms to experience a much larger attractive potential than on other facets such as [111] or [100]. This results in the Ag(I) ions stabilising the growth of these stepped facets, preventing them from disappearing and forming NRs, resulting in the final BP shape.

3.4 Nanostar synthesis

Nanostars (NSs) were synthesised using either a seed-mediated or seedless growth procedure involving the reduction of gold in $HAuCl_4$ from Au(III) to Au(0) by ascorbic acid (AA), in the presence of CTAB as a stabilising agent, and $AgNO_3$ as a structure directing agent.

For the seed mediated method (adapted from Fales *et al.*[116]), first 3.5 nm seeds ("Type III") were made using the method from Jana *et al.* [111]. 250 µL sodium citrate (10 mM) and 250 µL $HAuCl_4$ (10 mM) were added to a vial, followed by 9.5 mL water (resulting in final concentrations of 0.5 mM for each of sodium citrate and $HAuCl_4$). 0.3 mL $NaBH_4$ (0.1 M) solution was added to this, followed by shaking. This reduced the gold to form small seed particles. The seeds were allowed to grow for at least 3 hrs before use.

100 µL of these seeds were then added to 10 mL $HAuCl_4$ solution (0.25 mM), after adding 10 µL HCl (1 N) to modify the pH. To this solution was added 100 µL $AgNO_3$ (2 mM) and 50 µL ascorbic acid (0.1 M), either simultaneously or by adding the silver solution, agitating the mixture, and then adding the ascorbic acid solution. This order, as well as the precise quantities of each reagent solution, was varied to obtain different NS morphologies and optical properties. After synthesis, 100 µL CTAB (0.1 M) was added to the solution to stabilise the NSs. The solutions were washed (centrifuged, the supernatant removed, and the NSs redispersed in water) 2-3 times and kept without redispersing for further use. An SEM image of some seed-mediated NSs can be seen in Figure 3.4(b) below.

For the seedless method, 3 mL CTAB (0.1 M) and 1.748 mL Millipore water were added to a vial, along with 200 µL $HAuCl_4$. 40 µL ascorbic acid (0.1 M) was added to this solution, followed by shaking, changing the solution colour from pale yellow to colourless. Subsequently, 20 µL $AgNO_3$

26

was added, and the solution was shaken again. It was then placed in a 30-31°C water bath for 3 hours. In this time, seeds formed and then grew further into NSs. After approximately 20 minutes a blue colour was visible in the solution. The solutions were washed 2-3 times and the NSs kept for further use. This gave NSs with fewer and larger tips than those of the seed mediated NSs, as can be seen in the SEM image of seedless NSs in Figure 3.4(a).
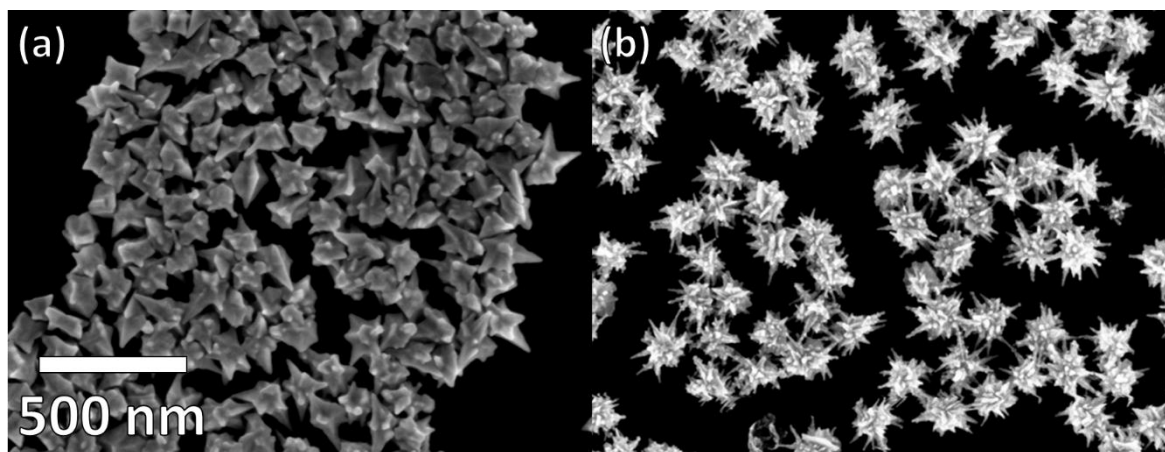
Figure 3.4: SEM images of (a) seedless and (b) seed-mediated NSs. Scale is the same for both.

3.5   Silica shelling

The NS silica shelling procedure was carried out using the method of Munkbhat *et al.*[117]. In order to add silica shells to the NSs, first a CTAB to MPEG ligand exchange was performed. The NSs were added to a 10 mL solution of MPEG-SH (5 x10^{-6} M) and left for 1hr. They were then washed and redispersed in 9 mL ethanol + 2 mL water. 100 μL NH$_4$OH was added, and 30 μL TEOS (10% v/v in ethanol), and the solution was left to stir overnight. The solution was then washed 3 times, followed by redispersing in ethanol. Figure 3.5 below shows a TEM image of gold NSs, each surrounded by a silica shell.
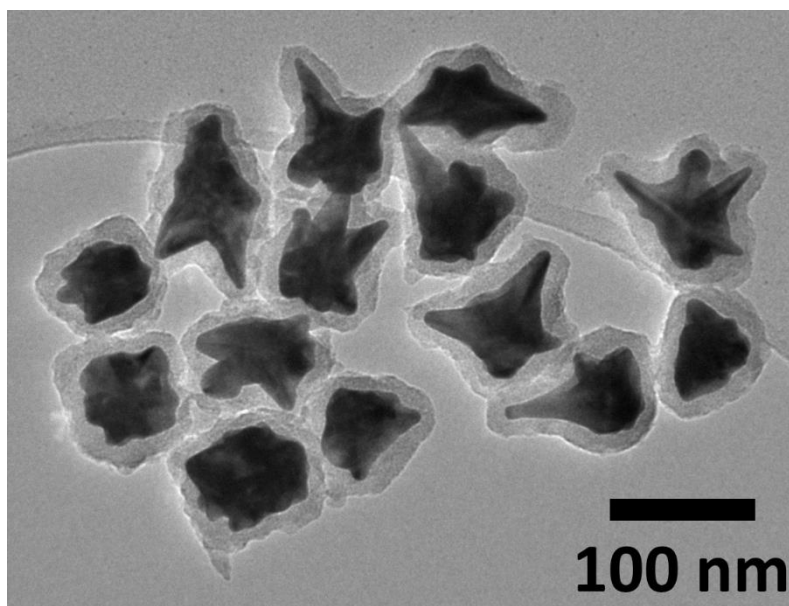
Figure 3.5: TEM image of silica-shelled gold NSs.

To silica-shell UCNPs, 1 mL citrate-capped UCNPs was added to 9 mL IPA. 1.2 mL ammonia (25%) was added, stirred at 34°C for 10 min, followed by the addition of 29 μL TEOS. The solution was left to react for 75 min. It was then centrifuged, redispersed in 25 mL water, centrifuged, redispersed in 4 mL water, centrifuged a final time, and redispersed in ~ 1.1 mL water.

To add a silica shell to the UCNPs and NSs together, 4 mL worth of MPEGylated NSs was cleaned and redispersed in 2 mL water + 9 mL ethanol. 25 μL of citrate-capped UCNPs were added to the 11 mL solution. 100 μL NH_3 + 30 μL TEOS (10% in ethanol) were then added to the solution, which was allowed to stir overnight. By varying the concentrations of nanoparticles added, the silica shell thickness could be varied from ≈ 10 to ≈ 20 nm.

3.6   Layer by layer deposition

Layer-by-layer (LbL) deposition, a method first developed by Decher et al.[118], was selected in order to allow for the attachment of two water-dispersible particles together in a controllable manner. LbL was carried out using methods previously used in the group[119]. Glass or quartz slides were cleaned using ultrasonication in Millipore water and subsequently dipped in a sequence of polyelectrolyte solutions in order to obtain a smooth, evenly charged substrate on which to deposit the charged UCNPs and NSs. In between each dipping, the glass slides were agitated in Millipore water (18.2 MΩ) for one minute. This removed any polyelectrolyte molecules which had not been fully electrostatically attached to the surface, preventing them from electrostatically attaching to each other in solution rather than to the slides.

The polyelectrolytes used were polyethyleneimine (PEI+), poly (diallyldimethylammonium chloride) (PDDA+), and poly(sodium styrene sulfonate) (PSS-). The solutions used were:

- **PSS stock:** 543 g PSS (molecular weight $\approx$ 70,000) in 10 mL water.
- **PDDA stock:** 20% w/v PDDA (molecular weight 100,000-200,000) in water.
- **0.5 M PSS LbL solution:** 2.240 mL PSS stock, 4 mL NaCl, 18 mL water.
- **0.5 M PDDA LbL solution:** 680 µL PDDA stock, 4 mL NaCl, 20 mL water.
- **PEI LbL solution:** 20 µL PEI in 21.58 mL water)

The charges in the NaCl cause the polyelectrolyte molecules to contract, giving rise to the specific layer thicknesses (7 nm per bilayer[119]) desired.

For quartz substrates (100 mm x 120 mm x 1.5 mm), the substrate can be treated to induce a native negative charge. The substrate was sequentially sonicated in the following solutions:

- **Millipore water** – 10 min
- **1 M NaOH** (4-5 g of NaOH in 75 mL Millipore water) – 15 min
- **Ethanol** + **NaOH** (4-6 pellets in ethanol) – 15 min
- **Fresh** **Millipore water** – 10 min

For glass slides (100x120x1 mm), the native charge cannot be induced. Therefore, glass slides were dipped in a solution of PEI (+) and left for 20 minutes, as PEI sticks strongly to the glass substrate and provides a charged surface onto which the subsequent layers can attach. They were then rinsed for 1 min.

After these initial charges were applied to the substrates, they were dipped in alternating solutions of PSS (-) and PDDA (+) for 10 minutes each, again rinsing for 1 min after each dip. Either 7 or 8 layers of the PSS and PDDA were applied (depending on the charge of the nanoparticle which was to be attached afterwards) as a buffer layer, to ensure a smooth surface onto which the nanoparticles could be attached[119]. Using 7 layers, the top layer would be PSS (-), and using 8 layers, the final layer would be PDDA (+). Finally, the slides were dipped in the nanoparticle solution and rinsed for 1 min. The UCNPs had a negative charge due to the PAA ligand, so they were attached onto a final layer of PDDA (+). The NSs were positively charged due to their CTAB ligand, so they were deposited onto a layer of PSS (-). These two cases can be seen in Figure 3.6 below.

−	**UCNPs**	−				
+	**PDDA**	+		**+**	**Nanostars**	**+**
−	**PSS**	−		−	**PSS**	−
+	**PDDA**	+		+	**PDDA**	+
−	**PSS**	−		−	**PSS**	−
+	**PDDA**	+		+	**PDDA**	+
−	**PSS**	−		−	**PSS**	−
+	**PDDA**	+		+	**PDDA**	+
−	**PSS**	−		−	**PSS**	−
+	**PEI**	+		+	**PEI**	+
	Glass				**Glass**	

Figure 3.6: LbL deposition – polyelectrolyte layers for deposition of UCNPs and NSs

After this, alternating layers of PSS and PDDA (starting with the electrolyte of opposite charge to the deposited nanoparticle) were applied to act as a spacer between the first nanoparticle layer and the second nanoparticle layer. When the desired spacer thickness was reached, the slides were dipped in the second nanoparticle solution and then rinsed for 1 min. The schematic for a sample with buffer layers, UCNPs, a spacer layer, and NSs is shown in Figure 3.7 below.
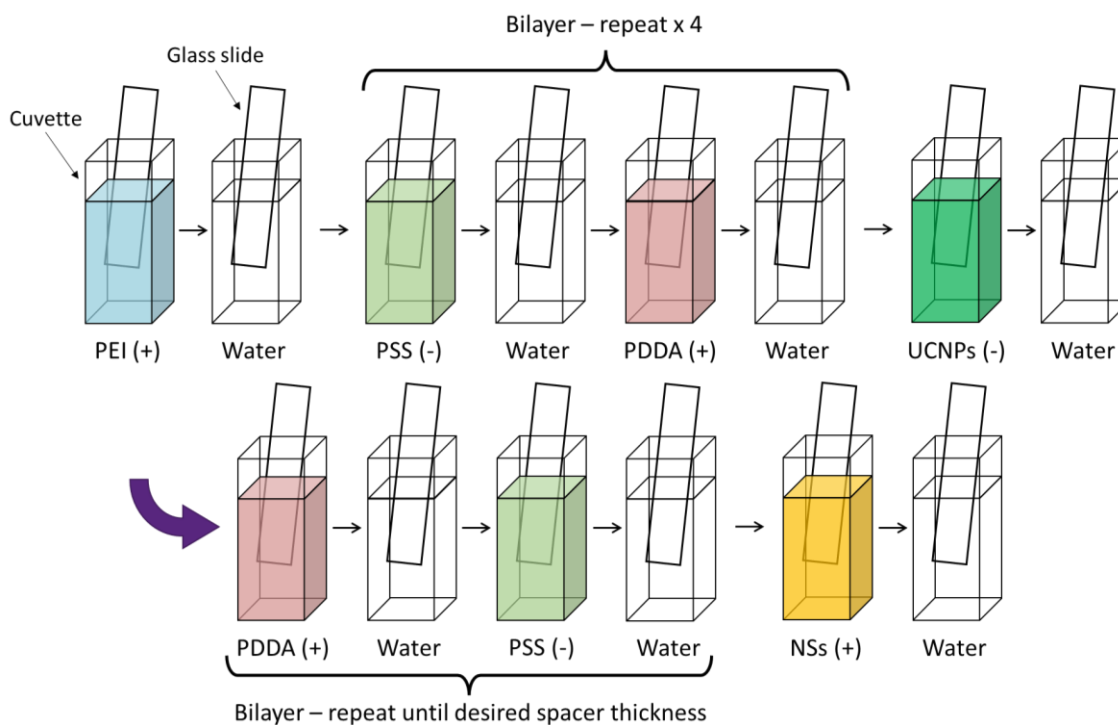
Figure 3.7: Schematic of LbL deposition, showing initial buffer layers, UCNP deposition, spacer layers, and NS deposition.

3.7 Darkfield/brightfield microscopy

Darkfield and brightfield microscopy were carried out using a custom-built setup, with a microscope from Olympus, and an Andor Solis 303i spectrometer. The setup for brightfield and darkfield microscopy can be seen in Figure 3.8 below.
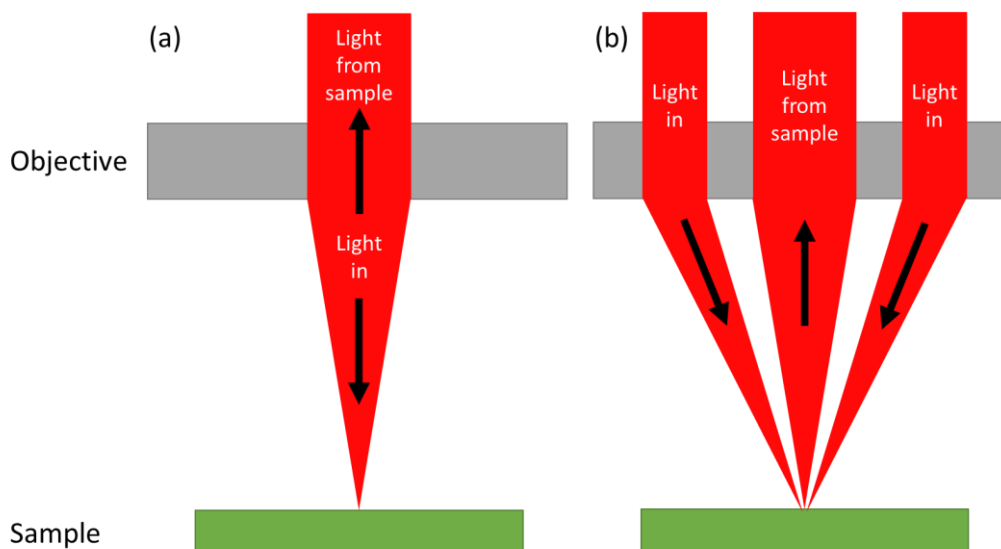
Figure 3.8: Schematic of (a) brightfield microscopy and (b) darkfield microscopy measurement.

Single particle scattering spectra were measured using an air-cooled CCD (charge coupled device), with the microscope in darkfield mode. The spectra were taken by selecting an area on a solid-state sample containing one metal nanoparticle, and another area with no nanoparticle as a background. The resulting scattering spectra were calculated as $\frac{(\text{scattering}-\text{background})}{\text{background}}$, to give the spectrum of the nanoparticle alone.

Polarisation-dependent single particle scattering measurements were taken by illuminating the sample in darkfield mode with unpolarised white light, and by polarising the output light with an adjustable polariser before it reached the spectrometer. A diagram of the polarisation-dependence setup is shown in Figure 3.9 below.
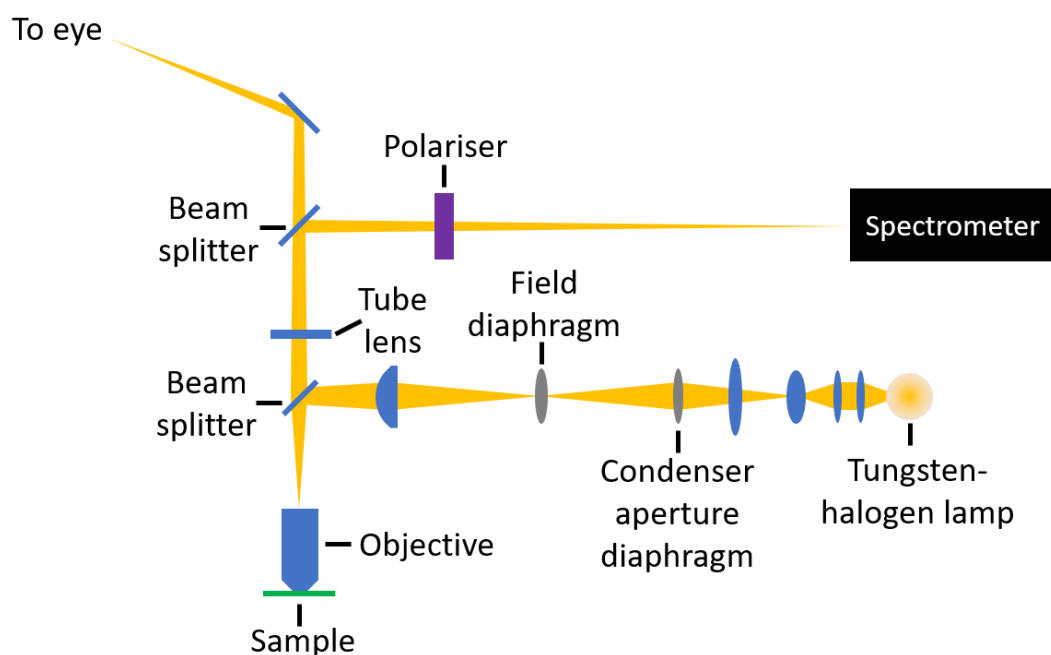
Figure 3.9: Beam path diagram of darkfield/brightfield reflection microscope with polarised output light.

3.8 Optical spectroscopy

UV-Visible extinction spectroscopy was carried out using a Cary 50 UV-Vis Spectrophotometer, with zero- and background-correction using a cuvette of the solvent used for each of the samples.

UC Emission spectroscopy of liquid and solid samples was carried out on a custom-built setup (See Figure 3.10 below). They were excited using the M Series 980nm Laser (2.5 W, continuous wave laser) from Dragon Lasers, and a 950 nm shortpass filter was placed in front of the spectrometer to protect it from the high laser intensity.

In the case of solid samples, a sample of UCNPs on glass substrates (created using LbL or spin-coating) were placed in front of the objective and the laser focused onto the sample at an angle to avoid reflecting too much laser light into the spectrometer. The sample could be moved vertically and horizontally to investigate different areas of the sample. The laser spot could be aligned using a strongly emitting Er^{3+}-doped sample, by coupling in white light along the detection pathway, and aligning the bright green emission in the laser spot to this white light spot.
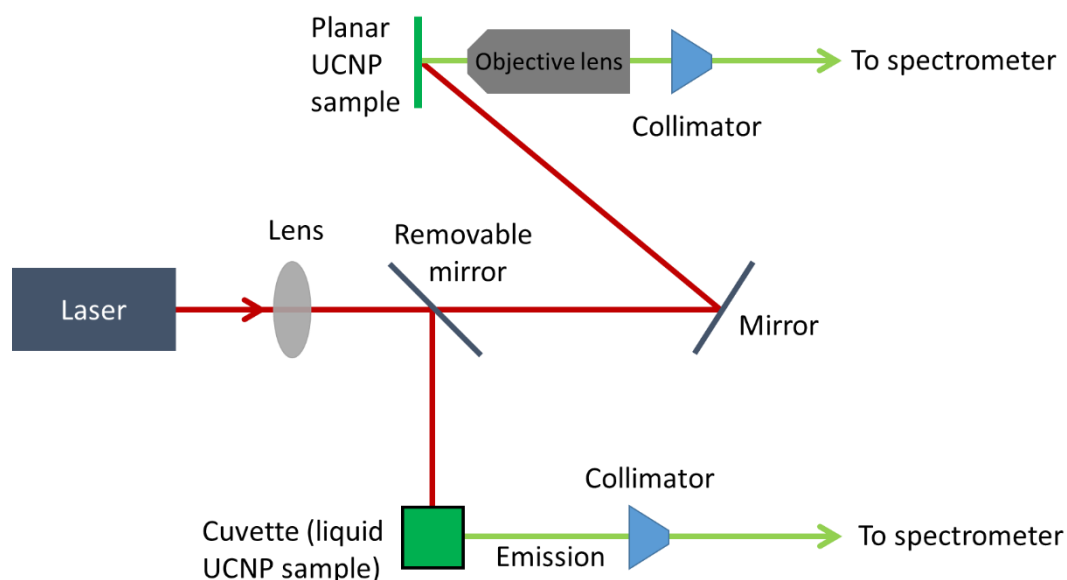
Figure 3.10: Diagram of UC emission setup.

In the case of liquid samples, the removable mirror was placed in the setup, the solution containing UCNPs was placed in the cuvette holder, and the UC emission was collected at a right angle to the laser path, to avoid directly shining the laser light into the spectrometer.

3.9 Electron microscopy

Transmission electron microscopy (TEM) was carried out using the JEOL 2100 at acceleration voltage 120kV. High-resolution TEM of UCNPs was carried out by Dr. Finn Purcell-Milton from the Gounko group using the Titan TEM. Scanning electron microscopy (SEM) was carried out using the SEM Ultra (Zeiss). All SEM images were taken using 5.00 kV power unless otherwise stated.

To prepare nanoparticles for SEM imaging, the nanoparticles needed to be deposited from solution onto a substrate. This was carried out by drop-casting 1.5 µL of concentrated nanoparticle solution onto a small substrate made of polished silicon. This was then left to allow NP deposition for 20 seconds, and most of the liquid then removed via pipette. The sample was left to air dry. The substrate was then affixed to an SEM stub using carbon tape, and two pieces of carbon tape connected from the stub to the top of the substrate to ensure good conductivity.

For samples with non-conductive substrates (such as glass, as in the samples in Section 3.13), the samples were plasma coated with 20:80 gold:palladium (5 nm). Conductive substrates such as silicon were left as-is.

3.10 Fluorescence lifetime imaging microscopy

For fluorescent samples (such as those described in Chapter 5), fluorescence lifetime imaging microscopy (FLIM) was carried out using a PicoQuant MicroTime200, which is detailed in Figure 3.11 below. (SPAD = single photon avalanche detector. CCD = charge coupled device. FC/APC = fibre channel/angled physical contact.)
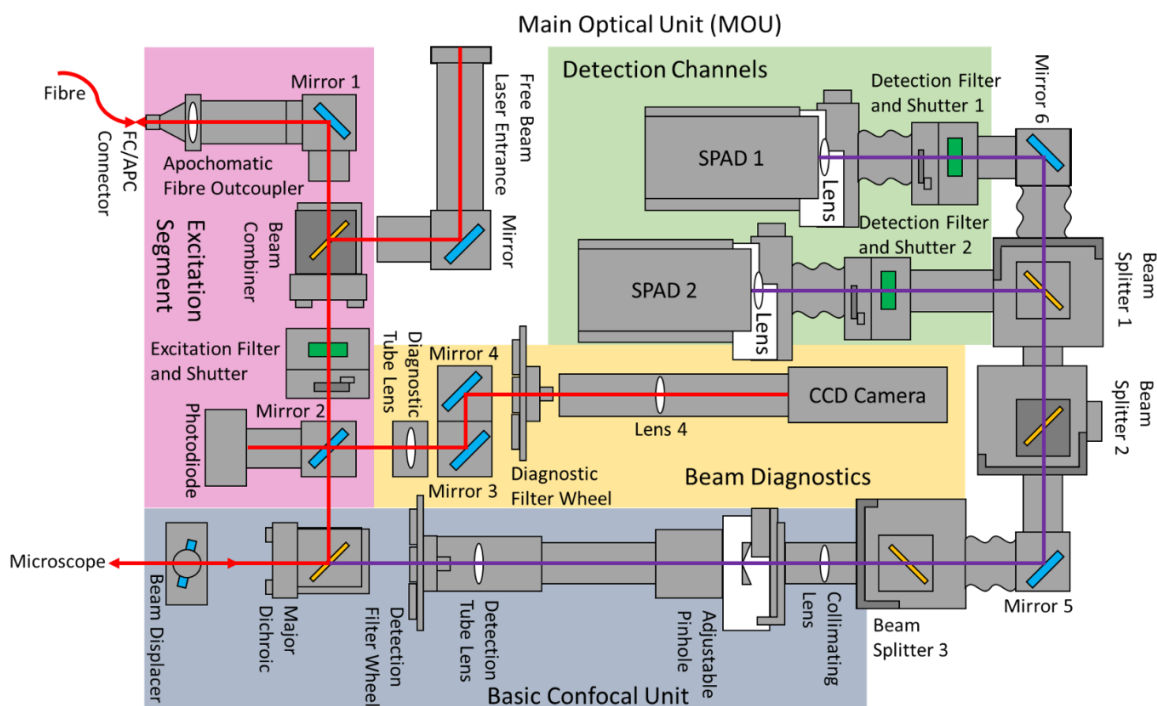
Figure 3.11: Diagram of PicoQuant MicroTime200 (FLIM). A pulsed laser is coupled in through the Excitation Segment and is reflected onto the sample in the microscope. The light emitted from different areas of the sample is then selected in the Basic Confocal Unit and detected through the Detection Channels.

The system is a time-resolved confocal microscope. A pulsed laser with an appropriate emission wavelength (lower than that of the fluorescent quantum dots in the sample) was chosen for each measurement. Bandpass filters were chosen at the excitation and emission wavelengths and placed in the system at the Excitation Filter and Detection Filter Wheel respectively. The sample was placed in the microscope and brought into focus, and a region of interest was selected. The laser was switched on and a small detection area selected by the Basic Confocal Unit. The stage was then moved to raster across the entire region of interest, and fluorescence lifetime and intensity data were collected from all detection areas within this region via the single photon avalanche detectors.

3.11 Spin coating

For gold nanoparticles (NSs, BPs), the nanoparticles were diluted in ethanol (typically around 5 μL with 400 μL ethanol), and then dropped onto a glass/ITO/silicon substrate in a spin coater. The sample was then spun at 500 rpm for 60 seconds, 2500 rpm for 5 seconds, and 5000 rpm for 50 seconds (to dry the sample).

For the UCNP/UCNP+NS samples, 100 μL UCNPs in cyclohexane were mixed with 500 μL PMMA (0.1 wt% in toluene) and dropped onto a glass slide. This slide was then spun at 1000 rpm for 60s, 2500 rpm for 5s, and 5000 rpm for 50s. After spinning, the slide was baked for 60s at 180°C in order to solidify the PMMA. 10 μL of varying concentrations of NSs in ethanol were then dropped onto the UCNP layer on the glass slide, which was then spun using the same speeds as above and any remaining ethanol allowed to evaporate.

3.12 FDTD simulations

Finite difference time domain (FDTD) simulations were performed using commercial Lumerical software. Lumerical provides many light source options; dipoles, plane wave sources, and total-field scattered-field sources (TFSF – needed to simulate scattering of small particles). A 3D rendering of the photonic structures is created, and the material's optical properties (via n and k values) are assigned to each. A large 3D mesh is automatically calculated based on preselected mesh accuracy and the material refractive index (conformal meshing – mesh size $\propto$ wavelength per refractive index unit[120]) and placed over the entire simulation region. The mesh size is manually reduced around areas where there are regions of interest and any sharp corners or curves, in order to get as faithful a representation of the shape as possible in the simulation, allowing for more accurate results.

Boundary conditions are either set as perfectly matched layer (PML), which absorb incoming light and minimise reflections, or symmetric/antisymmetric. Symmetric or antisymmetric boundaries are chosen when the electric field or magnetic field are parallel to the boundary, respectively, in order to reduce the simulation region and simulation time. The simulation ends after a certain amount of time, or when the E field reaches a steady state with the energy remaining in the system at a certain fraction of the injected energy.

FDTD as a method was first proposed by Yee in 1966[121] and popularised by Taflove and Brodwin in 1975[122,123], and it involves solving Maxwell's equations on a discrete mesh. The derivatives in Ampere's and Faraday's Laws are replaced with finite differences. The electric and magnetic field

components, E and H, are spaced apart by half a mesh step ($\frac{\Delta x}{2}$, $\frac{\Delta y}{2}$, and $\frac{\Delta z}{2}$), and calculated at half a time step apart ($\frac{\Delta t}{2}$). The equations based on these are used to calculate the future fields.

Maxwell's curl equations for an isotropic medium are evaluated, to calculate E and H at each point in the mesh:

$$\frac{\partial \vec{D}}{\partial t} = \nabla \times \vec{H} \tag{10}$$

$$\vec{D}(\omega) = \varepsilon_0 \varepsilon_r(\omega) \vec{E}(\omega) \tag{11}$$

$$\frac{\partial \vec{H}}{\partial t} = -\frac{1}{\mu_0} \nabla \times \vec{E} \tag{12}$$

where $\vec{D}$, $\vec{H}$, and $\vec{E}$ are the displacement field, the magnetic field, and the electric field, ε_0 and μ_0 are the permittivity and permeability of free space, and $\varepsilon_r(\omega)$ is the complex relative permittivity of the material used.
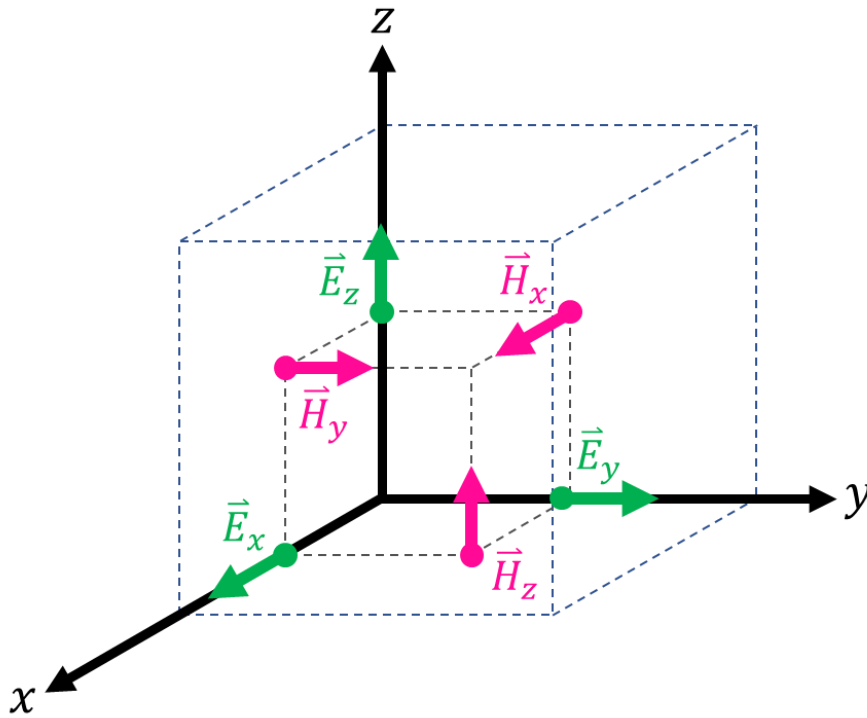
Figure 3.12: Yee cell [121], showing the positions where the field components are solved within each cell of the simulation mesh.

Every point in the simulation mesh represents one Yee cell (see Figure 3.12 above). The electric and magnetic field components ($\vec{E}_x$, $\vec{E}_y$, $\vec{E}_z$, $\vec{H}_x$, $\vec{H}_y$, and $\vec{H}_z$) are distributed in separate locations around the cell. The curl of the electric and magnetic fields are calculated using a leapfrog time-stepping algorithm[124] with time step Δt. $\vec{E}$ is measured at times t, $t + \Delta t$, $t + 2\Delta t$, etc., and $\vec{H}$ is measured at times $t + \frac{1}{2}\Delta t$, $t + \frac{3}{2}\Delta t$, $t + \frac{5}{2}\Delta t$, etc. The leapfrog algorithm is expressed as follows:

$$\vec{E}^{t+\Delta t} = \vec{E}^t + \alpha(\nabla \times \vec{H}^{t+\frac{1}{2}\Delta t}) \tag{13}$$

$$\vec{H}^{t+\frac{3}{2}\Delta t} = \vec{H}^{t+\frac{1}{2}\Delta t} + \beta(\nabla \times \vec{E}^{t+\Delta t}) \tag{14}$$

where α and β are simulation parameter-dependent proportionality terms.

Equations (10), (11), and (12) above are equivalent to the below scalar equations, where $\frac{\partial \vec{E}}{\partial t}$ is given by the curl of the $\vec{H}$ field as follows:

$$\frac{\partial H_z}{\partial y} - \frac{\partial H_y}{\partial z} = \varepsilon_0 \varepsilon_r \frac{\partial E_x}{\partial t} \tag{15}$$

$$\frac{\partial H_x}{\partial z} - \frac{\partial H_z}{\partial x} = \varepsilon_0 \varepsilon_r \frac{\partial E_y}{\partial t} \tag{16}$$

$$\frac{\partial H_y}{\partial x} - \frac{\partial H_x}{\partial y} = \varepsilon_0 \varepsilon_r \frac{\partial E_z}{\partial t} \tag{17}$$

And $\frac{\partial \vec{H}}{\partial t}$ is given by the curl of the $\vec{E}$ field as follows:

$$\frac{\partial E_z}{\partial y} - \frac{\partial E_y}{\partial z} = -\mu_0 \frac{\partial H_x}{\partial t} \tag{18}$$

$$\frac{\partial E_x}{\partial z} - \frac{\partial E_z}{\partial x} = -\mu_0 \frac{\partial H_y}{\partial t} \tag{19}$$

$$\frac{\partial E_y}{\partial x} - \frac{\partial E_x}{\partial y} = -\mu_0 \frac{\partial H_z}{\partial t} \tag{20}$$

FDTD can solve these equations ((15) – (20)) using the materials' optical properties and initial fields, by substituting the derivatives for finite differences.

The derivative of any function $f(x)$ can be expressed as:

$$f'(x) = \lim_{\Delta x \to 0} \frac{f(x + \Delta x) - f(x)}{\Delta x} \tag{21}$$

This can be approximated as the below forward difference (Equation (22)) for small values of Δx (a Taylor expansion ignoring higher order errors). The value of is chosen to be very small to get as close to 0 as is practically possible. The smaller the timestep and step in space, the more accurate the simulation.

$$f'(x) \approx \frac{f(x + \Delta x) - f(x)}{\Delta x} \tag{22}$$

However, the central difference approximation is more accurate than Equation (22) above, and so the derivative is approximated as:

$$f'(x) \approx \frac{f(x + \Delta x) - f(x - \Delta x)}{2\Delta x} \quad (23)$$

FDTD uses the central difference approximation to carry out its calculations.
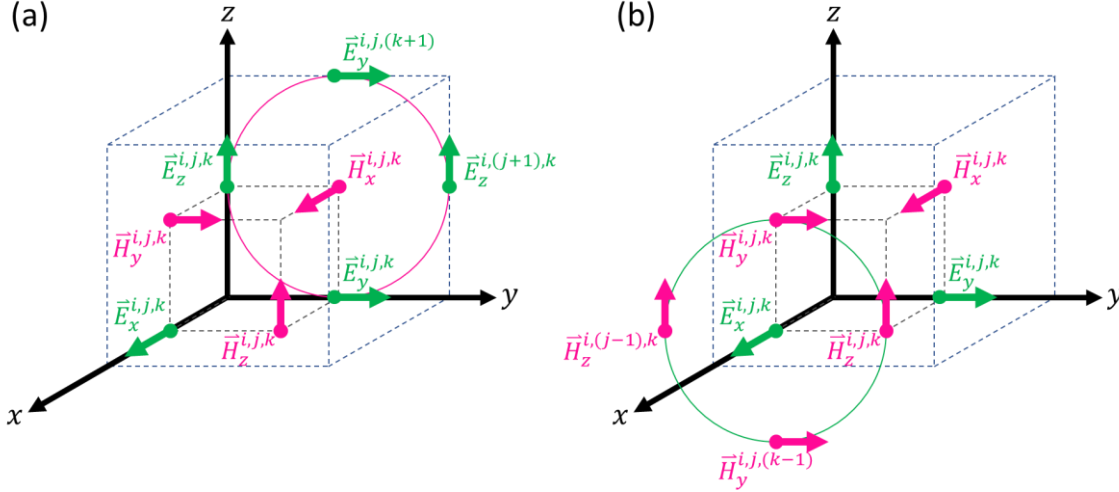
Figure 3.13: (a) A Yee cell showing $E_z^{i,(j+1),k}$, $E_z^{i,j,k}$, $E_y^{i,j,(k+1)}$, and $E_y^{i,j,k}$ being used to calculate $\nabla H_x^{i,j,k}$, and (b) A Yee cell showing $H_z^{i,j,k}$, $H_z^{i,(j-1),k}$, $H_y^{i,j,k}$, and $H_y^{i,j,(k-1)}$ being used to calculate $\nabla E_x^{i,j,k}$.

As can be seen in Figure 3.13(a) above, the curl of $\vec{E}$ is used to calculate the $\vec{H}$ field. This involves the use of the surrounding $\vec{E}$ field components, $E_z^{i,(j+1),k}$, $E_z^{i,j,k}$, $E_y^{i,j,(k+1)}$, and $E_y^{i,j,k}$, at time t, in order to calculate $\nabla H_x^{i,j,k}$. This is expressed as follows:

$$\frac{E_z^{i,(j+1),k}\big|_t - E_z^{i,j,k}\big|_t}{\Delta y} - \frac{E_y^{i,j,(k+1)}\big|_t - E_y^{i,j,k}\big|_t}{\Delta z} = -\mu_0 \frac{H_x^{i,j,k}\big|_{t+\frac{1}{2}\Delta t} - H_x^{i,j,k}\big|_{t-\frac{1}{2}\Delta t}}{\Delta t}$$

$$(24)$$

An analogous method can be used to find $\nabla H_y^{i,j,k}$ and $\nabla H_z^{i,j,k}$. Similarly, Figure 3.13(b) above shows the curl of $\vec{H}$ being used to calculate the $\vec{E}$ field. This involves the use of the surrounding $\vec{H}$ field components, $H_z^{i,j,k}$, $H_z^{i,(j-1),k}$, $H_y^{i,j,k}$, and $H_y^{i,j,(k-1)}$, at time $t + \frac{1}{2}\Delta t$.

$$\frac{H_z^{i,j,k}\big|_{t+\frac{1}{2}\Delta t} - H_z^{i,(j-1),k}\big|_{t+\frac{1}{2}\Delta t}}{\Delta y} - \frac{H_y^{i,j,k}\big|_{t+\frac{1}{2}\Delta t} - H_y^{i,j,(k-1)}\big|_{t+\frac{1}{2}\Delta t}}{\Delta z} = \varepsilon_0 \varepsilon_r \frac{E_x^{i,j,k}\big|_{t+\Delta t} - E_x^{i,j,k}\big|_t}{\Delta t}$$

$$(25)$$

An analogous method can be used to calculate $\nabla E_y^{i,j,k}$ and $\nabla E_z^{i,j,k}$.

The time signal of the dipole, plane wave, of TFSF source, $s(t)$, is a pulse. This can be transferred to the frequency domain by taking the Fourier transform.

$$s(\omega) = \int e^{i\omega t} s(t) dt \tag{26}$$

Ideally, we could choose the pulse to be a dirac delta function, and the value of $s(\omega)$ would be 1. Thus, we could find the response from the simulated system at every frequency by only carrying out one simulation. However, it increases accuracy and efficiency to excite the system using a short pulse. The pulse is chosen so the spectrum $|s(\omega)|^2$ has a large value over the range of frequencies in which we are interested.

The simulation returns the electric field in the system which arises in response to the input pulse $s(t)$:

$$\vec{E}_{sim}(\omega) = \int e^{i\omega t} \vec{E}(t) dt \tag{27}$$

However, as this depends on the system and the specific source used, it is more useful to measure just the impulse response of the system. This is achieved through continuous wave normalisation, by dividing by the source pulse:

$$\vec{E}(\omega) = \frac{\vec{E}_{sim}(\omega)}{s(\omega)} \tag{28}$$

The magnetic field is similarly normalised:

$$\vec{H}(\omega) = \frac{1}{s(\omega)} \int e^{i\omega t} \vec{H}(t) dt = \frac{\vec{H}_{sim}(\omega)}{s(\omega)} \tag{29}$$

These normalised values are independent of the pulse used and are thus more useful values to compute.

The Poynting vector is the directional energy flux of an electromagnetic field. It is calculated as the cross product of the electric field and the complex conjugate of the magnetic field:

$$\vec{P}(\omega) = \frac{\vec{E}_{sim}(\omega) \times \vec{H}_{sim}^*(\omega)}{|s(\omega)|^2} = \vec{E}(\omega) \times \vec{H}^*(\omega) \tag{30}$$

The Poynting vector is used to calculate power flow within the simulation.

The BPs were simulated as two truncated cones with hemispheroids at each end. The NSs were simulated similarly, with several truncated cones of varying sizes, with hemispheroid tips, placed around a spherical centre to represent the shape of one NS from a TEM image, or a generalised

NS. NRs were simulated as cylinders with hemispheres at each end. A schematic diagram of the shapes used can be seen in Figure 3.14.
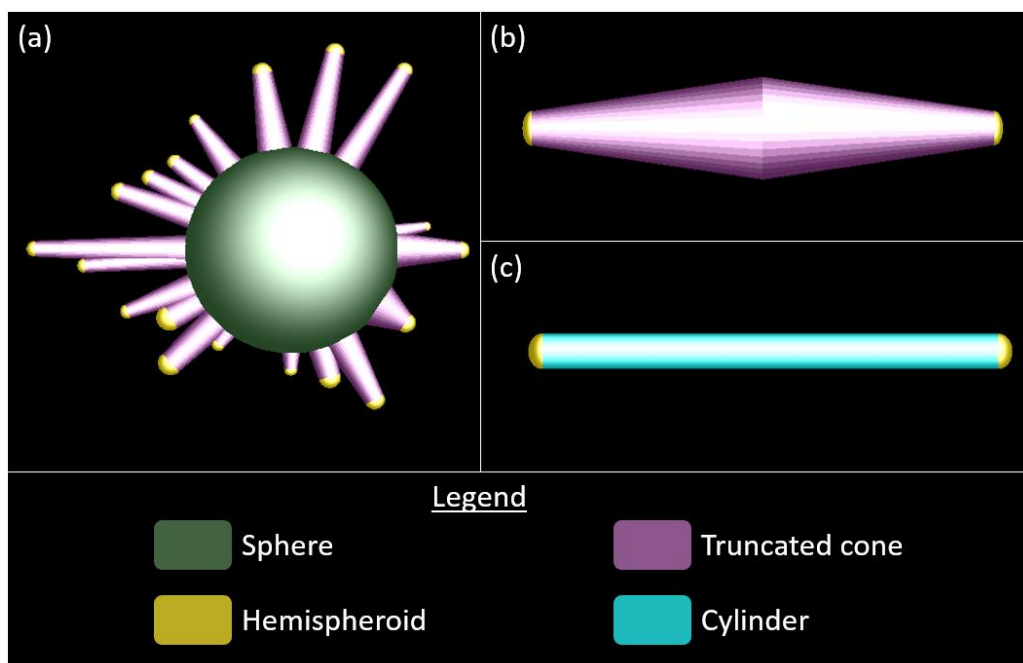
Figure 3.14: Colour-coded schematic diagrams of simulated nanoparticles, (a) nanostar, (b) bipyramid, and (c) nanorod, showing their constituent shapes.

Mesh sizes and power monitor sizes (in the case of dipole power monitors) were optimised to give the best numerical results (via convergence testing). Parameter sweeps were carried out in order to optimise structures, which then informed synthesis and fabrication methods.

3.13 Two-photon lithography

The two-photon lithography (TPL) system used in this work is the Photonic Professional GT2 by Nanoscribe. The 780 nm laser light used is circularly polarised. The maximum power of the system is 50 mW, and powers used to write the sample are annotated as percentages of this maximum power. The TPL was carried out by Teodora Faraone, under the supervision of Prof. Colm Delaney.

BPs were deposited onto glass slides via spin coating. A polymerisable solution of a monomer and photoinitiator (additionally containing quantum dots for samples where quantum dots were required) was dropped onto the top of the slide. The slide was inserted into the Nanoscribe 2-photon lithograph, above an oil immersion objective. This objective focused the 780 nm femtosecond laser onto the sample. Within the software of the lithograph, a pattern was laid out in a CAD interface to modify the core laser power (power applied onto the sample) and the interface value (related to the exact vertical position of the focal point of the laser). The pattern

was then written onto the slide by the laser, then the slide was removed, washed in isopropanol to remove any remaining unpolymerised solution, and dried.

The polymerisable solution used in this work was TMPET (Trimethylolpropane ethoxylate triacrylate – <u>monomer</u>) and PBPO (phenylbis (2, 4, 6-trimethylbenzoyl) phosphine oxide – Type I <u>photo-initiator</u>), with proportions of 99 wt% and 1 wt%, respectively.
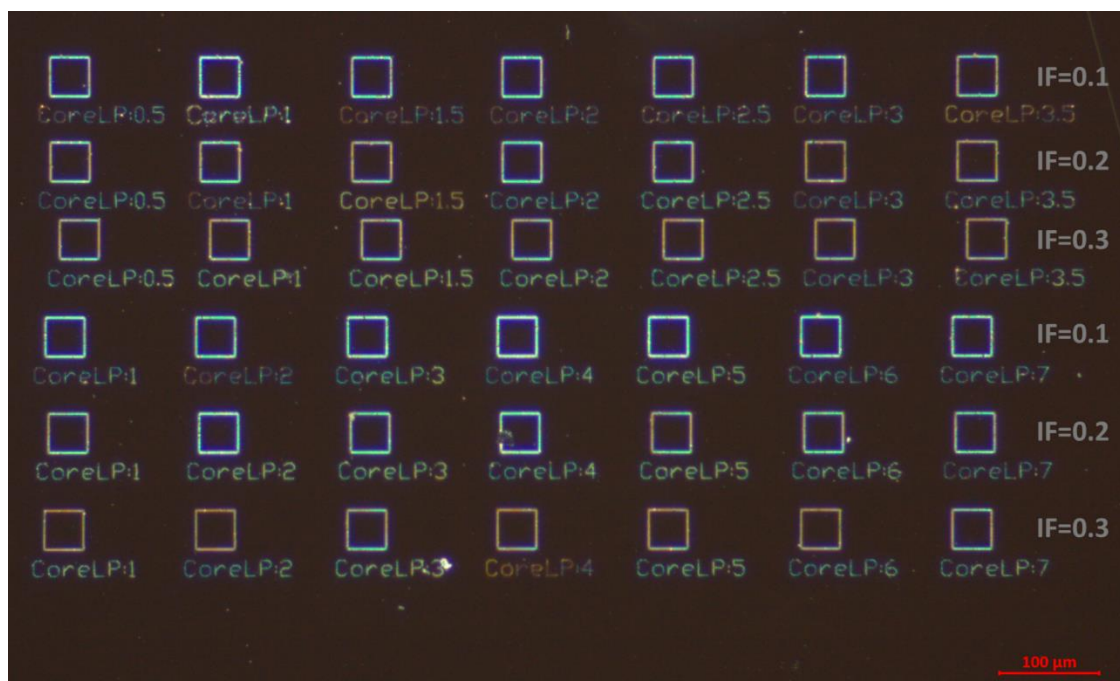
Figure 3.15: Optical microscope image of TPL grid, showing the core laser power (CoreLP) as a percentage of maximum power, and the interface (IF) values which correspond to the vertical position of the focal plane.

Figure 3.15 above shows the layout of a 2-photon polymerisation-patterned grid on a slide. The optimal interface values (vertical position of the focal plane) for these slides were found to be 0.1 and 0.2. The squares are written at high powers (30 %), so as to be easily visible under the microscope, and within each square the power used is ≤7%, which cannot typically induce polymerisation. In this system, the threshold value for polymerisation is 10% of the total laser power, thus any polymerisation seen in areas exposed to lower powers could only have been due to plasmonic enhancement (as described in Chapter 5).

3.14 Conclusion

In conclusion, the methods used in this work have been described. UCNP and plasmonic nanoparticle syntheses have been detailed, along with the silica shelling of nanostars. The process used for layer-by-layer deposition of nanoparticles and spacer polyelectrolyte layers on substrates has been explained, as well as the process used for spin-coating nanoparticles onto substrates.

The various forms of microscopy and spectroscopy used have been described, namely darkfield/brightfield microscopy, fluorescence lifetime imaging microscopy, electron microscopy, upconversion emission spectroscopy, and UV-visible extinction spectroscopy. The background theory for FDTD simulations is provided, as is the procedure for two-photon lithography.

4 Plasmonic Gold Nanoparticles

4.1 Introduction

Plasmonic nanoparticles have many uses. They can be used to enhance emission of luminescent materials, as well as to enhance the absorption of such materials (which results in overall emission enhancement also). Plasmonic nanoparticles have been used to enhance solar cells[125], to strongly couple with 2D nanomaterials[17], and to enhance single molecule fluorescence[126]. They can be created via bottom-up methods such as chemical synthesis or created in arrays using top-down methods such as electron beam lithography, as described in Chapter 1. The objective of this chapter is to investigate the tunability of plasmonic nanoparticles, and to use these particles to investigate specific light-matter interactions, such as enhancement of emitters and enhancement of photopolymerisation.

In a symmetrical plasmonic particle (such as a sphere), there will only be one dipole plasmon resonance mode (or rather, several degenerate modes which have the same resonance wavelength, as the particle has C∞v symmetry and is the same size in all three dimensions). The wavelength of this resonance is dependent on the material of the particle, and its diameter. There are also quadrupole, octupole, and higher order modes, as described in Section 2.1, but the dipole resonance dominates in particles much smaller than the wavelength of light[46]. Thus, in order to tune the resonance wavelength, you must increase the total size of the nanoparticle. It is not possible for the particle to be tuned to interact with multiple wavelengths at once, as its resonances are degenerate. However, this is possible with multiresonant particles. Multiresonant particles such as nanorods (NRs), bipyramids (BPs), and nanostars (NSs) have two or more resonances at different wavelengths. These can be tuned synthetically in order to align with desired wavelengths. Elongated nanoparticles such as NRs and BPs have two resonance peaks, a transverse mode and a longitudinal mode. While these can both interact with emitters, the longitudinal mode is stronger, and is best utilised using longitudinally polarised light. Adding more than two tips to nanoparticles can allow different plasmon resonance modes to be excited at different polarisations, as can be seen in Figure 4.1 below. For particles with many tips pointing in different directions, such as NSs, this can potentially result in strong E-field enhancements for light at any polarisation.
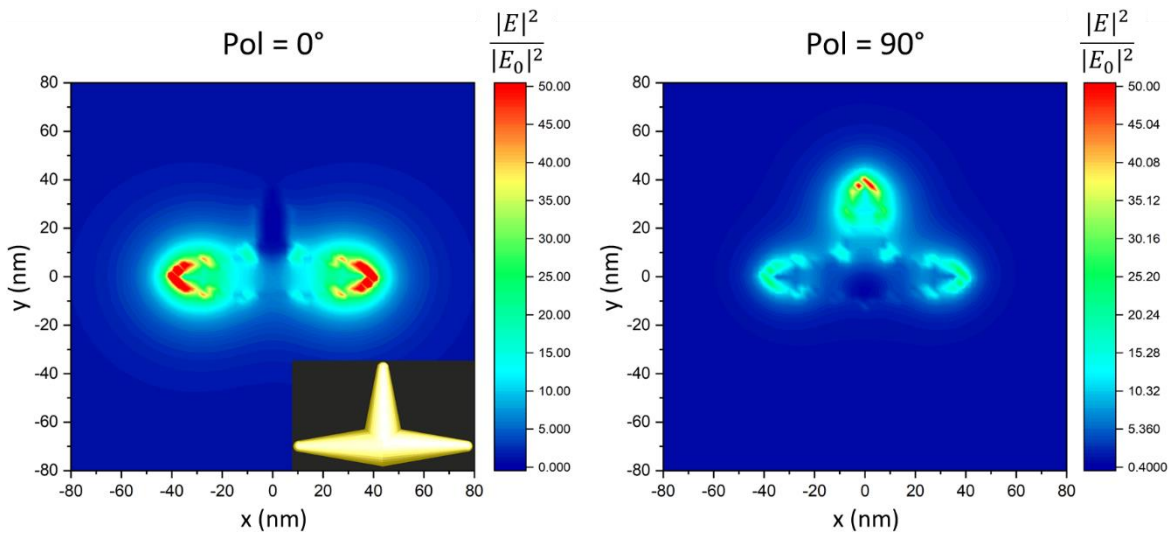
Figure 4.1: Electric field enhancement images for a three-pointed nanoparticle, at 0° and 90° polarisation. Schematic diagram of simulated particle, inset.

4.1.1 Spectral range

In general, for this project the aim was to tune the nanoparticle resonances to specific wavelengths, in order to potentially enhance different emitting nanoparticles. The wavelengths needed were in the visible and near IR ranges. For UCNP enhancement (see Chapter 6), 980 nm was the optimal excitation enhancement wavelength, while for emission enhancement the wavelengths were around 550, 650, and 800 nm (two Er^{3+} peaks and one Tm^{3+} peak). In order to facilitate 2-photon polymerisation and interaction with QDs (see Chapter 5), the wavelengths of interest were 780 nm (incoming laser wavelength for the 2-photon lithography system), and 665 nm (QD emission peak wavelength).

Different nanoparticles have different properties and different numbers of non-degenerate resonances, and thus could be more ideally suited for different applications. The small mode volume of the BP resonances made them potentially suitable for 2-photon polymerisation, which requires very high field intensities. NSs have multiple different plasmon resonance wavelengths due to their multiple tips of different lengths and orientations. This could make them potentially suitable for interaction with upconverting nanoparticles. Upconverting nanoparticles typically have their absorption wavelength (NIR) very far away in the spectrum from their emission wavelengths (typically UV, visible, or NIR), and may be optimally enhanced through the enhancement of both their absorption and emission wavelengths, which could potentially be achieved by NSs with resonances at both wavelengths.

4.2 Seeds

There are 3 types of gold seeds used in this work; Type I (Nikoobakht et al., 2003)[108], Type II (Liu et al. 2005[56], modified from Jana et al., 2001[111]), and Type III seeds (original 3.5 nm seeds from Jana et al., 2001[111]). Type I seeds are monocrystalline, and the Type II and Type III seeds are penta-twinned[56]. The penta-twinned structure of a Type III seed is shown in Figure 4.2(d), which highlights the 5 side facets of the seed. This difference in the seeds results in very different crystal structures in the nanoparticles which are grown from the seeds. Type I seeds will result in monocrystalline nanoparticles (ideal for NRs), whereas seeds II and III will result in penta-twinned nanoparticles (ideal for BPs or NSs).

When the penta-twinned seeds are used, high HCl concentrations will result in BPs, whereas lower HCl concentration will result in NSs. (10 µL HCl for NSs, 200 µL HCl for BPs). This is because the pH has a significant impact on the dominant growth direction, and at more neutral pH, the growth is not inclined along one growth axis, and stars are formed[127].
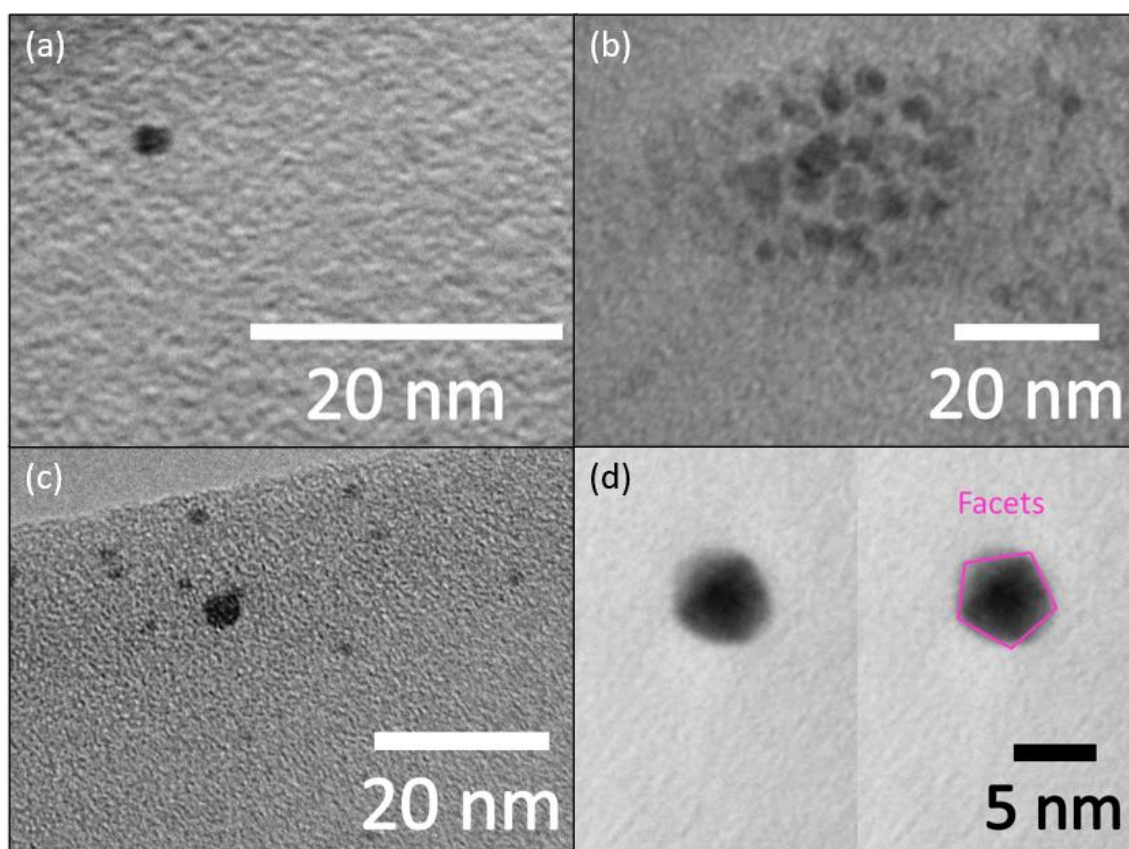
Figure 4.2: TEM images of (a) Type I seed, (b) Type II seeds, and (c) Type III seed. (d) TEM image of penta-twinned Type III seed, with the 5 side facets outlined.

Small seeds may undergo Ostwald ripening (increasing in size due to the smaller particles dissolving and redepositing onto the larger particles) on TEM grids as they dry[56], so the actual size of the seeds while in solution may be smaller than that seen in TEM images. Type I seeds (Figure

4.2(a)) are likely to be 1.5 nm in diameter, and Type II (Figure 4.2(b)) around 3 nm[56]. The Type III seeds (Figure 4.2(c), (d)) should be around 3.5 nm[111]; however, they are a bit larger in the above TEM images (measured size ≈ 4.1 nm), due to the aforementioned ripening.

4.3   Synthesis differences

There are many factors which can potentially affect the outcome of seemingly identical syntheses:

- The temperature in the room

- The humidity (esp. when weighing out hygroscopic chemicals)

- The age of reagents (how long since their opening)

- The age of reagent solutions (how long they have been dissolved in water)

- The person carrying out the synthesis (might decide the value from a fluctuating mass balance reading differently)

- Small accidents, i.e., not adding the full volume due to a small amount remaining in the pipette tip.

- Seed age (typically used within one week to avoid issues with this)

Thus, even with seemingly identical syntheses, the resulting particles can still vary. Therefore, it was found that utilising a variety of parameters around the expected ideal would be more likely to produce particles with the desired plasmon resonance wavelength. It is also most instructive to compare directly batches of nanoparticles made on the same day, while comparisons of trends can be made across different synthesis days.

The syntheses for BPs, NRs, and NSs are very similar, however small differences in concentrations of certain reagents give rise to very different results. These differences can be seen in Figure 4.3 and Figure 4.4 below.
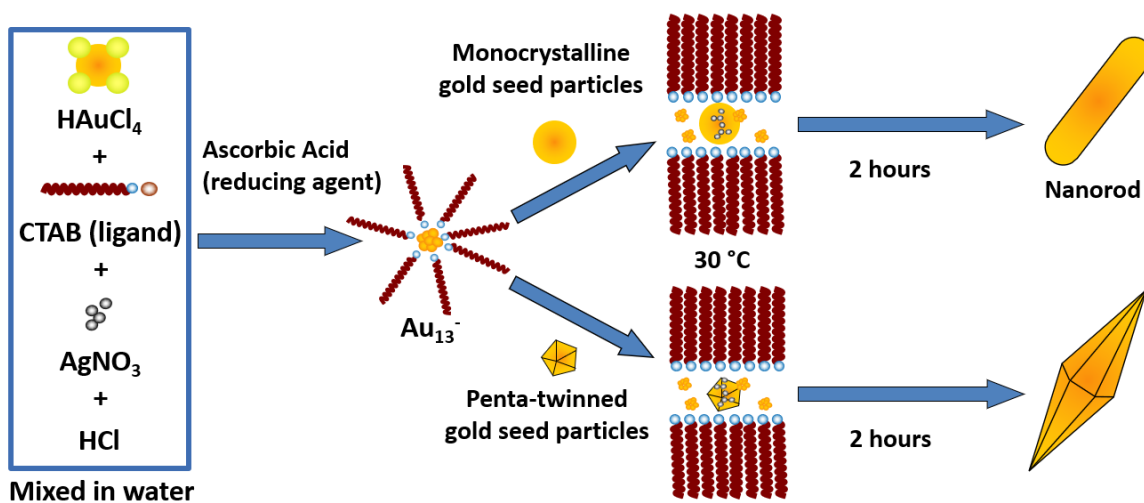
Figure 4.3: Schematic of gold nanorod and bipyramid syntheses, showing the difference in resulting nanoparticles due to using different seed types.
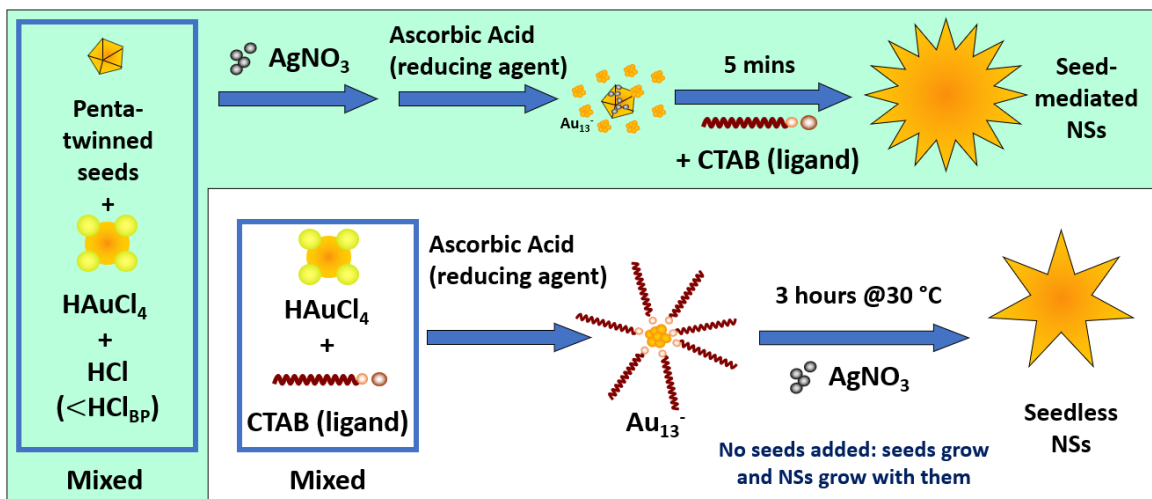
Figure 4.4: Schematic of seed-mediated and seedless gold nanostar syntheses, showing the difference in resulting nanoparticles due to presence/absence of seeds and HCl, the order in which reagents were added, and the amount of time taken for the NSs to grow.

4.4 Nanorods

NRs are elongated nanoparticles with two plasmon resonances, one transverse and one longitudinal (Figure 4.5(b)). The longitudinal plasmon mode is much stronger than the transverse mode and is more easily tuneable by varying synthetic parameters in order to change the aspect ratio.
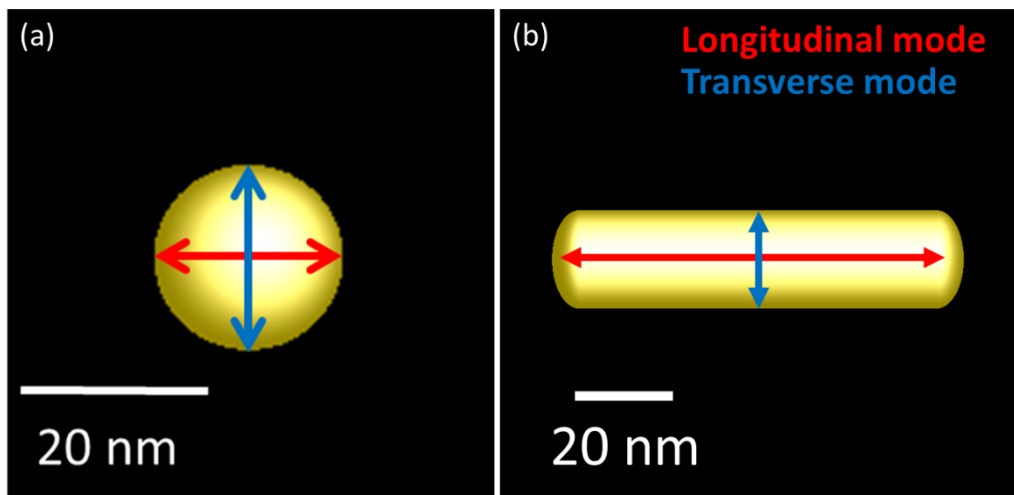
Figure 4.5: (a) Schematic of a gold nanosphere showing the directions of the two degenerate plasmon resonances, and (b) schematic of a gold NR, showing the directions of transverse and longitudinal plasmon resonance modes.

Two syntheses have been used, one which is similar to the BP synthesis[56,108], and one which involves adding additional growth solutions to the mixture as it is reacting[111].

In the first synthesis[56,108], the concentration of AgNO$_3$ was varied in order to change the aspect ratio and thus the plasmon resonance wavelength of the NRs. The extinction spectra of 4 batches of NRs, synthesised varying AgNO$_3$, can be seen in Figure 4.6 below.
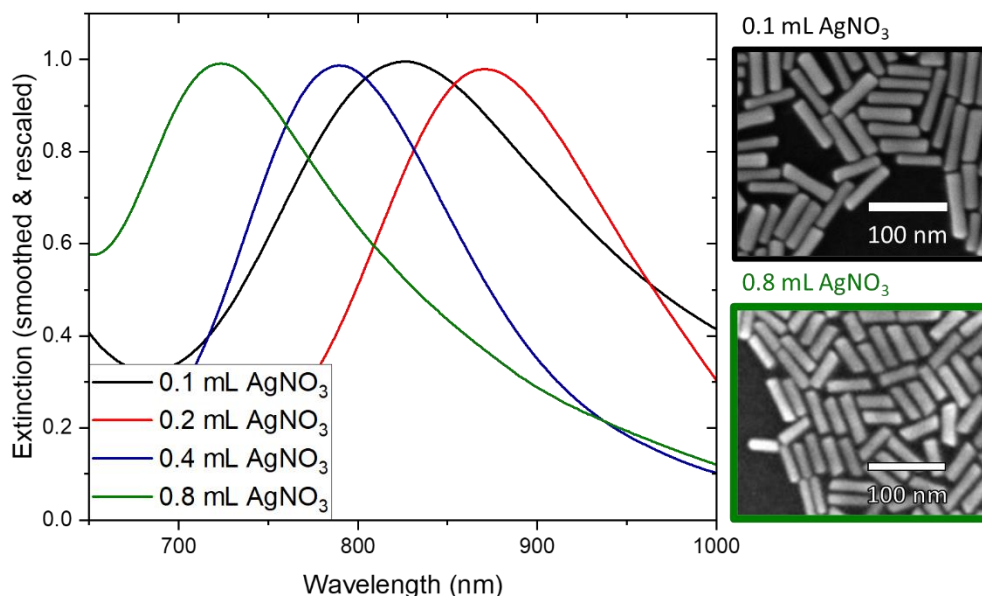
Figure 4.6: Extinction spectra of NRs, varying AgNO$_3$ concentration.
SEM images of the NRs, to right of graph.

At lower concentrations, an increase of Ag concentration resulted in an increase in the resonance wavelength (as has been shown in the literature[56]). Conversely at higher concentrations the increase in Ag concentration gave rise to a decrease in the plasmon wavelength (after a peak). This was not in line with the literature results, however, in their paper, Liu *et al.*[56] did not use as high concentrations as have been used in this work. This is a much stronger Ag concentration dependence than that seen for BPs.
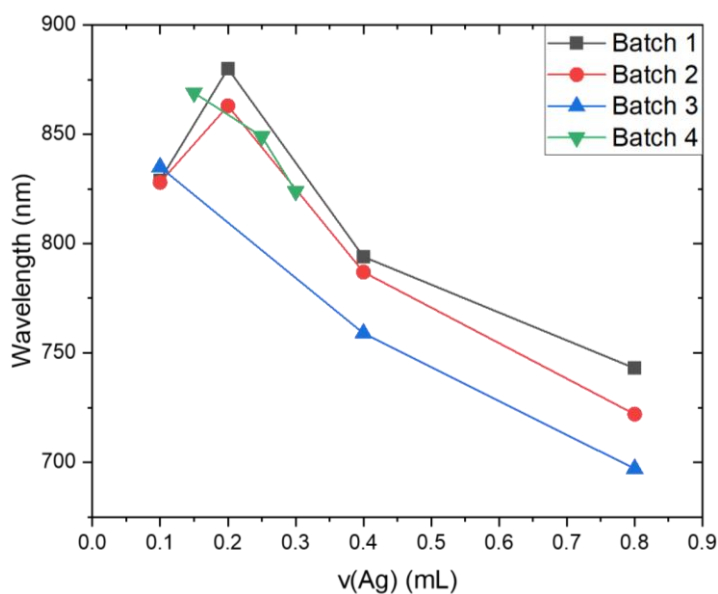
Figure 4.7: Extinction SPR peak wavelength versus volume of AgNO$_3$ added,
over several NR batches.

Unusually, batches of nanoparticles synthesised using one month old seeds rather than fresh seeds resulted in BPs and NSs rather than NRs, for the same synthetic parameters. This can be seen in the SEM images in Figure 4.8(a) and (b) below. Such a change in outcome is likely due to an increase in the proportion of penta-twinned seeds over time, resulting in these penta-twinned particles. Similar results have previously been seen by Park *et al.*[128].
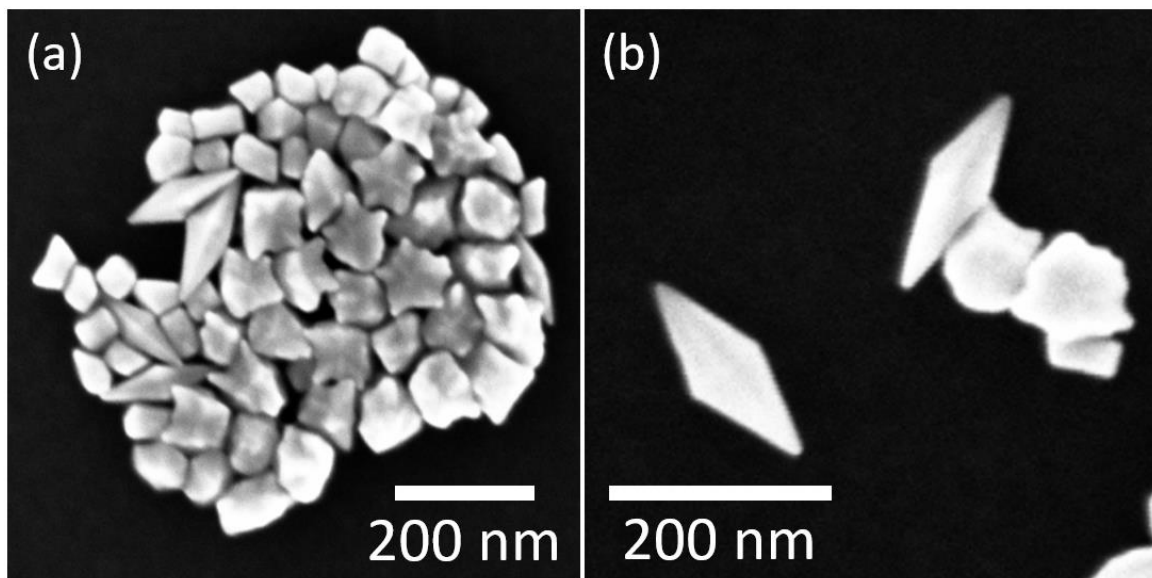
Figure 4.8: (a) SEM image of a sample prepared according to NR synthesis procedures, but with one-month aged seeds, showing BPs and NSs. (b) SEM image of another sample prepared with the same seeds, higher magnification.

Unfortunately, the synthesis method used to make the NR batches in Figure 4.7 was not able to produce any NRs with plasmon wavelengths above ≈ 870 nm. Thus, the second synthesis method was used to attain the longer wavelengths needed for UCNP excitation enhancement.

The second NR synthesis (batches labelled NR_B) method involved the addition of sequential 1 mL aliquots of a growth solution. Each 1 mL added shifted the wavelength of the NRs in solution by an average of 89 nm. This resulted in NRs with plasmon resonances up to above 1000 nm, thus allowing for the synthesis of 980 nm NRs for potential use in UCNP enhancement. This is in line with the literature, where NR plasmon resonances of 1250 and beyond have been shown[108]. The extinction spectra for these samples are shown in Figure 4.9 below.
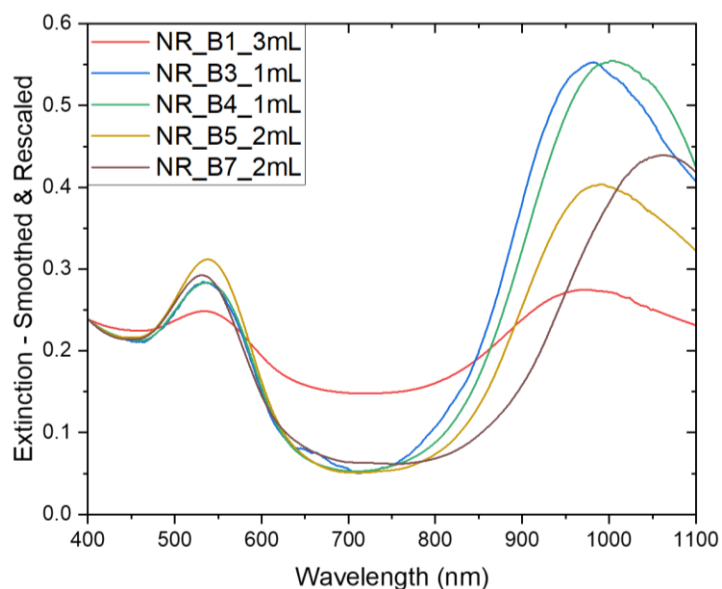
Figure 4.9: Extinction spectra of various samples synthesised using the second method, along with the number of mL of solution B which were added.

For several sample batches, the change in wavelength can be seen in Figure 4.10 below. This redshift is due to the addition of extra growth solution providing more gold which could deposit onto the seeds, increasing the size of the NRs. The dependence of the wavelength on the volume of the second solution added is shown in Figure 4.11.
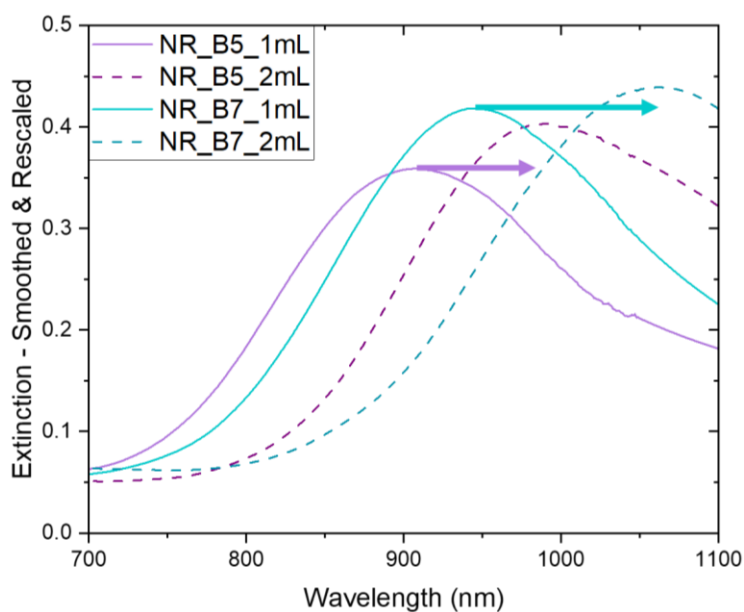
Figure 4.10: Extinction spectra of NRs showing redshift of peak position upon addition of an extra 1mL of solution B.
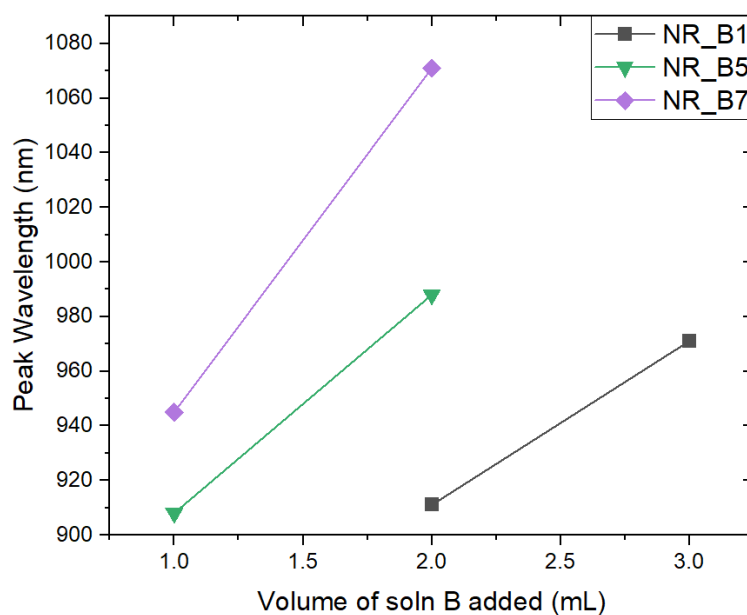
Figure 4.11: Dependence of peak wavelength on the amount of the growth solution (B) added.

Figure 4.12 shows the change in wavelength upon addition of an extra millilitre of the second solution. This varied across several samples; however, this may be due to variation in the amount of time elapsed before measuring the extinction spectra, or due to some other variations in the syntheses caused by them being carried out on separate days (humidity etc.).
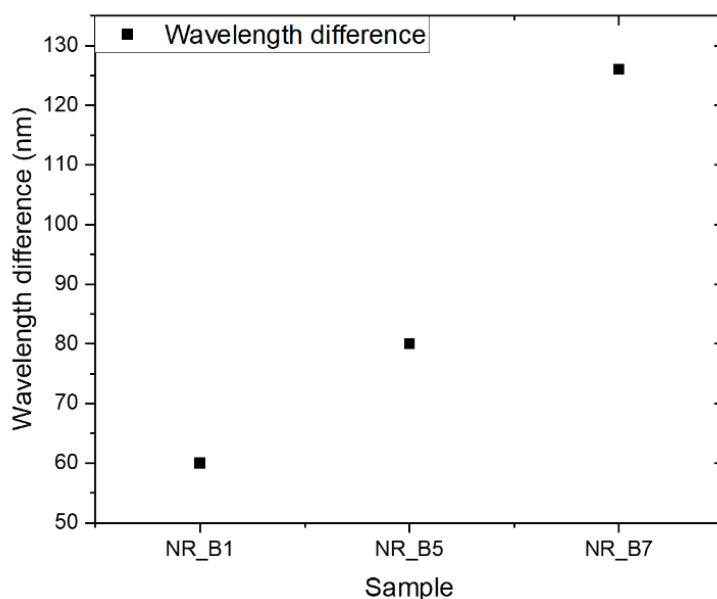
Figure 4.12: Wavelength differences upon addition of an extra 1 mL of solution B for 3 samples.

This second synthesis method was able to provide NRs with a plasmon resonance wavelength of 980 nm, which was suitable for use for potential UCNP enhancement.

4.5   Bipyramids

Similar to NRs, BPs are also elongated particles but have superior electric field enhancing benefits over NRs. Field enhancements are proportional to the curvature of a surface[55,56] due to the higher concentration of conduction electrons, and thus the high curvature of a sharp BP tip is what gives rise to this improved field enhancement. The localised field enhancement of BP can be seen in Figure 4.13 below.
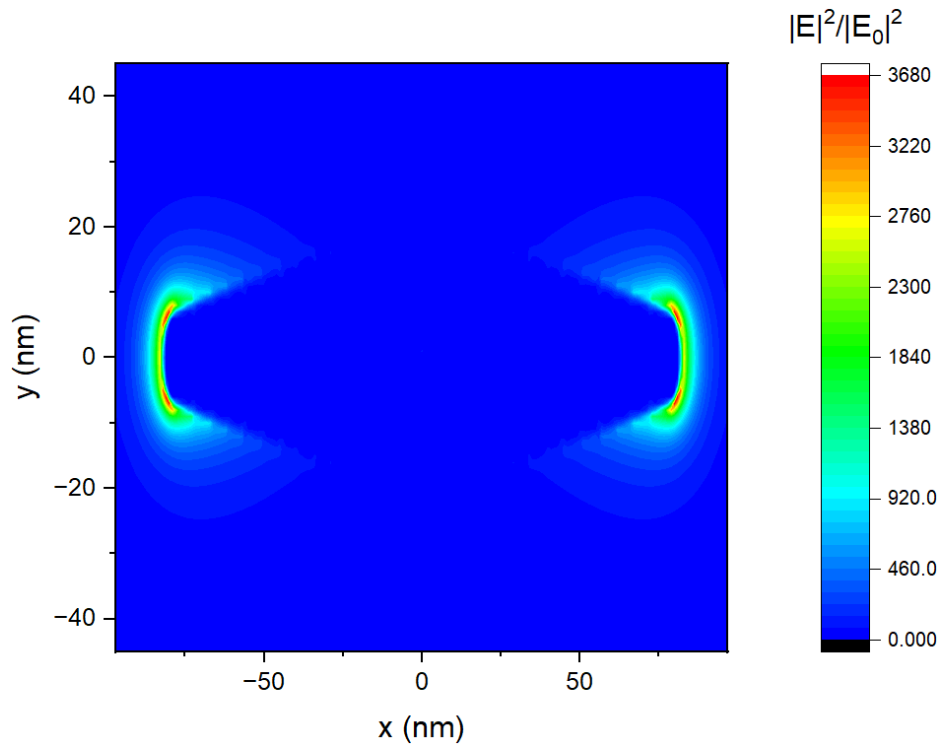
Figure 4.13: Map of electric field intensity enhancement at 780 nm, from a simulated BP. Width 42 nm, aspect ratio 3.9.

Unlike spheres, which have degenerate plasmon modes, BPs have a transverse mode and a longitudinal mode. Changing the width and length/aspect ratio of BPs can drastically change the resonance wavelength of the longitudinal dipole mode. This can be tuned synthetically as discussed in Section 3.3, giving rise to a broad range of potential wavelengths which can be plasmonically enhanced by appropriately sized BPs.
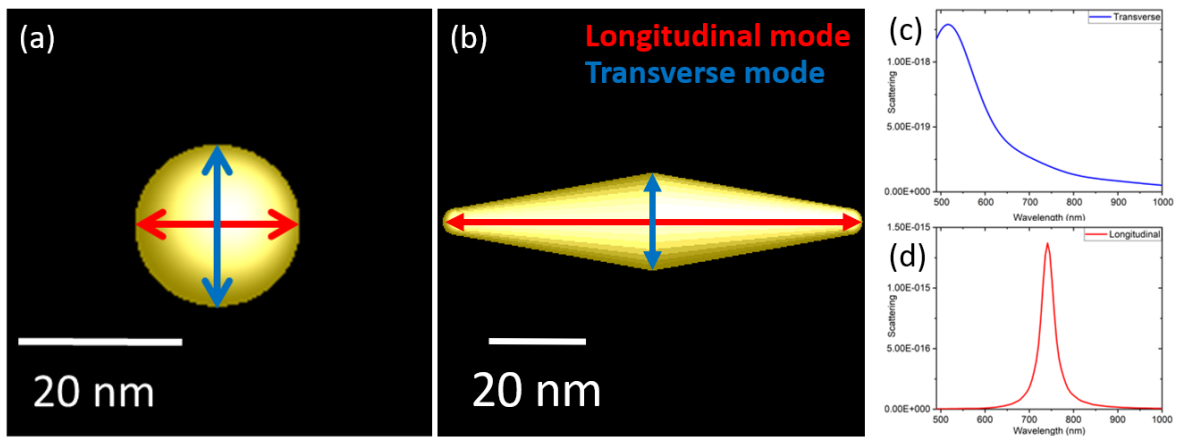
Figure 4.14: (a) Schematic of a gold nanosphere showing two of the degenerate plasmon resonances, (b) schematic of a gold BP, showing transverse and longitudinal modes, (c) and (d) simulated scattering spectra of a BP, for transverse and longitudinal modes.

4.5.1 Aspect ratio

BPs of varying aspect ratios were simulated with mesh size 1 nm, keeping the width constant, in order to identify which BP sizes would be optimal for use in enhancing specific wavelengths for UCNPs and QDs. As the length of the BPs increased, so did the peak wavelength of the longitudinal plasmon resonance.
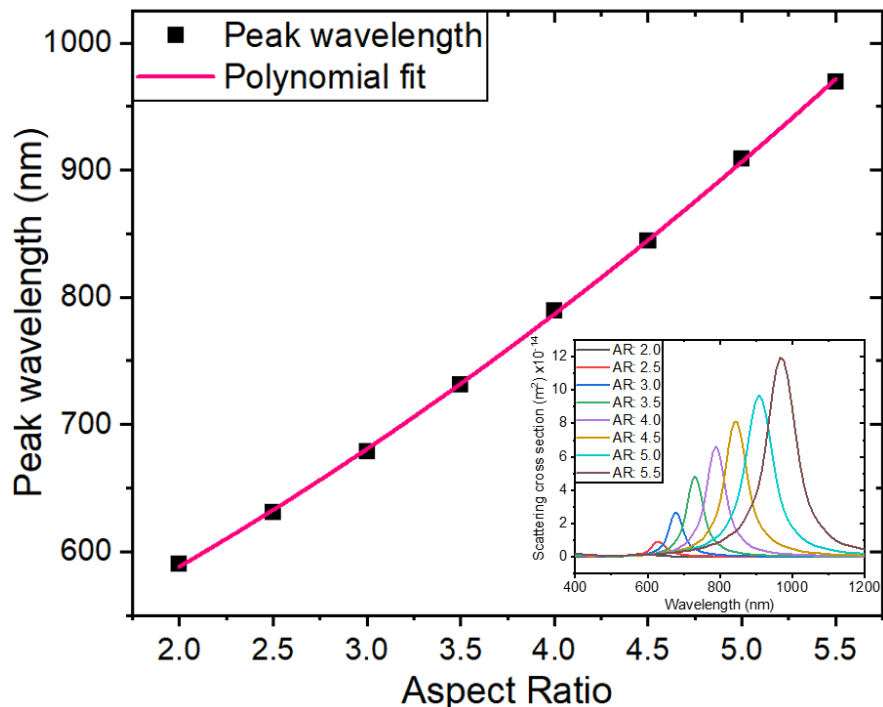
Figure 4.15: Plot of scattering peak wavelength vs aspect ratio for simulated single BPs in air, with polynomial fit. Simulated scattering spectra, inset.

Figure 4.15 above shows the relationship between scattering peak wavelength and BP aspect ratio, for a single BP with width 42 nm. This graph correlates with what might be expected, that

the plasmon resonance wavelength increases with an increase in particle aspect ratio. This data was then fitted with a 2nd order polynomial fit (the equation for this fit is $y = 444 \pm 9 + (58 \pm 5)x + (6.8 \pm 0.7)x^2$, with Adj. R^2 = 0.99974), in order to predict which BP sizes could be synthesised to best enhance the emitters in Chapters 5 and 6.

Figure 4.16 shows two batches of BPs with different aspect ratios but the same widths, as well as the relevant plasmon resonance wavelengths for each one. These agree with the relationship shown in Figure 4.15, with a redshift of the plasmon resonance wavelength with an increase in aspect ratio.
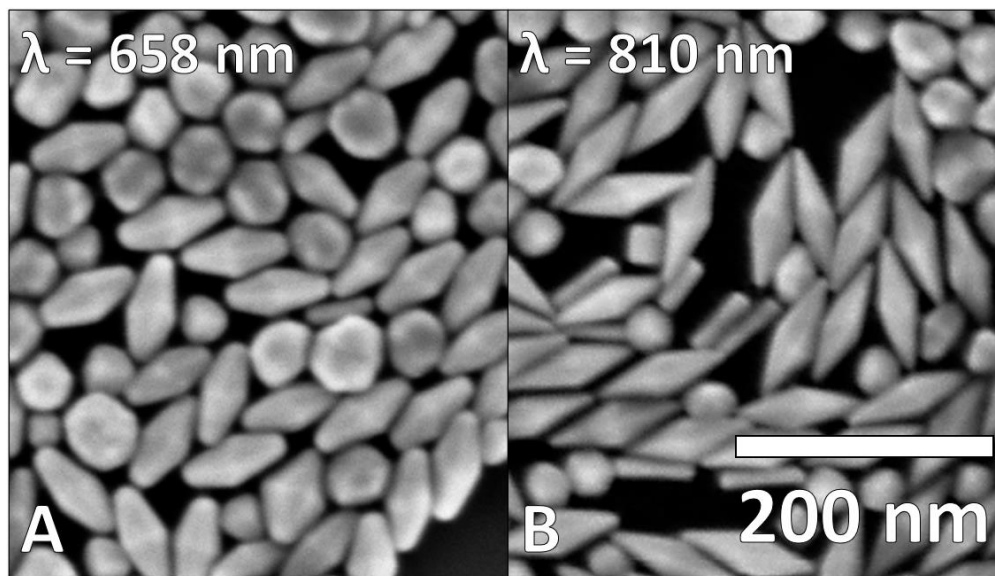
*Figure 4.16: SEM images of two batches of BPs with length L, width W, and aspect ratio AR: **Batch A**: L=83±5 nm, W=37±3 nm and AR=2.2±0.1, and **Batch B**: L=96±7 nm, W=32±4 nm, and AR=3.1±0.3. Plasmon resonance wavelengths in water, inset.*

The resonance wavelengths in Figure 4.16 were measured from the extinction spectra of the BPs in water, whereas those in Figure 4.15 were simulated in air. As the refractive index of the material surrounding the BPs has a significant impact on their resonance wavelengths, simulations were run in different materials to identify whether certain BP aspect ratios could be optimised for different wavelengths in different materials.
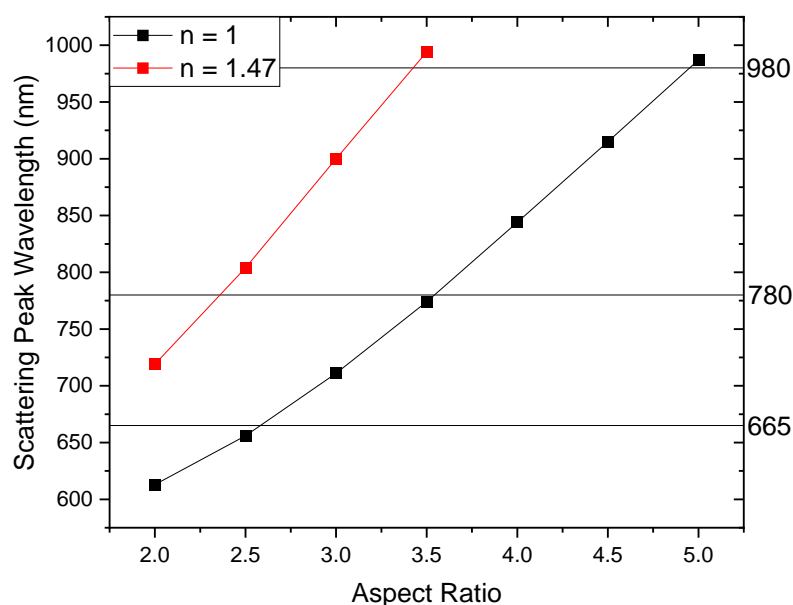
Figure 4.17: Simulated scattering peak vs aspect ratio of BPs at background indices 1 (~vacuum/air) and 1.47 (~monomer). Relevant wavelengths for UCNPs (980 nm), 2-photon polymerisation (780 nm), and QDs (665 nm) are shown.

For the two-photon lithography carried out in Chapter 5, first polymerisation enhancement occurs in a monomer liquid (n = 1.47) using a laser at 780 nm. Then any excess is removed, leaving a BP mainly surrounded by air (n = 1.00), with some quantum dots in the small amount of polymer around the BP, which emit at 665 nm. The simulated scattering peak wavelengths in Figure 4.17 above show that a BP with ideal aspect ratio for 780 nm in the monomer solution (AR 2.5) may have an ideal aspect ratio for enhancing/interacting with QDs after the monomer has been washed away, leaving mainly air. While it is unlikely that a similarly ideal overlap may be shown for the 980 nm absorption wavelength of UCNPs, there may be an opportunity to match well for the 800 nm emission wavelength of Tm^{3+}-UCNPs, for example.

This simulation can also be extended to include the substrate and a small polymer lobe. Figure 4.17 shows the difference in plasmon resonance peaks for BPs in polymer versus in air, as the TPL occurs in polymer, but the scattering will be measured in air. However, when there is even a small amount of polymer around a bipyramid, as is the case for the samples prepared in this chapter, the plasmon resonance wavelength still redshifts, but to a lesser extent. An example of this redshift is shown in Figure 4.18, with the extinction peak wavelength for the BP fully encased in polymer redshifted past 1000 nm.
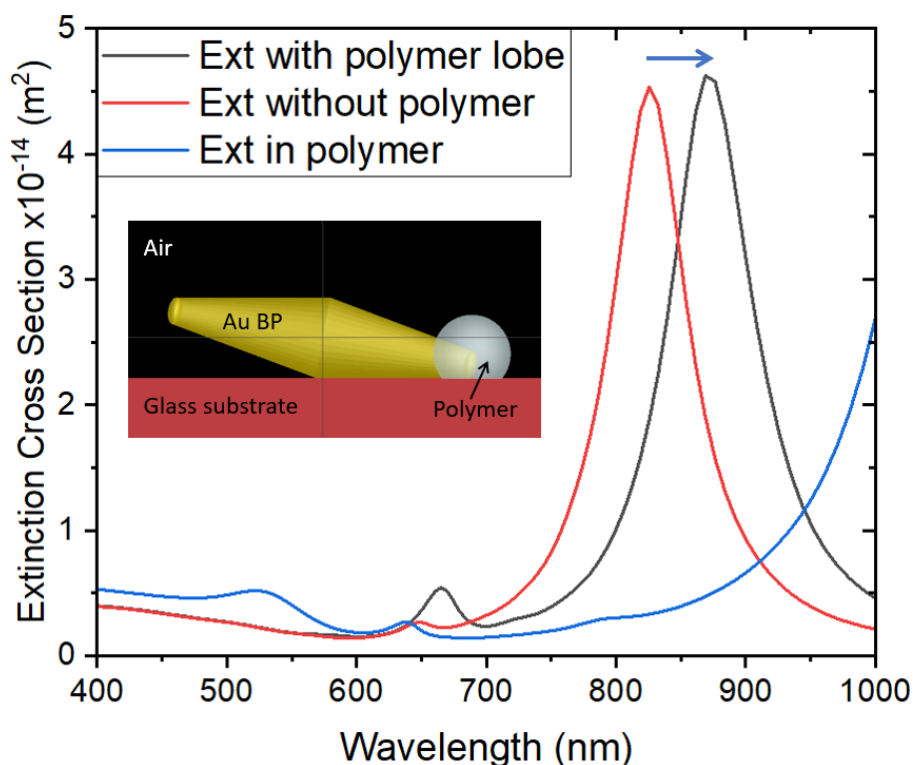
Figure 4.18: Extinction cross sections of a BP (AR = 3.86) on glass, showing the redshift from BP without polymer to a BP with a polymer lobe around one tip, compared to more extreme redshift for BP fully encased in polymer ($\lambda>1000$ nm). Inset: schematic of simulation layout.

4.5.2   Synthesis variation

For the BP synthesis, the concentration of certain reagents (controlled by the volume of each reagent solution added) has a significant impact on the BP size, shape, and aspect ratio. This subsequently affects the plasmon resonance wavelength. Thus, a wide range of wavelengths become available for various applications.

In Figure 4.19(a), the extinction spectra of different BP batches are shown, along with the different volumes of reagents added. Figure 4.19(b) and (c) show SEM images of the shortest and longest bipyramids from these synthesis batches. The ascorbic acid concentration had a strong impact on the wavelength of the plasmon resonance (see Figure 4.20), whereas the concentration of $AgNO_3$ did not have as significant of an effect (as noted by Liu *et al.*[56]). The ascorbic acid is responsible for reducing the Au^{3+} ions to Au^+ ions, which adsorb onto the seed surface in order to grow the BP. Thus, an increase in the amount of AA in the reaction vessel results in an increase in the amount of Au(I) available, thus increasing the overall size which the BP can attain.

At lower AA concentrations, a positive relationship between $AgNO_3$ concentration and wavelength can be seen. This is likely due to the $AgNO_3$ giving the opportunity for the steep stepped facets of the BPs to form, and so more Ag could stabilise steeper facets (allowing the

formation of longer BPs/higher aspect ratios). Geitner *et al.*[129] have also shown such a redshift of BP plasmon resonances with increasing $AgNO_3$ concentration (as well as noting that the BP growth rate increases with $AgNO_3$ concentration).
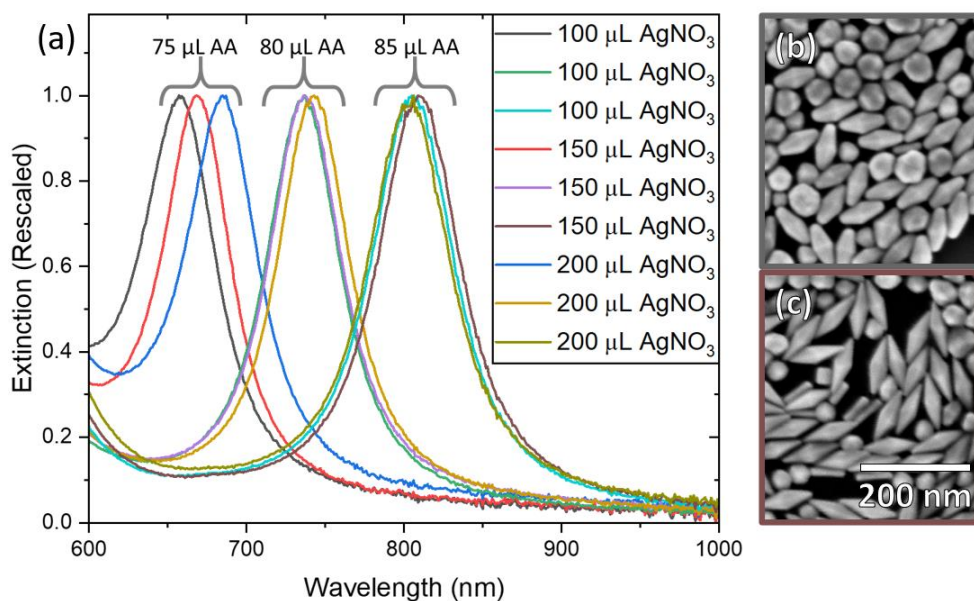
Figure 4.19: (a) Extinction spectra of BPs showing wavelength tuning via variation of the volume of ascorbic acid (AA) and $AgNO_3$ added. (b) and (c) SEM images of the BP batches with the bluest and reddest plasmon resonance wavelengths, respectively.
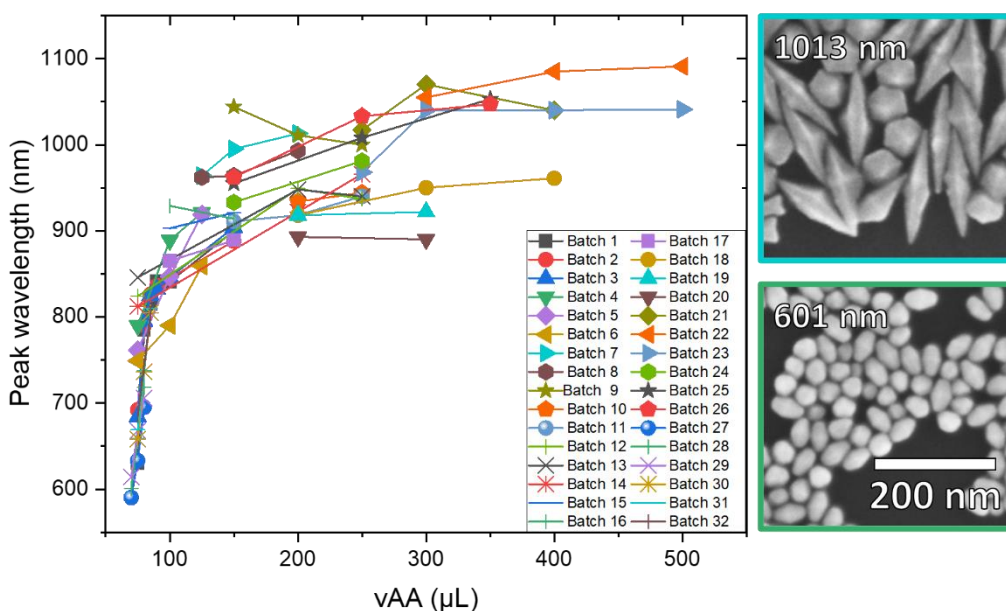
Figure 4.20: Graph of peak wavelength vs volume of ascorbic acid (reducing agent) added, over many synthesis batches. SEM images of very large and very small BPs, inset (same scales). Synthesis parameters can be found in Table 3, Appendices.

Figure 4.20 above shows a trend of increasing peak wavelength as volume of AA is increased. The particularly sharp increase in wavelength seen at lower volumes of AA is likely due to this being

close to the threshold for how much AA is needed to reduce the gold. The slight increases in AA at these low volumes may thus be rapidly increasing the amount of available gold for growing the BPs, rapidly increasing the BP size. The dependence here is nonlinear. At higher volumes, a plateau is seen. This plateau may be due to there being a smaller amount of gold ions available for reduction, as much of the gold has already been reduced by the large amounts of l-ascorbic acid. This likely shows the very limits of this dependence.

BPs are typically reported as having LSPRs which can be tuned down to around 700 nm[130], with some examples reducing the longitudinal resonance wavelength to 650 nm[131]. This work has shown BPs with a wavelength below 600 nm for the first time.

BPs with plasmon resonance wavelengths above 1000 nm have previously only been synthesised by using smaller BPs/truncated BPs as seeds, after which a regrowth step was carried out[1,2], or by significantly reducing the seed concentration[3]. However, this has not previously been achieved by only modifying the l-ascorbic acid concentration. Additionally, such an extensive investigation into the full shape of this l-ascorbic acid concentration dependence has not previously been shown.
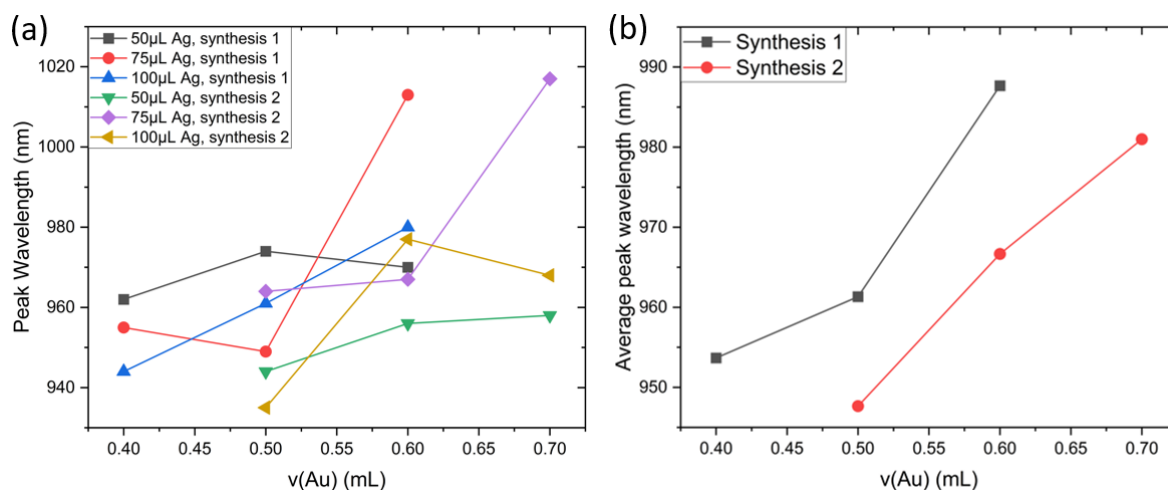
Figure 4.21: (a) Graph of peak wavelength vs volume of chloroauric acid (source of gold ions) added, over two sets of synthesis batches at different silver concentrations. (b) Average peak wavelength for each synthesis batch in (a), vs volume of gold added, showing an increase in wavelength with increasing gold volume.

Figure 4.21 above shows a clear increase in peak wavelength with increasing chloroauric acid (gold ion source) volume. This occurs as an increase in the amount of gold ions added will increase the amount of gold available to form the BPs. Thus, the size to which the BPs can grow is larger, redshifting the plasmon resonance peak.
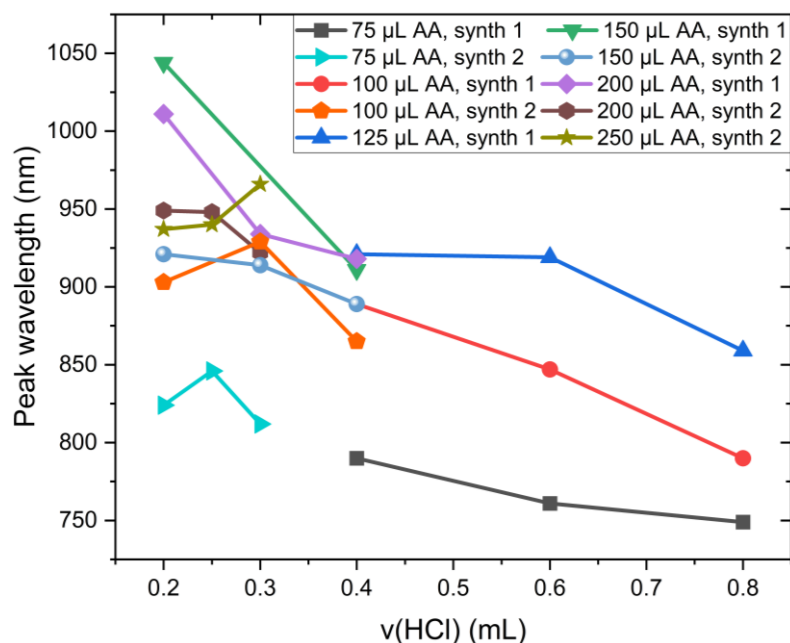
Figure 4.22: Graph of peak wavelength vs volume of HCl added over various syntheses. Each group of points connected by a line is a group of syntheses performed on the same day.

Figure 4.22 demonstrates the impact of changing HCl concentration on the longitudinal plasmon resonance wavelength of BPs. Over several synthesis batches, an increase in the volume of HCl added resulted in a decrease in the plasmon resonance wavelength. This is due to the change in pH altering the kinetics of growth along the ⟨100⟩ and ⟨110⟩ directions (by changing the amount of CTAB capping on the {110} facets[132]). At lower pH values, the growth in the longitudinal direction is slower than the growth in the transverse direction[127], and so the nanoparticles have a smaller aspect ratio. Thus, the plasmon resonance wavelength blueshifts. If the pH was very high (with very little or no HCl added), there was no preferential growth direction and NSs would grow, as described in Section 4.6 below.

The extinction spectra taken of the synthesised BPs in solution also show a peak at around 540 nm. This peak is a combination of the transverse peak of the BPs (weak) and the extinction of the spheroids which are also seen in solution. BPs can be purified post-synthesis to remove the spheres[133], however this was not deemed necessary for this work, as single BPs could be easily isolated in the spin-coated samples (See Chapter 5). Single particle spectra show little or no transverse peak but show a strong single longitudinal peak. This occurs because elongated particles have a stronger longitudinal resonance than transverse resonance, and the longitudinal:transverse ratio increases with an increase in nanoparticle aspect ratio[134]. This can be seen in Figure 4.23 below, which compares the ensemble and single particle spectra for BPs of the same batch. The transverse peak in the single BP scattering spectrum is very small, almost indistinguishable from noise, whereas there is a stronger spheroid peak visible in the ensemble extinction spectrum. There is also an overall blue-shift of the spectrum (as the ensemble spectrum

is in water, which redshifts the peak wavelength, and there is some variation in the exact peak wavelength among individual BPs).
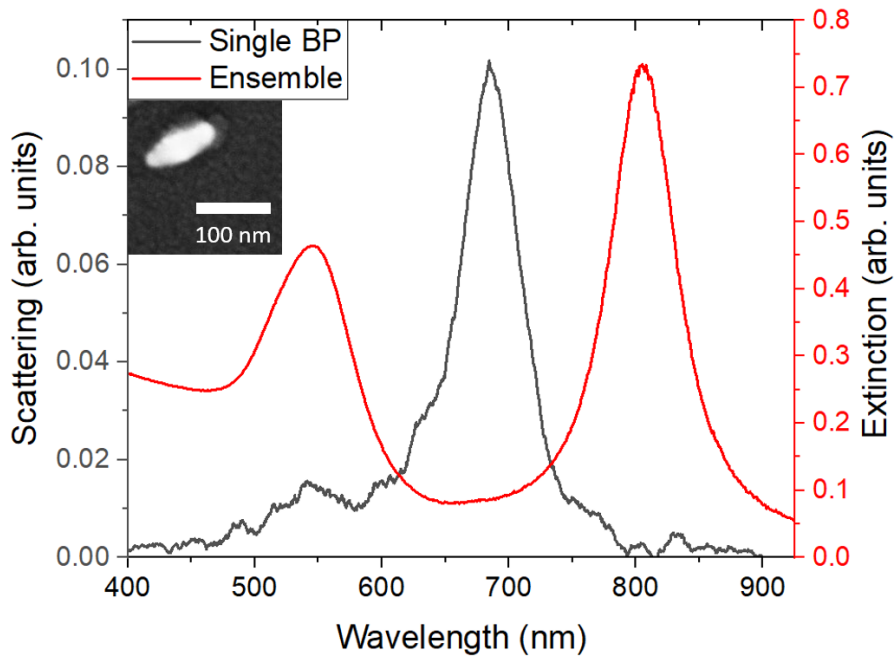
Figure 4.23: Ensemble extinction spectrum for a batch of BPs in water,
and single particle scattering spectrum of one BP from this batch.
SEM image of the single BP (with polymer, see Ch 5), inset.

Figure 4.24 below shows the simulated scattering cross section for the BP in Figure 4.23 above. The simulated scattering also does not show any significant transverse peak. It also shows strong agreement with the experimental scattering spectrum, thus showing that this is definitely a single BP spectrum.
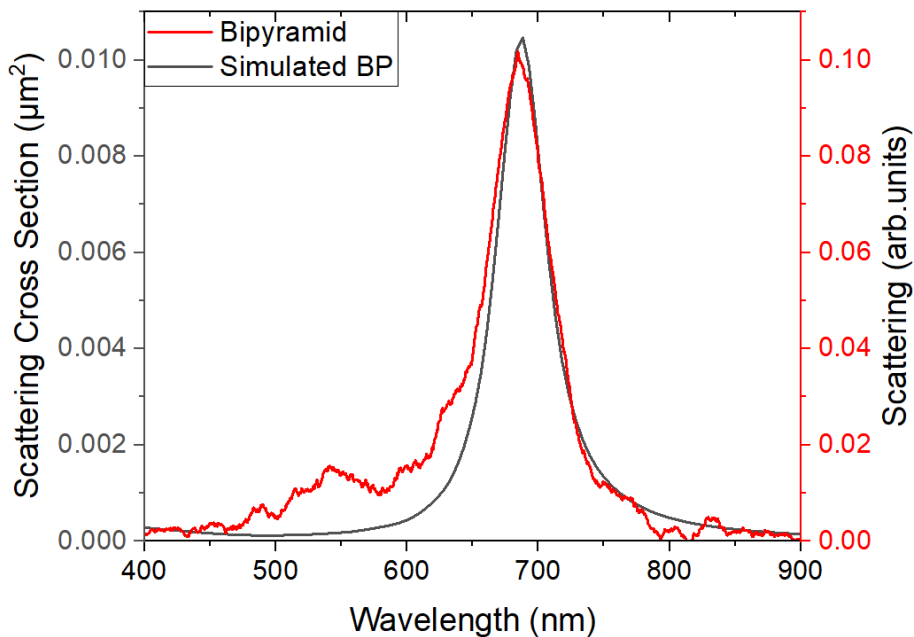
Figure 4.24: Experimental scattering and scattering cross section
for a BP and an identical simulated BP.

4.6   Nanostars
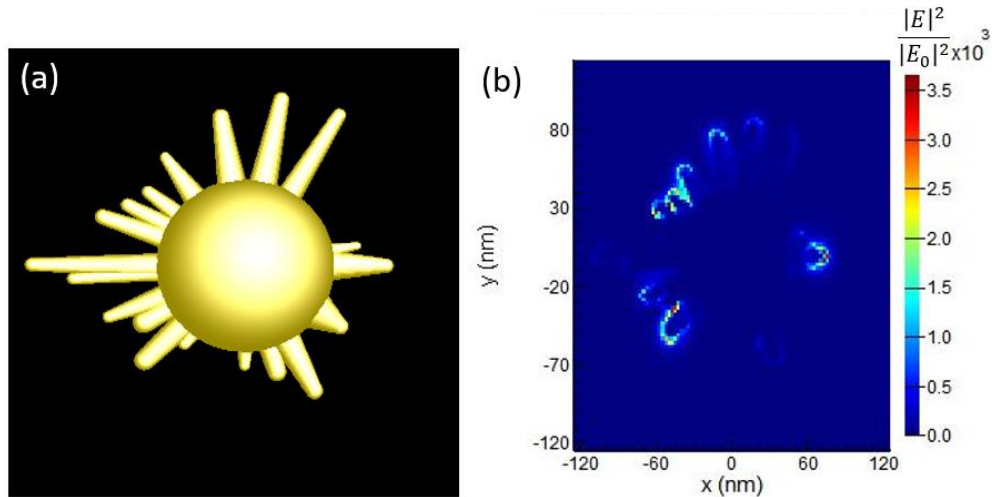
Figure 4.25: (a) Schematic of a NS with multiple pointed tips and (b) Electric field intensity map at 803 nm, showing the excitation of plasmon modes and strong field enhancement at the tips of a simulated NS.

Gold nanostars (NSs) are nanoparticles with multiple sharp tips. The tips, the core, and a core-tip hybridisation of the NSs can give rise to multiple different SPRs. The sharpness of the tips can also cause significant enhancement of the electric field (see Figure 4.25(b)), as is also the case with BPs (as discussed in Section 4.5). They can also give rise to polarisation-independent enhancement, as they have tips pointing in multiple directions and so light which is linearly polarised in any direction may algin with one of these tips. These advantageous properties mean that NSs have been used to enhance many optical phenomena, including Raman scattering[57], random lasing[135], and fluorescence[136]. Their multiple resonances and tunability mean that they can be used to enhance light across the optical spectrum and could potentially be used to enhance multiple wavelengths simultaneously.

As described in Section 3.4, gold NSs can be synthesised in two ways, seed-mediated and seedless. In the seedless NS synthesis, gold seeds are grown simultaneously with the rest of the synthesis, and then gold immediately grows upon them. The resulting NSs have a small number of broad, plate-like spikes, which retain good tip sharpness (tip radius: 5 ± 1 nm). These NSs have fewer plasmon resonances than the seed-mediated NSs, due to having fewer tips.
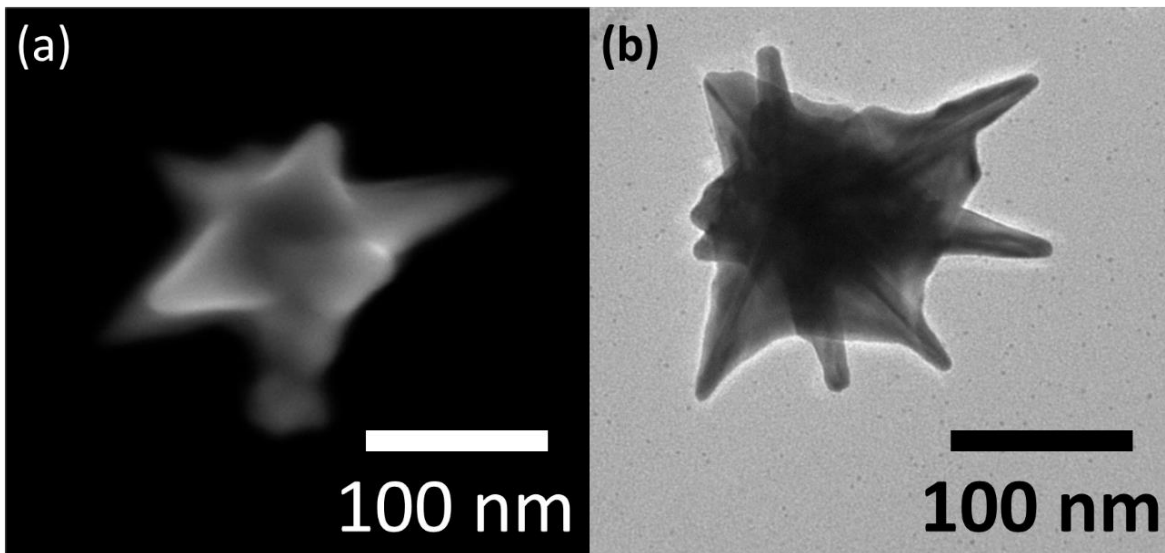
Figure 4.26: (a) SEM image of a single seedless NS, (b) TEM image of a seedless NS.

The seed-mediated NSs are grown on a base of the 3.5 nm seeds described in Section 0. These seeds are penta-twinned, so the crystal structure of the seed-mediated NSs is also penta-twinned rather than single crystalline. Seed-mediated NSs have a higher number of spikes, and each spike is considerably smaller than those on the seedless NSs (tip radius: 3 ± 1 nm).
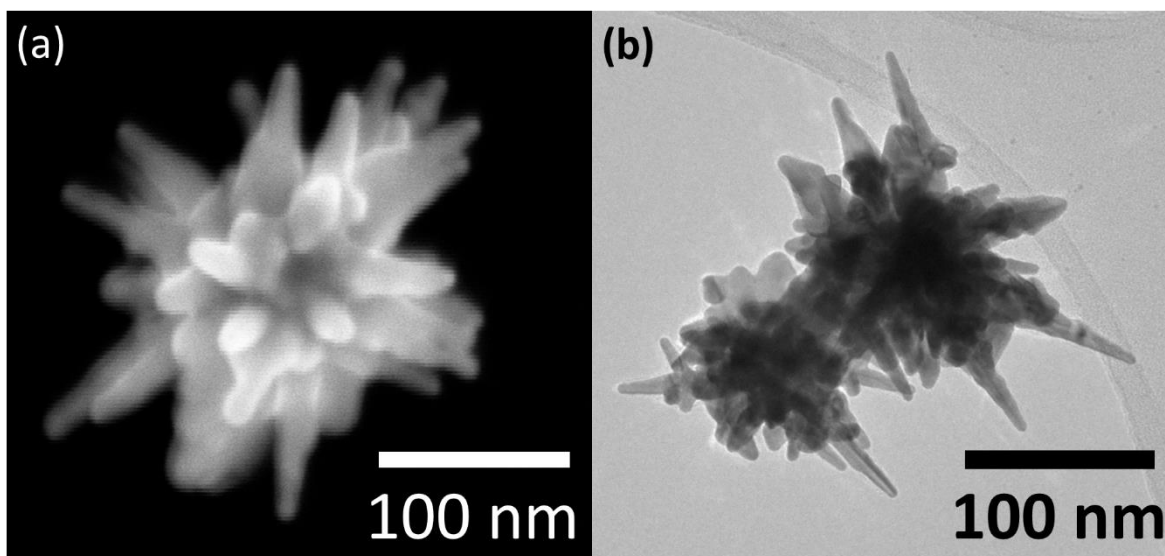
Figure 4.27: (a) SEM image of a seed-mediated gold NS, (b) TEM image of two seed-mediated NSs.

These NSs have different plasmonic properties, which can be varied synthetically (Section 4.6.1 below) and used for different applications.

4.6.1 Synthesis variation

Both types of NS give rise to broad ensemble spectra, as each individual NS will have variation in their SPR peaks. Thus, the sum of all these multi-peak spectra will be a broad peak rather than the

sharp peaks seen with more uniform spherical or elongated particles (such as NRs and BPs), which have only one or two SPR peaks. The concentration or age of certain reagents, as well as the order in which they are added, can be used to modify the synthesis.

4.6.1.1   Seed-mediated NSs
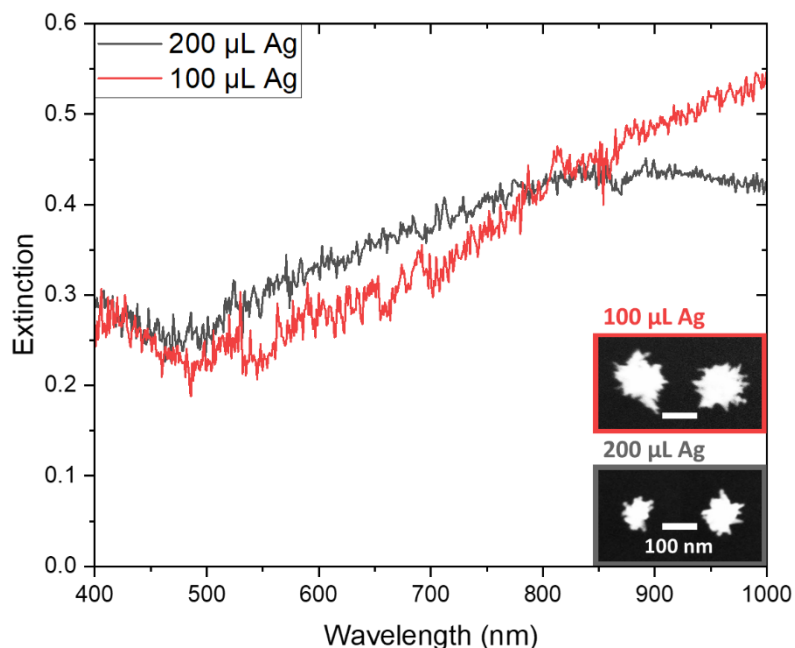
Figure 4.28: NS extinction spectra for seed-mediated NS batches synthesised using two different AgNO₃ concentrations. SEM images of NSs from each batch, inset, with same scale bars.

For seed mediated NSs, higher AgNO$_3$ concentration resulted in a slightly lower plasmon resonance peak. However, the peak was still very broad. This can be explained by the SEM images in Figure 4.28, which show a slight difference in size (which changes the overall peak position), but that both batches of NSs still have very many tips (which gives a broad spectrum). This correlates with some aspects of the results seen in literature, where higher Ag concentrations give rise to shorter tips overall[137]. However, others have shown a blue shift with a smaller amount of Ag added in seed-mediated syntheses[138]. This may be attributed to the reduced reproducibility found using this method. Figure 4.30 below shows a modified synthesis method which improves reproducibility.
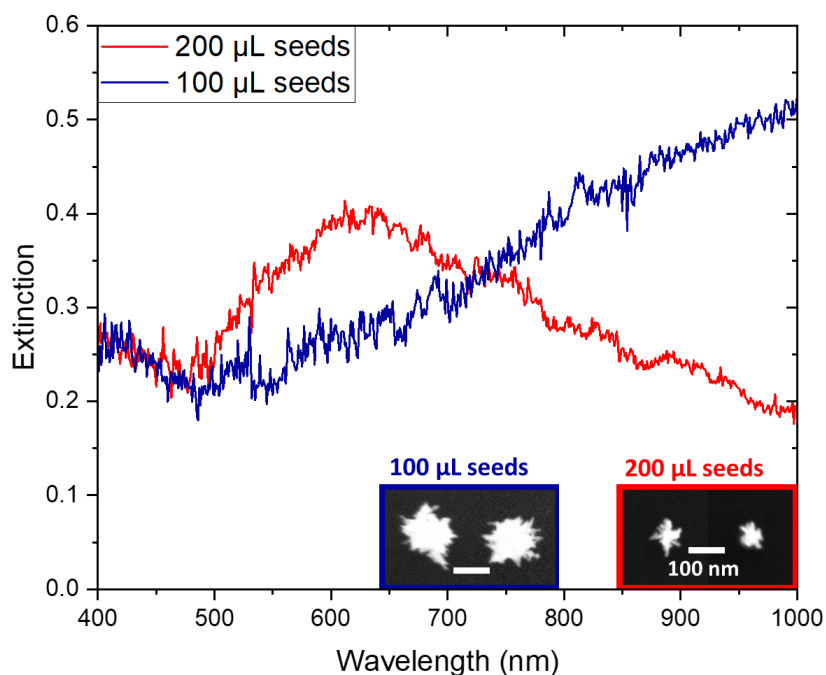
Figure 4.29: NS extinction spectra, varying seed concentration.
SEM images of NSs from each batch, inset, with same scale bars.

Figure 4.29 shows the influence of seed concentration on NS SPR peak wavelength. The higher seed concentration results in a blue shift of the peak. This is likely because a larger number of seeds results in a smaller amount of gold which can grow onto each seed. This gives rise to smaller nanoparticles overall, as the volume of gold which is available to form each nanoparticle is smaller. The inset SEM images demonstrate this, as the NSs made with more seeds are indeed smaller. They also have fewer tips, resulting in the slightly sharpened peak. The lower seed concentration resulted in a peak wavelength of > 1000 nm, which is within the bounds of the NS peak wavelengths which have been shown in the literature (wavelengths of 1100 nm and above have been shown[136]).

While the reagent/seed concentrations had a significant effect on the SPR wavelength and the nanoparticle shapes, another aspect of the seed-mediated synthesis which had a larger impact on the shape and sharpness of the NSs was the reagent addition order. The original synthesis involved combining $HAuCl_4$, HCl, and seeds, followed by the addition of $AgNO_3$ and ascorbic acid (AA) simultaneously. As was described in Section 3.4, the order of addition of the $AgNO_3$ and the AA was varied in order to optimise the synthesis.

Figure 4.30 demonstrates the impact of changing these parameters on the plasmon resonance wavelength of the NSs. The original method, adding the Ag and AA simultaneously, resulted in NSs with a broad plasmon resonance, with many blunt tips. Adding the AA first resulted in a significantly sharper, blue-shifted spectrum, and stars with a very rounded overall shape, with a shape akin to two intersecting cubes. Their tip angles could be seen to be around 90°. Adding the

AgNO$_3$ first gave rise to the most optimal of all three options. The particles had a more red-shifted peak (ideal for the goal of a 980 nm excitation enhancement) and had many sharp tips to increase the potential electric field enhancement. This is also the order of addition of reagents that is used in the BP synthesis. This has been shown in the literature to produce more homogenous and reproducible NSs[138].
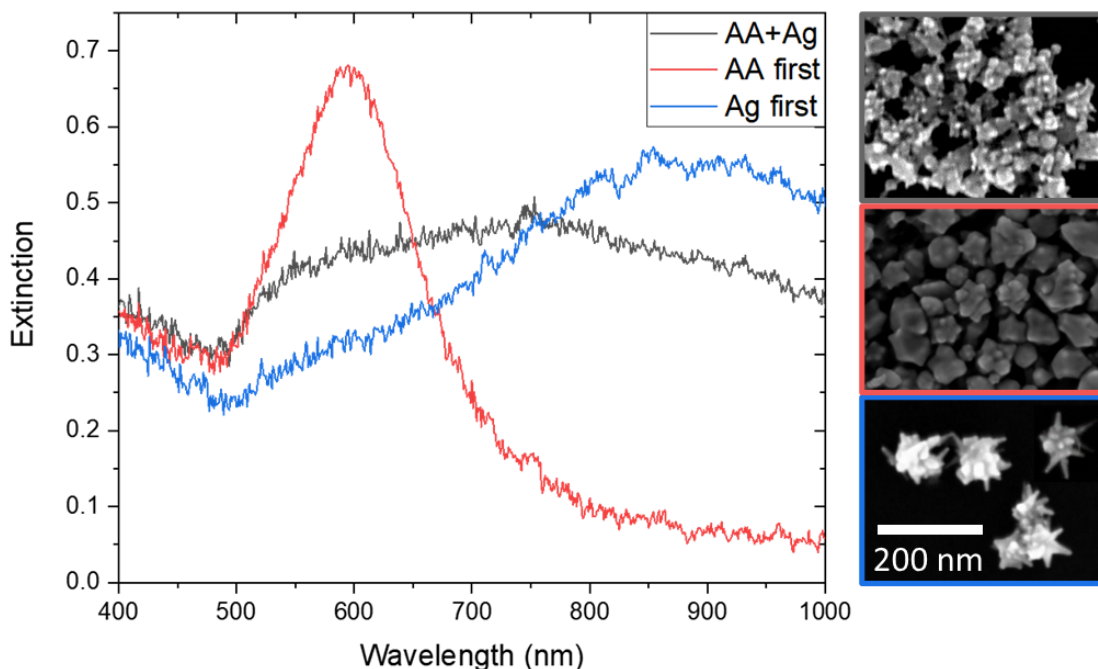
Figure 4.30: Extinction spectra of seed-mediated NSs synthesised varying the order of addition of AgNO$_3$ and AA. SEM images of these NSs, right. Scale for all SEM images is the same.
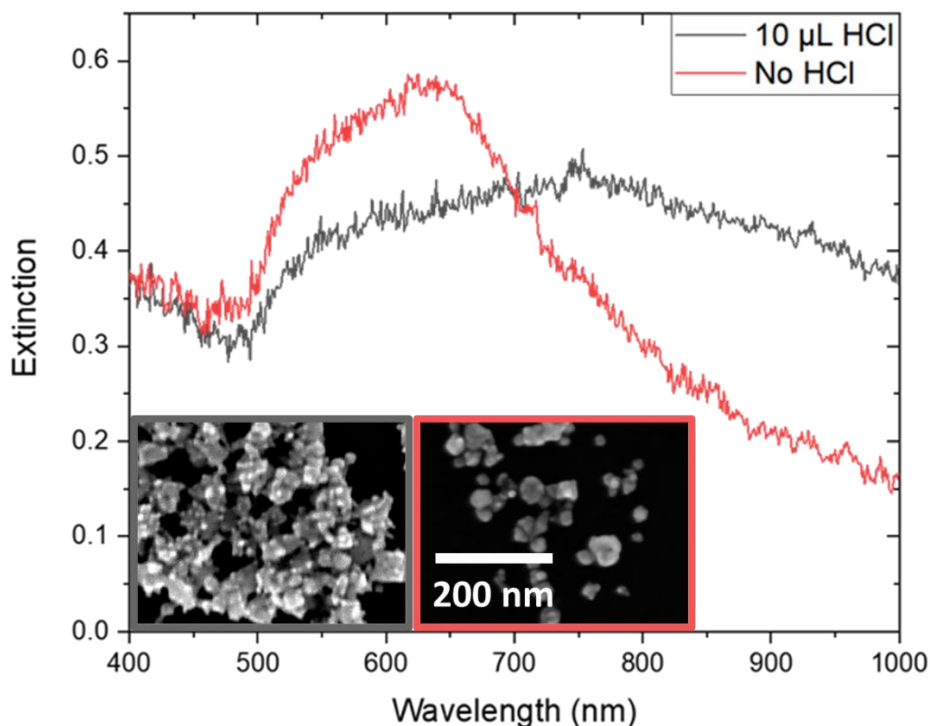
Figure 4.31: Extinction spectra of seed-mediated NSs synthesised with and without HCl. SEM images of these NSs, inset. The scale for both SEM images is the same.

Figure 4.31 shows the difference between seed-mediated NSs made with and without HCl. The NSs synthesised with HCl have a broad peak around 750 nm, and the NSs synthesised without HCl have a narrower and blue shifted peak. This narrowness is because the HCl-free nanoparticles do not have any tips and are thus more spherical. It has been previously shown that adding HCl improves the synthesis of elongated gold nanoparticles, and their stability in solution[56]. Due to the blue-shifting of the spectrum, these NSs are not suitable for use to plasmonically enhance absorption at red wavelengths, and due to the lack of sharp tips they will not provide a strongly enhanced electric field. As such, the HCl-free seed-mediated NSs were not used for the plasmon enhancement in this work.

4.6.1.2   Seedless NSs

Figure 4.32 shows the difference in extinction between batches at low and high $AgNO_3$ concentrations. The increased Ag concentration resulted in a significant blue shift of the spectrum. This can also be explained via the SEM images, with the high Ag concentration batch being smaller and with more blunted tips than the low Ag batch. They are closer in shape to spheroids than the low concentration batch. These features give rise to spectral changes, with the smaller particle size resulting in a blueshifted peak, and the more homogeneous shape of the particles resulting in a sharper peak, similar to that seen in the spectrum of a spherical nanoparticle.
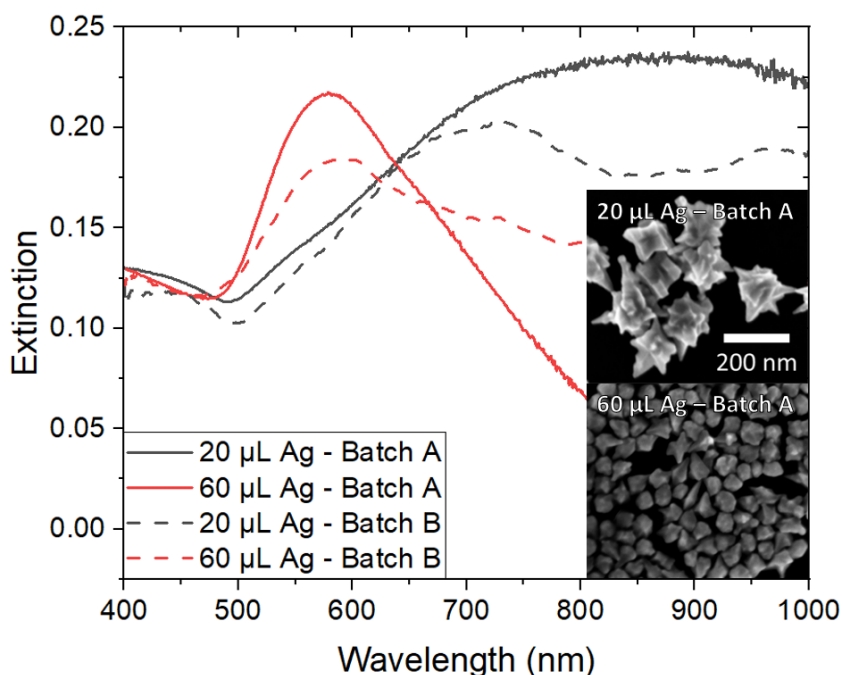
Figure 4.32: Extinction spectra of two seedless NS batches, at different $AgNO_3$ concentrations (Batch B spectra smoothed). Representative SEM images for Batch A, inset (to same scale).
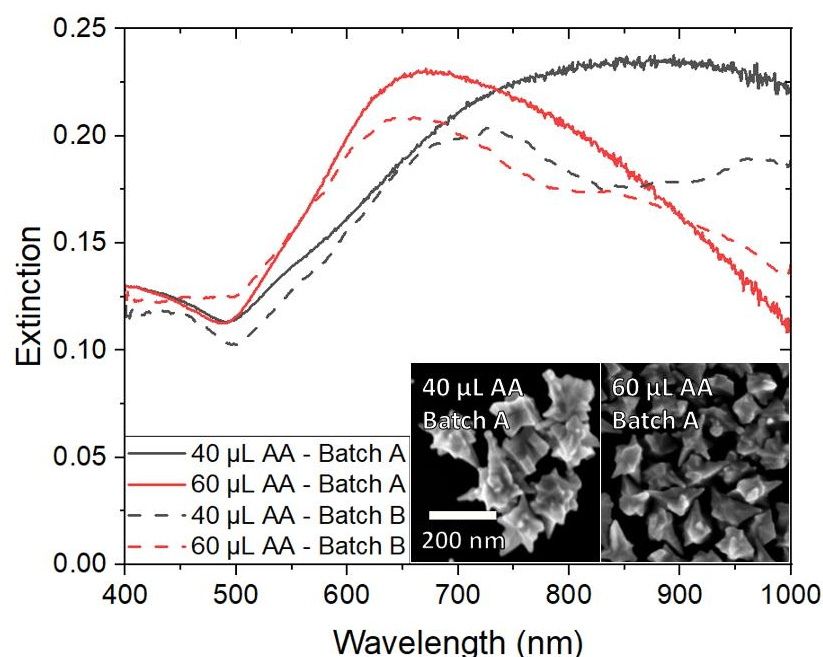
Figure 4.33: Extinction spectra of two seedless NS batches, at different ascorbic acid concentrations (Batch B spectra smoothed). SEM images of Batch A NSs, inset (to same scale).

The differences between seedless NSs synthesised using different concentrations of l-ascorbic acid are shown in Figure 4.33. The blueshift in peak wavelength with an increase of AA is mainly due to the nanoparticles being smaller. This may be due to the increase in AA causing more gold to reduce more quickly in the beginning of the synthesis, nucleating more individual nanoparticles. This would result in a higher concentration overall of smaller NSs.

All the above reagent concentrations could be varied in order to obtain the desired properties for the NSs. An increase in AA or seed concentration resulted in a blueshift of the spectrum. An increase in $AgNO_3$ concentration resulted in a slight blueshift of the spectrum for seed mediated NSs, but a significant blue-shift for the seedless NSs. The removal of HCl resulted in a blue shift of the spectrum and the disappearance of all tips, and the seedless NS synthesis was optimised for sharp tips and longer plasmon resonance wavelengths when $AgNO_3$ was added first. While synthetic tuning of the NSs was thus possible, the effects of the multiple resonances are all seen in ensemble, with resonances from many nanostars contributing to the overall broad spectrum. To further reveal their individual properties, single nanostar spectra were investigated.

4.6.2   Single nanostar spectra

While the ensemble extinction spectra of NS batches show generally broad peaks, the single particle scattering spectra have very different characteristics. Multiple peaks can be seen, with each peak corresponding to a different plasmon resonance. The peaks are sharper than that of the ensemble spectrum. The peaks also show polarisation dependence, as the tips or different

lengths cause different resonance wavelengths, and they are orientated in different directions around the NS.
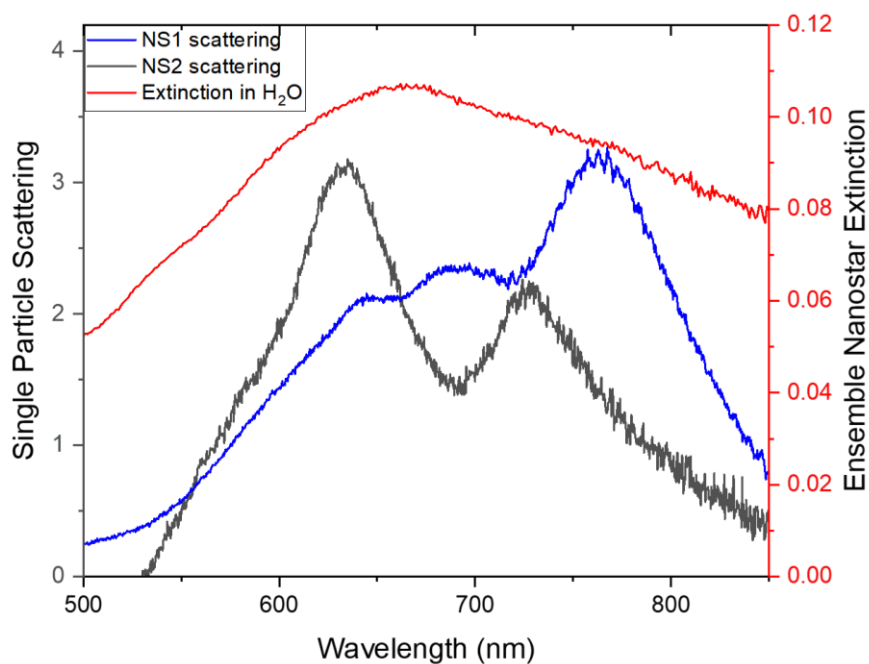
Figure 4.34: Single particle scattering spectra (unpolarised light) of two seedless NSs made in the same synthesis batch, along with the ensemble extinction spectrum of the whole NS batch in water.

Figure 4.34 compares the ensemble extinction spectrum of a batch of NSs in water with individual scattering spectra of two NSs from that batch, in air. This figure shows the difference between the individual peaks in the single particle spectra and the single broad peak in the ensemble spectrum. It also shows the significant difference in the spectra of individual NSs, which vary considerably within one batch, though all the peaks still fall under the overall broad ensemble peak.
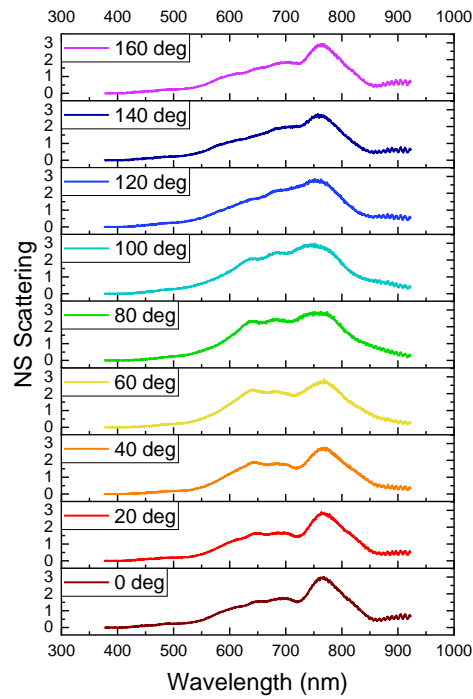
Figure 4.35: NS1 from Figure 4.34 above – polarisation dependent scattering spectra showing multiple plasmon resonances.

The polarisation dependence of the single NS scattering spectrum (method described in Section 3.7) can be seen in Figure 4.35. The peak at around 670 nm increases and decreases in height as the polarisation wavelength is changed, showing that this plasmon resonance is most strongly excited at a polarisation angle of 80°. In contrast, the peak at around 760 nm stays constant throughout all polarisation angles, showing that this plasmon resonance is polarisation independent (perhaps a resonance corresponding to the core of the NS or to multiple peaks).
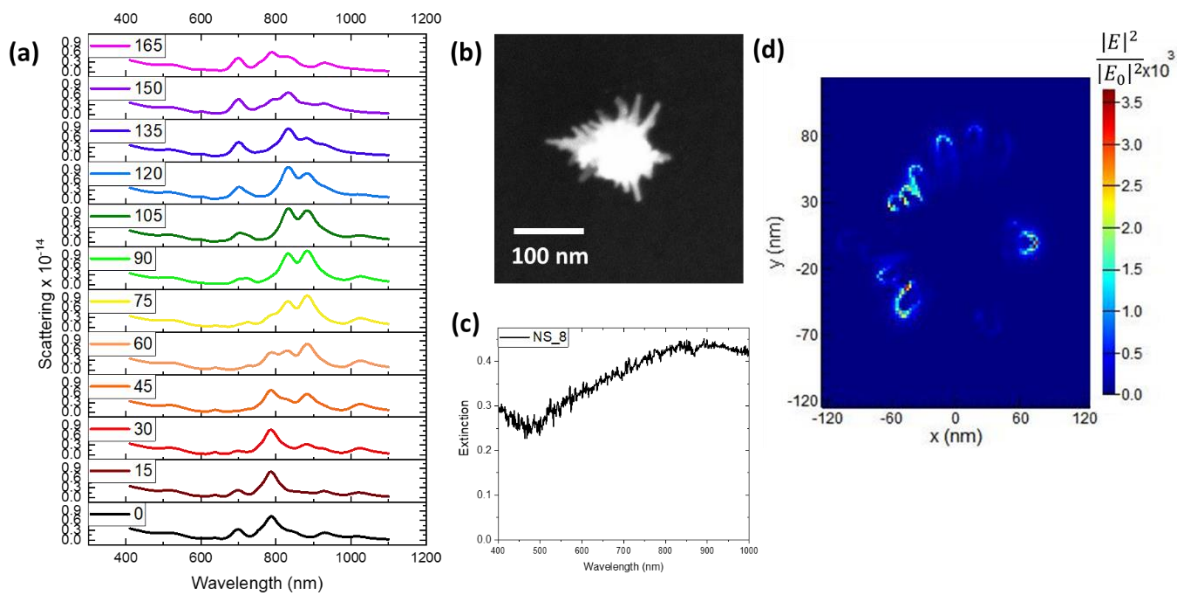
Figure 4.36: (a) Simulated polarisation-dependent scattering of a particular NS, (b) an SEM image of this NS, (c) ensemble extinction spectrum for the batch (NS_8) in water, and (d) field enhancement ($|E|^2 \propto I$, intensity) at 803 nm and at a polarisation angle of 60° for simulated NS.

Figure 4.36(a) shows the polarisation-dependence of the scattering for a simulated NS. Figure 4.36(b) shows strong electric field ($|E|^2 \propto$ light intensity) enhancement at 803 nm (around the Tm^{3+} emission peak in UCNPs) at the tips of the NSs. When the single particle scattering spectra (Figure 4.36(a)) are compared with the ensemble extinction spectrum for the sample this simulation was based on (Figure 4.36(c)), it can be seen that the plasmon resonance peaks in the simulated spectra overlap well with the overall plasmon peak of the extinction spectrum. It also shows similar behaviour to the single particle spectra shown in Figure 4.35 above, showing the simulation is in good agreement with the experimental observations.

Figure 4.37 shows the same spectra and images for a nanoparticle with fewer tips. By comparing Figure 4.36(a) with Figure 4.37(a), it can be seen that the nanostar with fewer tips has fewer plasmon resonance peaks, as the resonances are typically correlated with particular tips, multi-tip hybridisations, or tip-core hybridisations.
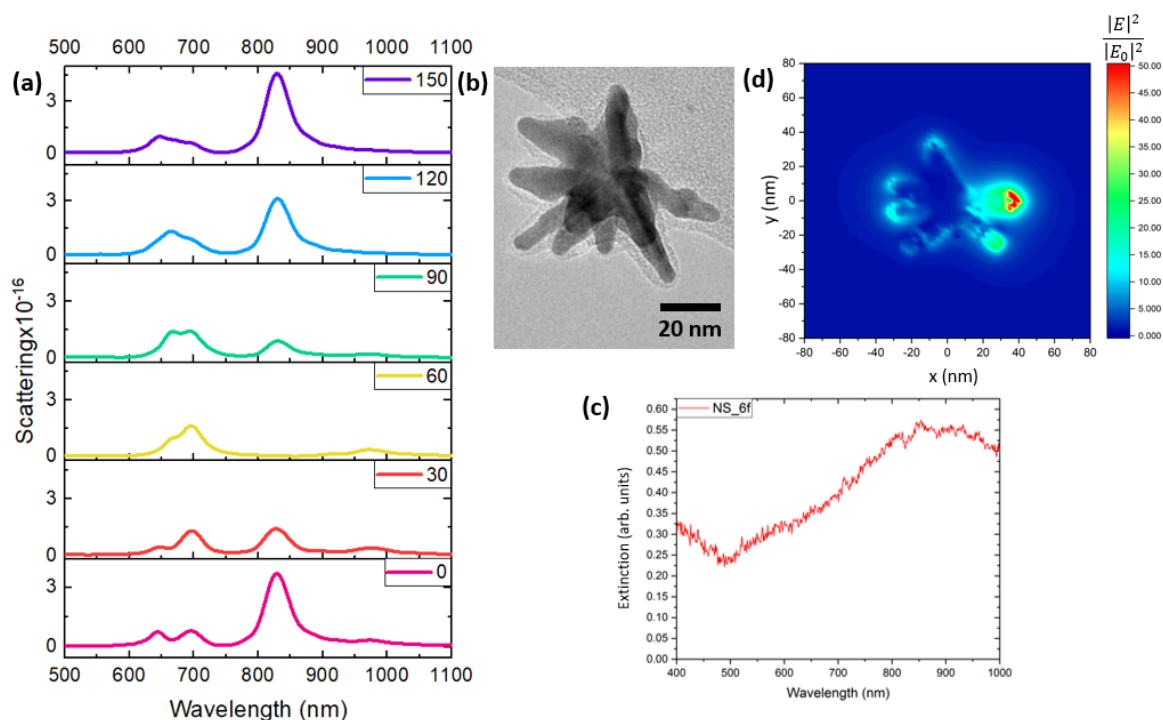
Figure 4.37: (a) Simulated polarisation-dependent scattering of a particular NS, (b) an SEM image of this NS, (c) ensemble extinction spectrum for the batch (NS_6f) in water, and (d) field enhancement ($|E|^2 \propto I$, intensity) at 834 nm and at a polarisation angle of 165° for simulated NS.

4.6.3   Comparison of all nanoparticle types

A shape comparison of a NR, BP, seedless NS, and seed-mediated NS can be seen in Figure 4.38. The difference in plasmon resonance peak sharpness can be seen in Figure 4.39, with BPs (single longitudinal resonance, very monodisperse, sharp tips) having the sharpest peak, NRs (single longitudinal resonance, less monodisperse, less sharp tips) having a less sharp peak than BPs, and

NSs (many overlapping resonances across the ensemble of particles, polydisperse, sharp tips) having the broadest resonance. For precise and reproducible tuning, where having multiple resonances is not important (such as in the case of two-photon polymerisation enhancement in Chapter 5), BPs were preferred.
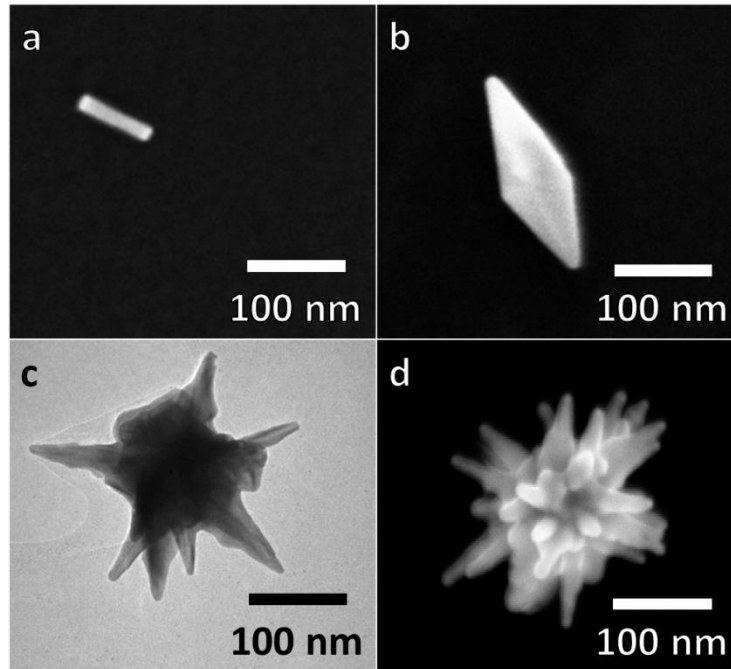
Figure 4.38: (a), (b) SEM images of a gold NR and a gold BP, respectively. (c) TEM image of a seedless gold NS. (d) SEM image of a seed-mediated gold NS.
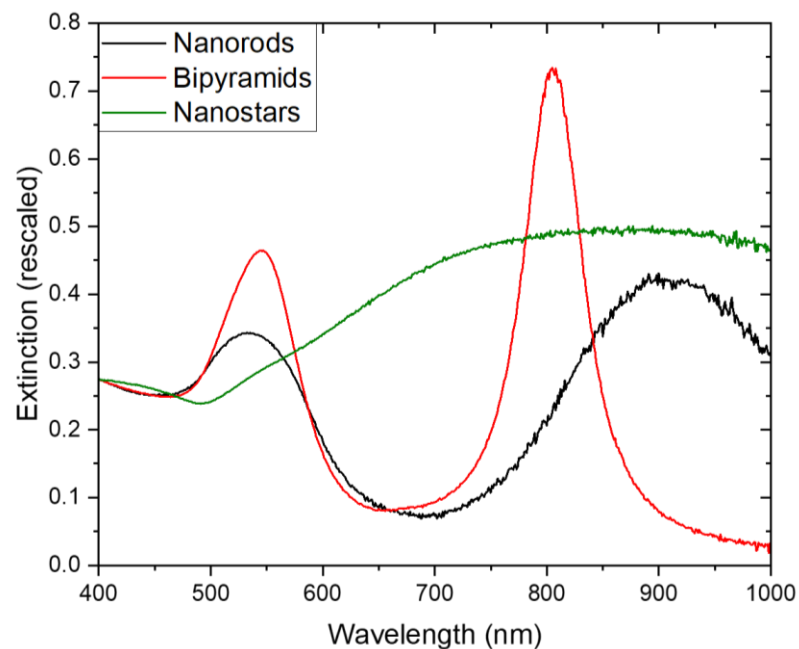
Figure 4.39: Comparison of extinction spectra for NRs, BPs, and NSs.

4.7 Silica coating
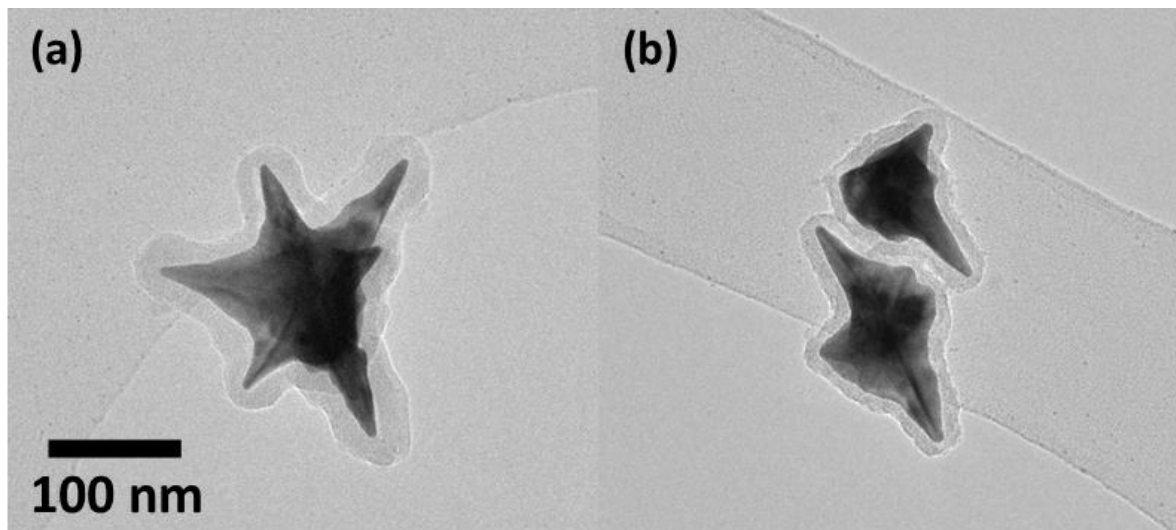
Figure 4.40: TEM images of seedless NSs with ≈(a) 18 nm silica shell and (b) 11 nm silica shell (same scale).

Silica encapsulation of the NSs was successfully carried out and resulted in shells with thicknesses of approximately 19 ± 4 nm (Figure 4.40(a)) and 11 ± 3 nm (Figure 4.40(b)). This difference in silica shell thickness was obtained by adding a larger amount of NSs to the silica shelling solution for Figure 4.40(b) (1.25x the volume). This higher concentration of NSs is likely the reason for the thinner shells, as the amount of silica which could be deposited on each NS was decreased.
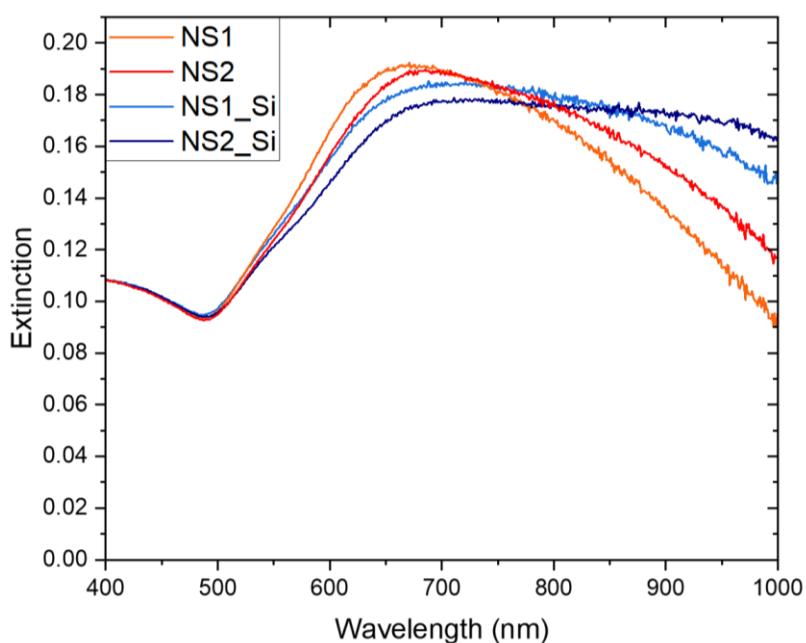
Figure 4.41: Extinction spectra of NS batches with and without silica shells. NS1: 60 µL AA, 200 µL HAuCl₄. NS2: 40 µL AA, 180 µL HAuCl₄.

As shown in Figure 4.41, silica shelling of the NSs resulted in a redshift of the spectrum and a broadening of the peak shape, as has been seen by Munkhbat *et al.* in the publication wherein the method for coating these NSs was detailed[117].

Silica shells of varying thicknesses were simulated, with mesh size 2.5 nm, in order to investigate the impact of shell thickness on potential enhancement of upconversion (see Chapter 6). Figure 4.42(b) and (c) show the increase in electric field intensity at the tips for no shell versus a 10 nm shell. This must be balanced with the potential for quenching of emission when emitters are placed at the surface of the plasmonic particle. Figure 4.42(a) below shows a red-shift and overall diminishing of the plasmon resonance peaks in the scattering spectra as the shell thickness is increased from 0-20 nm. This redshift is similar to that seen in Figure 4.41, a comparable measurement of ensemble particle extinction. This shows that such a red-shift needs to be considered when planning to incorporate silica shells in a UCNP-NS hybrid system (Chapter 6).
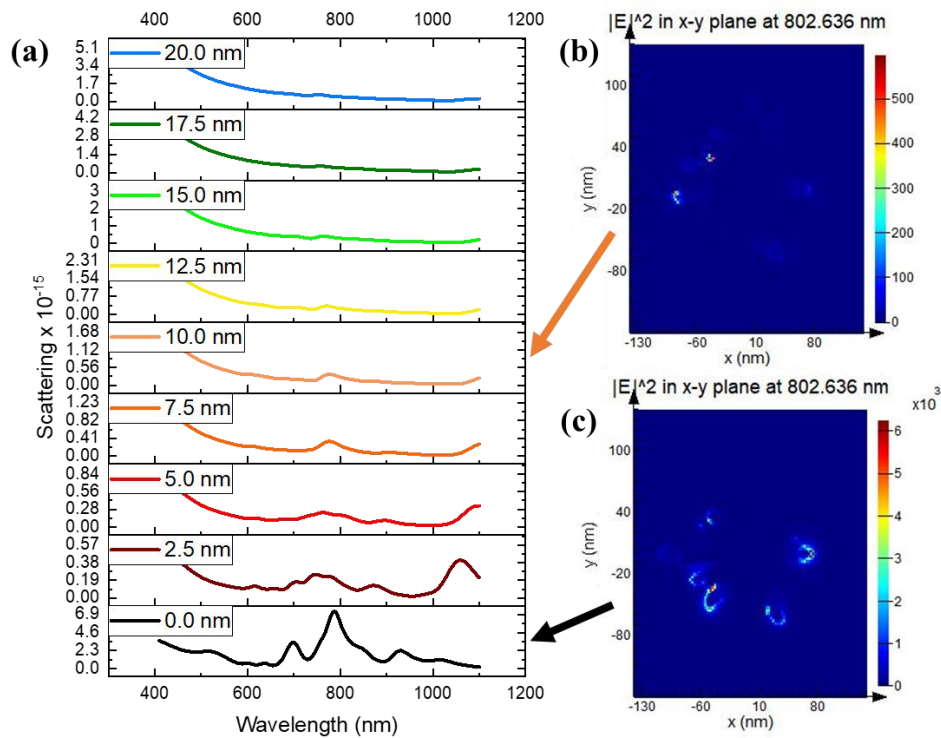
Figure 4.42: (a) Silica-shell-thickness dependence of scattering of simulated nanostar NS_8, (b) electric field intensity map for NS with 10 nm silica shell compared with (c) electric field intensity map for NS with no silica shell.

4.8   Conclusion

In conclusion, several forms of nanoparticle were synthesised using similar growth mechanisms. Varying the reagent concentrations, presence of seeds, and types of seeds, resulted in different particle shapes and sizes: nanorods, bipyramids, seedless nanostars, and seed-mediated nanostars. The nanorods and bipyramids produced single, narrow plasmon resonance peaks, whereas the nanostars produced broad ensemble plasmon resonance peaks due to the variation in nanostars within each batch, and their many overlapping resonances. Nanostars were also successfully silica shelled, with shell thicknesses varying from 10-20 nm, to potentially act as spacers for plasmonic enhancement of emitters.

Further variation of reagent concentrations within the bounds of each synthesis has been used to tune the plasmonic properties, resulting in sharp and broad ensemble surface plasmon resonance peaks across a range of wavelengths from below 600 nm to above 1100 nm, which opens up the potential for many applications due to the wide wavelength range. The specific plasmon resonances of differently shaped nanostars have been modelled, showing the influence of number of tips on the number of plasmon resonances. In addition, the impact of seed age on nanorod synthesis was explored, with one-month aged seeds found to produce penta-twinned BPs and NSs rather than NRs.

For bipyramids, the dependence on l-ascorbic acid (AA) concentration was extensively explored. It was found to be a nonlinear dependence, with a sharp increase at low amounts of AA, followed by a plateau at higher amounts of AA, explained by the interaction of the AA with the gold precursor, $HAuCl_4$. Such an investigation into the limits of this concentration dependence has not previously been carried out. Bipyramids with plasmon resonance wavelengths below 600 nm were synthesised for the first time. Additionally, bipyramids with plasmon resonance wavelengths above 1000 nm were synthesised by only modifying the AA concentration, which has not been previously achieved. This has previously only been done using overgrowth methods[1,2], or very low seed concentrations[3].

The small mode volume and high field enhancement of the bipyramids could be of particular use in enhancing 2-photon lithography, which requires a very high field intensity to polymerise the photopolymer. The nanostars have multiple resonances, which may potentially be used to enhance UCNPs, which absorb and emit at very disparate wavelengths.

74

5 Bipyramid-Enhanced Two-Photon Polymerisation

5.1 Introduction

Semiconductor quantum dots (QDs) can be nanoscopic single photon emitters, with stable and bright emission, narrow emission bands, and absorption over a broad wavelength range[59]. Their emission wavelengths and other properties are easily tuneable via changing the size of the dot. As quantum emitters, it can be of significant interest to investigate the interaction of QDs with plasmonic structures, which can significantly modify/enhance this emission. However, combining QDs with plasmonic structures can present some challenges.

Firstly, the quantum dots need to be attached to, or brought close to, the plasmonic structure in some manner. Secondly, the QDs need to be localised in an area where there is strong field modification/enhancement, not just anywhere on the plasmonic structure. Finally, in order to see any changes in decay wavelength, lifetime, or energy levels due to the presence of the plasmonic structure, it is ideal to have a single quantum dot combined with the plasmonic structure. If there are many quantum dots, the plasmonic effects will be seen in ensemble, where many of the QDs will be in suboptimal positions for enhancement[139].

Some previous approaches have involved placing a layer of QDs atop a layer of plasmonic particles[125], or an array type structure[140]. While these can certainly allow for the plasmonic enhancement of QD emission, single particle interaction effects cannot be easily interrogated using a layered system.

Single QDs have been confined into nanohole arrays and their emission enhanced using the arrays by Yang *et al.*, 2023[141]. The arrays were functionalised using 2 different ligands, one on the side walls of the holes to repel the QDs, and one at the base of the holes to attract and bind with the QDs. This is useful in terms of QD confinement, but as arrays are typically fabricated using electron beam lithography and subsequent etching (reactive ion etching in this case), they do not typically achieve high feature sharpness.

Synthesised nanoparticles have a significant advantage over the aforementioned arrays/other structures formed via EBL, as the bottom-up fabrication process can result in sharper features, thus increasing the potential electric field enhancement. Although there is no additional benefit from any periodic modes, there is the potential for a true single-particle-single emitter system to be explored.

In some articles, authors have attached the QDs to such individual nanoparticles, such as Zhang *et al.* 2018, who enhanced single QDs by single gold NRs[139]. However, they used a dilute solution of QDs dropped onto the NRs. They did not actually have a hybrid system with them locked/attached together, thus reducing their plasmonic interaction. They did not create any confinement of the QDs at a particular position (such as in an optimised location for plasmonic interactions).

Burgin *et al.* 2008, who have used mercaptoundecanoic acid as an attaching ligand, with a thiol group which binds to gold BPs and an acid group to bind to CdSe/CdS quantum dots[112]. However, this results in a full or partial layer of QDs on the BPs, which prevents true single-QD emissions from being observed, preventing single particle-single emitter interactions from being studied. The QDs are again not confined to an optimal location. BPs have also been used previously to enhance the absorption of QDs in solar cells[125]. However, this was in large layers, and does not allow for single particle-single emitter interactions to be observed and studied.

A solution to many of the issues mentioned above is to use plasmon-induced two-photon polymerisation (2PP). This allows for the localisation of QDs near the plasmonic structures, without requiring a high concentration of QDs (which can cause difficulty in identifying signals which have been modified by the plasmonic particles, as the background emission is very high).

This has been carried out by Ge *et al.*, where they formed hybrid plasmonic nano-emitters using plasmon-enhanced two-photon polymerisation by nanocubes[25]. Figure 5.1 shows the nanocube-polymer hybrid structures created by Ge *et al.* at different linear polarisations of light, along with the modulus of the electric field around the as-simulated cubes. There is always more than one hotspot around cubes as they have multiple sharp edges/corners in contact with the substrate at any time.

Two-photon polymerisation is a nonlinear optical process which involves the simultaneous absorption of two IR photons into virtual energy levels in a photoinitiator, instigating the typically UV-initiated formation of radicals which commence a cross-linking polymerisation reaction in the liquid monomer solution[142]. Any unpolymerized solution can then be washed away, leaving only the solid polymer behind. This occurs only in the focal volume of the femtosecond laser, which can result in sub-diffraction-limit-sized features, as 2-photon absorption requires a very high power, so the volume with sufficient power to start the process will be smaller than for single-photon absorption.

However, this has never been shown in the literature using BPs. BPs have many advantages over nanocubes, in that they have significantly sharper tips, which can result in greater field enhancements in a smaller volume[55,56], and they also have very easily modifiable plasmon

76

resonance wavelengths, as shown in Chapter 4. Additionally, BPs also provide a single plasmonic hotspot at the substrate air interface, unlike in the case of nanocubes, and this can potentially allow polymerisation to only occur at one BP tip. This can allow QDs to be localised at only one tip.
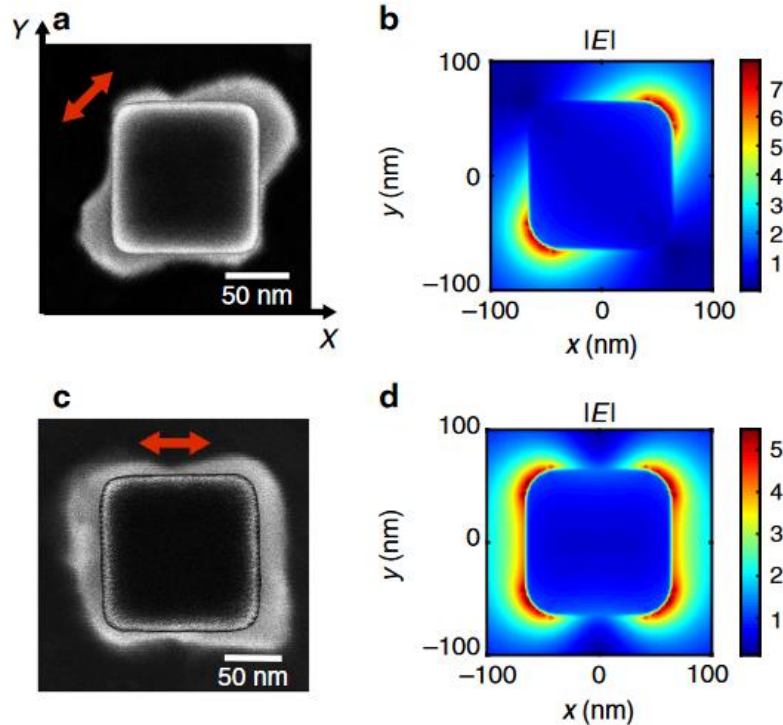
Figure 5.1: (a), (c) SEM images of the hybrid nanocube-polymer-QD structure, created using a diagonally polarised laser beam (a), and a laser polarised along the cube side (c), λ = 780 nm. A bare nanocube SEM image is added to contrast with the shape of the polymer shell. (b), (d) FDTD image of the field modulus |E| around the nanocube in polymer from images (a) and (c), respectively, λ = 780 nm. Reproduced from Ge et al.[25].
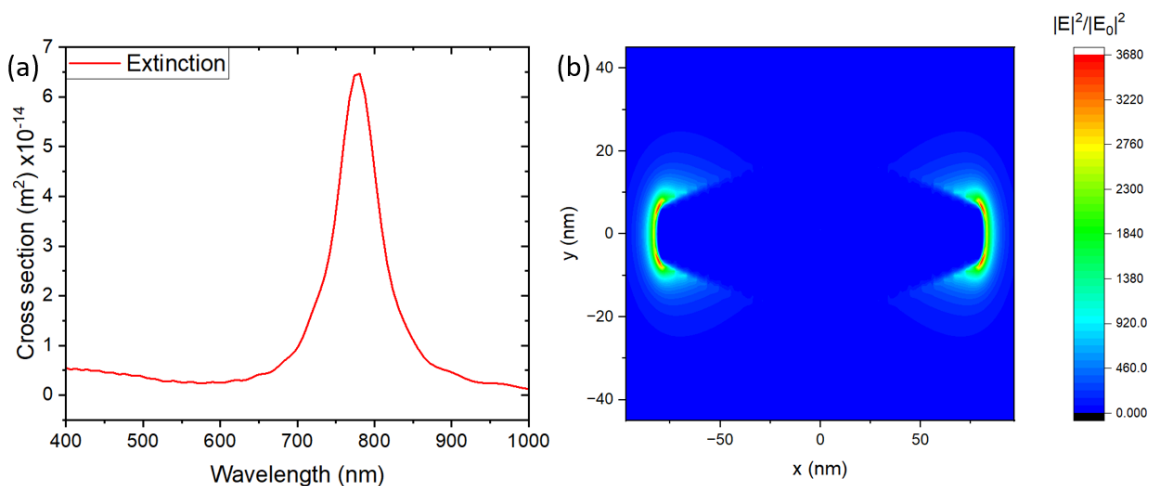
Figure 5.2: (a) Extinction cross section and (b) map of electric field intensity enhancement at 780 nm, from a simulated BP, taken along the midpoint of the BP. Width 42 nm, length 163.8 nm, aspect ratio 3.9. Plasmon resonance wavelength in air: 778 nm.

The BPs are useful because they encourage preferential location of the QDs where their electric field enhancement is naturally the strongest. This occurs most strongly at the tips, as shown in Figure 5.2, but also other areas around the BP. There is no need to simply hope that the QDs will be in the right place, as with some other particle-particle attachment methods.

There are several steps needed to obtain, and demonstrate proof of, this kind of 2-photon polymerised system. First, BPs of an appropriate size and plasmon wavelength must be synthesised and spin-coated onto a substrate. Then, polymerisation must be attempted using a lower power than would typically give rise to polymerisation. In the system used by this group, the maximum power which can be applied to a sample is 50 mW, and typically no polymerisation is shown for powers below 5 mW, or 10% of the maximum power. As mentioned in Section 3.13, the solution used in this work was 99 wt% TMPET (monomer) and 1 wt% PBPO (photoinitiator). After this, the quantum dots must be added in a way that allows them to remain only in polymerised areas.

5.2   Bipyramid tuning
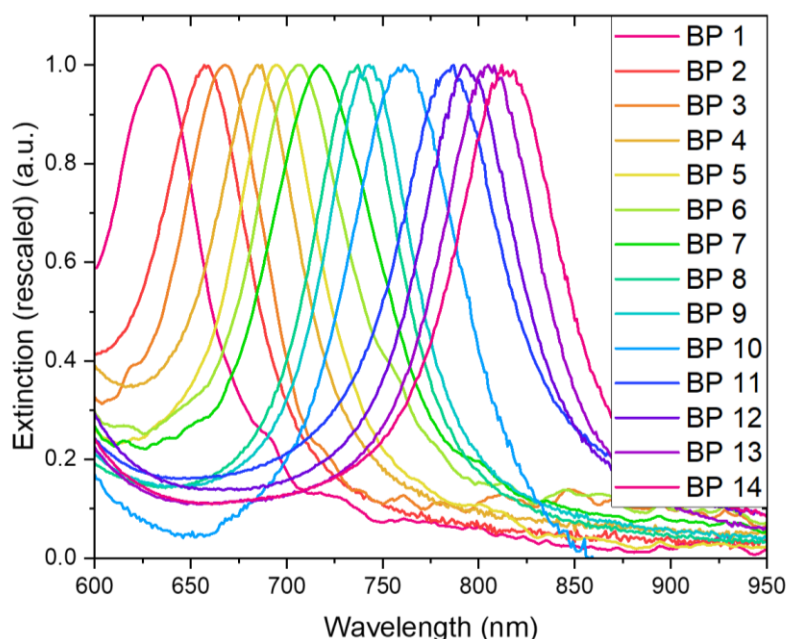
Figure 5.3: Extinction spectra (rescaled) in water of BPs showing wavelength tuning via variation of the volume of ascorbic acid, HCl, AgNO₃, seeds, and HAuCl₄ added. Synthesis parameters can be found in Table 4, Appendices.

Figure 5.3 above shows the extinction spectra of BPs tuned synthetically over a range of wavelengths. The synthesis and variation are described in Sections 3.3 and 4.5, and involved varying the concentrations of different reagents or seeds in the reaction solution in order to change the size and/or aspect ratio of the BPs.

Several of these BP batches were then deposited on a glass substrate in preparation for the 2-photon polymerisation step (without QDs). Two of these batches are shown in Figure 5.4 below, demonstrating a significant difference in plasmon resonance wavelength resulting from the different aspect ratios of the BPs in these batches.
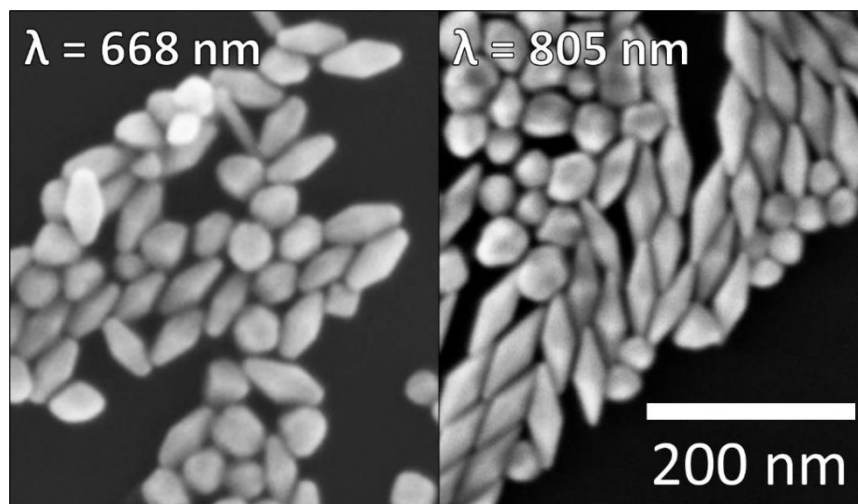
Figure 5.4: SEM images of BPs used for 2-photon polymerisation samples,
with different lengths/aspect ratios. Imaged on silicon substrate.

Target wavelengths of 665 nm and 780 nm were selected, in order to interact with the QD emission wavelength and 2-photon laser excitation wavelength, respectively. BPs with resonance wavelengths of 668 and 805 nm were chosen, to allow for a slight blue shift over time after synthesis and before spin coating. Gold spheres as a synthesis byproduct are also present in the solutions, but these can be excluded during subsequent analysis of the data.

5.2.1   Spin-coating

BPs were spin coated onto glass substrates, as described in Section 3.11. Glass was chosen as the substrate due to the orientation of the 2-photon polymerisation system, which deposits the monomer/photoinitiator solution on one side of the sample and excites it through an oil immersion objective from the other side, necessitating a transparent substrate. Several concentrations were used, and an optimal concentration found. The concentration of BPs needs to be high enough for several BPs to fit in each square of the polymerised grid, however if the concentration is too high then the BPs may be touching, or they may be too close together for accurate individual darkfield scattering spectra to be obtained. Additionally, an overly high concentration can also result in micro-explosions during the 2-photon polymerisation process, with any BP clusters causing a further enhanced electric field. Micro-explosions occur when the local power is increased far above the writing threshold. It is theorised that photo-ionisation of the material, causing plasma formation, may occur at high powers, which causes the micro-

explosions[143]. These micro-explosions can cause the polymerised material to be spread across the substrate, resulting in polymer in areas which were not treated by TPL. This can be mitigated by reducing the amount of BP clusters, which reduces the possibility of creating inter-BP plasmonic hotspots which enhance the power enough to cause micro-explosions. This can be achieved by sonicating the BP solutions and reducing the overall BP concentration.
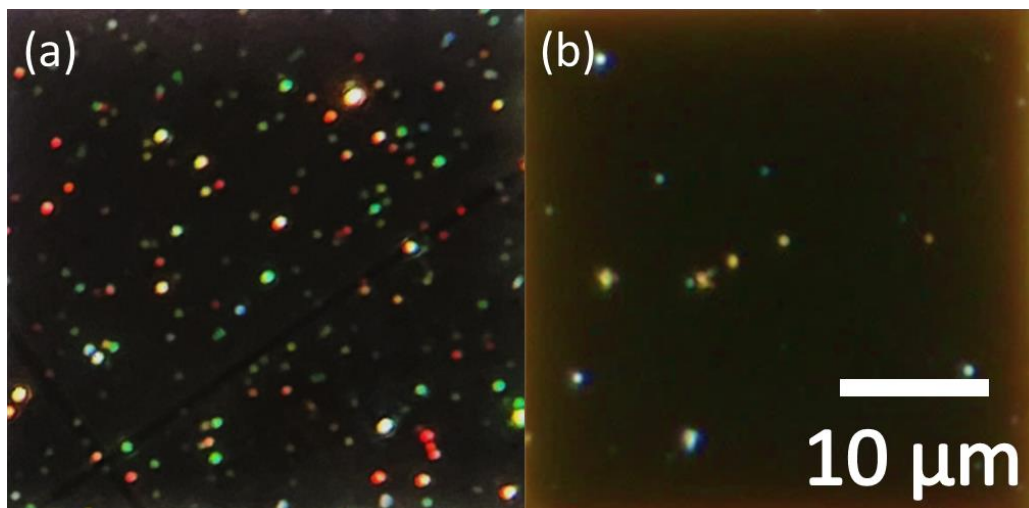
Figure 5.5: Laser-irradiated areas with (a) high concentration of BPs/spheres and (b) low concentration of BPs/spheres inside.

Figure 5.5(a) above shows a section of a sample with a high concentration of nanoparticles inside. Each bright spot is either a nanoparticle or cluster of nanoparticles. Typically, the red spots are bipyramids, the faint green spots are spheres, and the bright green, yellow, or white spots are clusters of nanoparticles. Many of these particles are too close together to obtain a sufficient background subtraction for their spectra. Some others are too close to the highly scattering polymer square which surrounds each laser-irradiated area, resulting in an inhomogeneous background or an overly saturated spectrum. Thus, samples with lower concentrations, as in Figure 5.5(b), were investigated for the remainder of the work. This optimal concentration was found to be around 3 μL concentrated BP solution in 400 μL ethanol, or an Au concentration of 0.124 mM. The exact optimal concentration could vary for each BP batch, as the gold and seed concentration were varied slightly.

5.3   Polymerisation

The typical threshold value for this TPL system, as mentioned in Section 5.1 above, is 10%. Thus, to demonstrate plasmon-induced polymerisation in order to confine the quantum dots, it was necessary to show polymerisation at powers < 10%. Powers from 1-7% were used, and a pattern with these powers was written on a glass substrate with BPs using the laser wavelength of 780

nm. The BPs chosen had an ensemble plasmon resonance wavelength in water of > 780 nm (≈ 805 nm), as there can be a blue shift of the BPs due to slight reshaping in solution before deposition (sharp tips can become blunter over time if nanoparticles are not sufficiently stabilised due to gold atoms migrating away from the tips[144]). Also, resonances close to the laser wavelength can still cause enhancement.
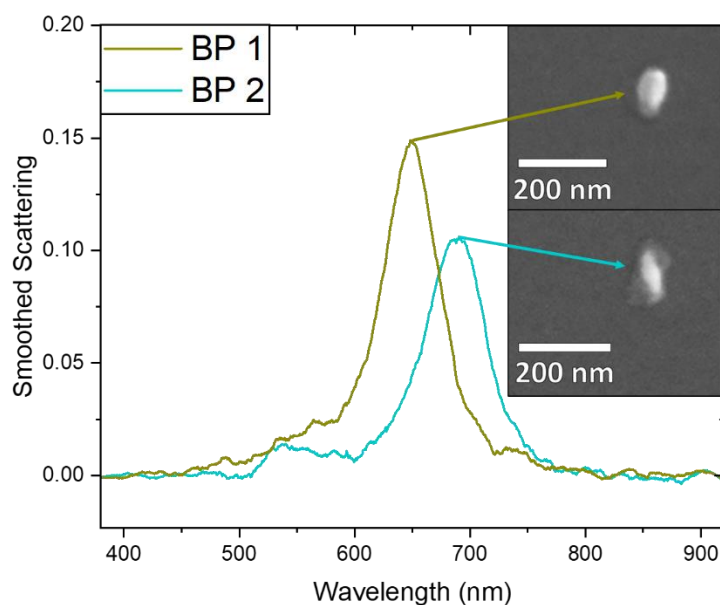
Figure 5.6: Scattering spectra and corresponding SEM images of single BPs (with polymer).

Darkfield scattering spectra of individual particles were taken, in order to identify those which were BPs and those which had relevant wavelengths. Figure 5.6 above shows the scattering spectra of two particles with different plasmon resonance wavelengths. The shape of the spectra, with a single sharp peak in the 600-800 nm range, is the same as that shown in the inset of Figure 4.15, indicating that these particles should be BPs. From the SEM images of these particles (Figure 5.6, inset), the shape of the particles can indeed be seen to be BPs, with slightly differing aspect ratios. Thus, any spectra showing such a pointed peak could be presumed to be a single BP, allowing any spheres, which would have a bluer peak, to be excluded from the analysis of BP spectra.

Due to the method used to identify BPs in the darkfield microscope (DFM), it was difficult to visually identify BPs with very red peaks. The nanoparticles were located and identified by eye, and the 780 nm wavelength that was expected for the majority of the BPs in this sample is beyond the visible spectrum. Thus, BPs which had a bluer plasmon wavelength peak were more likely to be identified and measured. In the future, an automated scanning approach will be utilised to be able to optically identify the redder BPs more easily.

Polymerisation was successfully shown in this range of subthreshold incident powers, as can be seen in Figure 5.7(a), showing 5% incident power (system threshold = 10% power). The BP can be

seen in a light grey colour, and the polymer is seen in a darker shade around one tip of the BP. This can be contrasted with Figure 5.7(b), showing BPs in an area of the sample which was not exposed to the laser. This section has no visible dark grey section around, thus proving that the polymerisation is indeed shown in Figure 5.7(a).

Polymerisation with this system was shown at powers as low as 0.5%. Ge *et al.* showed polymerisation at $\frac{1}{10}$ of their threshold power[25]. As the threshold for polymerisation for this system is 10% power, the fraction of the threshold power needed in this case was only $\frac{1}{20}$, demonstrating the effectiveness of the use of BPs for plasmonically inducing polymerisation.
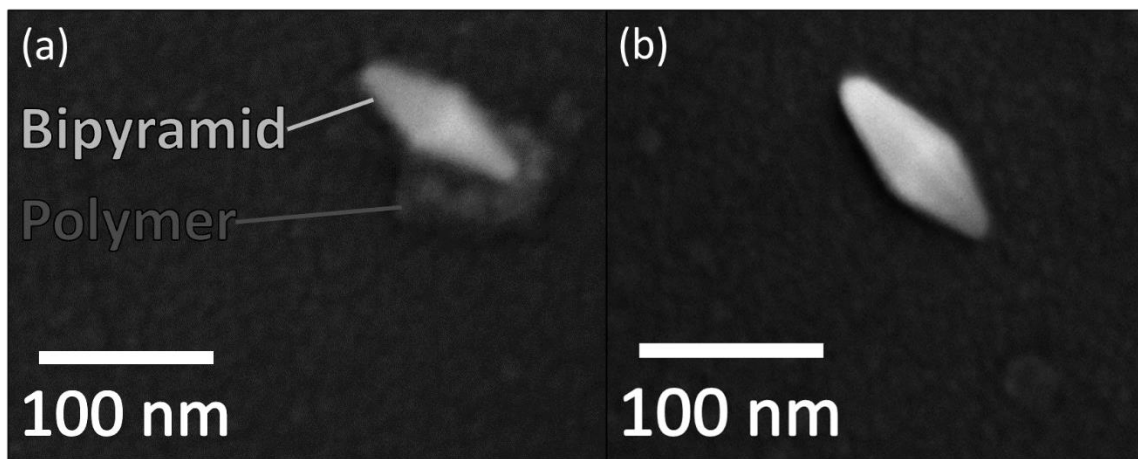
Figure 5.7: (a) SEM image of BP showing polymer around its tip. Laser power: 5%/2.5 mW.
(b) SEM image of BPs outside of the laser-written area, showing no polymer.
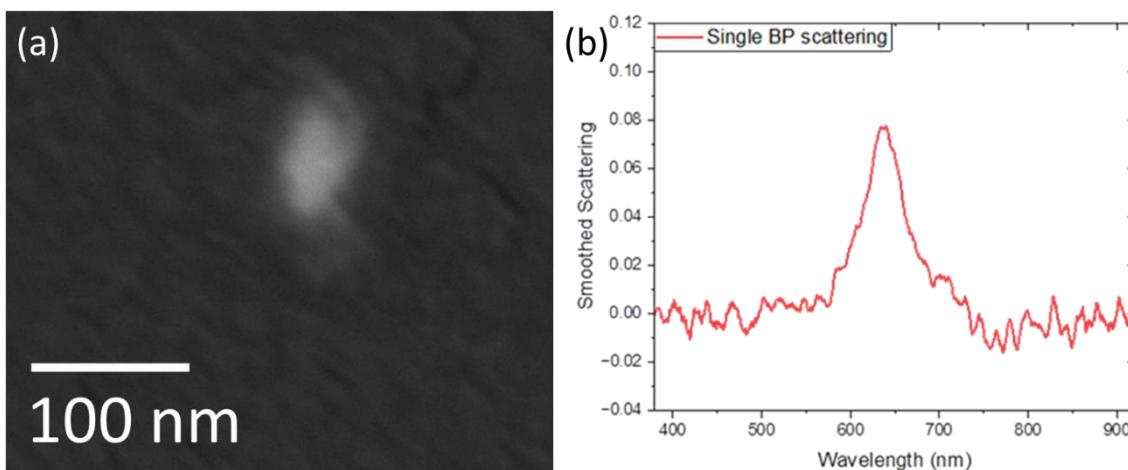
Figure 5.8: (a) A smaller sized BP, showing evidence of polymerisation.
(b) Single particle darkfield scattering of a similar BP.

An amount of polymerisation has also been shown in smaller BPs, such as that seen in Figure 5.8 above, which has a plasmon resonance wavelength of ≈ 650 nm in air. This is evidence that BPs can plasmonically enhance the incoming light, even with a small metal volume. This can be

attributed to an overlap in the side of the plasmon peak for this BP with the laser emission (in Figure 5.8(b), the side of this peak can be seen to extend past 750 nm).

It was also found that powers at 4% and above resulted in more frequent reshaping of the gold BPs (see Figure 5.9(a) vs (b) below). This is due to surface melting of the BPs, which can occur at lower temperature than the melting of bulk gold[145]. A small degree of this surface melting can occur even at the lowest powers, reducing the aspect ratio of elongated particles as can be seen in Figure 5.9(b). At the highest powers, all BPs are completely melted and become spheres[146].
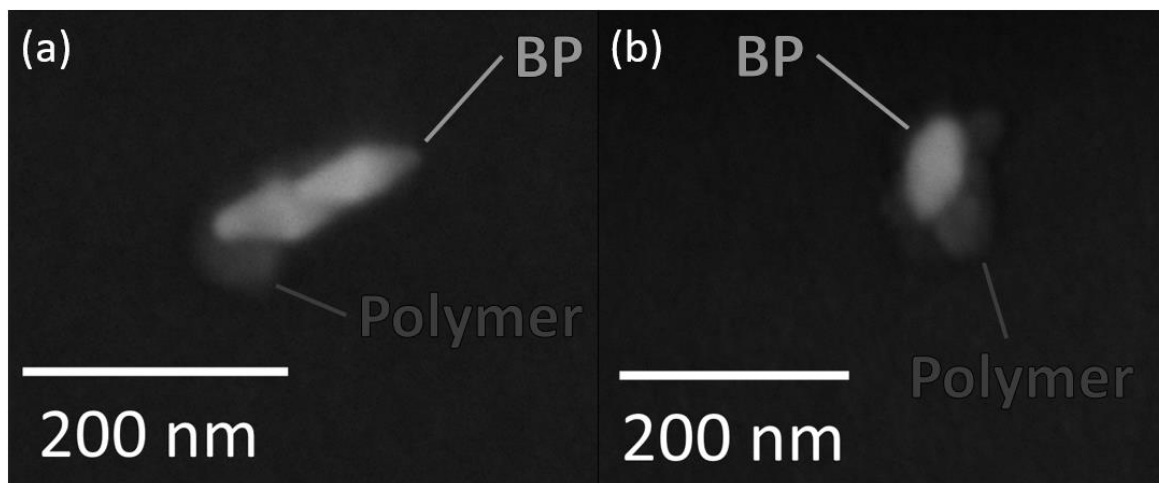
Figure 5.9: SEM images of (a) BPs treated with 3% power, with sharper tips, and (b) a BP treated with 7% power, showing melting. Both images show evidence of polymerisation around the BPs.

While this partial melting did not occur for every BP, the higher likelihood at higher powers meant that it was imperative to focus on using lower powers to ensure maintenance of the sharp tips (to potentially enhance the light-matter interaction using the QDs). Also, these lower powers give rise to a smaller polymer volume (described in Section 5.3.1 below), corresponding to a higher likelihood of single QDs being present.

Figure 5.9(a) also shows a brighter area around the tip. This can be differentiated from a BP which has simply undergone photothermal reshaping, or "melted", as the melted BPs typically do not show bulbous tips. BPs are not in an energetically favourable state[56], but when elongated nanoparticles melt, they will tend towards a spherical shape as it is more favourable[146]. Thus, the progression to bulbous tips is unlikely, and what can be seen at the tip may possibly be a higher density of polymer.
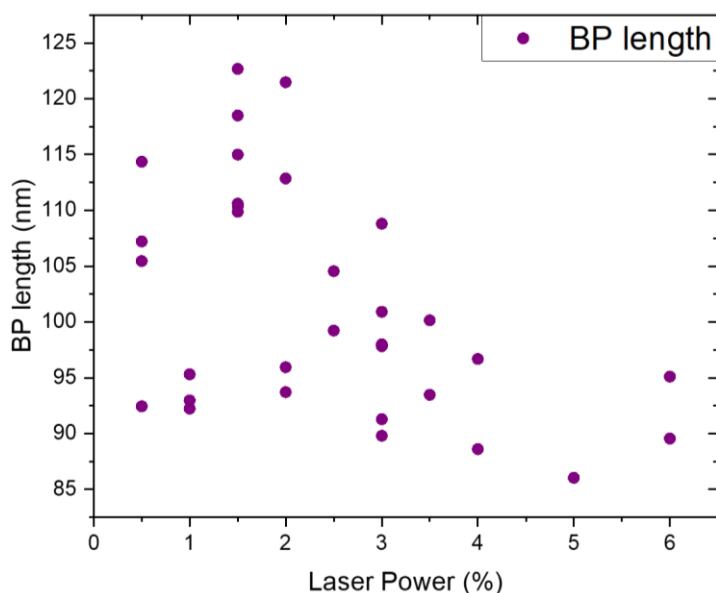
Figure 5.10: Graph of BP length vs laser power used during 2-photon lithography.

Figure 5.10 demonstrates the relationship between BP length after laser irradiation and the laser power used, for single BPs which showed polymerisation. The higher laser powers are associated with considerably shorter BP lengths, further corroborating the surface melting shown in Figure 5.9. The BPs irradiated with higher laser powers are melted more than those at lower powers, and thus are closer to a spherical shape, reducing their lengths. This melting did not prevent polymerisation around the BPs, however, as the BPs had sharp tips when first placed in the TPL system. Thus, they could still enhance the laser light and induce polymerisation, as can be seen in Figure 5.9(b), before undergoing surface melting.
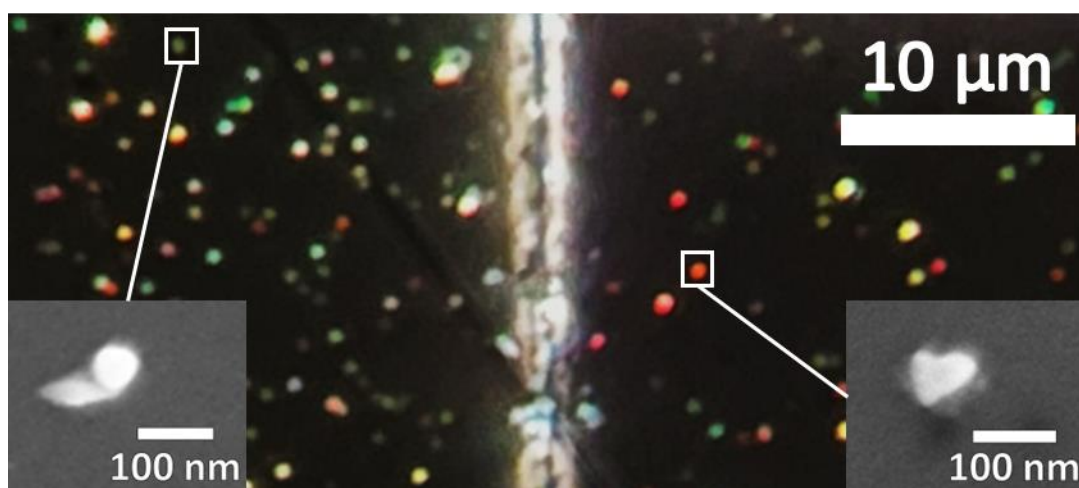
Figure 5.11: DFM image of BPs/spheres without being exposed to the laser (left) and having been irradiated at 5% power (right). Selected SEM images of unmelted and melted BPs, inset.

Melted nanoparticles can be easily seen under a darkfield microscope. Figure 5.11 demonstrates the visually identifiable difference of nanoparticles which have been melted by the laser irradiation and nanoparticles which have not. There are a higher number of visibly red and bright

84

green spots, potentially showing particle groups which have been melted together and BPs which have turned into spheres, respectively. These are not desirable for the potential intention of enhancing the emission of quantum dots, as their electric field enhancement will be significantly weaker due to the absence of sharp tips. Thus, preference was given to the use of powers of 3.5% and below, to increase the likelihood of BPs retaining their points.

Several interface (IF) values (corresponding to the vertical position of the focal plane of the laser) were also investigated for these BPs. IF values of 0.1 and 0.2 showed polymerisation on the nanoparticles, even at low powers (0.5%). IF values which were higher (0.4) gave rise to less polymerisation at low powers, and only gave more polymerisation at powers which commonly melted the nanoparticles, which was not optimal. Thus, IF values of 0.1 and 0.2 were used.

5.3.1 Power dependence of polymer area/volume
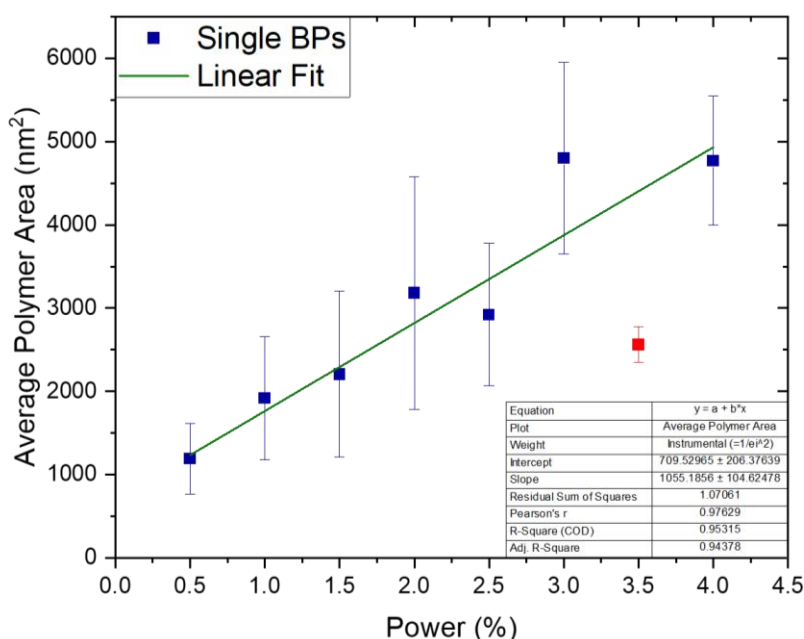
Figure 5.12: Average area of polymer around the BP visible in SEM vs incident power in % of 50 W. Interface value = 0.1. Red point at 3.5% power has been excluded as an outlier, as very few successfully polymerised single BPs were found at this power.

While Figure 5.11 shows the effect of higher laser powers on the nanoparticles themselves, there is another effect: a change in the volume of material polymerised depending on the power used. Figure 5.12 above shows the dependence of the average polymer area (representing volume) around BPs. Only single BPs which demonstrated successful polymerisation were included in the analysis.

A linear dependence of the average polymerisation area (as shown in SEM images) on the incident laser power has been shown. This can be seen in Figure 5.12 above. The point at 3.5% power has been excluded as an outlier. There were only two successfully polymerised single BPs at this laser power, and so this point may have been so much lower than the others due to these two BPs coincidentally having less polymer. With the creation of a larger number of samples, this discrepancy may be resolved.

The linear dependence can be easily explained via understanding the operating mechanism of the 2-photon lithography system used (from Nanoscribe), or indeed that of all 2-photon lithography systems. For 2-photon polymerisation to occur, very high laser powers are required. Typically, the laser's electric field strength near the focal area is Gaussian in nature[76], with a very small focal volume where the power is high enough to cause 2-photon polymerisation. When the laser power is decreased, the size of the focal volume with sufficient power also decreases[76]. Similarly, there is a volume around a BP where there can be a very high electric field strength due to the significant field enhancement. Figure 5.13 below shows the simulated field enhancement of a BP to demonstrate this.
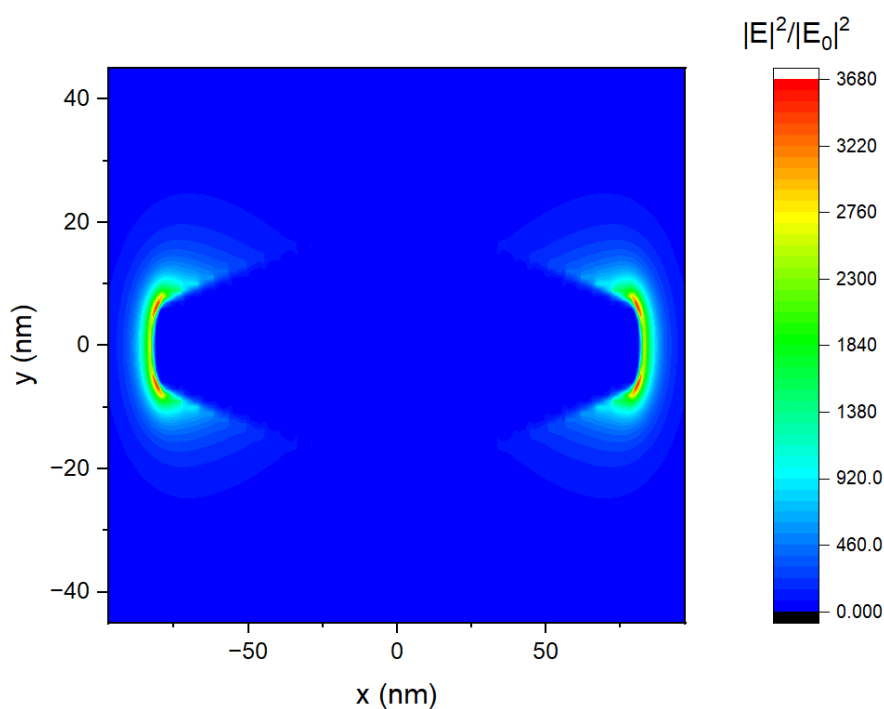
Figure 5.13: Electric field enhancement map of a BP, showing areas of high field enhancements at 780 nm unpolarised incident light. Simulated using FDTD.

However, when a low incident power is applied, only a small portion of this region will enhance the electric field enough to cause 2-photon polymerisation. When a higher power is applied, the volume which will be enhanced enough to provide the necessary power for polymerisation will be

larger. Thus, the relationship between the area of polymer visible in the SEM images (which is roughly proportional to the $volume^{2/3}$), and the incident laser power can be understood.

Many of the BPs showed polymerisation at points other than around the tips. This may be due to the vertical alignment of the samples in the 2-photon lithography system. The interface value (corresponding to the vertical position of the focal point) was changed, and some samples may be inserted at a slight slant, meaning that the precise vertical position of the highest laser power may not have exactly overlapped with the tips. However, there is still significant field enhancement around the entire BP, and while the sides may have less field enhancement than the tips, the images below demonstrate that they can still provide enough field enhancement to cause subthreshold polymerisation. An alternative explanation for the one-endedness of the polymer positioning may be that, as the BPs sit with one tip pointed onto the surface of the substrate, the interaction of the BP tip with the glass substrate may have some effect on the electric field enhancement.

Figure 5.14(a) and (b) show BPs with polymer at these different positions. Figure 5.14(a) shows polymer along one side and tip of the BP, possibly due to the vertical positioning/substrate interaction being optimised for field enhancement around that side. Figure 5.14(b) shows polymer at one tip only, meaning that the vertical positioning, any interaction with the substrate, and BP size were ideal to give rise to this very localised field enhancement and subsequent polymerisation.
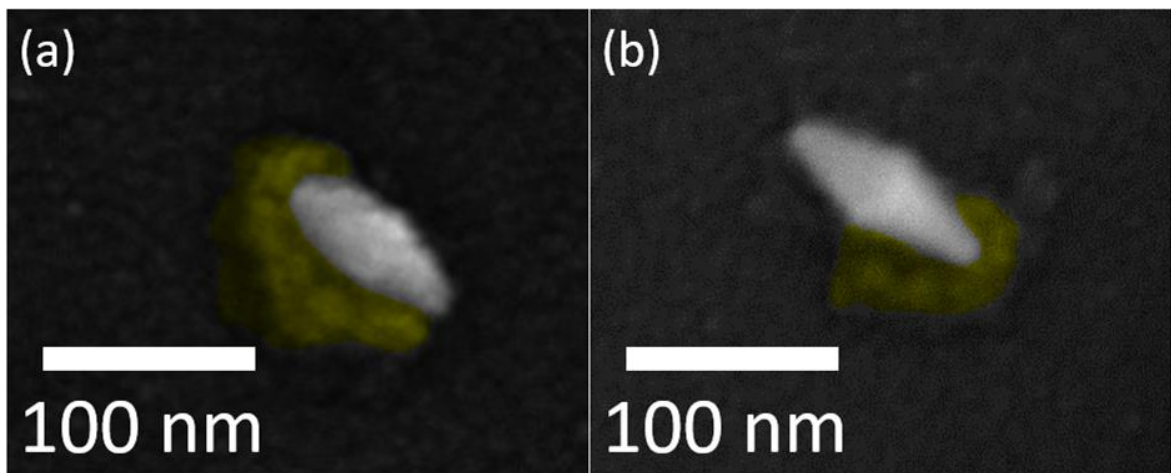
Figure 5.14: SEM images of (a) a BP with polymer along one side and one tip and (b) a BP with polymer only at one tip. Polymer shown in yellow (false colour). Both were treated with the same laser power. Same scale for both images.

In conclusion, it has been shown that this BP enhanced TPL system can successfully give rise to polymerisation around the BPs, which is a necessary first step in order to add quantum dots around the BPs to create hybrid nanoemitters. The power dependence of the area of polymer

visible around the BPs has also been shown and is linear. The conditions for two-photon polymerisation have been optimised, with powers under 4% used, and interface values of 0.1 and 0.2.

5.4   Addition/localisation of QDs

The QDs used were CdS_xSe_{1-x}:ZnS semiconductor quantum dots from Sigma-Aldrich (Product no: 753807).

As discussed in Section 5.1, QDs were deposited after demonstrating successful polymerisation around the BPs. Initially, a layer of quantum dots was spin-coated after the BP deposition, and the 2-photon polymerisation carried out on top of the QD-BP bilayer. After the samples were rinsed, the quantum dots remained adhered to the glass on all parts of the sample, creating a large background emission signal. The QDs may have required a solvent such as toluene to remove due to their nonpolar oleate ligands, which is not suitable for use on these samples as it can dissolve the patterned polymer. Mixing QDs directly into the monomer/photoinitiator solution was found to be more successful. When the unpolymerized solution with QDs was washed away, most of the QDs no longer adhered to the substrate, allowing only emission from the QDs trapped in polymer to be detected. This method was therefore used to create all the samples with QDs.

First, it was important to show that the QDs remained in the solid polymer on the substrates. This was carried out with samples using only the monomer/photoactivator mixed with QDs. The squares can be clearly seen as a brighter colour (higher intensity) in FLIM mapping of these TPL samples (see Figure 5.15 below). As these squares are polymerised, it is evident that areas with polymer show up as having higher intensity and are filled with QDs.
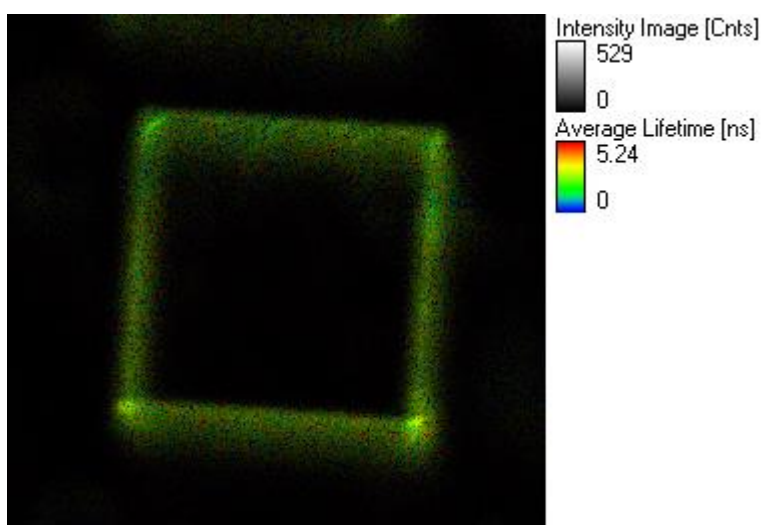
Figure 5.15: FLIM image showing lifetime and fluorescence intensity of a slide with no BPs, with a concentration of 9.9 µg/mL QDs in the polymerisation solution. This square was written with 30% on the outside edge, and 2% inside (below polymerisation threshold), and thus there is no polymer (and so no light-emitting QDs) inside the square.

Figure 5.15 above shows a confocal fluorescence microscope image of one such sample without BPs. The sample was prepared with a QD concentration of 9.9 µg/mL in the polymer precursor solution. This sample shows a clear band of high intensity at the periphery of the square, where there is polymerisation, as the squares are written with a laser power of 30%. There is no fluorescence intensity inside the square, which is as expected, as the inside of this square was only written with a laser power of 2%. Thus, in any samples where fluorescence can be seen inside a square, such fluorescence intensity can be presumed to come from polymerised areas inside the sample.

After these initial proof-of-concept samples, which also showed the appropriate concentration of QDs to use in order to be able to detect emission on the FLIM system, samples with BPs were prepared. These samples were also imaged using the FLIM, the DFM, and then gold/palladium coated and imaged using the SEM. The images and data were analysed and compared so as to identify any possible locations where the QDs were present within each square, i.e. in areas of polymer around the BPs.

The intensity map in Figure 5.16(a) of one square, below, shows areas of high intensity inside the square. It also shows areas of high intensity outside the square. The areas outside the square are sparser and are likely due to micro-explosions occurring in the polymer while writing the square (due to the presence of the BP/sphere clusters), causing polymer to spread outside the intended boundaries. However, this image shows that there is more emission occurring within the square (which was written at a subthreshold power) than outside it, as the overall intensity in the square is higher than the surroundings. Thus, the QDs are more concentrated inside the square. This demonstrates that they are being localised where there is polymerisation around the BPs.
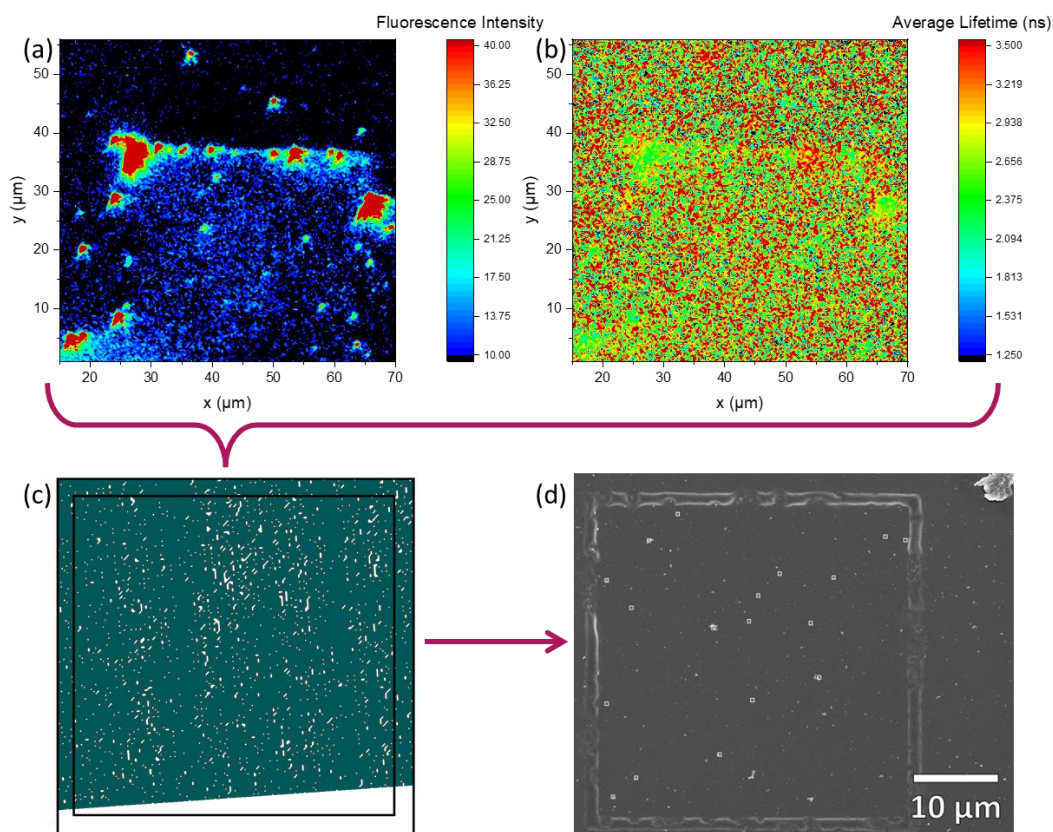
Figure 5.16: (a), (b) Fluorescence intensity and average lifetime maps, respectively, of a 2-photon polymerised sample. (c) Mask based on (a) and (b), with transparent pixels representing areas of increased intensity and decreased lifetime, relative to surrounding pixels. The black lines demarc the edges of the polymerised square. (d) SEM image of the same sample, overlaid with markings for each area shown through the mask which contained a nanoparticle. The mask was developed in collaboration with Kseniia Mamaeva.

In order to ensure that any intensity fluctuations are being caused by actual nanoparticles, image analysis was performed. The intensity map (Figure 5.16(a)) has very high intensity around the border of the square due to high QD concentrations in this area, within thick sections of polymer. However, it was observed that the intensity increased in certain areas within the square, where the BPs/other NPs were present. A mask was created (Figure 5.16(c)) to select for areas where the intensity was higher than surrounding pixels, and the lifetime (in Figure 5.16(b)) was lower than that in surrounding pixels. Reduced lifetime is a signature of QD-plasmon interaction.

Through this mask, the SEM image (Figure 5.16(d)) was analysed and the sections with nanoparticles noted on Figure 5.17 below. Some of these particles are BPs, while others are spheres or clusters of both. The spheres may have previously been BPs, as the power used for this sample was 7%, which is high enough to melt some the BPs into a more spherical shape. These particles originally being BPs would give the highest probability of polymerisation taking place. The increase in intensity and decrease in lifetime for these particles demonstrates that several particle shapes can enhance the QD radiative rate.

However, some of the BPs in this sample had tips which remained pointed. The inlaid image in Figure 5.17 below is a close-up SEM image of one such BP (with additional sphere next to it). This was an area of radiative rate enhancement. The SEM image clearly shows the polymer present. The inset graph shows the scattering spectrum of this BP, giving an SEM image of a BP with polymer, its scattering spectrum showing plasmon resonance wavelength, and radiative rate enhancement correlated to the same location, selected by the mask in Figure 5.16(d).
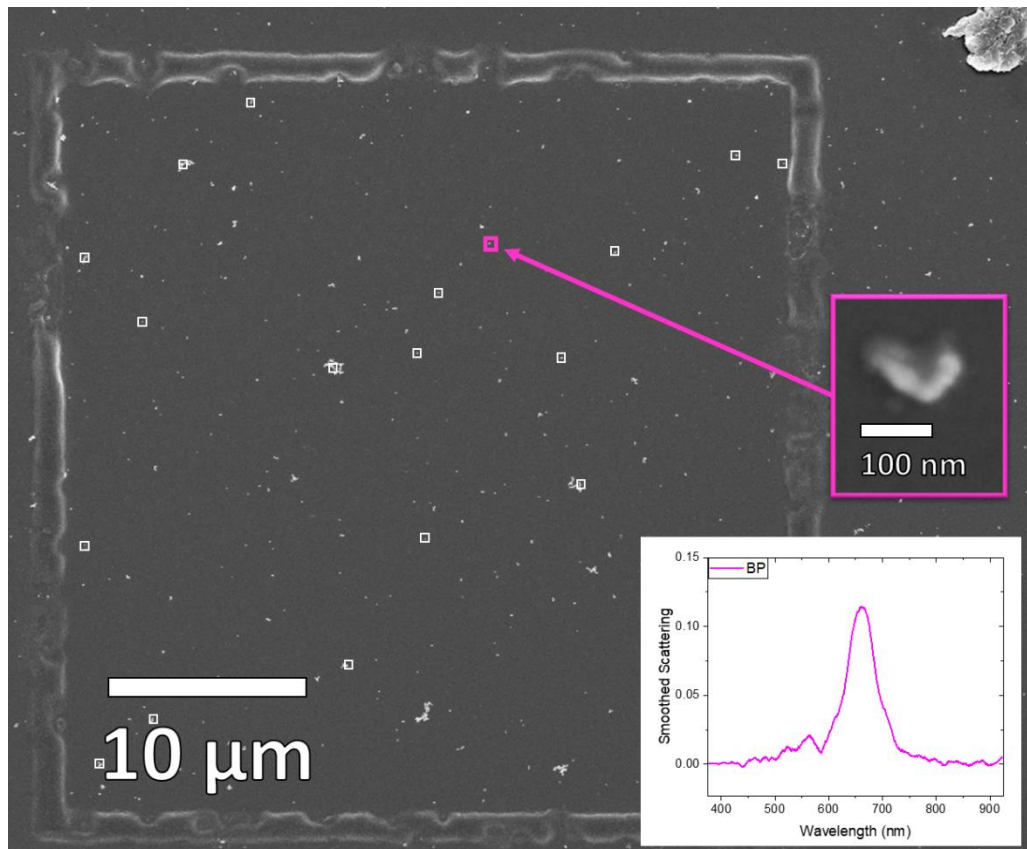
Figure 5.17: SEM image of a section of a sample, overlaid with markings for each area shown through the mask from Figure 5.16(b) which contained a nanoparticle. <u>Inset:</u> magnified image of a BP with a small cluster, along with its corresponding darkfield scattering spectrum.

In conclusion, quantum dots have been added to the monomer/photoactivator solution and have successfully been included in polymer around BPs. The enhancement of their radiative rate (relative to QDs with no plasmonic particles) by the plasmonic BPs has also been shown.

5.5   Strong coupling

The darkfield images and spectra were compared to the SEM images to identify individual BPs. While most of the spectra for single BPs showed the characteristic single longitudinal plasmon peak in their scattering spectrum (Figure 5.18(b)), some of the single BP spectra showed a double peak (Figure 5.18(a)). This was postulated to be due to strong coupling between the BPs and the QDs, as described in Section 2.2. This can occur in locations with high field strengths, which increases the coupling strength of the system, g[59].
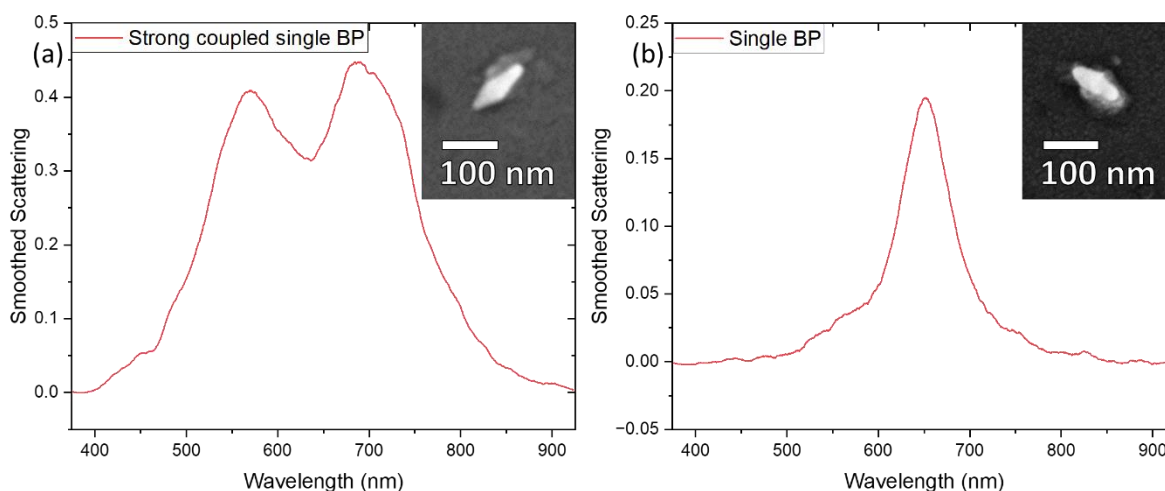
Figure 5.18: DF scattering spectrum of two single BPs with polymer + QDs from same sample, showing (a) strong coupling, and (b) no strong coupling. Inset: SEM images of same BPs.

The position of the centre of the doublet in Figure 5.18(a) is at 637 nm. The doublet should be centred around the absorption peak of the quantum dot, which is at a lower wavelength than its emission peak, known as the Stokes shift[147]. This shift has the following origins: (1) QD solutions are polydisperse and thus energy transfer between the QDs can occur, and (2) due to the electronic structure of QDs, the electron is excited by incoming light to a vibrational excited state in the QD, but experiences non-radiative relaxation to a lower vibrational state which cannot be directly excited by a photon, thus emitting a photon with less energy than the incoming photon, or a photon with a higher wavelength[148].

In this case, the emission peak wavelength is 665 nm, and so 637 nm is sufficiently blue shifted to correspond to the absorption peak of the QDs[149]. The BP in Figure 5.18(b) has a plasmon resonance wavelength of 651 nm, and the BP resonance wavelengths in the sample overall range from 608 – 749 nm. The size of the BP in Figure 5.18(a, inset), combined with the overall range of wavelengths in the sample, shows that this BP should have a resonance which overlaps the QD emission. This suggests that the doublet is indeed most likely due to strong coupling.

This strong coupling was shown for three BPs, with average Rabi splitting of 108 nm or 344 meV. This splitting energy is ≈ 17% of the original peak energy (1.99eV or 627 nm), and, as the splitting

energy is higher than 15%, this demonstrates that the system is in the ultrastrong coupling regime[150]. Such strong coupling has been seen in the literature with 2D materials and dye aggregates[151,152], but not for QDs.

Strong coupling of gold BPs and quantum dots has not previously been shown in the literature. Gold BPs have been used for strong coupling, including by this research group, in multilayers and monolayers of 2-dimensional materials[17,153], but not in QDs. In order to create the right circumstances for strong coupling rather than weak coupling, either the decay rates of the emitter and plasmonic structure must be decreased, or the coupling strength, g, increased[59]. g can be increased by the increasing of the emitter oscillator strength, the enhancement of the electric field in the vicinity of the emitter, or by the decreasing of the mode volume of the resonator[154].

This can be seen in the following. The coupling constant, g, is given by[153,155]:

$$g = \sqrt{N}\mu_e |E_{vac}| \propto \mu_e \sqrt{\frac{N}{V}} \propto \sqrt{f\frac{N}{V}}$$

(31)

Where N is how many excitons or emitters are coupled into the system, μ_e is the quantum emitter transition dipole moment, E_{vac} is the vacuum field, f is the quantum emitter oscillator strength ($f \propto \mu_e^2$), and V is the mode volume of the resonance. The energy splitting, Ω, is defined by[155]:

$$\Omega = \omega_+ - \omega_- = \sqrt{4g^2 - \frac{\left(\gamma_{pl} - \gamma_{ex}\right)^2}{4}}$$

(32)

Where ω_+ and ω_- are the upper and lower polariton energies, and γ_{pl} and γ_{ex} are the plasmon and exciton dissipation rates, respectively. The average values for ω_+ and ω_-, over the three doublets observed, were $\omega_+^{av} = 1.821$eV and $\omega_-^{av} = 2.165$eV, giving an average Rabi splitting of $\Omega^{av} = 344$ meV, as mentioned above.

From Equations (31) and (32), it can be seen that the coupling strength, and thus the energy splitting, are proportional to the square root of the oscillator strength, and the inverse of the square root of the mode volume. Quantum dots have high oscillator strengths[59], and BPs have both large electric field enhancement (as shown in Figure 5.13), and very small mode volumes[17,153], and are thus ideal candidates for strong coupling, as has been shown in the results above.

The laser powers for TPL which resulted in strong coupling were 1.5 and 2.0% (0.75 and 1mW, respectively), and the interface value was 0.1. The smaller volumes at these lower powers seemed to be ideal for having one QD or a small number of QDs close enough to the BP to have high field enhancement, thus inducing strong coupling. The overall QD concentration was based on the low

concentration solution used by Ge *et al.*, which was found to give rise to a single QD or few QDs in the polymer lobe[25].

Higher powers may have had too many QDs in the polymer, or too much blunting of the BP tips, as shown in Section 0. Lower powers may not have created large enough polymer lobes to have QDs inside them, as the polymerisation area scaled linearly with applied laser power, as shown in Section 5.3.1. Indeed, the polymer volumes for all three BPs which showed strong coupling were very similar, as shown in Figure 5.19 below.
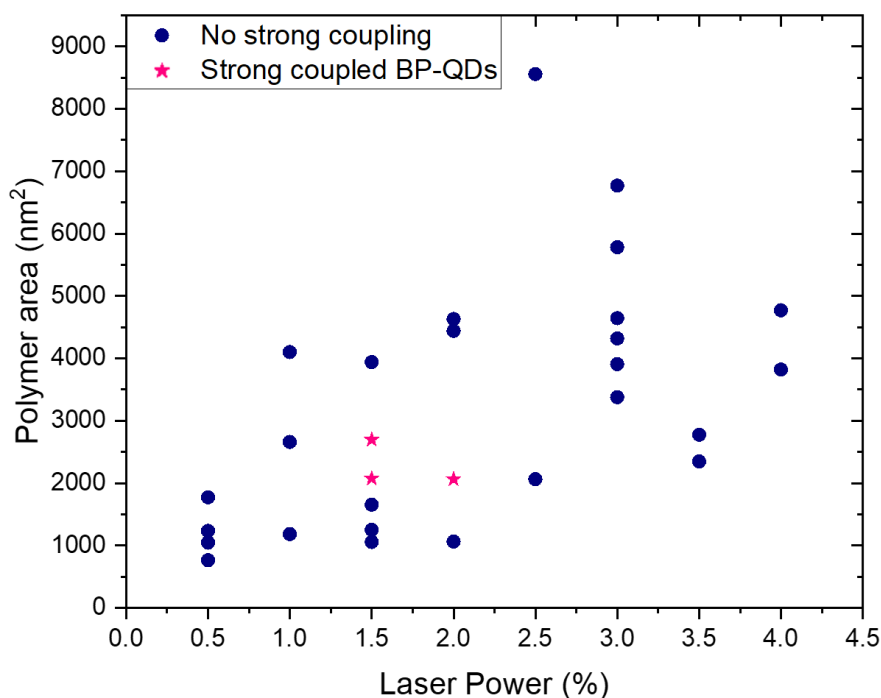
Figure 5.19: Graph of polymer area vs applied laser power, for strong coupled and non-strong coupled BPs.

In conclusion, preliminary evidence of strong coupling between quantum dots and gold BPs has been observed. This has been identified via the splitting in the scattering spectrum, and correlating this with SEM images of the same areas to ensure that the nanoparticles were definite BPs and not clusters. Optimum laser powers and an interface value have been identified for the fabrication of the strongly coupled QD-BP pair.

5.6   Conclusion

This chapter has investigated a novel method for the fabrication of BP-QD pairs with the QD localised at the tip of the BP where the electric field enhancement was highest. While plasmonic nanoparticles have been used to induce 2-photon polymerisation before[25], this has never been done using bipyramids. It has been shown that the strong field enhancements of bipyramids cause subthreshold polymerisation; in that they give rise to polymerisation in the TPL system at powers less than 0.1x the typical power required. The BPs also provide a single plasmonic hotspot at the interface of the substrate with air, allowing polymerisation to occur at just one tip, unlike in cubes which have two such hotspots.

Polymerisation area ($\propto vol^{\frac{2}{3}}$) around the BPs has been shown to increase linearly with an increased incident laser power. Two-photon polymerisation only occurs above certain powers. The BPs cause field enhancements, but the total volume in which there is high enough power to polymerise the monomer solution is dependent on the incident power.

Quantum dots have been shown to be confined in areas around the bipyramids within the solid polymer. This has occurred in precisely the location in which the plasmonic field enhancement occurs, resulting in a reduction of the QD lifetime.

Promising strong coupling of the BPs and the QDs has also been observed, via splitting seen in the scattering spectra of single BPs coupled with QDs. This further supports that the two-photon polymerisation method is suitable for the localisation of the QDs at the positions of maximum field enhancement near the tip of the BP, as coupling strength is increased in regions of high electric field strength[17].

6 Plasmon Enhancement of Upconversion

6.1 Introduction

There has been considerable research into plasmon-enhancement of upconversion[77], using a variety of different particles/structures. Initially many researchers investigated the plasmonic properties of spherical Ag nanoparticles[156,157], however more recently there has also been research into plasmonic structures such as Ag nanowires and Au NPs[96,97]. Au NRs have also had a recent increase in popularity as plasmonic structures for enhancing upconversion due to their multiple resonances[98]. They can give upconversion enhancement of up to tens of thousands of times[158]. As so many plasmonic particles/structures have been able to successfully enhance upconversion[77], it follows that nanostars could also be used to enhance upconversion also. In theory a nanostar (NS) could enhance both the emission and absorption wavelengths of the upconversion simultaneously, using its multiple resonances, which are notably absent in most of the previously investigated structures. Their sharp tips also give them an advantage over shapes such as NRs, as they can give significant electric field intensity enhancement at their tips. Enhancement by gold BPs will also be investigated, as they have strong field enhancements due to their sharp tips, as seen in Chapter 5 but have not yet been investigated in the literature.

There has previously been some investigation into NS-UCNP interactions in the literature. In two papers, He *et al.*[99,100] found that NSs caused quenching in UCNPs, but this may have been due to the fact that they only coupled one UCNP to a minimum of one NS, often coupling one UCNP to multiple NSs. They found that, the fewer NSs there were attached to each UCNP, the less quenching there was. This may, in fact, be a trend that would continue to enhancement if the UCNP:NS ratio were to go above 1:1. This work observes whether enhancement is possible with larger numbers of UCNPs in the vicinity of each NS, such as in a layer.

The authors of the papers where NSs were investigated also did not investigate the use of spacers between the UCNPs and the NSs. This work intends to ameliorate this issue by using spacers such as a silica shell to avoid quenching of the upconversion by the proximity of the NS, which is known in the literature to occur for other plasmonic particles[159]. Silica shells are a helpful addition to a plasmon-enhanced UC system for several reasons. Shells are useful for counteracting surface quenching and solvent quenching by water and can also be used to change the distance between UCNPs and plasmonic structures, and thus alter the plasmon-UCNP interaction. The addition of spacers will also open up the opportunity for future work on the distance dependence of any

enhancement shown. This work also investigates the deposition of UCNPs and plasmonic nanoparticles using layer-by-layer methods.

Martinez *et al.* published a paper detailing the enhancement of upconversion in small UCNPs by gold NSs. They found that, for UCNPs with a size less than 20 nm, the usual issue of plasmonic heating causing detriment to the emission of a fluorophore is reversed[160]. This shows that NSs can be used to enhance upconversion, but does not show enhancement for larger particles, and thus does not show direct plasmon enhancement of upconversion by NSs. This work will also investigate enhancement of upconverting particles > 20 nm by NSs and conclude if NS plasmon enhancement without relying on thermal effects is possible.

Ideally any plasmonic particles used will have a plasmon resonance wavelength of ≈ 980 nm, the UCNP absorption wavelength. This will give the highest likelihood of excitation enhancement. UC is a nonlinear process (2- or 3-photon, as shown in energy level diagrams, Figure 2.9 in Section 2.4), and so enhancing its absorbed light (at 980 nm) should give rise to a squared or cubic enhancement of the emission overall.

6.2   Size variation – synthesis

$NaYF_4$ nanoparticles doped with Yb^{3+} and Er^{3+} or Tm^{3+} were synthesised in collaboration with the Gounko group. The thermal decomposition synthesis is described in Section 3.1. These UCNPs are in the hexagonal phase and had strong upconversion emission. TEM images of two UCNP batches are shown in Figure 6.1 below.
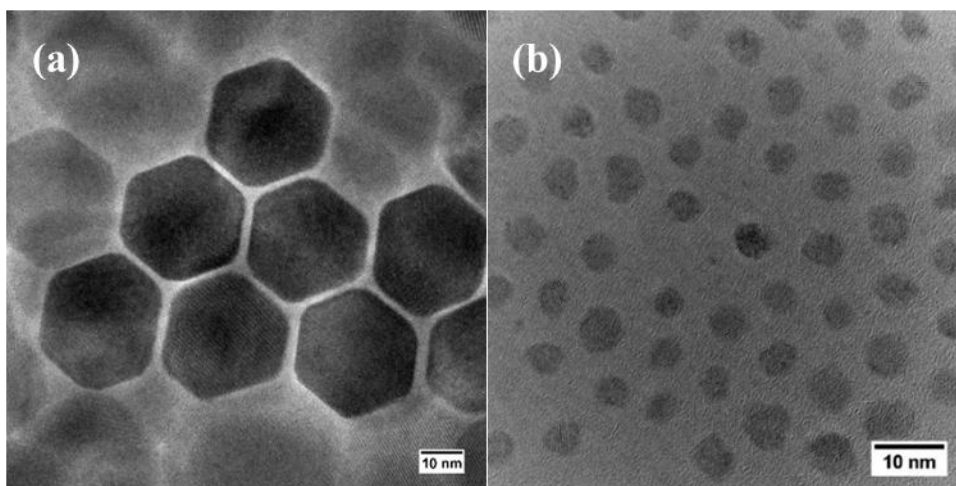
Figure 6.1: TEM images of UCNP samples, (a) large and Er^{3+}-doped, and
(b) small and Tm^{3+}-doped, imaged by collaborator Dr. Finn Purcell-Milton.

Both Er^{3+} and Tm^{3+}-doped UCNPs were chosen due to their variety of applications, as explained in Section 2.4. The emission wavelengths of the Er^{3+}-doped particles are 520 nm, 545 nm and 655

nm, and the emission wavelengths of the Tm^{3+}-doped particles are 405 nm, 475 nm, 650 nm, and 800 nm. The emission spectra of two UCNP samples, showing these emission peaks and the transitions associated with each, can be seen in Figure 6.2 below.
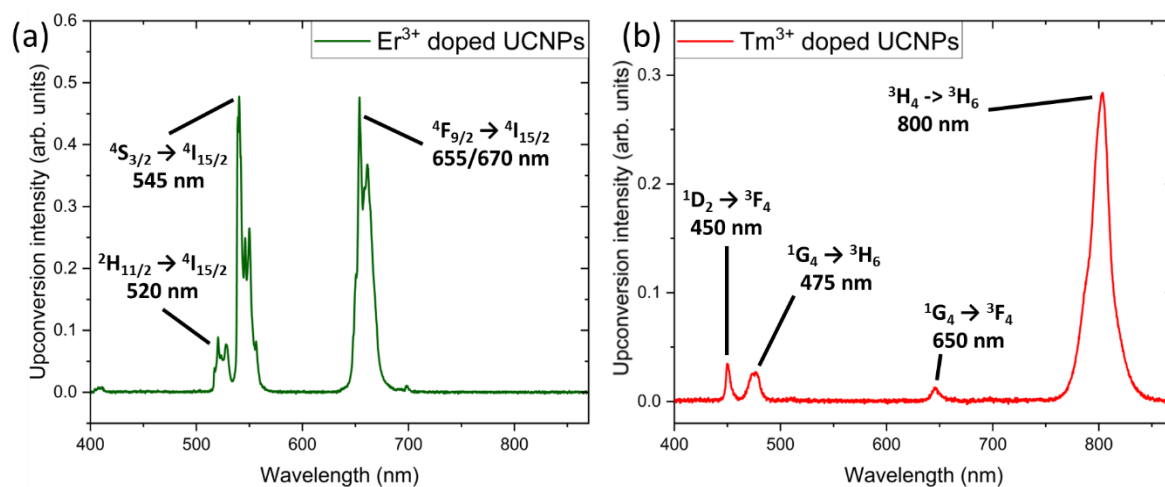
Figure 6.2: Upconversion emission of UCNP samples doped with
(a) Er^{3+} and (b) Tm^{3+}, under 2.00W 980 nm laser illumination.

For the first synthesis batches, methanol dried using a high surface area desiccant was used, as the presence of water in the synthesis can result in the accidental formation of hydrofluoric acid, a very dangerous compound. However, this proved less than ideal. The overly dry methanol resulted in larger nanoparticles than intended from the synthesis, as can be seen in Figure 6.3 below. The methanol did not fully dissolve the NaOH, resulting in sodium methoxide precipitating out of solution. This meant that an insufficient amount of Na was available upon injection to form $NaYF_4$, which resulted in fewer seeds forming. These seeds then grew into larger particles.
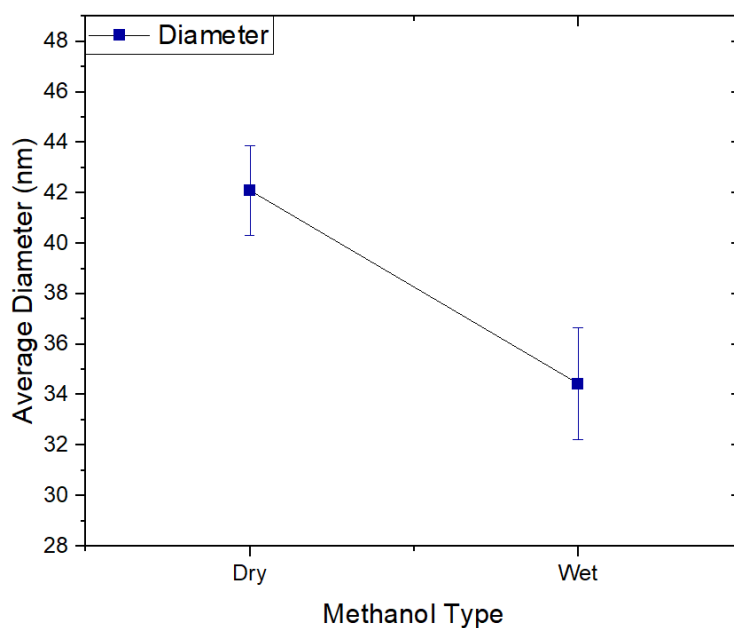
Figure 6.3: UCNP diameter averaged over several syntheses using dry methanol
(treated with desiccant to remove water) or wet methanol (untreated).

Figure 6.3 shows the reduction in average UCNP diameter when wet methanol (stored under lab conditions, untreated with desiccant) was used. As the intention in this work was to create in general smaller nanoparticles, and the overly dry methanol resulted in inconsistent amounts of Na entering the reaction vessel, this wet methanol method was used for all further syntheses.
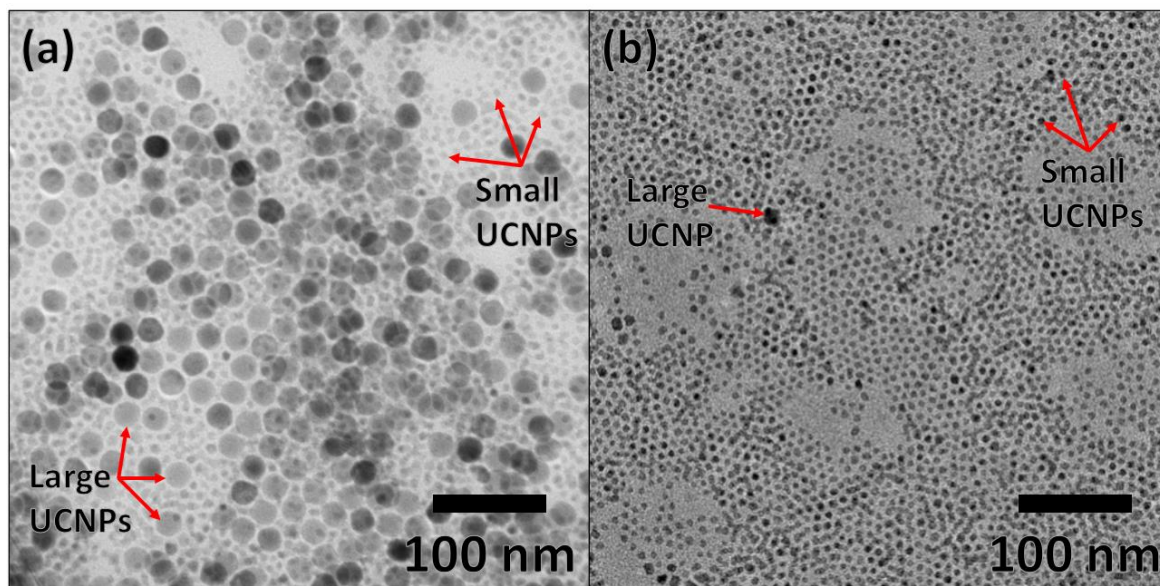
Figure 6.4: TEM images of (a) large-scale UCNP batch, showing significant variation in particle sizes (some smaller and some larger), and (b) large scale UCNP batch using slow injection rate, showing mainly small particles with one larger particle.

An increase of reaction volume by 4x also had an impact on UCNP size. Upscaling nanoparticle syntheses can result in significant changes to the mechanisms and kinetics of the UCNP growth, as well as of the initial seed formation[91]. In larger reaction vessels/reaction volumes, maintaining a consistent temperature and mixing becomes more difficult, which can result in more variation of the size and shape of the synthesised nanoparticles[161,162]. This size variation due to upscaling can be seen in Figure 6.4(a), which shows a mixture of large and small particles, of sizes 23 ± 1 nm and 7 ± 1 nm, respectively. Another large-scale batch of UCNPs was synthesised which contained mainly very small UCNPs (5.3 ± 0.1 nm), with very few larger UCNPs, as can be seen in Figure 6.4(b). This batch was synthesised using a very slow nucleation solution injection rate, which may have resulted in a larger number of nuclei being formed as the solution was added, resulting in overall more particles, each being smaller.
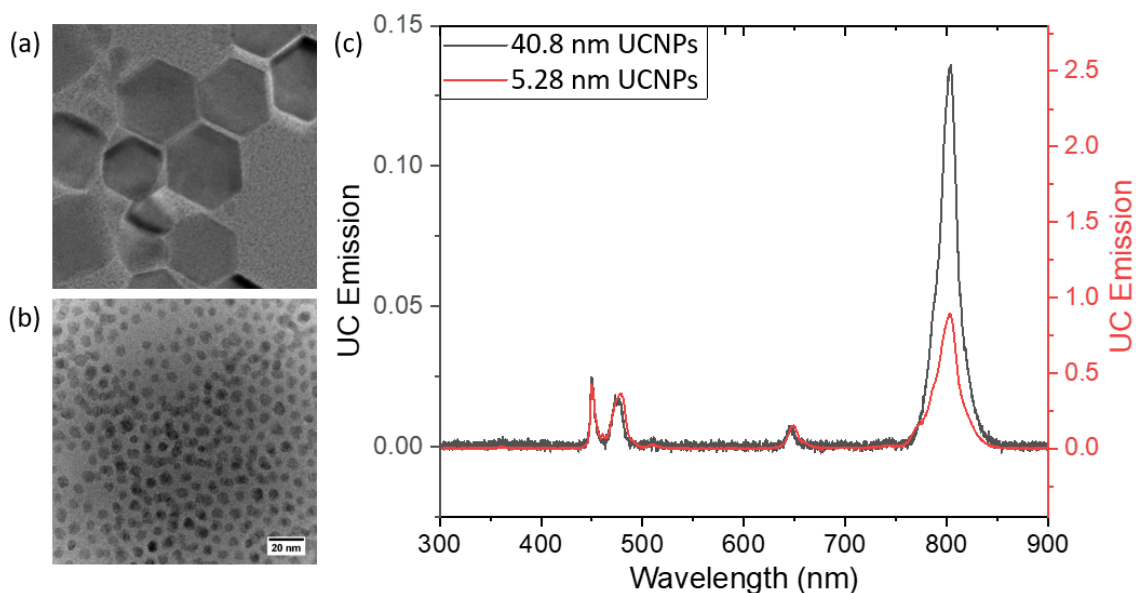
Figure 6.5: TEM images of UCNPs with average diameters (a) 40.8 ± 4.2 nm (≈ 41 ± 4 nm) and (b) 5.28 ± 0.08 nm (≈ 5.3 ± 0.1 nm). Same scale for both. (c) Upconversion emission of these same UCNPs, scaled to 450 nm peak, showing difference in peak ratios.

Figure 6.5 above shows the emission of large and small Tm^{3+}-doped UCNPs. The larger (40.8 nm) UCNPs have a stronger infrared peak than the smaller (5.28 nm) UCNPs. This is in agreement with the literature, as this size dependent peak height ratio is commonly seen with UCNPs[163]. While quantum dots may show a quantum confinement effect, where their emission wavelength changes directly with size, UCNPs are too large for this to be the case[164]. Wang *et al.*[94] showed that the blue-to-infrared ratio in Yb^{3+}/Tm^{3+}-codoped $NaGDF_4$ UCNPs decreased with increasing size, i.e. the IR peak was stronger than the blue peak. They then passivated the surface using a protective undoped $NaGdF_4$ shell. This prevented the decrease in blue peak, showing that the change in emission intensity ratio is caused by surface quenching (see Section 2.4.1). Wang *et al.* were the first to show this size dependent photoluminescence of UCNPs. The larger UCNPs also have stronger emission over the entire spectrum than the smaller UCNPs, which again is due to surface quenching, as the smaller UCNPs have a larger surface area-to-volume ratio.

To create a spacer between gold nanoparticles and UCNPs, silica shelling of the UCNPs was carried out, after an oleate-citrate ligand exchange as described in Section 3.1.1. Preliminary attempts at silica shelling the UCNPs alone showed aggregation and large plate-like structures (Figure 6.6(a)). It is likely that the UCNP concentration was too high for individual shells to form around each of them, and thus a lower concentration was needed to obtain more consistent shells. To try to connect the UCNPs and NSs together in solution, they were silica shelled simultaneously, with a much lower UCNP concentration (40x lower).

Many aggregates were formed with multiple UCNPs and NSs (Figure 6.6(b)). This suggests that some manner of individually attaching the UCNPs to the NSs prior to shelling would be optimal, in

order to connect them in solution. However, the much lower concentration of UCNPs in this method proved advantageous, as individually-shelled UCNPs were also formed (Figure 6.6(c)).
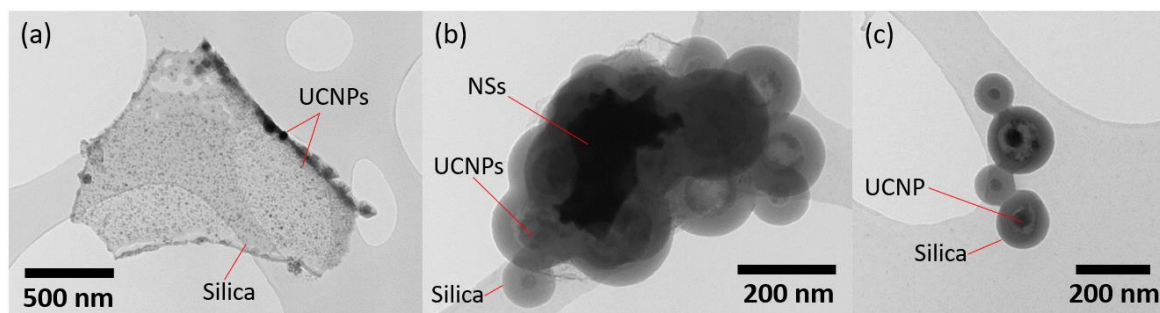
Figure 6.6: (a) Silica encapsulated UCNPs: a plate of silica showing many UCNPs within it, (b) an aggregate of NSs + UCNPs in silica shells, and (c) UCNPs in silica shells, from a batch of simultaneously shelled NSs + UCNPs

As the NSs could be easily silica shelled by themselves (as discussed in Section 4.7), it was decided that unshelled UCNPs would be used, and silica shelled NSs could be placed on top of them. The results of this type of system can be seen in Sections 6.4 and 6.5. As both nanoparticle types can be silica shelled, if combination in solution was required in any future work, a thiol-terminated shell precursor (such as MPTES) could be used to create a silica shell around the UCNPs. Thiols strongly bind to gold, and so such shells could be easily attached to the NSs.

6.3   Layer-by-layer deposition

Layer-by-layer deposition is a method used to deposit layers of polyelectrolytes and charged nanoparticles onto a substrate. LbL can give rise to a very uniform spread of nanoparticles across a substrate, as well as good reproducibility. It can be used to deposit monolayers of UCNPs[165], as well as monolayers of gold nanoparticles[166]. As described in Section 3.6, the polyelectrolyte layers can be built up in order to create spacers between nanoparticles, with well-defined and controllable thicknesses, with nanometre precision[119,167]. To create samples with controllable inter-particle distances, layer-by-layer deposition was chosen as a sample preparation method.

6.3.1   UCNPs

LbL requires that the particles be charged and in aqueous solution. The gold nanoparticles have a charged ligand on their surface post-synthesis; CTAB (which gives rise to a positively charged CTA^+ micelle around the nanoparticle and a negatively charged Br^- counterion)[168]. The UCNPs were synthesised in nonpolar solvents, with an uncharged oleate ligand on the surface, so a ligand exchange was carried out on the UCNPs to make them water soluble. Polyacrylic acid (PAA) was chosen as the ligand, which has a strong negative charge. The ligand exchange procedure is

described in Section 3.1.1 and successfully produced water soluble UCNPs with strong emission (shown in Figure 6.7(a)). The emission spectroscopy setup for liquid and deposited samples is described in Section 3.8.
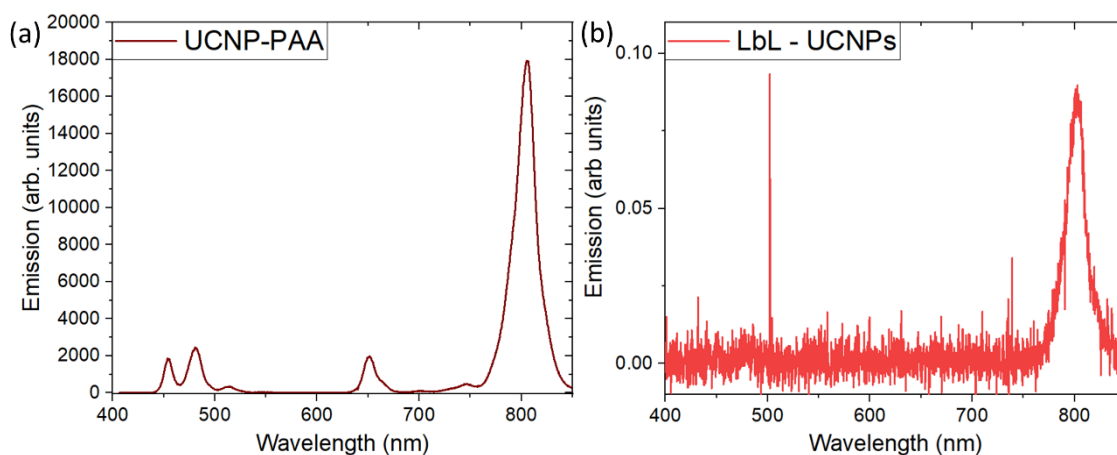
Figure 6.7: Upconversion emission of Tm³⁺-doped UCNPs with PAA ligand, (a) in aqueous solution and (b) deposited on glass via LbL (sharp line at 500 nm due to noise in measurement or subtracted background).

LbL samples were created using the method described in Section 3.6. The difference between the emission of UCNPs in solution and when they have been deposited via LbL is shown in Figure 6.7(a) vs (b). The emission from the LbL sample is much weaker than that from the UCNPs in solution, with only the most intense peak visible above the noise level, because the LbL UCNP layer is very thin, and thus a much smaller number of UCNPs are present in the area irradiated by the laser in the LbL sample. The differences in emission of LbL samples made using Er³⁺-doped and Tm³⁺-doped UCNPs can be seen in Figure 6.8, with the 520, 545 and 670 nm peaks clearly visible in the Er-UCNP spectrum, and the 800 nm peak (the strongest emission) visible in the Tm-UCNP spectrum.
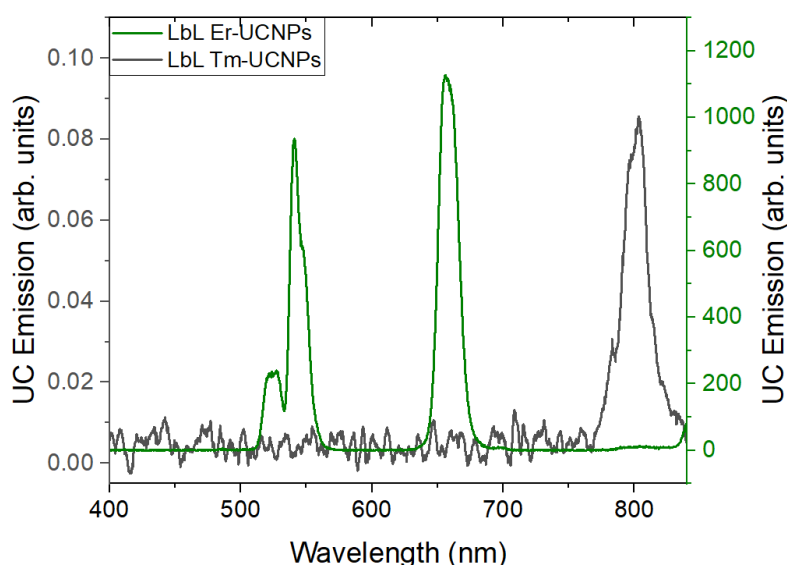
Figure 6.8: Emission from LbL samples created using Er³⁺- and Tm³⁺-doped UCNPs.

The LbL method also provided an even layer of UCNPs on the samples, which can be seen in Figure 6.9 below, *via* the consistent emission peak heights across multiple areas of the sample.
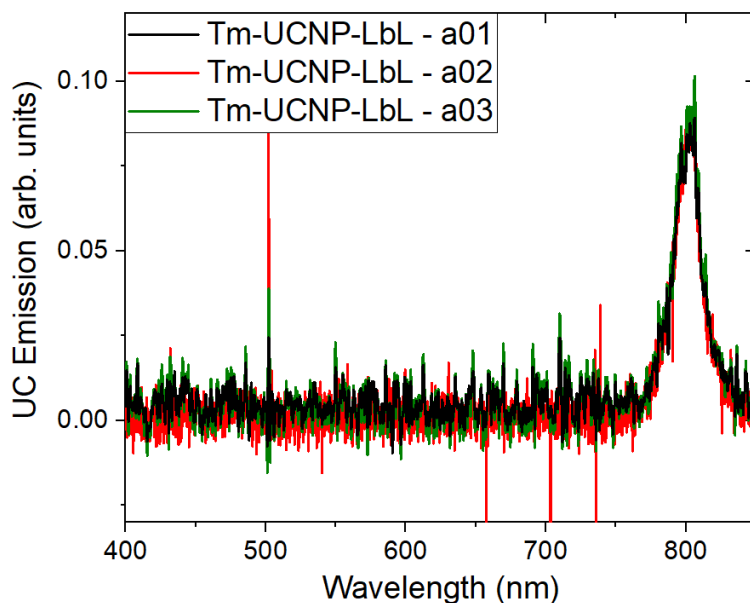
Figure 6.9: Upconversion emission from a Tm-UCNP LbL sample, showing emission from three areas. Sharp lines at 500 and 650-750 nm due to noise in measurement or subtracted background.
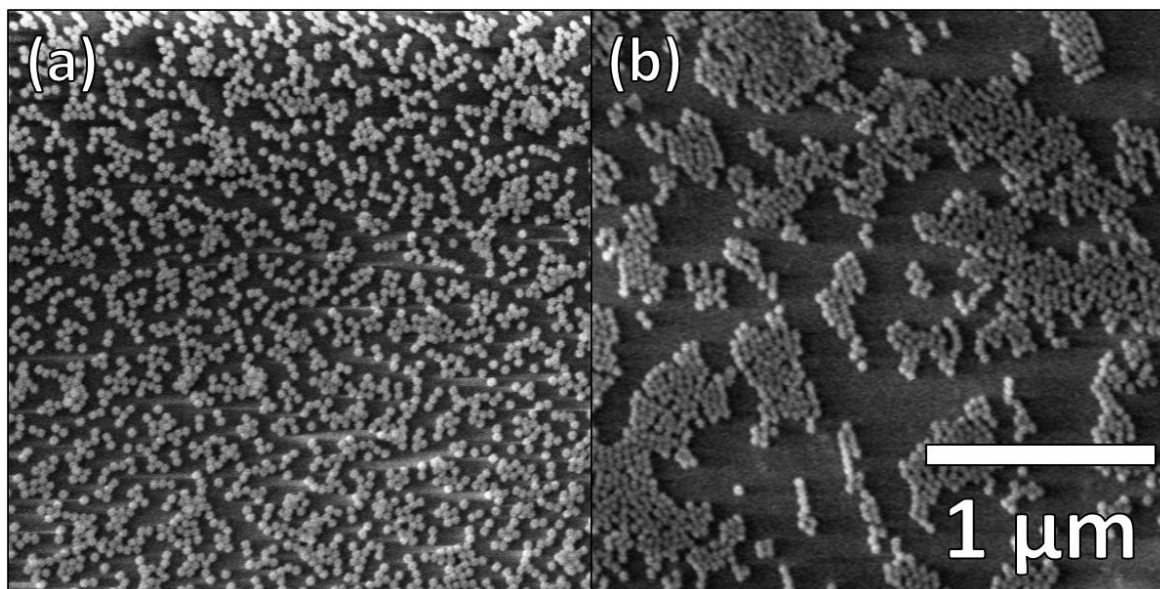
Figure 6.10: SEM images of LbL samples with UCNPs, created via dipping in (a) fresh UCNP solution, and (b) a previously used UCNP solution. The particle concentrations are (a) 332 and (b) 206 particles/μm^2. Same scale used for both images.

On some samples, UCNP solutions which had previously been used for LbL were reused. The resulting samples had a significantly lower UCNP concentration, as well as clustering of the UCNPs, which is not ideal for consistent plasmon enhancement. This can be seen in Figure 6.10, which compares the SEM images of a sample made using fresh UCNP solution (Figure 6.10(a)), and one made using a reused solution (Figure 6.10(b)). The clustering may occur because of small

amounts of polyelectrolytes, which were not completely removed from the previous sample in the rinsing step, being released from the substrate into the solution and binding with the UCNPs. The difference in concentration may be due to the most strongly charged UCNPs attaching to the previous sample, leaving fewer strongly charged UCNPs available in the solution to attach to the second substrate. Thus, the UCNP LbL solutions were only used for dipping one substrate each. The samples made using a fresh solution (Figure 6.10(a)), displayed more evenly distributed UCNPs, though some inhomogeneity remained.

6.3.2   Nanostars

In order to plasmonically enhance the UCNPs on the LbL samples, gold nanoparticles were also deposited. NSs were chosen, as they have multiple resonances at their many tips and across the cores, as described in Section 2.1, and as can be seen in Figure 6.11(c) below. The resonance peaks shown in these graphs change with a change in incident light polarisation, demonstrating that they come from tips on the NSs oriented in different directions.
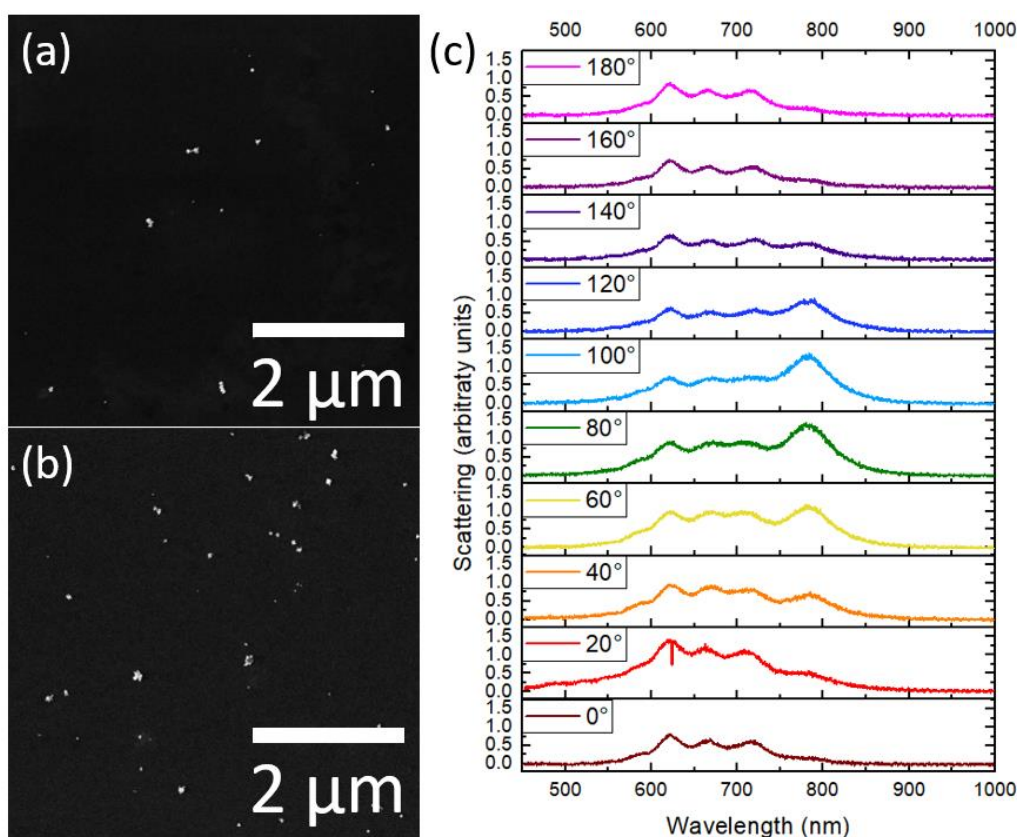
Figure 6.11: (a) and (b), SEM images of LbL samples prepared with NSs. The concentration of NSs deposited on (b) is 2x the concentration deposited on (a). (c) Single particle scattering spectra of a NS, varying the polarisation.

As the NSs are positively charged (due to their ligand, CTAB, which disassociates into a positively charged ligand, CTA^+, and negatively charged counterion, Br^-), which was confirmed via zeta-

potential measurements, the final polyelectrolyte layer deposited before the NSs⁺ was PSS (negatively charged), and the LbL deposition was carried out as described in Section 3.6. Figure 6.11(a) and (b) show SEM images of LbL samples prepared with NSs. Figure 6.11(b) was prepared with a higher concentration of NSs in solution than Figure 6.11(a), and as such has a higher concentration of NSs on the sample. However, the overall concentration of NSs on these samples was very low, and nowhere close to a monolayer, which is more likely what would be needed to induce enhancement over a large enough area to be seen in the emission detection spot (≈ 2 mm^2 spot size). When the samples are not covered in a monolayer, certain NS/UCNP pairs may not actually be the spacer distance apart (only in the z direction). Rather, they might be further apart due to the additional distance in the x-y directions. These concentration dependent effects can be seen in Figure 6.12 below.
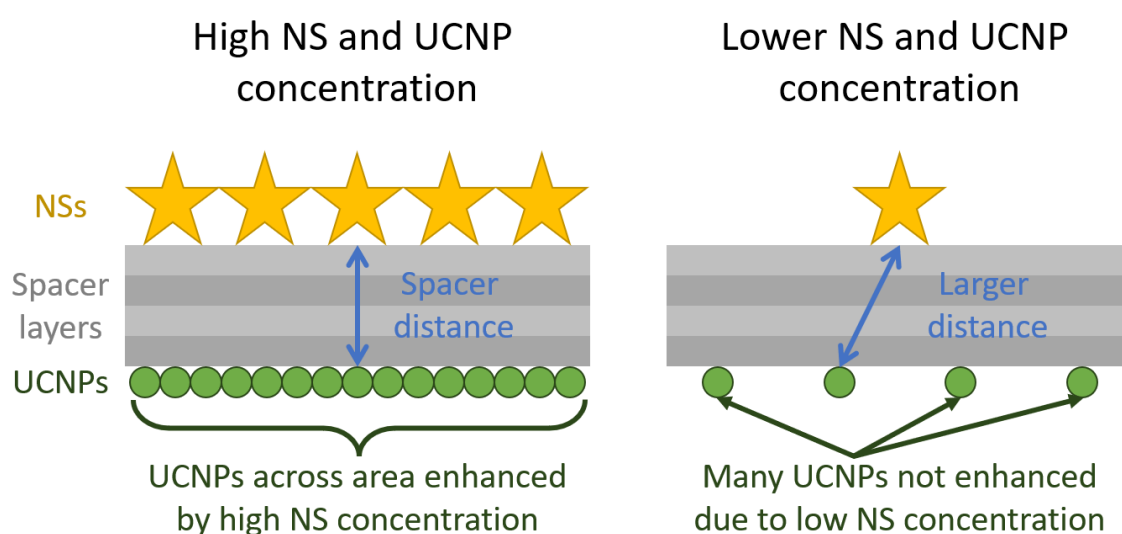
Figure 6.12: Schematic of UCNP enhancements and inter-particle distances in LbL samples with high and low NS and UCNP concentrations.

6.3.3   Nanorods

As the concentration of NSs was found to be very low with the LbL deposition method, investigations were carried out using a different type of plasmonic particles, which had an established record in the literature of UCNP enhancement. This was the case for gold NRs[158], and as such, synthesised NRs were deposited. In this way, the concentration could be better optimised with the knowledge that the enhancement was likely to occur.
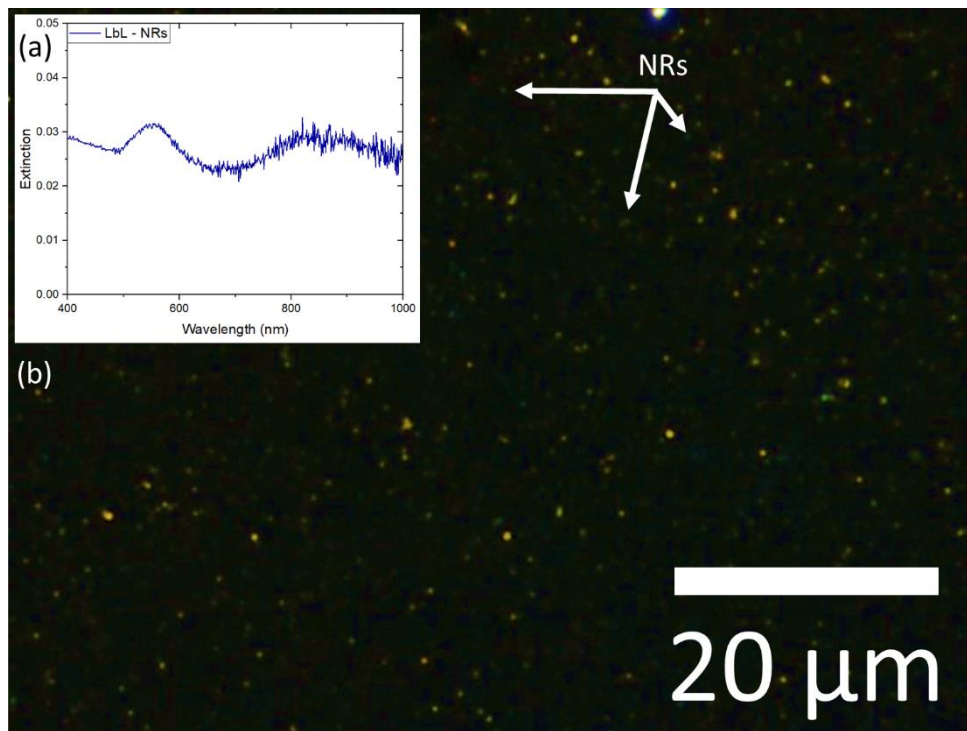
Figure 6.13: (a) Extinction spectrum of LbL sample made using synthesised gold NR batch, showing plasmon peak from spheres in solution (around λ = 550 nm) and longitudinal NR peak (around λ = 860 nm). (b) DFM image of a LbL sample showing the NRs (visible as green dots) on its surface.

Figure 6.13(a) shows the extinction spectrum of a LbL sample, with the strong plasmon peaks suggesting a reasonably high concentration of NRs. Figure 6.13(b) shows a DFM image of this sample, confirming a moderate concentration of NRs (less than a monolayer), and showing that the sample has an even spread of NRs. For an LbL sample, an even layer is ideal to obtain consistency across the sample. However, this sample did not result in upconversion enhancement. The less than monolayer concentration may have occurred due to difficulty in obtaining sufficiently high NR concentrations in solution.
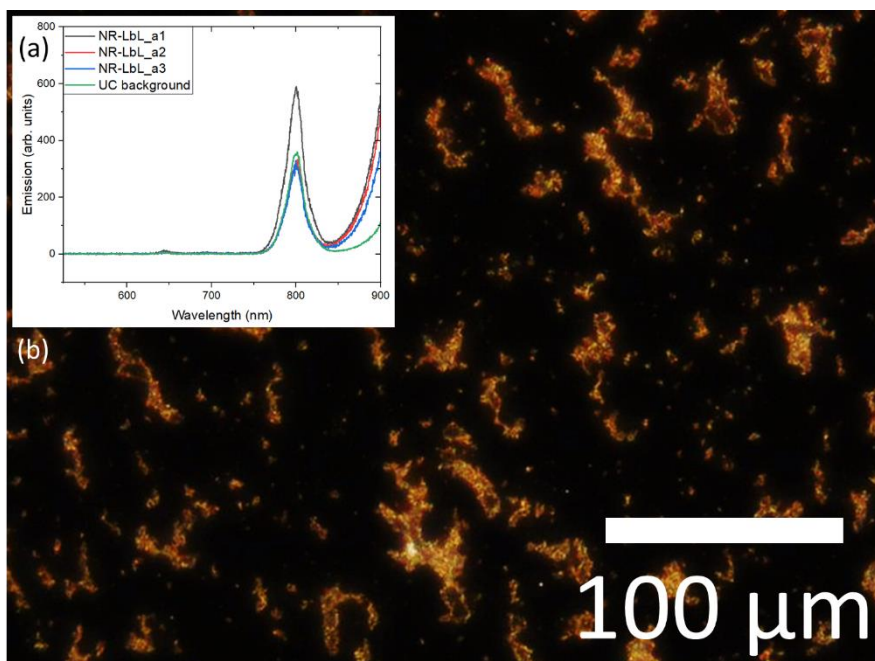
Figure 6.14: (a) Graph of upconversion emission of an LbL sample with UCNPs+NRs, demonstrating enhancement in one area (with a NR cluster). (b) DFM image of this LbL sample, showing the NR clusters.

Figure 6.14(b) shows a DFM image of another LbL sample made with NRs, which features NR clusters across the sample. These clusters likely occurred due to insufficient sonication of the NR solution. This sample showed upconversion enhancement on one area, likely in the vicinity of a NR cluster. Plasmonic nanoparticle clusters can show hotspots between the particles, which can result in significant light intensity enhancement[169]. The single area upconversion enhancement of a factor of 1.7x, calculated by dividing the integrated area under the enhanced peak ($\propto$ emission intensity) by the area under the UC background peak, is shown in Figure 6.14(a), where two areas on the sample are not enhanced in comparison to the background upconversion. While this enhancement factor is lower than some results which have been seen in the literature, with Feng *et al.* obtaining enhancement of up to 22.6x[167], however it is difficult to make a direct comparison to this work due to the difference in orientation of the sample (NRs on top), and the presence of the NR clusters. The impact of clusters is further discussed in Section 6.5.

6.3.4   Bipyramids

LbL samples were also prepared using BPs as the plasmonic particles. As explained in Chapter 5, BPs have very pointed tips and thus can achieve higher field enhancements than NRs of a similar length/width. Since enhancement has thus far been seen in clusters, which have high field enhancement at inter-particle hotspots, BPs have the potential to be an alternative particle to enhance upconversion. BPs were successfully deposited via the same method as the NRs, as

shown in Figure 6.15 below, where the SEM images of BPs deposited can be seen in Figure 6.15(a)-(c), and their characteristic spectral features can clearly be seen in the extinction spectra in Figure 6.15(d).
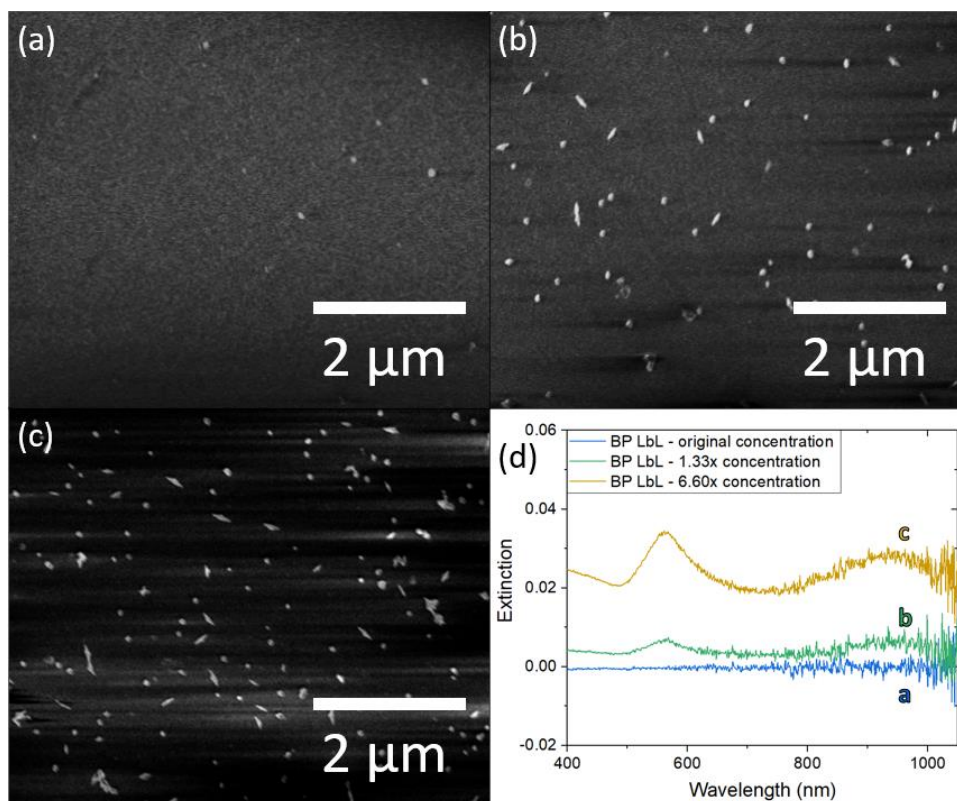
Figure 6.15: SEM images of LbL samples with BPs; (a) a low concentration (0.35 particles/μm²), (b) a higher concentration (3.10 particles/μm²) and (c) the highest concentration (6.82 particles/μm²). Same scale for all images. (d) Extinction spectra of the samples in (a) – (c). Peak extinction values a: 0.0, b: 0.00639, c: 0.02836.

Figure 6.15(a) shows a LbL sample with very few gold nanoparticles on the surface (0.35 particles/μm²), which corresponds to the extinction spectrum (Figure 6.15(d)), which shows 0 extinction from this sample. Figure 6.15(b) and (c) show samples created using solutions with higher BP concentrations (by 1.33x and 6.60x, respectively), which as a result have higher particle concentrations on the sample surface (3.10 and 6.82 particles/μm², respectively). These increased concentrations can also be seen *via* an increase in the UV-Vis spectra in Figure 6.15(d), where the peak extinction values are ≈ 0.006 and 0.028.

The SEM images in Figure 6.15(a)-(c) show an increase in gold nanoparticle concentration on the surface of the samples. Figure 6.15(d) shows the difference in extinction spectra for these same samples, where the extinction peak heights are proportional to the concentrations. The solutions which were used to make the samples in Figure 6.15 (b) and (c) have ratios of 1.33:1 and 6.60:1 to the lowest concentration sample, respectively. This shows that final nanoparticle concentrations

on the samples have a strong dependence on the original concentration of nanoparticles in the LbL deposition solutions.
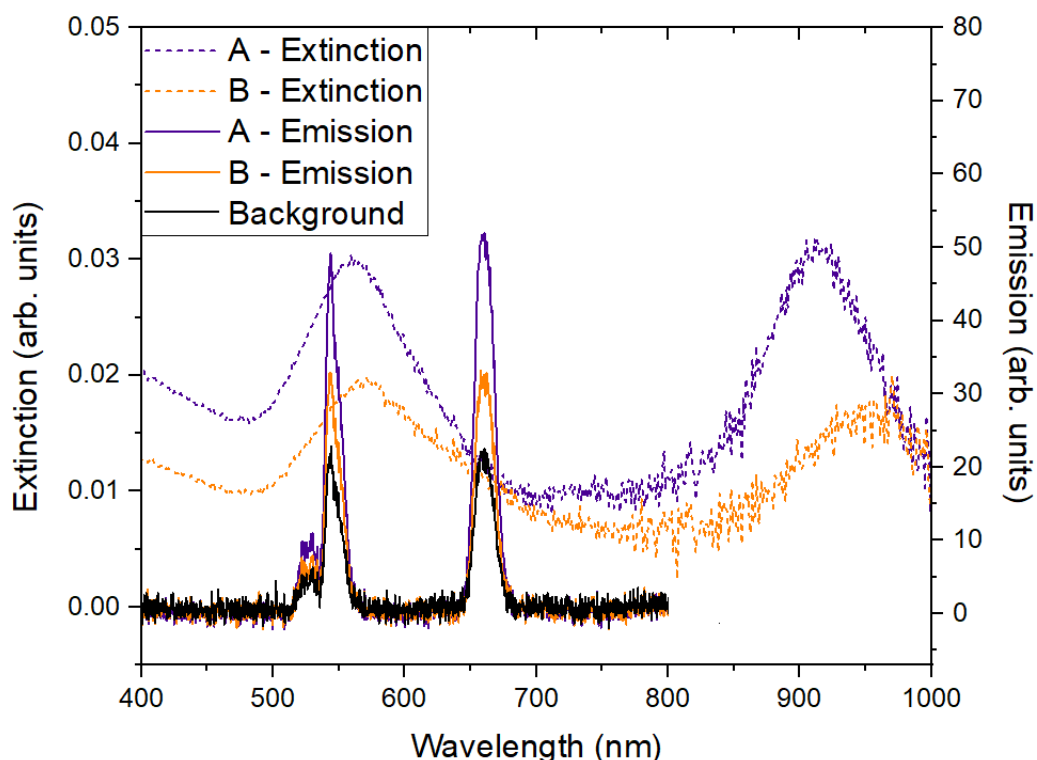
Figure 6.16: Extinction and emission spectra of two LbL samples made with UCNPs and 2 different BP concentrations. Additionally, the emission spectrum of a background sample made with only UCNPs.

It is evident from Figure 6.16 that the increase in BP concentration across the two samples (as expressed by the extinction, dashed lines), is correlated with an increase in the UC emission (solid lines). The enhancements of these samples are seen in Table 1 below:

Table 1: LbL sample emission peak enhancement values.

Sample / Peak	Green (545 nm)	Red (665 nm)
A	2.10	2.21
B	1.45	1.41

However, it is clear from the SEM images in Figure 6.15(a) – (c) that these samples did not contain a BP monolayer. Comparing the extinction values in Figure 6.16 (≤ 0.03) to those in Figure 6.15(d) (max 0.028), it is likely that the BPs did not form a full monolayer in the samples in Figure 6.16, either. Thus, it may be the case that a lack of consistent BP-UCNP interactions across the whole sample is the reason for the moderate enhancements (≤ 2.2x) which have been seen thus far

using the LbL deposition method. However, as these enhancements were being measured in ensemble, it may be possible to obtain single particle enhancements from such samples in future.

To obtain higher concentrations on LbL samples, some samples were prepared using an unconventional LbL method. For the BP deposition step, after the initial polyelectrolyte layers were deposited, a highly concentrated BP solution was pipetted directly onto the substrate. This resulted in samples which had uneven BP distributions, but some sections displayed visibly very high BP concentrations.
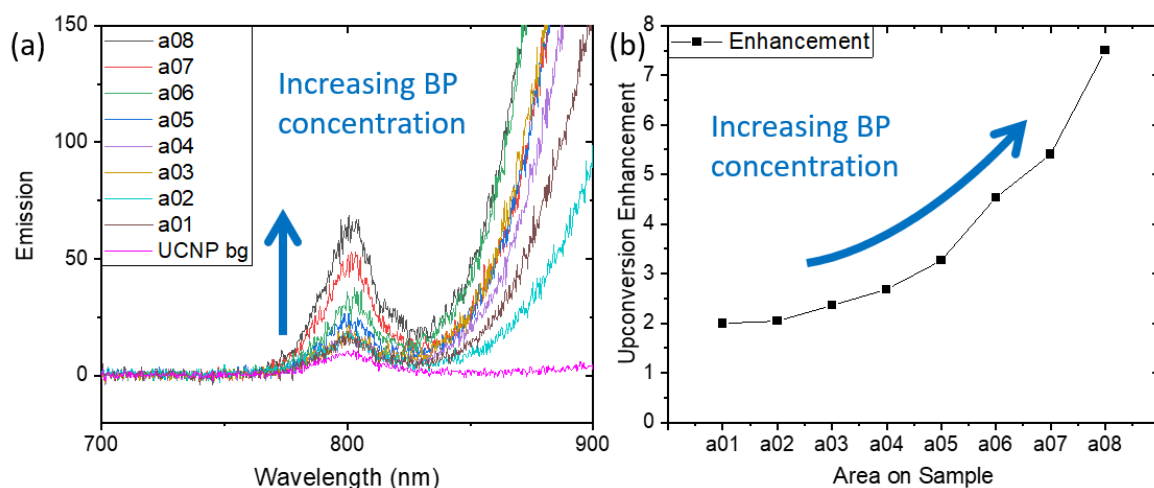
Figure 6.17: (a) emission of UCNPs with and without 980 nm BPs, at sample areas with increasing BP concentrations (part of an additional peak due to scattering of the incoming 980 nm laser light visible at right of graph), (b) enhancement across these areas of the sample.

One such sample, with BPs with a plasmon resonance wavelength of 980 nm, demonstrated significant UC enhancement. The UC emission spectra (a) and enhancement values (b) for various areas across this sample are shown in Figure 6.17 above. As the BP concentration increased, so did the enhancement, up to a maximum enhancement of 7.5x. This may be for a similar reason as the enhancement seen using NR clusters. Enhancement of upconversion by BPs has not been previously shown in the literature.

In all LbL samples, the plasmonic nanoparticles were placed underneath the UCNPs, to avoid any shadowing. However, this may mean that they have less light reaching them (as it has to travel through the UCNP layer first, which is transparent but may still have some degree of attenuation of the light due to scattering). This, as well as the fact that many of the samples did not achieve a very high plasmonic nanoparticle concentration, resulted in the decision to try spin coating the UCNPs and plasmonic NPs onto glass substrates, in order to obtain higher NP concentrations, as well as placing the plasmonic NPs on top of the UCNPs, to potentially achieve better enhancement.

6.4 Spin coating

Spin coating involves nanoparticles being suspended in a volatile liquid and dropped onto a substrate. The substrate is affixed in place via vacuum and spun at various speeds to ensure a reasonably consistent spread of nanoparticles across the substrate. While spin-coating can result in a more inhomogeneous distribution of nanoparticles, it can achieve very high nanoparticle concentrations[170].

Er^{3+}-doped UCNPs were synthesised and spin-coated onto glass slides, using the method described in Section 3.11. This resulted in samples with consistent UC emission measured at several points across the sample, implying an even distribution of UCNPs across the slide. Gold NSs were coated in silica shells, as described in Sections 3.5 and 4.7, and spin-coated on top of the UCNPs, with the silica shells acting as a spacer layer. A schematic of the sample and the detection setup can be seen in Figure 6.18(a).
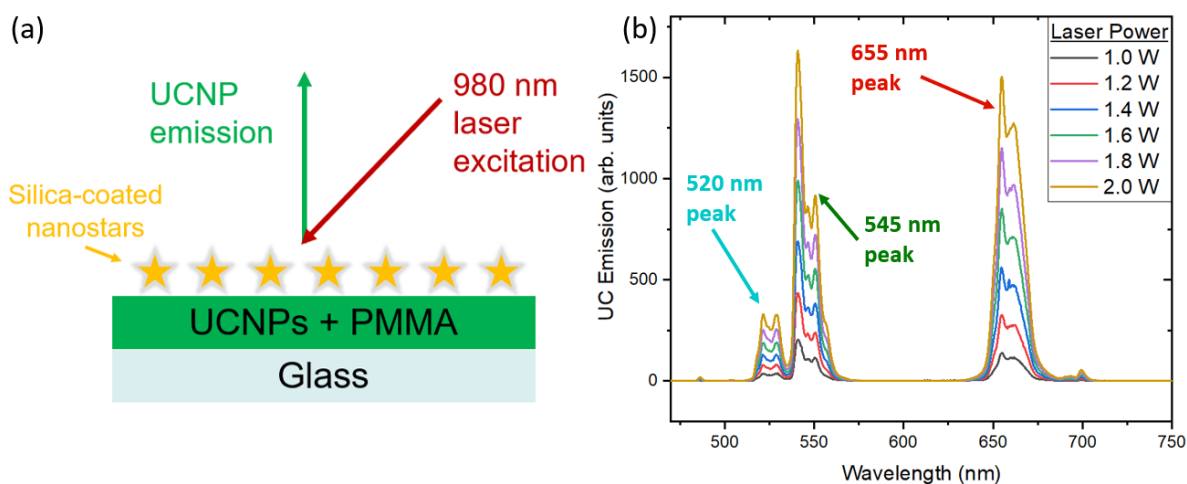
Figure 6.18: (a) Diagram of sample and detection setup. NSs have a silica shell thickness of 10 ± 1 nm. (b) Power-dependent NS-enhanced UC emission spectrum of Yb, Er- doped NaYF4 UCNPs.

Samples were made with even layers of silica-shelled NSs on top of the UCNP layer. However, these samples did not result in any enhancement. However, samples with more uneven NS layers gave rise to a different outcome. Figure 6.19 shows a DFM image of one such sample (Sample 16) with an irregular NS film. Areas of low NS concentrations can be seen, as well as a "coffee stain" type region, with a high NS concentration in the centre and a very high NS concentration at the edge[171].
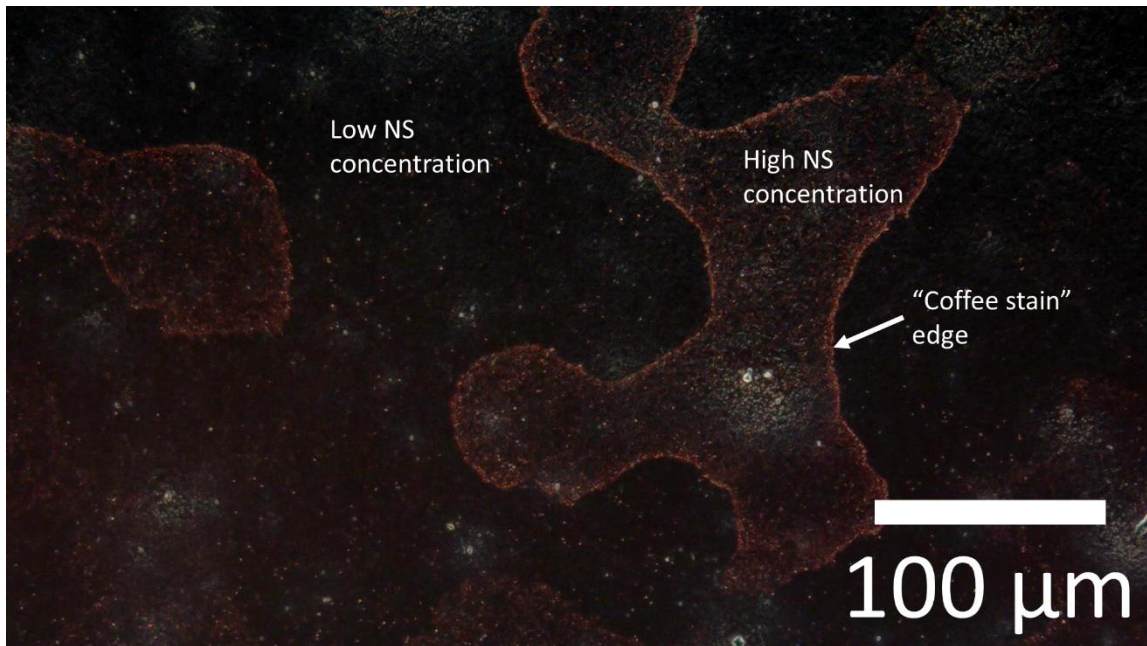
Figure 6.19: DFM image of a spin-coated sample, Sample 16, featuring a "coffee stain" type irregular film of NSs, showing regions of high and low NS concentrations (high within the "coffee stain" and even higher at its edge, and low outside the "coffee stain"). The NSs are visible as red dots.

Figure 6.20 shows another DFM image of the sample in Figure 6.19, at 5x higher magnification. This allows for a closer look at the considerable difference in NS concentrations between the "coffee stain" edges and the rest of the sample.
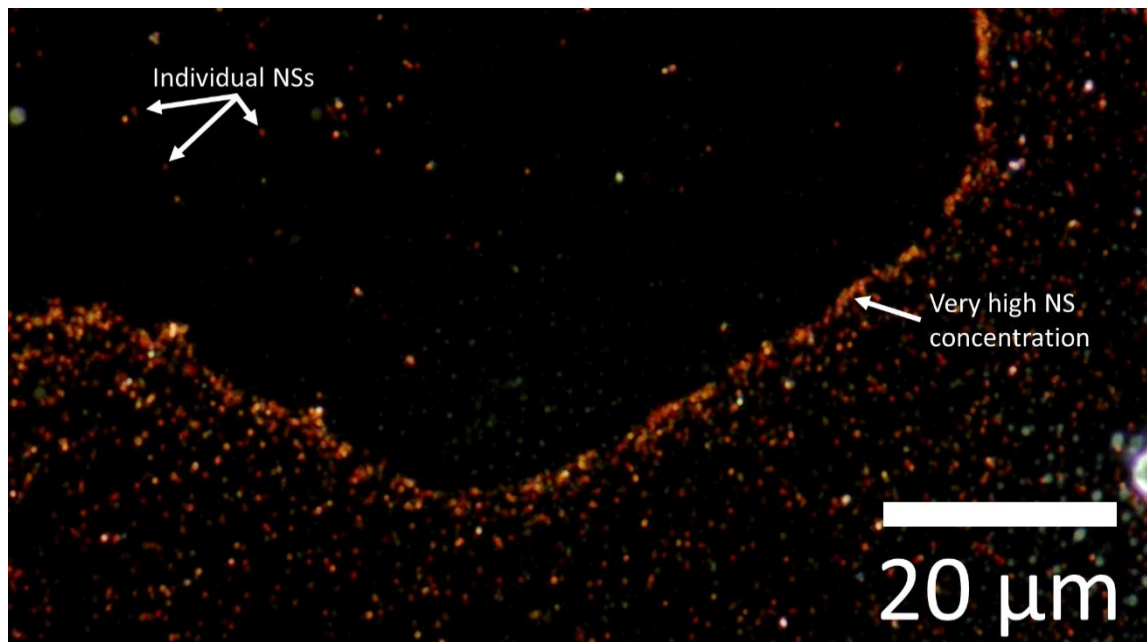
Figure 6.20: DFM image of the spin-coated sample from Figure 6.19, at 5x higher magnification, showing the distances between individual NSs in the low concentration region, and the clustering of NSs at the edge of the "coffee stain" region.

Several samples with "coffee stain" regions were created, and the upconversion emission measured before and after the deposition of the silica-shelled NS layer. The integrated area under the emission peaks (emission intensity) was measured, and the results can be seen in Figure 6.21.

Figure 6.21(a) shows the emission intensity from Sample 17, averaged over three areas on the sample before the addition of NSs, and the emission intensity from an enhanced area after the addition of NSs. Figure 6.21(b), (c), and (d) show the enhancement factors of the emission intensity for this and two other samples (Samples 15, 16, and 17). The enhanced areas of the samples in Figure 6.21 were all at the edge of "coffee stain" regions, where the highest NS concentration was. The impact of high nanoparticle concentration and clustering is discussed in Section 6.5.
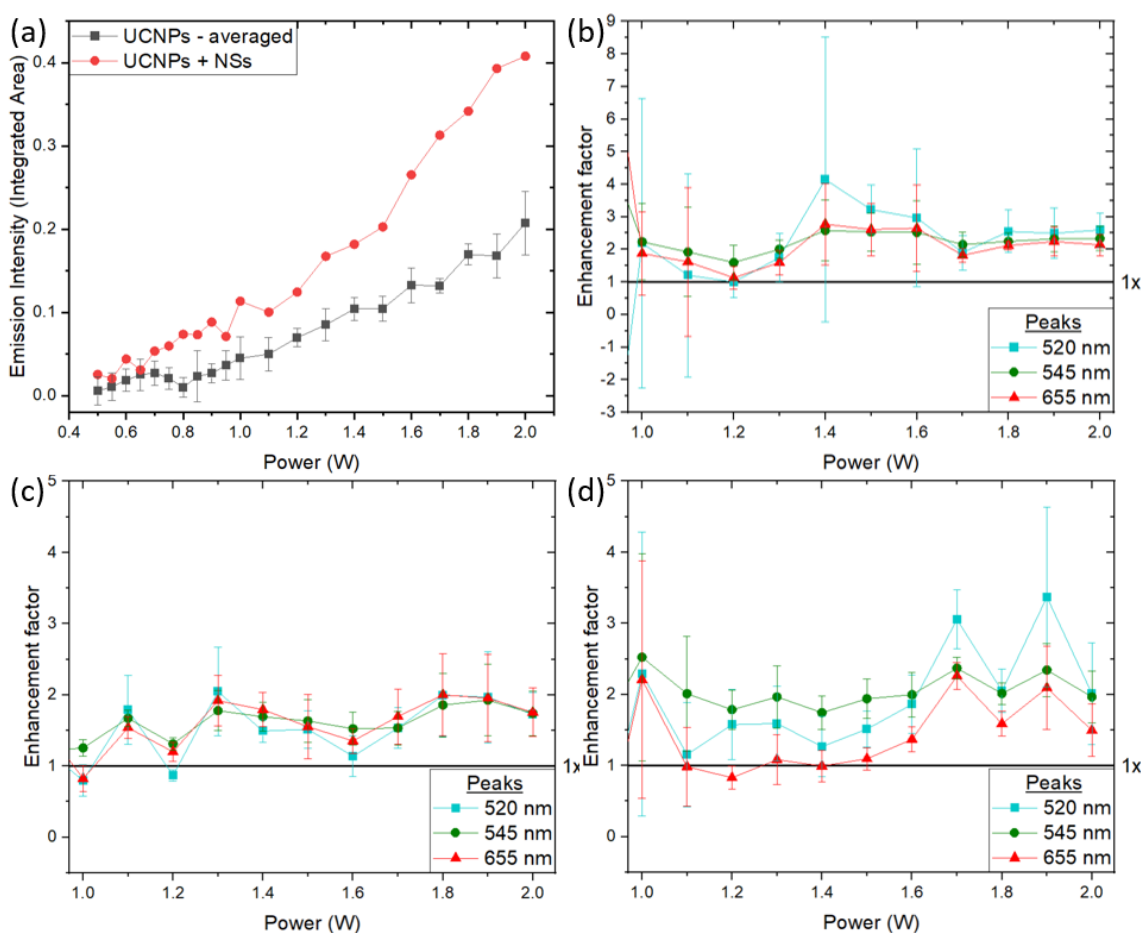
Figure 6.21: (a) Sample 17, comparison of integrated areas under 545 nm peak (i.e. peak emission intensity), with and without NSs, (b), (c), and (d), enhancement factors of the three peaks for samples 15, 16, and 17, respectively.

Table 2 summarises the enhancements across the three samples with "coffee stain" areas. There was on average 1.9x enhancement over all peaks and all samples, where previously literature has shown NS quenching[99,100]. The enhancement of the samples is wavelength-independent. This implies that the mechanism may be absorption enhancement, rather than emission enhancement, as absorption enhancement results in an even increase in light emission at all

114

wavelengths, whereas emission enhancement will differ depending on the emission wavelength, as it occurs only in emission bands which overlap with a plasmonic structure[172].

Table 2: Enhancement values of 3 UC peaks across three samples. Average value over all peaks & samples = 1.9 ± 0.1.

	520 nm Peak	545 nm Peak	655 nm Peak	Average enhancement
Sample 15	2.4 ± 0.7	2.2 ± 0.2	2.1 ± 0.3	2.2 ± 0.3
Sample 16	1.5 ± 0.1	1.5 ± 0.1	1.6 ± 0.1	1.6 ± 0.1
Sample 17	2.0 ± 0.1	2.1 ± 0.2	1.5 ± 0.2	1.8 ± 0.1
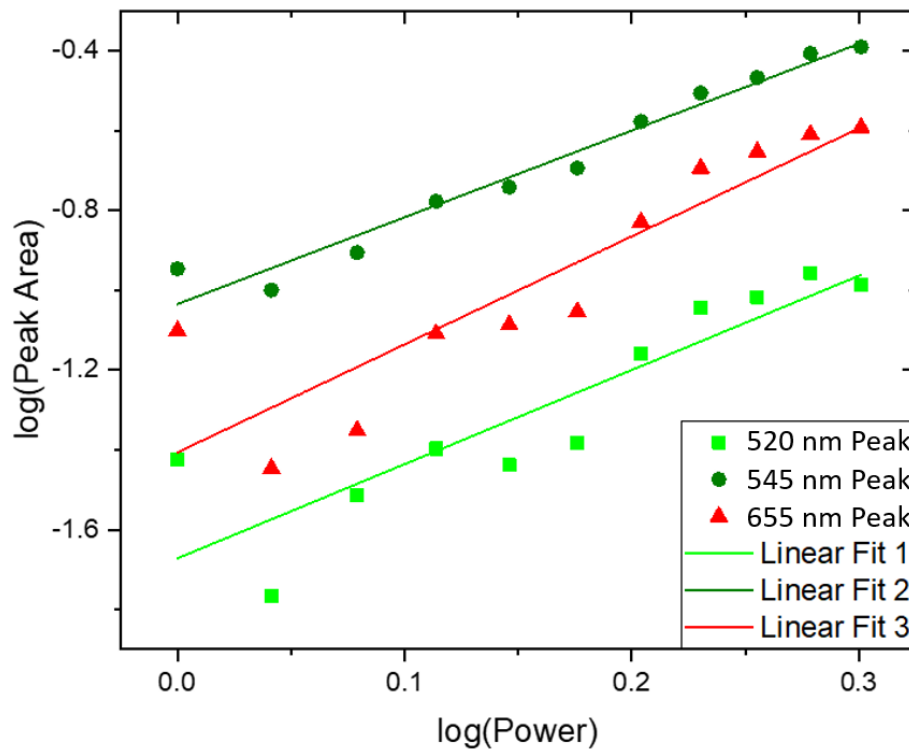
Figure 6.22: Log-log plot of peak area ($\propto$ intensity) vs power, with slopes: 520 nm Peak: 2.4 ± 0.4, 545 nm Peak: 2.2 ± 0.1, 655 nm Peak: 2.7 ± 0.4. Average slope over all samples and peaks: 2.6 ± 0.1.

For a nonlinear process, such as upconversion, when the log of the peak intensity (I) (or area under peak in emission spectrum) is plotted against the log of the laser power (P),

$$\log(I) \propto n \log(P),$$

where (n = number of photons involved in the emission process)[80]. Figure 6.22 shows the log-log plot for Sample 17 after the addition of NSs. The slope ($\propto n$) over all 3 samples increases from 1.9 ± 0.1 (for sample without NSs) to 2.6 ± 0.1. This might imply a move from 2-photon to 3-photon processes dominating, which is possible for all Er^{3+} emission peaks[173], as can be seen in Figure 6.23 below.

Figure 6.23: Energy level diagrams of Yb³⁺+ Er³⁺upconversion system, showing (a) two-photon processes and (b) three-photon processes for Er³⁺ emission.

This commonly happens with intense excitation[174], which further supports that the enhancement mechanism for these samples may be absorption/excitation enhancement.

6.5 Clusters

While the samples in the previous section had a maximum enhancement of 2.4x, one sample showed an area of much higher enhancement. The enhancement, as shown in Figure 6.24(a), was wavelength dependent, and thus more likely due to UCNP emission enhancement than absorption/excitation enhancement, which is wavelength independent.

Figure 6.24: (a) Upconverted emission at 2.00W excitation with and without NSs, showing the enhancement of each of the main peaks, as well as the appearance of a small peak at around 408 nm. (b) Overlap of emission spectrum of UCNPs with in-solution extinction spectra of these NSs. The UCNP absorption peak and excitation wavelength is shown by the dashed line.

The enhancement of the emission from the Er³⁺-doped UCNPs, shown in Figure 6.24(a), varied from 5.4x (520 nm peak) to 9.7x (655 nm peak). The enhancement of the peaks towards longer wavelengths is larger, which is in agreement with the stronger overlap between the NS plasmon resonances and the UCNPs in this region, shown in Figure 6.24(b). However, there may be a combination of emission enhancement and absorption enhancement, as an upconverted peak at

around 408 nm also appears (the $^2H_{9/2} \rightarrow {}^4I_{15/2}$ transition, which has been seen in the literature for Er-doped UCNPs[175]), which may be now visible due to an increase in absorbed light.
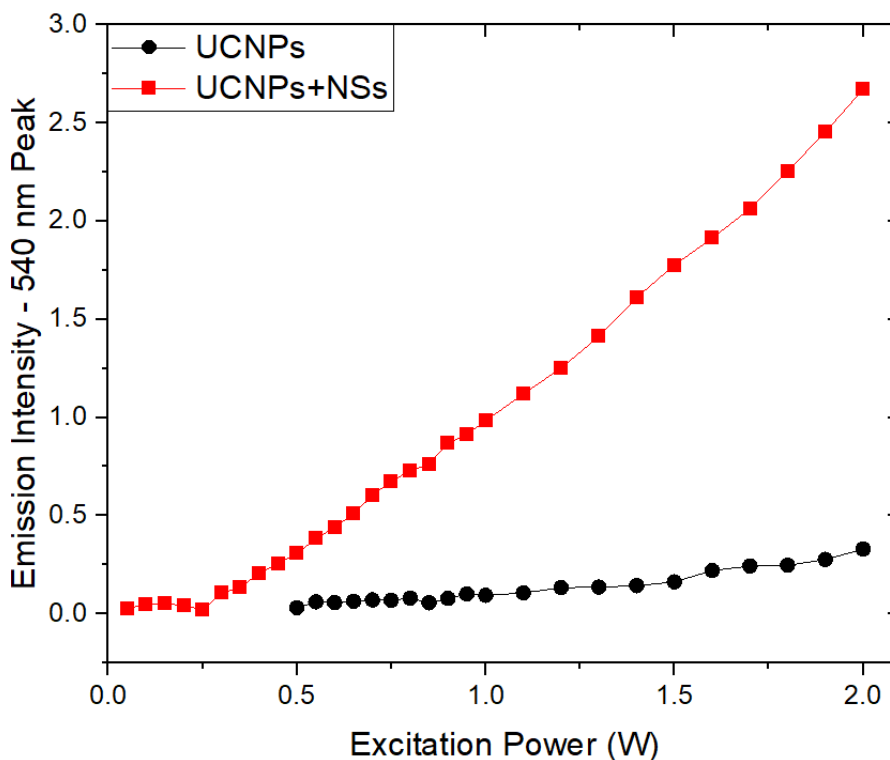
Figure 6.25: Integrated area of the 540 nm upconverted emission peak with and without NSs, showing the threshold at which upconverted emission could be measured.

The threshold at which upconversion was detectable in the measured spectra also decreased, from ≈ 0.75 W to ≈ 0.30 W (shown in Figure 6.25), which occurs with enhancement as the overall amount of light being emitted increases, allowing for detectable upconversion at lower powers.The enhancement factors of between 5 and 10 are in a similar range to many values for plasmon enhancement of upconversion previously reported in the literature (values between 0.2 and 100 reported by Wu et al.[77]). However, previous investigations of UCNP-NS interactions report emission quenching[99,100].

The optimal UCNP-plasmonic nanoparticle distance for plasmonic enhancement using NRs was found to be 7 nm[167], and the NS silica shell thicknesses for these samples were approx. 10 nm. This means that the NSs are at a near-optimal distance from the UCNPs.

The sample which demonstrated this wavelength-dependent enhancement was created using a solution of NSs which was not sufficiently sonicated as to produce an even layer of NSs. Instead, some clusters of silica-shelled NSs were formed. DFM images of one such cluster can be seen in Figure 6.26, at 20x magnification and 100x magnification (inset).
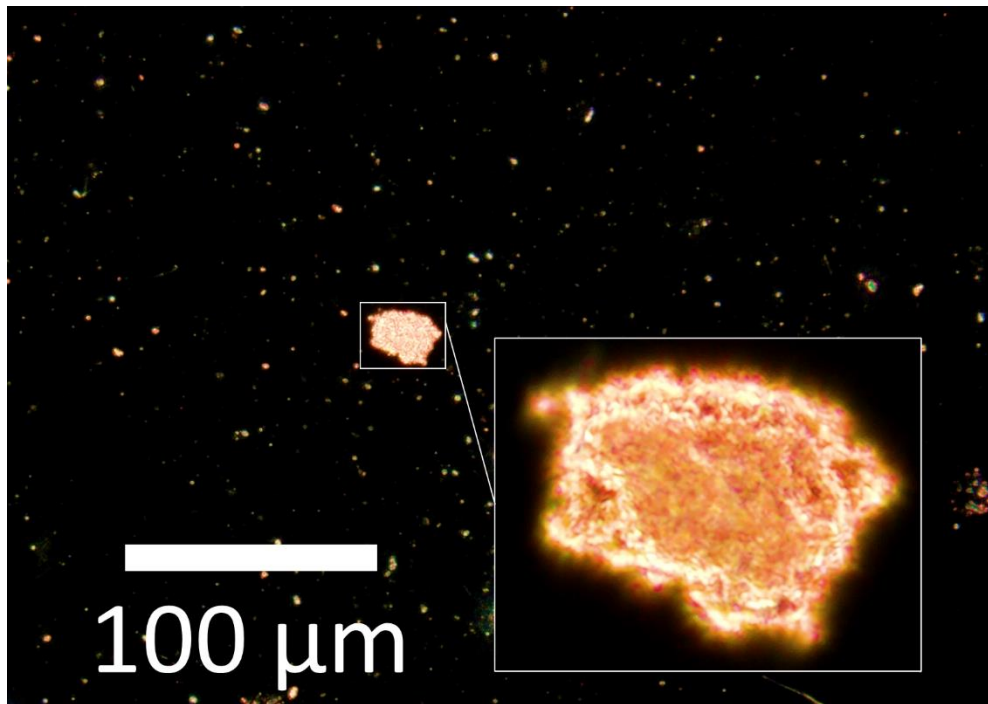
Figure 6.26: DFM image of a spin-coated sample, showing a large cluster of silica-shelled NSs, with the cluster inset at 5x higher magnification to show the scattering of the individual NSs.

Nanoparticles which are very close together experience a redshift and broadening of their plasmon resonance peaks due to plasmon coupling of the particles[176]. Vial *et al.* found that when nanoparticles, specifically NRs in their case, are separated from each other *via* silica shells, the redshift and broadening is reduced, with a stronger reduction as the shell thickness increased. At a shell thickness greater than the NR short axis length, this redshift and broadening is minimised. In this work, silica shells of approx. 10 nm coat each of the NSs, which may have prevented some degree of the redshift and broadening; however, in the case of this work, the redshift of the resonance may be causing increased overall enhancement, as the resonance wavelength moves closer to that of the UCNP excitation wavelength, 980 nm.

The area of the sample which produced the stronger enhancement seen in Figure 6.24(a) and Figure 6.25 featured a cluster of NSs. In Section 6.3.3 of this work, clusters of NRs also gave rise to an increase in upconversion enhancement. Nanoparticle dimers or clusters with small interparticle distances can produce plasmonic hotspots in the nanogaps between the particles. This has been seen using NSs in the literature by Chatterjee *et al.*, who created nanogaps between gold NS tips and gold spheres[169].

It is evident from the above results that the NS clusters, with hotspots between them, have caused stronger enhancement than samples without clusters. While such clusters are difficult to precisely reproduce, even a variable enhancement by larger clusters could be suitable for use in UCNP-enhanced solar cells to increase the UCNP emission, as spin-coating is a facile method

already used to apply UCNPs to solar cells[177]. The enhancement is likely not due to thermoplasmonic effects, as the UCNPs here are ≈ 30 nm, whereas it has previously been shown that thermoplasmonic interactions negatively affect the emission of UCNPs > 20 nm[160].

6.6   Conclusion

This chapter has shown the synthesis of UCNPs, the combination of UCNPs with plasmonic particles on substrates, and the plasmonic enhancement of the UCNPs. $NaYF_4$ UCNPs were successfully synthesised, and the synthesis parameters varied to change the size of the particles, resulting in UCNPs as small as ≈ 5 nm. The particles were synthesised with Yb^{3+} and Er^{3+} or Tm^{3+} dopants, in order to obtain a wide range of visible and infrared emission wavelengths.

Layer-by-layer deposition was carried out, giving samples with a high concentration of UCNPs resulting in an even and consistent UC emission. Plasmonic nanoparticles were also deposited *via* LbL, giving rise to upconversion enhancement for both NRs and BPs, with enhancement of up to 7.5x for BPs. Enhancement of upconversion by BPs has not yet been seen in the literature.

Enhancement of the UC emission was seen in areas on spin-coated samples with very high NS concentrations. This is most likely due to inter-nanoparticle interactions causing plasmonic hotspots. While this can be difficult to precisely reproduce, this enhancement means that there is the potential to use NS clusters to enhance upconversion efficiency for applications such as solar cell efficiency improvement.

7 Conclusion and Future Work

In this thesis, interactions of plasmonic nanoparticles with photoluminescent materials, namely upconverting nanoparticles and quantum dots, were investigated. All objectives set out at the beginning of this work were achieved. Several types of plasmonic nanoparticles were synthesised; nanorods, bipyramids, and nanostars. Their plasmon resonances were tuned over a wavelength range from 600 nm to > 1100 nm, allowing for interactions with absorption and/or emission wavelengths of upconverting nanoparticles and quantum dots. Bipyramids were successfully used to induce two-photon polymerisation for the first time. This allowed for the trapping of quantum dots in the vicinity of the bipyramids, evidenced by a reduction in quantum dot emission lifetime and an increase in emission intensity, as well as the presence of Rabi splitting in the bipyramid scattering spectra. Upconverting nanoparticles of various sizes and dopants were synthesised, and were deposited *via* layer-by-layer deposition and spin-coating. Enhancement of upconverting nanoparticles was shown using nanorods and nanostar clusters, and shown for the first time using bipyramids.

In **Chapter 4**, the synthesis and variation of plasmon resonance wavelengths of three types of gold nanoparticles were explored: nanorods, bipyramids, and nanostars. While the syntheses for the three nanoparticle types are similar, the types of seeds and the concentration of the reagents used gave rise to different particles, with penta-twinned seeds giving rise to bipyramids and nanostars, and monocrystalline seeds giving rise to nanorods. The reagent concentrations within each synthesis have also been extensively varied to tune the plasmonic properties, with both sharp and broad ensemble surface plasmon resonance peaks across a range of wavelengths from 600 nm to above 1100 nm as a result. Additionally, the plasmon resonances of differently shaped nanostars have been modelled, showing the influence of number of tips on the number of plasmon resonances. The impact of seed age on nanorod synthesis have also been explored, with one-month aged seeds found to produce penta-twinned BPs and NSs rather than NRs.

In particular, the effect of varying l-ascorbic acid concentration on bipyramid plasmon resonance wavelength has been explored, with a nonlinear dependence found. At small volumes of l-ascorbic acid, any increase corresponded to a sharp increase in resonance wavelength, whereas at higher volumes, a plateau was seen. This dependence was explained with respect to the interaction of the l-ascorbic acid and chloroauric acid at the two concentration extremes. Such an investigation into this dependence has not been previously performed. Bipyramids with very short

plasmon resonance wavelengths (below 600 nm) were synthesised for the first time. Additionally, bipyramids with long resonance wavelengths (>1000 nm) were synthesised for the first time without using a regrowth step[1,2] or reducing seed concentration[3], but simply by varying AA concentration.

The bipyramids also showed a very small mode volume and high field enhancement, which was advantageous for use in enhancing 2-photon lithography in Chapter 5. The multiresonant nature of the nanostars, as well as the very sharp tips obtained, were considered promising for enhancing upconversion in Chapter 6. Nanostars were also coated in silica shells of thickness ≈10-20 nm, to be used as spacers for this plasmonic enhancement of upconversion.

Chapter 5 demonstrated a novel fabrication method for bipyramid-quantum dot pairs using plasmon-enhanced two-photon polymerisation. The strong field enhancement around the bipyramids gave rise to polymerisation below the typical laser power threshold, at 5% of the typical threshold value. The relationship between polymerisation area around the BPs and applied laser power was found to be linear. The bipyramids enhanced the incoming light, and the volume which was hit by light with sufficient power to polymerise the monomer solution was dependent on the incoming laser power.

Quantum dots added to the monomer solution were successfully included in the polymerised sections after TPL. This allowed quantum dots to be selectively localised around the bipyramids at the area with highest electric field enhancement, as this was the only area which was polymerised. Such a fabrication method has been shown before using nanocubes[25], but has never been carried out using bipyramids. The bipyramids also provided a single plasmonic hotspot at the substrate air interface, allowing for QDs to be localised at one tip, unlike in the case of nanocubes. The QD lifetimes were also reduced in this particle arrangement because they were confined to the plasmonically enhanced regions.

Rabi splitting was also observed in the scattering spectra of the BPs coupled to QDs, indicating the presence of strong coupling. This demonstrates that the QDs are localised in regions of maximum field enhancement, as coupling strength is increased in regions of high electric field strength[17].

Chapter 6 showed the successful synthesis of UCNPs and their enhancement by plasmonic nanoparticles. $NaYF_4$ UCNPs were synthesised with either Yb^{3+} + Er^{3+} or Yb^{3+} + Tm^{3+} dopants, giving a wide range of emission wavelengths from 450-800 nm. The parameters of the syntheses, such as injection speed and reaction volume, were varied in order to obtain UCNP sizes from ≈ 5 nm to ≈ 40 nm.

Samples with even and consistent UC emission were prepared via layer-by-layer deposition of the UCNPs. Spacer layers and plasmonic nanoparticles were also deposited using this method. Upconversion enhancement was seen for bipyramids and nanorods, with bipyramid enhancement of up to 7.5x. UCNP enhancement has not previously been shown in the literature using bipyramids.

In samples prepared *via* spin-coating, samples with very high nanostar concentrations, especially in the case of clusters, gave rise to UC enhancement of up to 9.7x. This enhancement is likely occurring due to plasmonic hotspots between the nanoparticles caused by their interaction. The exact parameters for each sample can be difficult to reproduce, however nanostar clusters can easily be formed in un-sonicated nanostar batches. The enhancement by these clusters could have potential to be used in applications such as solar cell efficiency improvement by UCNPs[4,5], where very small particle sizes are not as necessary as in the case of *in vivo* biological applications[178].

7.1   Future work

The results shown in this thesis give rise to several potential routes of future investigation.

In order to more thoroughly investigate the interaction of UCNPs with individual nanostars, a modification could be made to the silica shelling method. It is likely that using a thiol-terminated shell precursor (such as MPTES), which will strongly bind to the nanostars, could result in a silica shell around the UCNPs which could be easily attached to the nanostars. This could be carried out and the particle interactions observed in solution or after spin-coating on a substrate.

To expand on the UC enhancement seen from the nanostar clusters, electrophoretic deposition (EPD) could be used to create very dense thin films of UCNPs, to ensure that all samples were perfectly even across all scales. These samples could then be spin-coated with nanostars to investigate their enhancement.

For the plasmon-enhanced two-photon lithography system, different sizes of BPs could be investigated, in order to quantify the strong coupling seen[17]. Additionally, the QD concentration in monomer solution could be reduced until there is likely only one QD in the volume of polymer on any BP. This could potentially create a single photon emitter, and autocorrelation studies could be carried out to confirm this[25]. As the two-photon system is optimised for bipyramid resonances in the 600-800nm range, upconverting nanoparticles could also be confined in the ideal enhanced region using this method, and potentially emission from UCNPs at 655 nm (Er^{3+}-doped) or 800 nm (Tm^{3+}-doped) could be enhanced.

8 Bibliography

(1)   Lee, J.-H.; Gibson, K. J.; Chen, G.; Weizmann, Y. Bipyramid-Templated Synthesis of Monodisperse Anisotropic Gold Nanocrystals. *Nat. Commun.* **2015**, *6*, 7571. https://doi.org/10.1038/ncomms8571.

(2)   Chateau, D.; Desert, A.; Lerouge, F.; Landaburu, G.; Santucci, S.; Parola, S. Beyond the Concentration Limitation in the Synthesis of Nanobipyramids and Other Pentatwinned Gold Nanostructures. *ACS Appl. Mater. Interfaces* **2019**, *11* (42), 39068–39076. https://doi.org/10.1021/acsami.9b12973.

(3)   Kou, X.; Zhang, S.; Tsung, C.-K.; Yeung, M. H.; Shi, Q.; Stucky, G. D.; Sun, L.; Wang, J.; Yan, C. Growth of Gold Nanorods and Bipyramids Using CTEAB Surfactant. *J. Phys. Chem. B* **2006**, *110* (33), 16377–16383. https://doi.org/10.1021/jp0639086.

(4)   Goldschmidt, J. C.; Fischer, S. Upconversion for Photovoltaics – a Review of Materials, Devices and Concepts for Performance Enhancement. *Adv. Opt. Mater.* **2015**, *3* (4), 510–535. https://doi.org/10.1002/adom.201500024.

(5)   Ende, B. M. van der; Aarts, L.; Meijerink, A. Lanthanide Ions as Spectral Converters for Solar Cells. *Phys. Chem. Chem. Phys.* **2009**, *11* (47), 11081–11095. https://doi.org/10.1039/B913877C.

(6)   Helden, A. V. *The Origins of the Telescope*; KNAW Press, 2010.

(7)   *Light - Particle, Wave, Theories | Britannica*. https://www.britannica.com/science/light/Early-particle-and-wave-theories (accessed 2023-12-27).

(8)   Zghal, M.; Bouali, H.-E.; Lakhdar, Z. B.; Hamam, H. The First Steps for Learning Optics: Ibn Sahl's, Al-Haytham's and Young's Works on Refraction as Typical Examples. In *Education and Training in Optics and Photonics (2007), paper ESB2*; Optica Publishing Group, 2007; p ESB2. https://doi.org/10.1364/ETOP.2007.ESB2.

(9)   Sabra, A. I. *Theories of Light: From Descartes to Newton*; CUP Archive, 1981.

(10)   Young, T. I. The Bakerian Lecture. Experiments and Calculations Relative to Physical Optics. *Philos. Trans. R. Soc. Lond.* **1997**, *94*, 1–16. https://doi.org/10.1098/rstl.1804.0001.

(11)   Maxwell, J. C. VIII. A Dynamical Theory of the Electromagnetic Field. *Philos. Trans. R. Soc. Lond.* **1865**, *155*, 459–512. https://doi.org/10.1098/rstl.1865.0008.

(12)   Radio Transmission. In *The Worldwide History of Telecommunications*; John Wiley & Sons, Ltd, 2003; pp 199–216. https://doi.org/10.1002/0471722243.ch12.

(13)   *The Collected Papers of Albert Einstein, Volume 3 (English)*; 1994.

(14)   Feynman, R. P. Plenty of Room at the Bottom. **1959**.

(15)   *Nanomaterials Handbook*; Gogotsi, Y., Ed.; CRC Press: Boca Raton, 2006. https://doi.org/10.1201/9781420004014.

(16)   Gao, E.; Lin, S.-Z.; Qin, Z.; Buehler, M. J.; Feng, X.-Q.; Xu, Z. Mechanical Exfoliation of Two-Dimensional Materials. *J. Mech. Phys. Solids* **2018**, *115*, 248–262. https://doi.org/10.1016/j.jmps.2018.03.014.

(17)   Lawless, J.; Hrelescu, C.; Elliott, C.; Peters, L.; McEvoy, N.; Bradley, A. L. Influence of Gold Nano-Bipyramid Dimensions on Strong Coupling with Excitons of Monolayer MoS2. *ACS Appl. Mater. Interfaces* **2020**, *12* (41), 46406–46415. https://doi.org/10.1021/acsami.0c09261.

(18)   Bayda, S.; Adeel, M.; Tuccinardi, T.; Cordani, M.; Rizzolio, F. The History of Nanoscience and Nanotechnology: From Chemical–Physical Applications to Nanomedicine. *Molecules* **2019**, *25* (1), 112. https://doi.org/10.3390/molecules25010112.

(19)   Freestone, I.; Meeks, N.; Sax, M.; Higgitt, C. The Lycurgus Cup — A Roman Nanotechnology. *Gold Bull.* **2007**, *40* (4), 270–277. https://doi.org/10.1007/BF03215599.

(20)   *X. The Bakerian Lecture. —Experimental relations of gold (and other metals) to light*. https://doi.org/10.1098/rstl.1857.0011.

(21)   Turkevich, J.; Garton, G.; Stevenson, P. C. The Color of Colloidal Gold. *J. Colloid Sci.* **1954**, *9*, 26–35. https://doi.org/10.1016/0095-8522(54)90070-7.

(22)   Cunningham, S.; Hrelescu, C.; Bradley, A. L. Plasmonic Nanodiscs on Vanadium Dioxide Thin Films for Tunable Luminescence Enhancement. *Opt. Express* **2021**, *29* (14), 22288. https://doi.org/10.1364/OE.434135.

(23)   Zhan, C.; Wang, G.; Yi, J.; Wei, J.-Y.; Li, Z.-H.; Chen, Z.-B.; Shi, J.; Yang, Y.; Hong, W.; Tian, Z.-Q. Single-Molecule Plasmonic Optical Trapping. *Matter* **2020**, *3* (4), 1350–1360. https://doi.org/10.1016/j.matt.2020.07.019.

(24)   Jandt, K. D.; Mills, R. W. A Brief History of LED Photopolymerization. *Dent. Mater.* **2013**, *29* (6), 605–617. https://doi.org/10.1016/j.dental.2013.02.003.

(25)   Ge, D.; Marguet, S.; Issa, A.; Jradi, S.; Nguyen, H.; Nahra, M.; Béal, J.; Deturche, R.; Chen, H.; Blaize, S.; Plain, J.; Fiorini, C.; Douillard, L.; Soppera, O.; Dinh, X. Q.; Dang, C.; Yang, X.; Xu, T.; Wei, B.; Bachelot, R. Hybrid Plasmonic Nano-Emitters with Controlled Single Quantum Emitter Positioning on the Local Excitation Field. *Nat. Commun.* **2020**, *11*. https://doi.org/10.1038/s41467-020-17248-8.

(26)   McDonald, S. A.; Konstantatos, G.; Zhang, S.; Cyr, P. W.; Klem, E. J. D.; Levina, L.; Sargent, E. H. Solution-Processed PbS Quantum Dot Infrared Photodetectors and Photovoltaics. *Nat. Mater.* **2005**, *4* (2), 138–142. https://doi.org/10.1038/nmat1299.

(27)   Royce, M. R. Rare Earth Activated Yttrium and Gadolinium Oxy-Chalcogenide Phosphors. US3418246A, December 24, 1968.

(28)   Levine, A. K.; Palilla, F. C. A NEW, HIGHLY EFFICIENT RED-EMITTING CATHODOLUMINESCENT PHOSPHOR (YVO4:Eu) FOR COLOR TELEVISION. *Appl. Phys. Lett.* **1964**, *5* (6), 118–120. https://doi.org/10.1063/1.1723611.

(29)   Desurvire, E. The Golden Age of Optical Fiber Amplifiers. *Phys. Today* **1994**, *47* (1), 20–27. https://doi.org/10.1063/1.881418.

(30)   McArthur, D. A. Lasers, Nuclear Pumped. In *Encyclopedia of Physical Science and Technology (Third Edition)*; Meyers, R. A., Ed.; Academic Press: New York, 2003; pp 409–417. https://doi.org/10.1016/B0-12-227410-5/00369-0.

(31)   *Rare Earth Doped Fibers | Coherent*. https://www.coherent.com/news/blog/rare-earth-doped-fibers (accessed 2023-12-28).

(32)   Werts, M. H. V. Making Sense of Lanthanide Luminescence. *Sci. Prog.* **2005**, *88* (2), 101–131. https://doi.org/10.3184/003685005783238435.

(33)   Wilhelm, S. Perspectives for Upconverting Nanoparticles. *ACS Nano* **2017**, *11* (11), 10644–10653. https://doi.org/10.1021/acsnano.7b07120.

(34)   Dühnen, S.; Haase, M. Study on the Intermixing of Core and Shell in NaEuF4/NaGdF4 Core/Shell Nanocrystals. *Chem. Mater.* **2015**, *27* (24), 8375–8386. https://doi.org/10.1021/acs.chemmater.5b03846.

(35)   Boyer, J.-C.; Veggel, F. C. J. M. van. Absolute Quantum Yield Measurements of Colloidal NaYF 4 : Er3+ , Yb3+ Upconverting Nanoparticles. *Nanoscale* **2010**, *2* (8), 1417–1419. https://doi.org/10.1039/C0NR00253D.

(36)   Li, D.; Ågren, H.; Chen, G. Near Infrared Harvesting Dye-Sensitized Solar Cells Enabled by Rare-Earth Upconversion Materials. *Dalton Trans.* **2018**, *47* (26), 8526–8537. https://doi.org/10.1039/C7DT04461E.

(37)   van Sark, W. G.; de Wild, J.; Rath, J. K.; Meijerink, A.; Schropp, R. E. Upconversion in Solar Cells. *Nanoscale Res. Lett.* **2013**, *8* (1), 81. https://doi.org/10.1186/1556-276X-8-81.

(38)   Chen, T.; Shang, Y.; Hao, S.; Tian, L.; Hou, Y.; Yang, C. Enhancement of Dye Sensitized Solar Cell Efficiency through Introducing Concurrent Upconversion/Downconversion Core/Shell Nanoparticles as Spectral Converters. *Electrochimica Acta* **2018**, *282*, 743–749. https://doi.org/10.1016/j.electacta.2018.06.111.

(39)   Chen, F.; Zhang, S.; Bu, W.; Chen, Y.; Xiao, Q.; Liu, J.; Xing, H.; Zhou, L.; Peng, W.; Shi, J. A Uniform Sub-50 Nm-Sized Magnetic/Upconversion Fluorescent Bimodal Imaging Agent Capable of Generating Singlet Oxygen by Using a 980 Nm Laser. *Chem. – Eur. J.* **2012**, *18* (23), 7082–7090. https://doi.org/10.1002/chem.201103611.

(40)   Liu, J.; Bu, W.; Pan, L.; Shi, J. NIR-Triggered Anticancer Drug Delivery by Upconverting Nanoparticles with Integrated Azobenzene-Modified Mesoporous Silica. *Angew. Chem. Int. Ed.* **2013**, *52* (16), 4375–4379. https://doi.org/10.1002/anie.201300183.

(41)   Zou, W.; Visser, C.; Maduro, J. A.; Pshenichnikov, M. S.; Hummelen, J. C. Broadband Dye-Sensitized Upconversion of near-Infrared Light. *Nat. Photonics* **2012**, *6* (8), 560–564. https://doi.org/10.1038/nphoton.2012.158.

(42)   Huang, X. Broadband Dye-Sensitized Upconversion: A Promising New Platform for Future Solar Upconverter Design. *J. Alloys Compd.* **2017**, *690*, 356–359. https://doi.org/10.1016/j.jallcom.2016.08.142.

(43)   Li, X.; Wang, R.; Zhang, F.; Zhao, D. Engineering Homogeneous Doping in Single Nanoparticle To Enhance Upconversion Efficiency. *Nano Lett.* **2014**, *14* (6), 3634–3639. https://doi.org/10.1021/nl501366x.

(44)   Vetrone, F.; Naccache, R.; Mahalingam, V.; Morgan, C. G.; Capobianco, J. A. The Active-Core/Active-Shell Approach: A Strategy to Enhance the Upconversion Luminescence in Lanthanide-Doped Nanoparticles. *Adv. Funct. Mater.* **2009**, *19* (18), 2924–2929. https://doi.org/10.1002/adfm.200900234.

(45)   Han, S.; Deng, R.; Xie, X.; Liu, X. Enhancing Luminescence in Lanthanide-Doped Upconversion Nanoparticles. *Angew. Chem. Int. Ed.* **2014**, *53* (44), 11702–11715. https://doi.org/10.1002/anie.201403408.

128

(46)   You, E.-A.; Zhou, W.; Suh, J. Y.; Huntington, M. D.; Odom, T. W. Polarization-Dependent Multipolar Plasmon Resonances in Anisotropic Multiscale Au Particles. *ACS Nano* **2012**, *6* (2), 1786–1794. https://doi.org/10.1021/nn204845z.

(47)   Rodrigo, S. G.; García-Vidal, F. J.; Martín-Moreno, L. Influence of Material Properties on Extraordinary Optical Transmission through Hole Arrays. *Phys. Rev. B* **2008**, *77* (7), 075401. https://doi.org/10.1103/PhysRevB.77.075401.

(48)   Mcmahon, M. D.; Lopez, R.; Meyer, H. M.; Feldman, L. C.; Haglund, R. F. Rapid Tarnishing of Silver Nanoparticles in Ambient Laboratory Air. *Appl. Phys. B* **2005**, *80* (7), 915–921. https://doi.org/10.1007/s00340-005-1793-6.

(49)   Maier, S. A. *Plasmonics: Fundamentals and Applications*; Springer US: New York, NY, 2007. https://doi.org/10.1007/0-387-37825-1.

(50)   Mie, G. Beiträge Zur Optik Trüber Medien, Speziell Kolloidaler Metallösungen. *Ann. Phys.* **1908**, *330* (3), 377–445. https://doi.org/10.1002/andp.19083300302.

(51)   Fan, X.; Zheng, W.; Singh, D. J. Light Scattering and Surface Plasmons on Small Spherical Particles. *Light Sci. Appl.* **2014**, *3* (6), e179–e179. https://doi.org/10.1038/lsa.2014.60.

(52)   Jain, P. K.; Lee, K. S.; El-Sayed, I. H.; El-Sayed, M. A. Calculated Absorption and Scattering Properties of Gold Nanoparticles of Different Size, Shape, and Composition: Applications in Biological Imaging and Biomedicine. *J. Phys. Chem. B* **2006**, *110* (14), 7238–7248. https://doi.org/10.1021/jp057170o.

(53)   Bohren, C. F.; Huffman, D. R. *Absorption and Scattering of Light by Small Particles*; John Wiley & Sons, Chichester, West Sussex, 2008.

(54)   Evanoff, D. D.; Chumanov, G. Size-Controlled Synthesis of Nanoparticles. 2. Measurement of Extinction, Scattering, and Absorption Cross Sections. *J. Phys. Chem. B* **2004**, *108* (37), 13957–13962. https://doi.org/10.1021/jp0475640.

(55)   Gersten, J.; Nitzan, A. Electromagnetic Theory of Enhanced Raman Scattering by Molecules Adsorbed on Rough Surfaces. *J. Chem. Phys.* **1980**, *73* (7), 3023–3037. https://doi.org/10.1063/1.440560.

(56)   Liu, M.; Guyot-Sionnest, P. Mechanism of Silver(I)-Assisted Growth of Gold Nanorods and Bipyramids. *J. Phys. Chem. B* **2005**, *109* (47), 22192–22200. https://doi.org/10.1021/jp054808n.

(57)   Hrelescu, C.; Sau, T. K.; Rogach, A. L.; Jäckel, F.; Feldmann, J. Single Gold Nanostars Enhance Raman Scattering. *Appl. Phys. Lett.* **2009**, *94* (15), 153113. https://doi.org/10.1063/1.3119642.

(58)   Frenkel, J. On the Transformation of Light into Heat in Solids. I. *Phys. Rev.* **1931**, *37* (1), 17–44. https://doi.org/10.1103/PhysRev.37.17.

(59)   Bitton, O.; Gupta, S. N.; Haran, G. Quantum Dot Plasmonics: From Weak to Strong Coupling. *Nanophotonics* **2019**, *8* (4), 559–575. https://doi.org/10.1515/nanoph-2018-0218.

(60)   Rossetti, R.; Ellison, J. L.; Gibson, J. M.; Brus, L. E. Size Effects in the Excited Electronic States of Small Colloidal CdS Crystallites. *J. Chem. Phys.* **1984**, *80* (9), 4464–4469. https://doi.org/10.1063/1.447228.

(61)   Efros, Al. L.; Rosen, M. The Electronic Structure of Semiconductor Nanocrystals. *Annu. Rev. Mater. Sci.* **2000**, *30* (1), 475–521. https://doi.org/10.1146/annurev.matsci.30.1.475.

(62)   Purcell, E. M. Spontaneous Emission Probabilities at Radio Frequencies. In *Confined Electrons and Photons: New Physics and Applications*; Burstein, E., Weisbuch, C., Eds.; NATO ASI Series; Springer US: Boston, MA, 1995; pp 839–839. https://doi.org/10.1007/978-1-4615-1963-8_40.

(63)   Cao, E.; Lin, W.; Sun, M.; Liang, W.; Song, Y. Exciton-Plasmon Coupling Interactions: From Principle to Applications. *Nanophotonics* **2018**, *7* (1), 145–167. https://doi.org/10.1515/nanoph-2017-0059.

(64)   Wang, B.; Zeng, X.-Z.; Li, Z.-Y. Quantum versus Optical Interaction Contribution to Giant Spectral Splitting in a Strongly Coupled Plasmon–Molecules System. *Photonics Res.* **2020**, *8* (3), 343–351. https://doi.org/10.1364/PRJ.375135.

(65)   Göppert-Mayer, M. Über Elementarakte Mit Zwei Quantensprüngen. *Ann. Phys.* **1931**, *401* (3), 273–294. https://doi.org/10.1002/andp.19314010303.

(66)   Kaiser, W.; Garrett, C. G. B. Two-Photon Excitation in Ca F 2 : Eu 2 +. *Phys. Rev. Lett.* **1961**, *7* (6), 229–231. https://doi.org/10.1103/PhysRevLett.7.229.

(67)   Sheik-Bahae, M.; Hasselbeck, M. P. THIRD-ORDER OPTICAL NONLINEARITIES. In *Handbook of Optics: Volume IV - Optical Properties of Materials, Nonlinear Optics, Quantum Optics*; Bass, M., Ed.; McGraw-Hill Education, 2010.

(68)   Boyd, R. W. Chapter 1 - The Nonlinear Optical Susceptibility. In *Nonlinear Optics (Fourth Edition)*; Boyd, R. W., Ed.; Academic Press, 2020; pp 1–64. https://doi.org/10.1016/B978-0-12-811002-7.00010-2.

(69)   Zhao, Y.; Iftimia, N. V. 13 - Overview of Supercontinuum Sources for Multiphoton Microscopy and Optical Biopsy. In *Neurophotonics and Biomedical Spectroscopy*; Alfano, R. R., Shi, L., Eds.; Nanophotonics; Elsevier, 2019; pp 329–351. https://doi.org/10.1016/B978-0-323-48067-3.00013-5.

(70)   Kamali, T.; Farrell, S. R.; Baldridge, W. H.; Fischer, J.; Chauhan, B. C. Two-Photon Scanning Laser Ophthalmoscope. In *High Resolution Imaging in Microscopy and Ophthalmology: New Frontiers in Biomedical Optics*; Bille, J. F., Ed.; Springer: Cham (CH), 2019.

(71)   Eibel, A.; E. Fast, D.; Gescheidt, G. Choosing the Ideal Photoinitiator for Free Radical Photopolymerizations: Predictions Based on Simulations Using Established Data. *Polym. Chem.* **2018**, *9* (41), 5107–5115. https://doi.org/10.1039/C8PY01195H.

(72)   Yang, N.-C.; Feit, E. D.; Hui, M. H.; Turro, N. J.; Dalton, J. C. Photochemistry of Di-Tert-Butyl Ketone and Structural Effects on the Rate and Efficiency of Intersystem Crossing of Aliphatic Ketones. *J. Am. Chem. Soc.* **1970**, *92* (23), 6974–6976. https://doi.org/10.1021/ja00726a046.

(73)   Chemistry (IUPAC), T. I. U. of P. and A. *IUPAC - Norrish Type I photoreaction (N04219)*. https://doi.org/10.1351/goldbook.N04219.

(74)   Petko, F.; Świeży, A.; Ortyl, J. Photoinitiating Systems and Kinetics of Frontal Photopolymerization Processes – the Prospects for Efficient Preparation of Composites and Thick 3D Structures. *Polym. Chem.* **2021**, *12* (32), 4593–4612. https://doi.org/10.1039/D1PY00596K.

(75)   Kawata, S.; Sun, H.-B.; Tanaka, T.; Takada, K. Finer Features for Functional Microdevices. *Nature* **2001**, *412* (6848), 697–698. https://doi.org/10.1038/35089130.

(76)   Harinarayana, V.; Shin, Y. C. Two-Photon Lithography for Three-Dimensional Fabrication in Micro/Nanoscale Regime: A Comprehensive Review. *Opt. Laser Technol.* **2021**, *142*, 107180. https://doi.org/10.1016/j.optlastec.2021.107180.

(77)   Wu, D. M.; García-Etxarri, A.; Salleo, A.; Dionne, J. A. Plasmon-Enhanced Upconversion. *J. Phys. Chem. Lett.* **2014**, *5* (22), 4020–4031. https://doi.org/10.1021/jz5019042.

(78)   Zhou, J.; Sun, Y.; Du, X.; Xiong, L.; Hu, H.; Li, F. Dual-Modality in Vivo Imaging Using Rare-Earth Nanocrystals with near-Infrared to near-Infrared (NIR-to-NIR) Upconversion Luminescence and Magnetic Resonance Properties. *Biomaterials* **2010**, *31* (12), 3287–3295. https://doi.org/10.1016/j.biomaterials.2010.01.040.

(79)   Kong, J.; Shang, X.; Zheng, W.; Chen, X.; Tu, D.; Wang, M.; Song, J.; Qu, J. Revisiting the Luminescence Decay Kinetics of Energy Transfer Upconversion. *J. Phys. Chem. Lett.* **2020**, *11* (9), 3672–3680. https://doi.org/10.1021/acs.jpclett.0c00619.

(80)   Suyver, J. F.; Aebischer, A.; García-Revilla, S.; Gerner, P.; Güdel, H. U. Anomalous Power Dependence of Sensitized Upconversion Luminescence. *Phys. Rev. B* **2005**, *71* (12), 125123. https://doi.org/10.1103/PhysRevB.71.125123.

(81)   Verhoeven, J. W. Glossary of Terms Used in Photochemistry (IUPAC Recommendations 1996). *Pure Appl. Chem.* **1996**, *68* (12), 2223–2286. https://doi.org/10.1351/pac199668122223.

(82)   Wen, S.; Zhou, J.; Zheng, K.; Bednarkiewicz, A.; Liu, X.; Jin, D. Advances in Highly Doped Upconversion Nanoparticles. *Nat. Commun.* **2018**, *9* (1), 2415. https://doi.org/10.1038/s41467-018-04813-5.

(83)   Dejneka, M. J.; Streltsov, A.; Pal, S.; Frutos, A. G.; Powell, C. L.; Yost, K.; Yuen, P. K.; Müller, U.; Lahiri, J. Rare Earth-Doped Glass Microbarcodes. *Proc. Natl. Acad. Sci.* **2003**, *100* (2), 389–393. https://doi.org/10.1073/pnas.0236044100.

(84)   Krämer, K. W.; Biner, D.; Frei, G.; Güdel, H. U.; Hehlen, M. P.; Lüthi, S. R. Hexagonal Sodium Yttrium Fluoride Based Green and Blue Emitting Upconversion Phosphors. *Chem. Mater.* **2004**, *16* (7), 1244–1251. https://doi.org/10.1021/cm031124o.

(85)   Chen, G. Y.; Liu, Y.; Zhang, Y. G.; Somesfalean, G.; Zhang, Z. G.; Sun, Q.; Wang, F. P. Bright White Upconversion Luminescence in Rare-Earth-Ion-Doped Y2O3 Nanocrystals. *Appl. Phys. Lett.* **2007**, *91* (13), 133103. https://doi.org/10.1063/1.2787893.

(86)   Chen, G.; Somesfalean, G.; Liu, Y.; Zhang, Z.; Sun, Q.; Wang, F. Upconversion Mechanism for Two-Color Emission in Rare-Earth-Ion-Doped ZrO2 Nanocrystals. *Phys. Rev. B* **2007**, *75* (19), 195204. https://doi.org/10.1103/PhysRevB.75.195204.

(87)   Dong, A.; Ye, X.; Chen, J.; Kang, Y.; Gordon, T.; Kikkawa, J. M.; Murray, C. B. A Generalized Ligand-Exchange Strategy Enabling Sequential Surface Functionalization of Colloidal Nanocrystals. *J. Am. Chem. Soc.* **2011**, *133* (4), 998–1006. https://doi.org/10.1021/ja108948z.

(88)   Wilhelm, S.; Kaiser, M.; Würth, C.; Heiland, J.; Carrillo-Carrion, C.; Muhr, V.; S. Wolfbeis, O.; J. Parak, W.; Resch-Genger, U.; Hirsch, T. Water Dispersible Upconverting Nanoparticles: Effects of Surface Modification on Their Luminescence and Colloidal Stability. *Nanoscale* **2015**, *7* (4), 1403–1410. https://doi.org/10.1039/C4NR05954A.

(89)   Wu, S.; Han, G.; Milliron, D. J.; Aloni, S.; Altoe, V.; Talapin, D. V.; Cohen, B. E.; Schuck, P. J. Non-Blinking and Photostable Upconverted Luminescence from Single Lanthanide-Doped

Nanocrystals. *Proc. Natl. Acad. Sci.* **2009**, *106* (27), 10917–10921. https://doi.org/10.1073/pnas.0904792106.

(90)   Zijlmans, H. J. M. A. A.; Bonnet, J.; Burton, J.; Kardos, K.; Vail, T.; Niedbala, R. S.; Tanke, H. J. Detection of Cell and Tissue Surface Antigens Using Up-Converting Phosphors: A New Reporter Technology. *Anal. Biochem.* **1999**, *267* (1), 30–36. https://doi.org/10.1006/abio.1998.2965.

(91)   Andresen, E.; Islam, F.; Prinz, C.; Gehrmann, P.; Licha, K.; Roik, J.; Recknagel, S.; Resch-Genger, U. Assessing the Reproducibility and Up-Scaling of the Synthesis of Er,Yb-Doped NaYF4-Based Upconverting Nanoparticles and Control of Size, Morphology, and Optical Properties. *Sci. Rep.* **2023**, *13*, 2288. https://doi.org/10.1038/s41598-023-28875-8.

(92)   Wu, Q.; Huang, B.; Peng, X.; He, S.; Zhan, Q. Non-Bleaching Fluorescence Emission Difference Microscopy Using Single 808-Nm Laser Excited Red Upconversion Emission. *Opt. Express* **2017**, *25* (25), 30885. https://doi.org/10.1364/OE.25.030885.

(93)   Wang, F.; Han, Y.; Lim, C. S.; Lu, Y.; Wang, J.; Xu, J.; Chen, H.; Zhang, C.; Hong, M.; Liu, X. Simultaneous Phase and Size Control of Upconversion Nanocrystals through Lanthanide Doping. *Nature* **2010**, *463* (7284), 1061–1065. https://doi.org/10.1038/nature08777.

(94)   Wang, F.; Wang, J.; Liu, X. Direct Evidence of a Surface Quenching Effect on Size-Dependent Luminescence of Upconversion Nanoparticles. *Angew. Chem. Int. Ed.* **2010**, *49* (41), 7456–7460. https://doi.org/10.1002/anie.201003959.

(95)   Dibaba, S. T.; Xiaoqian Ge; Ren, W.; Sun, L. Recent Progress of Energy Transfer and Luminescence Intensity Boosting Mechanism in Nd3+-Sensitized Upconversion Nanoparticles. *J. Rare Earths* **2019**, *37* (8), 791–805. https://doi.org/10.1016/j.jre.2019.02.001.

(96)   Feng, W.; Sun, L.-D.; Yan, C.-H. Ag Nanowires Enhanced Upconversion Emission of NaYF4:Yb,Er Nanocrystalsvia a Direct Assembly Method. *Chem. Commun.* **2009**, *0* (29), 4393–4395. https://doi.org/10.1039/B909164E.

(97)   Schietinger, S.; Aichele, T.; Wang, H.-Q.; Nann, T.; Benson, O. Plasmon-Enhanced Upconversion in Single NaYF4:Yb3+/Er3+ Codoped Nanocrystals. *Nano Lett.* **2010**, *10* (1), 134–138. https://doi.org/10.1021/nl903046r.

(98)   He, J.; Zheng, W.; Ligmajer, F.; Chan, C.-F.; Bao, Z.; Wong, K.-L.; Chen, X.; Hao, J.; Dai, J.; Yu, S.-F.; Lei, D. Y. Plasmonic Enhancement and Polarization Dependence of Nonlinear Upconversion Emissions from Single Gold nanorod@SiO$_2$@CaF$_2$:Yb^{3+},Er^{3+} Hybrid Core–Shell–Satellite Nanostructures. *Light Sci. Appl.* **2017**, *6* (5), e16217. https://doi.org/10.1038/lsa.2016.217.

(99)   He, L.; Dragavon, J.; Cho, S.; Mao, C.; Yildirim, A.; Ma, K.; Chattaraj, R.; Goodwin, A. P.; Park, W.; Cha, J. N. Self-Assembled Gold Nanostar–NaYF4:Yb/Er Clusters for Multimodal Imaging, Photothermal and Photodynamic Therapy. *J. Mater. Chem. B* **2016**, *4* (25), 4455–4461. https://doi.org/10.1039/C6TB00914J.

(100)   He, L.; Mao, C.; Cho, S.; Ma, K.; Xi, W.; Bowman, C. N.; Park, W.; Cha, J. N. Experimental and Theoretical Photoluminescence Studies in Nucleic Acid Assembled Gold-Upconverting Nanoparticle Clusters. *Nanoscale* **2015**, *7* (41), 17254–17260. https://doi.org/10.1039/C5NR05035A.

(101)   Wang, F.; Deng, R.; Liu, X. Preparation of Core-Shell NaGdF4 Nanoparticles Doped with Luminescent Lanthanide Ions to Be Used as Upconversion-Based Probes. *Nat. Protoc.* **2014**, *9* (7), 1634–1644. https://doi.org/10.1038/nprot.2014.111.

(102)   Wisser, M. D.; Fischer, S.; Siefe, C.; Alivisatos, A. P.; Salleo, A.; Dionne, J. A. Improving Quantum Yield of Upconverting Nanoparticles in Aqueous Media via Emission Sensitization. *Nano Lett.* **2018**, *18* (4), 2689–2695. https://doi.org/10.1021/acs.nanolett.8b00634.

(103)   Huang, Y.; Hemmer, E.; Rosei, F.; Vetrone, F. Multifunctional Liposome Nanocarriers Combining Upconverting Nanoparticles and Anticancer Drugs. *J. Phys. Chem. B* **2016**, *120* (22), 4992–5001. https://doi.org/10.1021/acs.jpcb.6b02013.

(104)   Zhang, H.; Li, Y.; Ivanov, I. A.; Qu, Y.; Huang, Y.; Duan, X. Plasmonic Modulation of the Upconversion Fluorescence in NaYF4:Yb/Tm Hexaplate Nanocrystals Using Gold Nanoparticles or Nanoshells. *Angew. Chem. Int. Ed.* **2010**, *49* (16), 2865–2868. https://doi.org/10.1002/anie.200905805.

(105)   Sigma Aldrich. *Material Safety Data Sheet for Sodium Borohydride*. https://www.sigmaaldrich.com/deepweb/assets/sigmaaldrich/product/documents/248/707/s9125pis.pdf (accessed 2023-10-12).

(106)   Wagner, B. A.; Buettner, G. R. Stability of Aqueous Solutions of Ascorbate for Basic Research and for Intravenous Administration. *Adv. Redox Res.* **2023**, *9*, 100077. https://doi.org/10.1016/j.arres.2023.100077.

(107)   Sigma-Aldrich. *Material Safety Data Sheet for Silver Nitrate, 209139*. https://www.sigmaaldrich.com/IE/en/sds/sigald/209139.

(108)   Nikoobakht, B.; El-Sayed, M. A. Preparation and Growth Mechanism of Gold Nanorods (NRs) Using Seed-Mediated Growth Method. *Chem. Mater.* **2003**, *15* (10), 1957–1962. https://doi.org/10.1021/cm020732l.

(109)   Sau, T. K.; Murphy, C. J. Seeded High Yield Synthesis of Short Au Nanorods in Aqueous Solution. *Langmuir* **2004**, *20* (15), 6414–6420. https://doi.org/10.1021/la049463z.

(110)   Zweifel, D. A.; Wei, A. Sulfide-Arrested Growth of Gold Nanorods. *Chem. Mater.* **2005**, *17* (16), 4256–4261. https://doi.org/10.1021/cm0506858.

(111)   Jana, N. R.; Gearheart, L.; Murphy, C. J. Wet Chemical Synthesis of High Aspect Ratio Cylindrical Gold Nanorods. *J. Phys. Chem. B* **2001**, *105* (19), 4065–4067. https://doi.org/10.1021/jp0107964.

(112)   Burgin, J.; Liu, M.; Guyot-Sionnest, P. Dielectric Sensing with Deposited Gold Bipyramids. *J. Phys. Chem. C* **2008**, *112* (49), 19279–19282. https://doi.org/10.1021/jp807465p.

(113)   Johnson, C. J.; Dujardin, E.; Davis, S. A.; Murphy, C. J.; Mann, S. Growth and Form of Gold Nanorods Prepared by Seed-Mediated, Surfactant-Directed Synthesis. *J. Mater. Chem.* **2002**, *12* (6), 1765–1770. https://doi.org/10.1039/B200953F.

(114)   Herrero, E.; Buller, L. J.; Abruña, H. D. Underpotential Deposition at Single Crystal Surfaces of Au, Pt, Ag and Other Materials. *Chem. Rev.* **2001**, *101* (7), 1897–1930. https://doi.org/10.1021/cr9600363.

(115)   Kolb, D. M.; Przasnyski, M.; Gerischer, H. Underpotential Deposition of Metals and Work Function Differences. *J. Electroanal. Chem. Interfacial Electrochem.* **1974**, *54* (1), 25–38. https://doi.org/10.1016/S0022-0728(74)80377-3.

(116)   Fales, A. M.; Yuan, H.; Vo-Dinh, T. Development of Hybrid Silver-Coated Gold Nanostars for Nonaggregated Surface-Enhanced Raman Scattering. *J. Phys. Chem. C* **2014**, *118* (7), 3708–3715. https://doi.org/10.1021/jp4091393.

(117)   Munkhbat, B.; Ziegler, J.; Pöhl, H.; Wörister, C.; Sivun, D.; Scharber, M. C.; Klar, T. A.; Hrelescu, C. Hybrid Multilayered Plasmonic Nanostars for Coherent Random Lasing. *J. Phys. Chem. C* **2016**, *120* (41), 23707–23715. https://doi.org/10.1021/acs.jpcc.6b05737.

(118)   Decher, G.; Hong, J.-D. Buildup of Ultrathin Multilayer Films by a Self-Assembly Process, 1 Consecutive Adsorption of Anionic and Cationic Bipolar Amphiphiles on Charged Surfaces. *Makromol. Chem. Macromol. Symp.* **1991**, *46* (1), 321–327. https://doi.org/10.1002/masy.19910460145.

(119)   Zhang, X. Localised Surface Plasmon Mediated Energy Transfer in Quantum Dot Systems, Trinity College Dublin, 2015.

(120) *Understanding Mesh Refinement and Conformal Mesh in FDTD*. Ansys Optics. https://optics.ansys.com/hc/en-us/articles/360034382594-Understanding-Mesh-Refinement-and-Conformal-Mesh-in-FDTD (accessed 2023-09-08).

(121) Kane Yee. Numerical Solution of Initial Boundary Value Problems Involving Maxwell's Equations in Isotropic Media. *IEEE Trans. Antennas Propag.* **1966**, *14* (3), 302–307. https://doi.org/10.1109/TAP.1966.1138693.

(122) Taflove, A.; Brodwin, M. E. Numerical Solution of Steady-State Electromagnetic Scattering Problems Using the Time-Dependent Maxwell's Equations. *IEEE Trans. Microw. Theory Tech.* **1975**, *23* (8), 623–630. https://doi.org/10.1109/TMTT.1975.1128640.

(123) Taflove, A.; Brodwin, M. E. Computation of the Electromagnetic Fields and Induced Temperatures Within a Model of the Microwave-Irradiated Human Eye. *IEEE Trans. Microw. Theory Tech.* **1975**, *23* (11), 888–896. https://doi.org/10.1109/TMTT.1975.1128708.

(124) Taflove, A.; Hagness, S. C.; Piket-May, M. 9 - Computational Electromagnetics: The Finite-Difference Time-Domain Method. In *The Electrical Engineering Handbook*; Chen, W.-K., Ed.; Academic Press: Burlington, 2005; pp 629–670. https://doi.org/10.1016/B978-012170960-0/50046-3.

(125) Chen, S.; Wang, Y. jie; Liu, Q.; Shi, G.; Liu, Z.; Lu, K.; Han, L.; Ling, X.; Zhang, H.; Cheng, S.; Ma, W. Broadband Enhancement of PbS Quantum Dot Solar Cells by the Synergistic Effect of Plasmonic Gold Nanobipyramids and Nanospheres. *Adv. Energy Mater.* **2018**, *8* (8), 1701194. https://doi.org/10.1002/aenm.201701194.

(126) Khatua, S.; Paulo, P. M. R.; Yuan, H.; Gupta, A.; Zijlstra, P.; Orrit, M. Resonant Plasmonic Enhancement of Single-Molecule Fluorescence by Individual Gold Nanorods. *ACS Nano* **2014**, *8* (5), 4440–4449. https://doi.org/10.1021/nn406434y.

(127) Zhang, X.; Gallagher, R.; He, D.; Chen, G. pH Regulated Synthesis of Monodisperse Penta-Twinned Gold Nanoparticles with High Yield. *Chem. Mater.* **2020**, *32* (13), 5626–5633. https://doi.org/10.1021/acs.chemmater.0c01090.

(128) Park, K.; Hsiao, M.-S.; Koerner, H.; Jawaid, A.; Che, J.; Vaia, R. A. Optimizing Seed Aging for Single Crystal Gold Nanorod Growth: The Critical Role of Gold Nanocluster Crystal Structure. *J. Phys. Chem. C* **2016**, *120* (49), 28235–28245. https://doi.org/10.1021/acs.jpcc.6b08509.

(129) Geitner, N. K.; Doepke, A.; Fickenscher, M. A.; Yarrison-Rice, J. M.; Heineman, W. R.; Jackson, H. E.; Smith, L. M. The Morphology and Evolution of Bipyramidal Gold Nanoparticles. *Nanotechnology* **2011**, *22* (27), 275607. https://doi.org/10.1088/0957-4484/22/27/275607.

(130)   Chow, T. H.; Li, N.; Bai, X.; Zhuo, X.; Shao, L.; Wang, J. Gold Nanobipyramids: An Emerging and Versatile Type of Plasmonic Nanoparticles. *Acc. Chem. Res.* **2019**, *52* (8), 2136–2146. https://doi.org/10.1021/acs.accounts.9b00230.

(131)   Ngo, V. K. T.; Huynh, T. P.; Nguyen, D. G.; Nguyen, H. P. U.; Lam, Q. V.; Huynh, T. D. Synthesis and Spectroscopic Characterization of Gold Nanobipyramids Prepared by a Chemical Reduction Method. *Adv. Nat. Sci. Nanosci. Nanotechnol.* **2015**, *6* (4), 045017. https://doi.org/10.1088/2043-6262/6/4/045017.

(132)   Cheng, J.; Ge, L.; Xiong, B.; He, Y. Investigation of pH Effect on Gold Nanorod Synthesis. *J. Chin. Chem. Soc.* **2011**, *58* (6), 822–827. https://doi.org/10.1002/jccs.201190128.

(133)   Li, Q.; Zhuo, X.; Li, S.; Ruan, Q.; Xu, Q.-H.; Wang, J. Production of Monodisperse Gold Nanobipyramids with Number Percentages Approaching 100% and Evaluation of Their Plasmonic Properties. *Adv. Opt. Mater.* **2015**, *3* (6), 801–812. https://doi.org/10.1002/adom.201400505.

(134)   Long Truong, P.; Ma, X.; Jun Sim, S. Resonant Rayleigh Light Scattering of Single Au Nanoparticles with Different Sizes and Shapes. *Nanoscale* **2014**, *6* (4), 2307–2315. https://doi.org/10.1039/C3NR05211G.

(135)   Ziegler, J.; Djiango, M.; Vidal, C.; Hrelescu, C.; Klar, T. A. Gold Nanostars for Random Lasing Enhancement. *Opt. Express* **2015**, *23* (12), 15152–15159. https://doi.org/10.1364/OE.23.015152.

(136)   G. Theodorou, I.; Jiang, Q.; Malms, L.; Xie, X.; Charles Coombes, R.; O. Aboagye, E.; E. Porter, A.; P. Ryan, M.; Xie, F. Fluorescence Enhancement from Single Gold Nanostars: Towards Ultra-Bright Emission in the First and Second near-Infrared Biological Windows. *Nanoscale* **2018**, *10* (33), 15854–15864. https://doi.org/10.1039/C8NR04567D.

(137)   Becerril-Castro, I. B.; Calderon, I.; Pazos-Perez, N.; Guerrini, L.; Schulz, F.; Feliu, N.; Chakraborty, I.; Giannini, V.; Parak, W. J.; Alvarez-Puebla, R. A. Gold Nanostars: Synthesis, Optical and SERS Analytical Properties. *Anal. Sens.* **2022**, *2* (3), e202200005. https://doi.org/10.1002/anse.202200005.

(138)   De Silva Indrasekara, A. S.; Johnson, S. F.; Odion, R. A.; Vo-Dinh, T. Manipulation of the Geometry and Modulation of the Optical Response of Surfactant-Free Gold Nanostars: A Systematic Bottom-Up Synthesis. *ACS Omega* **2018**, *3* (2), 2202–2210. https://doi.org/10.1021/acsomega.7b01700.

(139)   Zhang, W.; Caldarola, M.; Lu, X.; Orrit, M. Plasmonic Enhancement of Two-Photon-Excited Luminescence of Single Quantum Dots by Individual Gold Nanorods. *ACS Photonics* **2018**, *5* (7), 2960–2968. https://doi.org/10.1021/acsphotonics.8b00306.

(140)   Guo, R.; Derom, S.; Väkeväinen, A. I.; Dijk-Moes, R. J. A. van; Liljeroth, P.; Vanmaekelbergh, D.; Törmä, P. Controlling Quantum Dot Emission by Plasmonic Nanoarrays. *Opt. Express* **2015**, *23* (22), 28206–28215. https://doi.org/10.1364/OE.23.028206.

(141)   Yang, Y.; Dev, A.; Sychugov, I.; Hägglund, C.; Zhang, S.-L. Plasmon-Enhanced Fluorescence of Single Quantum Dots Immobilized in Optically Coupled Aluminum Nanoholes. *J. Phys. Chem. Lett.* **2023**, *14* (9), 2339–2346. https://doi.org/10.1021/acs.jpclett.3c00468.

(142)   Maruo, S.; Nakamura, O.; Kawata, S. Three-Dimensional Microfabrication with Two-Photon-Absorbed Photopolymerization. *Opt. Lett.* **1997**, *22* (2), 132–134. https://doi.org/10.1364/OL.22.000132.

(143)   Mueller, J. B.; Fischer, J.; Mange, Y. J.; Nann, T.; Wegener, M. In-Situ Local Temperature Measurement during Three-Dimensional Direct Laser Writing. *Appl. Phys. Lett.* **2013**, *103* (12), 123107. https://doi.org/10.1063/1.4821556.

(144)   Vega, M. M.; Bonifacio, A.; Lughi, V.; Marsi, S.; Carrato, S.; Sergo, V. Long-Term Stability of Surfactant-Free Gold Nanostars. *J. Nanoparticle Res.* **2014**, *16* (11), 2729. https://doi.org/10.1007/s11051-014-2729-z.

(145)   Inasawa, S.; Sugiyama, M.; Yamaguchi, Y. Laser-Induced Shape Transformation of Gold Nanoparticles below the Melting Point: The Effect of Surface Melting. *J. Phys. Chem. B* **2005**, *109* (8), 3104–3111. https://doi.org/10.1021/jp045167j.

(146)   Taylor, A. B.; Siddiquee, A. M.; Chon, J. W. M. Below Melting Point Photothermal Reshaping of Single Gold Nanorods Driven by Surface Diffusion. *ACS Nano* **2014**, *8* (12), 12071–12079. https://doi.org/10.1021/nn5055283.

(147)   Demchenko, D. O.; Wang, L.-W. Optical Transitions and Nature of Stokes Shift in Spherical CdS Quantum Dots. *Phys. Rev. B* **2006**, *73* (15), 155326. https://doi.org/10.1103/PhysRevB.73.155326.

(148)   Voznyy, O.; Levina, L.; Fan, F.; Walters, G.; Fan, J. Z.; Kiani, A.; Ip, A. H.; Thon, S. M.; Proppe, A. H.; Liu, M.; Sargent, E. H. Origins of Stokes Shift in PbS Nanocrystals. *Nano Lett.* **2017**, *17* (12), 7191–7195. https://doi.org/10.1021/acs.nanolett.7b01843.

(149)   Hao, J.; Liu, H.; Miao, J.; Lu, R.; Zhou, Z.; Zhao, B.; Xie, B.; Cheng, J.; Wang, K.; Delville, M.-H. A Facile Route to Synthesize CdSe/ZnS Thick-Shell Quantum Dots with Precisely Controlled Green Emission Properties: Towards QDs Based LED Applications. *Sci. Rep.* **2019**, *9* (1), 12048. https://doi.org/10.1038/s41598-019-48469-7.

(150)   Balci, S. Ultrastrong Plasmon–Exciton Coupling in Metal Nanoprisms with J-Aggregates. *Opt. Lett.* **2013**, *38* (21), 4498–4501. https://doi.org/10.1364/OL.38.004498.

(151)   Li, B.; Zu, S.; Zhang, Z.; Zheng, L.; Jiang, Q.; Du, B.; Luo, Y.; Gong, Y.; Zhang, Y.; Lin, F.; Shen, B.; Zhu, X.; Ajayan, P. M.; Fang, Z. Large Rabi Splitting Obtained in Ag-WS2 Strong-Coupling Heterostructure with Optical Microcavity at Room Temperature. *Opto-Electron. Adv.* **2019**, *2* (5), 190008. https://doi.org/10.29026/oea.2019.190008.

(152)   Guvenc, C. M.; Balci, F. M.; Sarisozen, S.; Polat, N.; Balci, S. Colloidal Bimetallic Nanorings for Strong Plasmon Exciton Coupling. *J. Phys. Chem. C* **2020**, *124* (15), 8334–8340. https://doi.org/10.1021/acs.jpcc.0c01011.

(153)   Stührenberg, M.; Munkhbat, B.; Baranov, D. G.; Cuadra, J.; Yankovich, A. B.; Antosiewicz, T. J.; Olsson, E.; Shegai, T. Strong Light–Matter Coupling between Plasmons in Individual Gold Bi-Pyramids and Excitons in Mono- and Multilayer WSe2. *Nano Lett.* **2018**, *18* (9), 5938–5945. https://doi.org/10.1021/acs.nanolett.8b02652.

(154)   Lee, Y.-M.; Kim, S.-E.; Park, J.-E. Strong Coupling in Plasmonic Metal Nanoparticles. *Nano Converg.* **2023**, *10* (1), 34. https://doi.org/10.1186/s40580-023-00383-5.

(155)   Törmä, P.; Barnes, W. L. Strong Coupling between Surface Plasmon Polaritons and Emitters: A Review. *Rep. Prog. Phys. Phys. Soc. G. B.* **2015**, *78* (1), 013901. https://doi.org/10.1088/0034-4885/78/1/013901.

(156)   Kassab, L. R. P.; Silva, D. M.; Garcia, J. A. M.; Silva, D. S. da; Araújo, C. B. de. Silver Nanoparticles Enhanced Photoluminescence of Nd3+ Doped Germanate Glasses at 1064 Nm. *Opt. Mater.* **2016**, *C* (60), 25–29. https://doi.org/10.1016/j.optmat.2016.07.006.

(157)   Kassab, L. R. P.; Bomfim, F. A.; Martinelli, J. R.; Wetter, N. U.; Neto, J. J.; de Araújo, C. B. Energy Transfer and Frequency Upconversion in Yb3+–Er3+-Doped PbO-GeO2 Glass Containing Silver Nanoparticles. *Appl. Phys. B* **2009**, *94* (2), 239–242. https://doi.org/10.1007/s00340-008-3249-2.

(158)   Zhan, Q.; Zhang, X.; Zhao, Y.; Liu, J.; He, S. Tens of Thousands-Fold Upconversion Luminescence Enhancement Induced by a Single Gold Nanorod. *Laser Photonics Rev.* **2015**, *9* (5), 479–487. https://doi.org/10.1002/lpor.201500013.

(159)   Yuan, P.; Lee, Y. H.; Gnanasammandhan, M. K.; Guan, Z.; Zhang, Y.; Xu, Q.-H. Plasmon Enhanced Upconversion Luminescence of NaYF4:Yb,Er@SiO2@Ag Core–Shell Nanocomposites for Cell Imaging. *Nanoscale* **2012**, *4* (16), 5132–5137. https://doi.org/10.1039/C2NR31241G.

(160)   Martínez, E. D.; Urbano, R. R.; Rettori, C. Thermoplasmonic Enhancement of Upconversion in Small-Size Doped NaGd(Y)F4 Nanoparticles Coupled to Gold Nanostars. *Nanoscale* **2018**, *10* (30), 14687–14696. https://doi.org/10.1039/C8NR01639A.

(161)   Jiao, Y.; Ling, C.; Wang, J.-X.; Amanico, H.; Saczek, J.; Wang, H.; Sridhar, S.; Xu, B. B.; Wang, S.; Wang, D. Controllable Synthesis of Upconversion Nanophosphors toward Scale-Up Productions. *Part. Part. Syst. Charact.* **2020**, *37* (9), 2000129. https://doi.org/10.1002/ppsc.202000129.

(162)   Klinkova, A.; Larin, E. M.; Prince, E.; Sargent, E. H.; Kumacheva, E. Large-Scale Synthesis of Metal Nanocrystals in Aqueous Suspensions. *Chem. Mater.* **2016**, *28* (9), 3196–3202. https://doi.org/10.1021/acs.chemmater.6b00936.

(163)   Yin, A.; Zhang, Y.; Sun, L.; Yan, C. Colloidal Synthesis and Blue Based Multicolor Upconversion Emissions of Size and Composition Controlled Monodisperse Hexagonal NaYF4 : Yb,Tm Nanocrystals. *Nanoscale* **2010**, *2* (6), 953–959. https://doi.org/10.1039/B9NR00397E.

(164)   Chen, G.; Yang, C.; Prasad, P. N. Nanophotonics and Nanochemistry: Controlling the Excitation Dynamics for Frequency Up- and Down-Conversion in Lanthanide-Doped Nanoparticles. *Acc. Chem. Res.* **2013**, *46* (7), 1474–1486. https://doi.org/10.1021/ar300270y.

(165)   Lu, D.; Cho, S. K.; Ahn, S.; Brun, L.; Summers, C. J.; Park, W. Plasmon Enhancement Mechanism for the Upconversion Processes in NaYF4:Yb3+,Er3+ Nanoparticles: Maxwell versus Förster. *ACS Nano* **2014**, *8* (8), 7780–7792. https://doi.org/10.1021/nn5011254.

(166)   Kubiak, K.; Adamczyk, Z.; Maciejewska, J.; Oćwieja, M. Gold Nanoparticle Monolayers of Controlled Coverage and Structure. *J. Phys. Chem. C* **2016**, *120* (22), 11807–11819. https://doi.org/10.1021/acs.jpcc.6b02683.

(167)   Feng, A. L.; You, M. L.; Tian, L.; Singamaneni, S.; Liu, M.; Duan, Z.; Lu, T. J.; Xu, F.; Lin, M. Distance-Dependent Plasmon-Enhanced Fluorescence of Upconversion Nanoparticles Using Polyelectrolyte Multilayers as Tunable Spacers. *Sci. Rep.* **2015**, *5* (1), 7779. https://doi.org/10.1038/srep07779.

(168)   Zhang, W.; Hu, G.; Zhang, W.; Qiao, X.; Wu, K.; Chen, Q.; Cai, Y. Surfactant-Directed Synthesis of Silver Nanorods and Characteristic Spectral Changes Occurred by Their Morphology Evolution. *Phys. E Low-Dimens. Syst. Nanostructures* **2014**, *64*, 211–217. https://doi.org/10.1016/j.physe.2014.07.029.

(169)   Chatterjee, S.; Ricciardi, L.; Deitz, J. I.; Williams, R. E. A.; McComb, D. W.; Strangi, G. Heterodimeric Plasmonic Nanogaps for Biosensing. *Micromachines* **2018**, *9* (12), 664. https://doi.org/10.3390/mi9120664.

(170)   Hepperle, P.; Baek, W. Y.; Nettelbeck, H.; Rabus, H. Deposition of Gold Nanoparticles on a Self-Supporting Carbon Foil. *Part. Part. Syst. Charact.* **2022**, *39* (11), 2200136. https://doi.org/10.1002/ppsc.202200136.

(171)   Ahmad, I.; Jan, R.; Khan, H. U.; Khattak, S. A.; Murad, Y. Assembly of Nanoparticles at Symmetric Coffee Stain Locations. *Colloids Surf. Physicochem. Eng. Asp.* **2024**, *682*, 132833. https://doi.org/10.1016/j.colsurfa.2023.132833.

(172)   Kang, F.; He, J.; Sun, T.; Bao, Z. Y.; Wang, F.; Lei, D. Y. Plasmonic Dual-Enhancement and Precise Color Tuning of Gold Nanorod@SiO2 Coupled Core–Shell–Shell Upconversion Nanocrystals. *Adv. Funct. Mater.* **2017**, *27* (36), 1701842. https://doi.org/10.1002/adfm.201701842.

(173)   Zhang, H.; Xu, D.; Huang, Y.; Duan, X. Highly Spectral Dependent Enhancement of Upconversion Emission with Sputtered Gold Island Films. *Chem. Commun.* **2011**, *47* (3), 979–981. https://doi.org/10.1039/C0CC03566A.

(174)   Menyuk, N.; Dwight, K.; Pierce, J. w. NaYF4 : Yb,Er—an Efficient Upconversion Phosphor. *Appl. Phys. Lett.* **1972**, *21* (4), 159–161. https://doi.org/10.1063/1.1654325.

(175)   Martínez, R.; Polo, E.; Barbosa, S.; Taboada, P.; del Pino, P.; Pelaz, B. 808 Nm-Activable Core@multishell Upconverting Nanoparticles with Enhanced Stability for Efficient Photodynamic Therapy. *J. Nanobiotechnology* **2020**, *18* (1), 85. https://doi.org/10.1186/s12951-020-00640-3.

(176)   Vial, S.; Pastoriza-Santos, I.; Pérez-Juste, J.; Liz-Marzán, L. M. Plasmon Coupling in Layer-by-Layer Assembled Gold Nanorod Films. *Langmuir* **2007**, *23* (8), 4606–4611. https://doi.org/10.1021/la063753t.

(177)   Lee, K.-T.; Park, J.-H.; Kwon, S. J.; Kwon, H.-K.; Kyhm, J.; Kwak, K.-W.; Jang, H. S.; Kim, S. Y.; Han, J. S.; Lee, S.-H.; Shin, D.-H.; Ko, H.; Han, I.-K.; Ju, B.-K.; Kwon, S.-H.; Ko, D.-H. Simultaneous Enhancement of Upconversion and Downshifting Luminescence via Plasmonic Structure. *Nano Lett.* **2015**, *15* (4), 2491–2497. https://doi.org/10.1021/nl5049803.

(178)   Wang, F.; Banerjee, D.; Liu, Y.; Chen, X.; Liu, X. Upconversion Nanoparticles in Biological Labeling, Imaging, and Therapy. *Analyst* **2010**, *135* (8), 1839–1854. https://doi.org/10.1039/C0AN00144A.

142

9 Appendices

9.1 Python script for masking FLIM images

```python
import pandas as pd
import os


# Step 3: Specify the directory where your *.dat files are located
directory = r"C:\Users\mamaevak\Desktop\Experiments\FLIM\Masks"


# Step 4: Iterate over the *.dat files in the directory
for filename in os.listdir(directory):
    if filename.endswith("_2.dat"):  # Filter for files ending with "_2.dat"
        base_name = filename.split("_2")[0]  # Extract the name before "_2"


        with open(os.path.join(directory, filename), 'r') as file:
            lines = file.readlines()


        # Find the start indices for intensity and average lifetime data
        intensity_start = [i for i, line in enumerate(lines) if "Intens. :" in line]
        av_lifetime_start = [i for i, line in enumerate(lines) if "Aver. LT:" in line]


        if intensity_start and av_lifetime_start:
            intensity_start_index = intensity_start[0] + 1
            av_lifetime_start_index = av_lifetime_start[0] + 1


            # Extract intensity and average lifetime data
            intensity_data = [line.split() for line in lines[intensity_start_index:intensity_start_index + 300]]
            av_lifetime_data = [line.split() for line in lines[av_lifetime_start_index:av_lifetime_start_index + 300]]


            # Create a dataframe for each dataset
            intensity_df = pd.DataFrame(intensity_data).astype(float)
```

```
av_lifetime_df = pd.DataFrame(av_lifetime_data).astype(float)


# Set negative values to zero

intensity_df[intensity_df < 0] = 0

av_lifetime_df[av_lifetime_df < 0] = 0


# Create an Excel file with three sheets

output_filename = f"{base_name}.xlsx"

writer = pd.ExcelWriter(output_filename, engine='xlsxwriter')

intensity_df.to_excel(writer, sheet_name=f"{base_name}_intensity", index=False)

av_lifetime_df.to_excel(writer, sheet_name=f"{base_name}_av_lifetime", index=False)


# Calculate cell by cell data from both sheets

combined_df    =    (intensity_df    >    intensity_df.shift())    &    (av_lifetime_df    <
av_lifetime_df.shift())

combined_df = combined_df.astype(int)

combined_df.to_excel(writer, sheet_name=f"{base_name}_combined", index=False)


writer._save()
```

9.2   Synthesis parameters

Table 3: Synthesis parameters for BPs shown in Figure 4.20.

	v(AgNO₃) (μL)	v(HAuCl₄) (mL)	v(HCl) (mL)	v(seeds) (μL)		v(AgNO₃) (μL)	v(HAuCl₄) (mL)	v(HCl) (mL)	v(seeds) (μL)
Batch 1	100	0.5	0.30	60	Batch 17	100	0.5	0.40	60
Batch 2	150	0.5	0.30	60	Batch 18	100	0.5	0.40	60
Batch 3	200	0.5	0.30	60	Batch 19	200	0.5	0.40	60
Batch 4	100	0.5	0.40	60	Batch 20	400	0.5	0.40	60
Batch 5	100	0.5	0.60	60	Batch 21	75	0.7	0.40	60
Batch 6	100	0.5	0.80	60	Batch 22	85	0.7	0.40	60
Batch 7	100	0.5	0.30	60	Batch 23	100	0.7	0.40	60
Batch 8	100	0.5	0.40	60	Batch 24	50	0.6	0.40	60
Batch 9	100	0.5	0.20	60	Batch 25	75	0.6	0.40	60
Batch 10	100	0.5	0.30	60	Batch 26	100	0.6	0.40	60
Batch 11	100	0.5	0.40	60	Batch 27	100	0.5	0.30	60
Batch 12	100	0.5	0.20	60	Batch 28	150	0.5	0.30	60
Batch 13	100	0.5	0.25	60	Batch 29	200	0.5	0.30	60
Batch 14	100	0.5	0.30	60	Batch 30	100	0.5	0.30	60

| Batch 15 | 100 | 0.5 | 0.20 | 60 | Batch 31 | 150 | 0.5 | 0.30 | 60 |
| Batch 16 | 100 | 0.5 | 0.30 | 60 | Batch 32 | 200 | 0.5 | 0.30 | 60 |

Table 4: Synthesis parameters for BPs shown in Figure 5.3.
Samples with same number (e.g. 23a and 23c) were synthesised on the same day.

BP	Sample name	v(ascorbic acid) (µL)	v(AgNO₃) (µL)	v(HAuCl₄) (mL)	v(HCl) (mL)	v(seeds) (µL)	Seed type and synthesis day	v(CTAB) (mL)
1	22d	75	100	0.5	0.3	60	Type II (previous day)	10
2	23a	75	100	0.5	0.3	60	Type II (same day)	10
3	22f	75	200	0.5	0.3	60	Type II (previous day)	10
4	23c	75	200	0.5	0.3	60	Type II (same day)	10
5	22g	80	100	0.5	0.3	60	Type II (previous day)	10
6	22i	80	200	0.5	0.3	60	Type II (previous day)	10
7	22h	80	150	0.5	0.3	60	Type II (previous day)	10
8	23d	80	100	0.5	0.3	60	Type II (same day)	10
9	23f	80	200	0.5	0.3	60	Type II (same day)	10
10	2b	75	100	0.5	0.6	60	Type II (same day)	10
11	16a	80	100	0.5	0.3	60	Type II (same day)	10
12	16c	80	200	0.5	0.3	60	Type II (same day)	10
13	23g	85	100	0.5	0.3	60	Type II (same day)	10
14	16d	85	100	0.5	0.3	60	Type II (same day)	10